# Large Amplitude Oscillatory Shear investigations of colloidal systems: experiments and constitutive model predictions

Zur Erlangung des akademischen Grades eines
DOKTORS DER NATURWISSENSCHAFTEN
(Dr. rer. nat.)
KIT-Fakultät für Chemie und Biowissenschaften
Karlsruher Institut fär Technologie (KIT) - Universitätsbereich
genehmigte
DISSERTATION
von
Dipl.-Chem. Dimitri Merger
aus
Rubzowsk

KIT-Dekan: Prof. Dr. Willem M. Klopper
Referent: Prof. Dr. Manfred Wilhelm
Korreferent: Prof. Dr. Rolf Schuster
Tag der mündlichen Prüfung: 23.10.2015

Diese Arbeit wurde in der Zeit vom 1. August 2012 bis zum 9. September 2015 am Institut für Technische Chemie und Polymerchemie des Karlsruher Instituts für Technologie unter Anleitung von Prof. Dr. Manfred Wilhelm durchgeführt.

Hiermit versichere ich, dass ich die von mir vorgelegte Arbeit selbstständig verfasst habe, dass ich die verwendeten Quellen und Hilfsmittel vollständig angegeben und die Stellen der Arbeit, die anderen Werken im Wortlaut oder dem Sinn nach entnommen sind, entsprechend kenntlich gemacht habe.

Karlsruhe, den 04.09.2015

# Zusammenfassung

In der vorliegenden Arbeit werden rheologische Experimente zur Charakterisierung der nichtlinearen viskoelastischen Eigenschaften disperser Systeme angewendet. Einen Großteil der Experimente stellen oszillatorische Scherversuche bei großen Deformationsamplituden dar (engl. Large Amplitude Oscillatory Shear, LAOS). Mit Hilfe von LAOS-Experimenten lassen sich sowohl Frequenzabhängigkeiten, die Auskunft über elastisches und viskoses Verhalten geben, als auch Nichtlinearitäten im mechanischen Verhalten mit dem gleichen Versuch messen. Die dispersen Materialien, die untersucht worden sind, sind konzentrierte Partikelsuspensionen und kolloidale Gele aus Nanoemulsionen. Weiterhin wurden zusätzlich Tensidlösungen, die wurmartige Mizellen ausbilden, Polymerschmelzen und -lösungen mittels LAOS charakterisiert.

In der Arbeit wurde ein möglichst grundlegendes, phänomenologisches, skalares Modell zur mathematischen Beschreibung von LAOS-Experimenten entwickelt. Basierend auf dem linearen Maxwell-Modell zur Beschreibung viskoelastischer Stoffe wurde eine scherratenabhängige Viskosität eingeführt. Dadurch, ist das Modell in der Lage sowohl eine Abhängigkeit des Speicher- und Verlustmoduls von der Deformationsamplitude, als auch das Vorkommen von höheren Harmonischen im Frequenzspektrum des Schubspannungssignals zu beschreiben. Für die Validierung des Modells wurde das vorhergesagte LAOS-Verhalten mit experimentellen Ergebnissen einer Tensidlösung von Cetyltrimethyammoniumbromid verglichen. Gute Übereinstimmung für die deformationsabhängigen Speicher- und Verlustmodule, sowie für die relative Intensität der dritten harmonischen Oberwelle wurde bei niedrigen Frequenzen gefunden, bei denen das viskose Verhalten dominiert.

An einer Suspension von thermosensitiven Kern-Schale Partikeln wurde die Frequenzabhängigkeit des nichtlinearen Verhaltens von konzentrierten Suspensionen in der Nähe des Glasübergangas untersucht. Die Ergebnisse wurden mit Voraussagen der Modenkopplungstheorie verglichen. Qualitative Übereinstimmung zwischen Theorie und Experiment wurde anhand der intrinsischen Nichtlinearität $Q_0$ festgestellt, welche ein Maß dafür ist, wie klein der lineare Bereich ist.

Der Fließübergang, das heißt der Wechsel von hauptsächlich elastischem Verhalten zu viskosem Verhalten, eines kolloidalen Gels wurde mit dem LAOS-Experiment untersucht. Das Gel wurde durch Gelierung einer Nanoemulsion mittels verbrückender kurzkettiger Polymere erhalten. Durch Korrelation von nichtlinearen mechanischen Parametern, die aus einer Wellenformanalyse erhalten wurden, mit Strukturparametern aus Neutronen-

streuexperimenten konnte eine Verbindung zwischen Mikrostruktur des Gels und seinen makroskopischen mechanischen Eigenschaften hergestellt werden. Dabei ist für das untersuchte Gelsystem die Bildung von großen lösungsmittelgefüllten Poren der wichtigste Vorgang des Fließübergangs im LAOS Experiment.

Weiterhin wurden instrumentelle Aspekte der LAOS Meßtechnik behandelt. Es wurde gezeigt welche Einflüsse Faktoren wie Temperaturkontrolle, Geometriewahl und aktive Steuerungsschleifen in der Anregungskontrolle auf die Reproduzierbarkeit von LAOS Ergebnissen haben können. Bei optimierten Parametern ist zu erwarten, daß nichtlineare mechanische Kenngrößen wie $Q_0$ mit einer relativen Abweichung von unter 12% zu bestimmen sind.

Die Dissertation zeigt auf wie LAOS-Experimente an verschiedensten viskoelastischen Materialien, vor allem Dispersionen, genutzt werden können, um eine erweiterte mechanische Charakterisierung im nichtlinearen Bereich durchzuführen. Dabei führt die Kombination von mathematischer Modellierung, Experiment und zusätzlichen strukturaufklärenden Methoden zu fundamentalen Erkenntissen im Bereich der nichtlinearen Viskoelastizität, die in Zukunft zur rheologischen Optimierung von weicher Materie und für neue Analysemethoden ihrer Mikrostruktur genutzt werden können.

# Contents

# Nomenclature

| | |
|---|---|
| $2\pi\beta_{max}^{-1}$ ..... | Characteristic length scale of the phase separation in a bicontinuous structure [$\mu$m] |
| $\Gamma$ ..... | decay rate in the MCT [$s^{-1}$] |
| $\gamma$ ..... | Shear strain [-] |
| $\gamma_0$ ..... | Strain amplitude [-] |
| $\gamma_c$ ..... | Yield strain [-] |
| $\dot{\gamma}$ ..... | Shear rate [$s^{-1}$] |
| $\dot{\gamma}_0$ ..... | Shear rate amplitude [$s^{-1}$] |
| $\delta$ ..... | Phase angle [rad] |
| $\delta_n$ ..... | Phase angle of $n$th harmonic [rad] |
| $\delta(\omega)$ ..... | Phase spectrum [rad] |
| $\epsilon$ ..... | separation parameter in the MCT [-] |
| $\eta$ ..... | Shear viscosity [Pas] |
| $\eta'$ ..... | Dynamic viscosity [Pas] |
| $\eta''$ ..... | Out of phase viscosity [Pas] |
| $\eta_0$ ..... | Zero shear viscosity [Pas] |
| $\eta_r$ ..... | Relative viscosity, normalized to the viscosity of the solvent [-] |
| $\eta_s$ ..... | Solvent viscosity [Pas] |
| $\eta_\infty$ ..... | High shear rate limiting viscosity [Pas] |
| $\lambda$ ..... | Relaxation time in rheological models [s] |
| $\Sigma$ ..... | Specific surface area of voids in a heterogeneous gel structure [$m^{-1}$] |
| $\sigma$ ..... | Shear stress [Pa] |
| $\sigma_0$ ..... | Stress amplitude [Pa] |
| $\sigma_c$ ..... | Yield stress [Pas] |
| $\sigma_{red}$ ..... | Reduced stress [-] |
| $\Phi(t)$ ..... | Density fluctuation correlation function [-] |
| $\phi$ ..... | Volume fraction [-] |
| $\phi_{eff}$ ..... | Effective volume fraction determined from the high frequency behavior [-] |
| $\omega$ ..... | Angular frequency [$rads^{-1}$] |
| $a$ ..... | Particle radius in suspensions [nm] |
| $\mathbf{B}(t)$ ..... | Binormal vector |
| CMT ..... | Combined motor transducer rheometer |

CS-80 ..... core shell suspension with a particle radius of 80 nm
$c$ ..... Power index in the Ostwald-de-Waele viscosity model [-]
$D_0$ ..... Diffusion coefficient [$m^2s^{-1}$]
$De = \lambda\omega$ ..... Deborah number [-]
FCO ..... Forced convection oven
FRT ..... Force rebalance transducer
FT ..... Fourier transform
$G$ ..... Shear modulus [Pa]
$G'$ ..... Storage modulus [Pa]
$G''$ ..... Loss modulus [Pa]
$G_R$ ..... Residual modulus [Pa]
$G'_{mn}$ ..... Elastic nonlinear coefficient for the strain amplitude power $m$ and the harmonic number $n$ [Pa]
$G''_{mn}$ ..... Viscous nonlinear coefficient for the strain amplitude power $m$ and the harmonic number $n$ [Pa]
$I(\omega)$ ..... Intensity spectrum [-]
$I_{n/1}$ ..... $n$-th harmonic normalized to the first harmonic [-]
$K$ ..... Consistency in the Ostwald-de-Waele viscosity model
$k_B$ ..... Boltzmann constant [$m^2kgs^{-2}K^{-1}$]
LAOS ..... Large Amplitude Oscillatory Shear
LVR ..... Linear viscoelastic regime
$M$ ..... Torque [Nm]
MCT ..... Mode coupling theory
$M_e$ ..... Entanglement molecular weight [g/mol]
$M_n$ ..... Number averaged molecular weight [g/mol]
$M_w$ ..... Weight averaged molecular weight [g/mol]
$m(t)$ ..... memory function
$\mathbf{N}(t)$ ..... Normal vector
PDMS ..... Polydimethylsiloxane
PEGDA ..... poly(ethylene glycol) diacrylate
$Pe_0$ ..... Péclet number in steady shear [-]
$Pe_\omega$ ..... Péclet number in oscillatory shear [-]
PNipam ..... Poly(N-isopropylacrylamide)
PI ..... Polyisoprene
PIB ..... Polyisobutylene
$Q_0$ ..... Intrinsic nonlinearity [-]
$\mathbf{q}$ ..... Scattering wave vector [$nm^{-1}$] or [$Å^{-1}$]
$q$ ..... Absolute value of the scattering wave vector [$nm^{-1}$] or [$Å^{-1}$]
$R'(t)$ ..... Time dependent storage modulus [Pa] from the sequence of physical processes analysis
$R''(t)$ ..... Time dependent loss modulus [Pa] from the sequence of physical processes

| | |
|---|---|
| | analysis |
| $R_H$ ..... | Hydrodynamic radius in suspensions as determined by dynamic light scattering [nm] |
| SANS ..... | Small angle neutron scattering |
| SAOS ..... | Small Amplitude Oscillatory Shear |
| SAXS ..... | Small angle X-ray scattering |
| SMT ..... | Separated motor transducer rheometer |
| $S/N$ ..... | Signal-to-Noise ratio |
| $\mathbf{T}(t)$ ..... | Tangential vector |
| $T$ ..... | Temperature [°C] |
| $T_g$ ..... | Glass transition temperature [°C] |
| $T_{gel}$ ..... | Gelation temperature [°C] |
| USANS ..... | Ultra small angle neutron scattering |
| $Wi = \lambda\dot{\gamma}$ ..... | Weissenberg number [-] |
| WLM ..... | Wormlike micelle |
| $v_\sigma$ ..... | stress parameter in the MCT |

# Chapter 1

# Introduction

If our world consisted of solids and liquids that were as ideal as those described by Hooke and Newton, quite unusual situations would occur. Applying a purely Newtonian paint to a wall would either be rather exhaustive due to the high viscosity of the paint or the paint would simply run down the wall before it was dry if the viscosity was too low. This example shows that a Newtonian fluid, which has a shear rate independent viscosity, is undesirable for certain applications.

Another example of a liquid that is not ideal, is dough. When mixing dough of sufficiently high flour concentration, it climbs up the stirrer instead of flowing to the walls of the bowl. This effect is known as the Weissenberg effect and is caused by an elastic component of the dough. Therefore, dough is neither an ideal fluid nor an ideal solid.

It turns out that the definitions of solid and liquid depend on the timescale of observation and on the applied loads, deformations and rates of deformations. In fact, most everyday materials appear to be solid at certain deformations/deformation rates, but liquid at others, they are therefore viscoelastic. Additionally, all real life materials display nonlinear mechanical properties at high enough stresses, large enough deformations or high rates of deformation. Nonlinear means that the stress is not proportional to the deformation or the deformation rate. Wall paint with its variable viscosity is a classic example of a material with nonlinear mechanical properties.

The term 'complex fluid' is used for many viscoelastic materials which surround us: they are foods, biomaterials, such as blood and joint fluid, or personal care products (Larson 1999). Some are not as obvious in everyday life but are of equal technological importance: electronic/optical materials, oil field fluids and freshly mixed cement. It is imperative to study complex fluids by rheological methods to improve production and application performance of these products. An intriguing overview of complex fluids, which is not supposed to be exhaustive, has been recently presented (McKinley 2015). It is reproduced in reduced form in Fig. 1.1 and contains three main classes: dispersions, surfactant micelles and polymers. The complexity of the systems' structures and rheological properties increases with a characteristic system property, such as volume fraction $\phi$ or concentration $c$. Encircled classes - particulate gels, concentrated suspensions, wormlike micelles and

polymer melt and solutions - have been studied in this thesis by means of rheology in order to characterize their nonlinear viscoelastic behavior. They represent a rather broad selection from the available possibilities. The boundaries in Fig. 1.1 are by no means strict and many combinations exist that are not specifically mentioned, for example particulate dispersions in viscoelastic media or wormlike micelle - nanoparticle mixtures (Helgeson 2010).

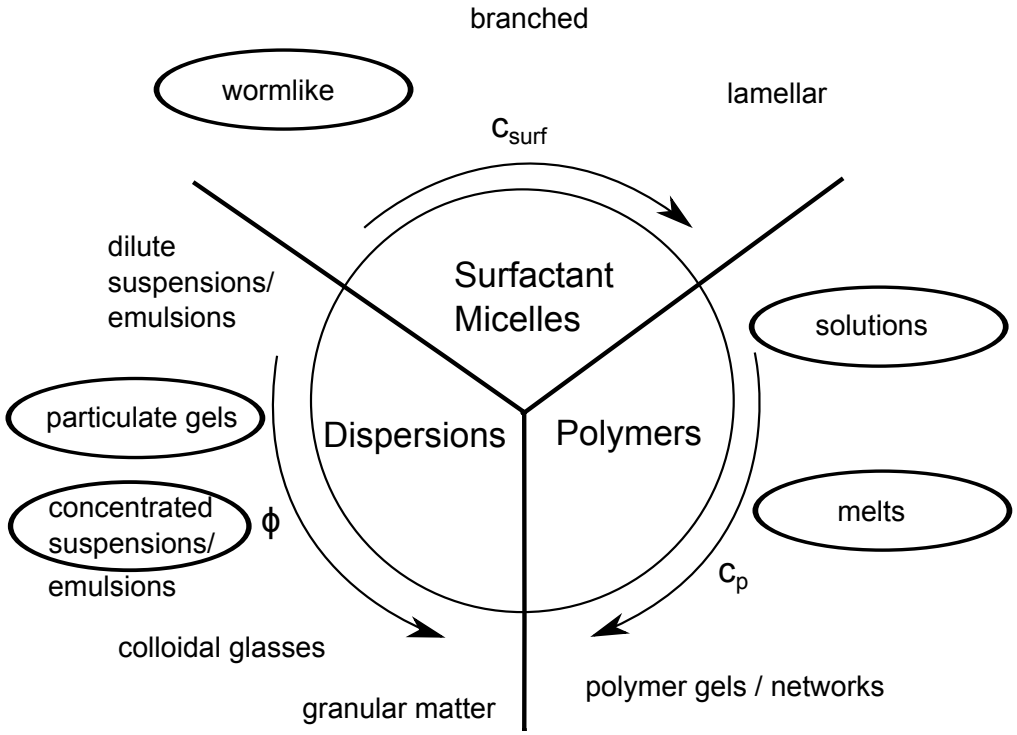


**Figure 1.1:** Overview of complex fluids, reproduced after McKinley (2015). Three main classes can be defined: dispersions, surfactant micelles and polymers. The complexity of the systems' structures and rheological properties increases with a characteristic system property, volume fraction $\phi$, concentration of the surfactant $c_{surf}$ or polymer concentration $c_p$. Classes that have been investigated in this thesis are encircled. Note that this overview is not exhaustive and other classes or combinations of the mentioned classes exist at the interfaces.

Dispersions, which are systems of at least two immiscible phases, are typical complex fluids that exhibit viscoelastic behavior over a wide range of compositions. Prominent examples are concentrated suspensions, emulsions, foams or particulate gels. It is viscoelasticity, linear and nonlinear, that often provides the necessary functionality of a substance. Dispersions, such as the previously mentioned wall paint, display nonlinear rheological properties. They are designed so that their viscosity decreases under increasing stress. This means that they are easy to apply to a wall but do not flow too fast under the influence of gravity. An example where viscous and elastic properties are desired is filled rubber, which can in principle be viewed as a dispersion of carbon black particles in a cross-linked polymer matrix. Filled rubbers for tires need to be more elastic at lows frequencies to have a small rolling resistance, but, at high frequencies, they need viscous properties to maintain contact with the road, especially when the road is wet (Saeed2011 et al. 2011).

Viscoelasticity originates from the specific microscopic structure of a material, therefore tuning the structure modifies the initial mechanical properties. These mechanical properties determine the processing conditions but at the same time certain final properties are desired for the application of the product. The two requirements often do not coincide. Additionally, the processing itself can modify the structure. The mutual interdependence of structure, processing and application conditions can become very complex. Therefore, sophisticated characterization techniques are required, which provide information about the viscoelastic properties as a function of the structure. Rheology has therefore been combined with small angle neutron (Porcar et al. 2011), X-ray (Struth et al. 2011; Meins et al. 2012) and light scattering (Medronho et al. 2005; McMullan and Wagner 2009) as well as birefringence measurements (Clasen and Kulicke 2001).

The shear history has an important effect on the final properties of complex fluids in general and on those of dispersions in particular. First of all, aging and crystallization alter the dispersion's structure in the absence of shear (Crassous, Siebenbürger, et al. 2008). Moreover, pre-shear protocols can be used to rejuvenate dispersions to a reproducible disordered state (Mewis and Wagner 2012) or to crystallize them (Koumakis et al. 2008; McMullan and Wagner 2009). For colloidal gels, it has been reported that weak steady shear leads to more heterogeneous gels with lower moduli whereas high shear homogenizes the sample. The subsequently reformed gel then exhibit higher moduli than the heterogeneous gel (Koumakis et al. 2015).

The use of Large Amplitude Oscillatory Shear (LAOS) experiments, where a sample is subjected to a sinusoidal shear deformation $\gamma(t) = \gamma_0 \sin(\omega_1 t)$, has become a widely known technique to probe the nonlinear viscoelasticity of complex fluids (Pearson and Rochefort 1982; Giacomin and Jeyaseelan 1995; Wilhelm 2002; Hyun et al. 2011). Its main advantage is the possibility to investigate the effect of both characteristic dynamic variables, the Deborah number $De$ and the Weissenberg number $Wi$ using the same experiment.

The Deborah number $De = \lambda/\tau_o$ is defined as the ratio of a characteristic relaxation time of the material $\lambda$ and a characteristic time of observation $\tau_o$, which is the inverse of the angular frequency $\tau_o = 1/\omega$ for oscillatory shear. $De$ measures the degree to which the elastic effects influence the overall mechanical response. For $De < 1$ viscous effects dominate, whereas for $De > 1$ elasticity is the main contribution. The Weissenberg number $Wi = \lambda/\tau_d$, is the ratio of $\lambda$ and a characteristic time $\tau_d$ of the deformation, where $\tau_d$ is the inverse of the shear rate $\tau_d = 1/\dot{\gamma}$ for steady shear or $\tau_d = 1/\dot{\gamma_0} = 1/(\omega\gamma_0)$ for oscillatory shear (Dealy 2010). $Wi$ can be interpreted as a dimensionless deformation rate that indicates the importance of nonlinear behavior. For $Wi$ numbers approaching and exceeding 1, nonlinear effects cannot be neglected.

Further advantages of using LAOS are of instrumental nature and include the omission of sudden signal jumps in the input, as in step experiments, and the ability to probe large strain rates without accumulating very large strains that may lead to edge failure (Blackwell and Ewoldt 2014).

First applications of LAOS to characterize properties which are important for processing

include relating blow moldability (Giacomin et al. 1994) to nonlinear shear rheology and quantification of the branching degree in comb polymers (Kempf et al. 2013). Furthermore, LAOS has been used to infer microscopic properties of emulsions, such as the droplet radius or the interfacial tension (Reinheimer et al. 2011; Reinheimer et al. 2012), from nonlinear oscillatory rheological measurements.

Modeling of LAOS flow by nonlinear constitutive equations is crucial for the development of such applications and for predictions of flow behavior in complex geometries via fluid dynamics calculations. Nonlinear models of varying complexity exist already, but so far they are not powerful enough to quantitatively predict different nonlinear flows (Bird et al. 1987; Morrison 2001; Giacomin et al. 2011). Usually, they are solved numerically due to their complexity. Recent efforts in constitutive modeling have led to asymptotic solutions that provide material functions for a couple of nonlinear models, including the corotational Maxwell model (Giacomin et al. 2011), the Giesekus model (Gurnon and Wagner 2012), the Pompom model (Hoyle et al. 2014), the molecular stress function model (Wagner et al. 2011; Abbasi et al. 2013) and a Jefferson model, which includes thixotropic behavior (Blackwell and Ewoldt 2014). Although analytical solutions are generally to be preferred because material functions can be calculated explicitly, arriving at these solutions usually involves careful tedium. In most cases, only truncated power series expanded in strain amplitude or shear rate amplitude can be obtained. Furthermore, the work needed to determine higher order terms of the expansions increases disproportionately but yields only little improvement in accuracy. Therefore, one part of the thesis contains a modeling approach based on the widely known 1D-Maxwell model, the simplest model of a viscoelastic fluid, which is modified to account for nonlinear behavior.

The main objective of this thesis is to investigate selected soft matter systems under LAOS flow in order to gain insight into their microscopic structure. Since rheology is a macroscopic method, direct interpretations are difficult. Nevertheless, with the help of constitutive modeling and additional techniques for structural investigation under flow, such as neutron scattering, correlations are possible.

The thesis begins with introducing the fundamental concepts of shear rheology and Large Amplitude Oscillatory shear in Chapter 2. Basic physico-chemical descriptions of the systems under investigation can be found in Chapter 3. Experimental chapters contain technical aspects of LAOS rheometry (Chapter 4) and results from rheological experiments on a wormlike micellar solution (Chapter 5), dense colloidal dispersions (Chapter 6) and colloidal gels based on nanoemulsions (Chapter 7). The wormlike micelles results are used for the validation of a simple phenomenological model to describe nonlinear viscoelasticity in LAOS experiments. Measurements of dispersions are compared to predictions of the mode coupling theory. Colloidal gel data is correlated to a structural investigation by small angle neutron scattering.

# Chapter 2

# Linear and nonlinear shear rheology

This chapter contains some fundamental concepts of rheology and in particular oscillatory shear rheology, that can be found in every basic text on rheology. Especially recommended are the works of Macosko (1994); Morrison (2001); Shaw (2012) and Larson (1999). Based on the fundamentals of linear oscillatory rheology, often called small amplitude oscillatory shear (SAOS), the extension to larger amplitudes, where nonlinear effects occur, will be presented. The focus will be set on showing that large amplitude oscillatory shear (LAOS) experiments are a natural and useful extension of the rheological methods already known.

## 2.1 Fundamentals of rheology

Rheology is defined as the science of deformation and flow of materials. It is based on two fundamental quantities: First, the deformation of a body (and connected to it the deformation rate). Second, the stress acting on the body that is necessary to produce this deformation. Measuring and describing the relationship between deformation and stress via constitutive models is the most important goal in rheology. The obvious application for these relationships is the closure of the Navier-Stokes equations that in principle allow solving any flow problem. Furthermore, rheology can be used as an analytical tool to investigate microscopic properties of a material, if appropriate models are available that connect microstructure and macroscopic flow behavior. An example for such a microscopic model has been developed for emulsions, where a tensor that describes the deformed droplets depending on the deformation, was connected to the macroscopic stress (Reinheimer et al. 2011; Reinheimer et al. 2012).
In the most simple, scalar version, the stress and the deformation can be defined using the simple shear experiment, as depicted in Fig. 2.1. If a cuboid of height $h$ and the area $A$ is fixed on one side, then a force $F$ acting on the other side in x-direction produces a shear stress $\sigma$ equal to the force normalized by the area $A$, therefore the stress has units of pressure. The stress leads to a deformation of the body's dimensions. If the body is a fluid,

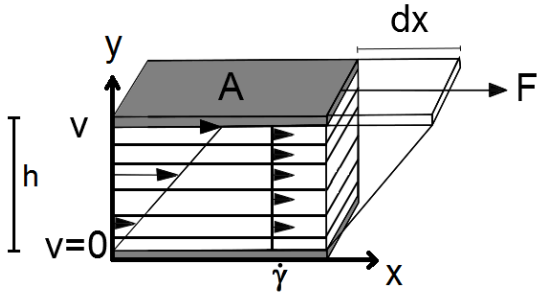


**Figure 2.1:** Simple shear experiment on a cuboid body between two plates: The lower plate is fixed, the upper plate is pulled by a force $F$. Geometry independent rheological quantities can be defined as stress $\sigma = F/A$, strain $\gamma = \mathrm{d}x/h$ and shear rate $\dot{\gamma} = \mathrm{d}\gamma/\mathrm{d}t = v/h$.

then the upper side will be moving with a velocity $v = \mathrm{d}x/\mathrm{d}t$ in x-direction. Normalizing the length $\mathrm{d}x$ by the height $h$, gives the unitless quantity of deformation $\gamma$, called strain. Henceforth in this thesis only the term strain will be used for $\gamma$. In the general case, strain and stress are tensorial quantities of order 2, but in this thesis all descriptions will be kept scalar.

$$\sigma = \frac{F}{A} \tag{2.1}$$

$$\gamma = \frac{\mathrm{d}x}{h} \tag{2.2}$$

$$\dot{\gamma} = \frac{\mathrm{d}\gamma}{\mathrm{d}t} = \frac{v}{h} \tag{2.3}$$

Two idealized archetypes of material behavior that connect $\sigma$ and $\gamma$ exist: For the ideal elastic solid, as defined by Hooke, $\sigma$ is proportional to $\gamma$, with the proportionality constant $G$, called the shear modulus (Eq. 2.4) and measured in units of Pa. Equation 2.4 is the essentially the same law as for a one dimensional spring, where the force $F$ is proportional to the elongation $\mathrm{d}x$. Examples for ideals solids are pure metals, alloys or amorphous solid glasses (aluminum, $G \sim 25$ GPa, steel, ~80 GPa, $SiO_2$, ~26 GPa, Crandall et al. 2012 ). Values of $G$ are generally temperature dependent and the ones stated are for $T = 25°\mathrm{C}$.

$$\sigma = G\gamma \tag{2.4}$$

For an ideal liquid, $\sigma$ is not a function of $\gamma$ but of its time derivative, the shear rate. Newton's law states that the ideal liquid resists shear, whereby $\sigma$ is linear in the shear rate $\dot{\gamma}$. The quantity measuring this resistance is the viscosity $\eta$ (Eq. 2.5) in units of Pascal seconds, Pas. Examples for ideal Newtonian liquids are fluids of low molecular weight molecules, for example water ($\eta = 0.89$ mPas, Weast 1976), organic solvents (e.g. tetrahydrofuran, 0.47 mPas, Hayduk et al. 1973) or biological oils, which are triglycerides of fatty acids (palm oil ~77 mPas, *Chempro*). Viscosities are temperature dependent as

well, again $T = 25°\mathrm{C}$ for the stated values.

$$\sigma = \eta\dot{\gamma} \tag{2.5}$$

### 2.1.1 The Maxwell model

Complex fluids behave neither like Hookean solids nor like Newtonian liquids for a wide range of concentrations and/or molecular weights, but show an intricate combination of both elastic and viscous effects. The simplest way of incorporating elastic effects for a fluid is a serial combination of a Hookean solid with a Newtonian liquid, introduced by Maxwell. A schematic for the Maxwell model is depicted in Fig. 2.2, where the spring is Hookean and the dashpot is Newtonian.

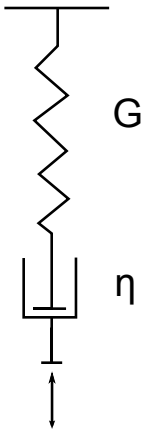


**Figure 2.2:** Simplest model that incorporates elastic effects for a fluid: a serial combination of a Hookean solid with a Newtonian liquid, known as the Maxwell model.

The differential equation for this model can be set up by considering that the stress $\sigma$ in the spring (indexed with an s) and the dashpot (indexed with a d) are equal, and the sum of the individual strains equals the total strain. Furthermore, the sum of the individual shear rates equals the overall shear rate.

$$\sigma_s = \sigma_d \tag{2.6}$$

$$\gamma_t = \gamma_s + \gamma_d \tag{2.7}$$

$$\dot{\gamma}_t = \dot{\gamma}_s + \dot{\gamma}_d \tag{2.8}$$

Using Hooke's and Newton's laws, $\dot{\gamma}_s$ can be replaced by $\dot{\sigma}/G$ and $\dot{\gamma}_d$ by $\sigma/\eta$. Inserting these expressions into Eq. 2.8 leads to a first order differential Eq. 2.10, where a relaxation time $\lambda = \eta/G$ has been introduced.

$$\dot{\gamma}_t = \dot{\sigma}/G + \sigma/\eta \tag{2.9}$$

$$\dot{\sigma} = G\dot{\gamma}_t - \sigma/\lambda \tag{2.10}$$

The Maxwell model predicts an exponential start-up behavior (Eq. 2.11) for an experiment in which a constant $\dot{\gamma}$ is applied at $t = 0$ due to the elastic contribution of the spring. The start-up behavior is depicted in Fig. 2.3 for $G = 10$ Pa and $\lambda = 1$ s at $\dot{\gamma} = 0.3$, 1 and 3 $s^{-1}$. After some time, that depends on $\lambda = \eta/G$ a steady state is reached. In the steady state the material flows with a stress that is set by the viscosity according to Newton's law $\sigma = \eta\dot{\gamma}$ as shown in the inset of Fig. 2.3.

$$\sigma(t) = G\lambda(1 - \exp(-t/\lambda)) \tag{2.11}$$

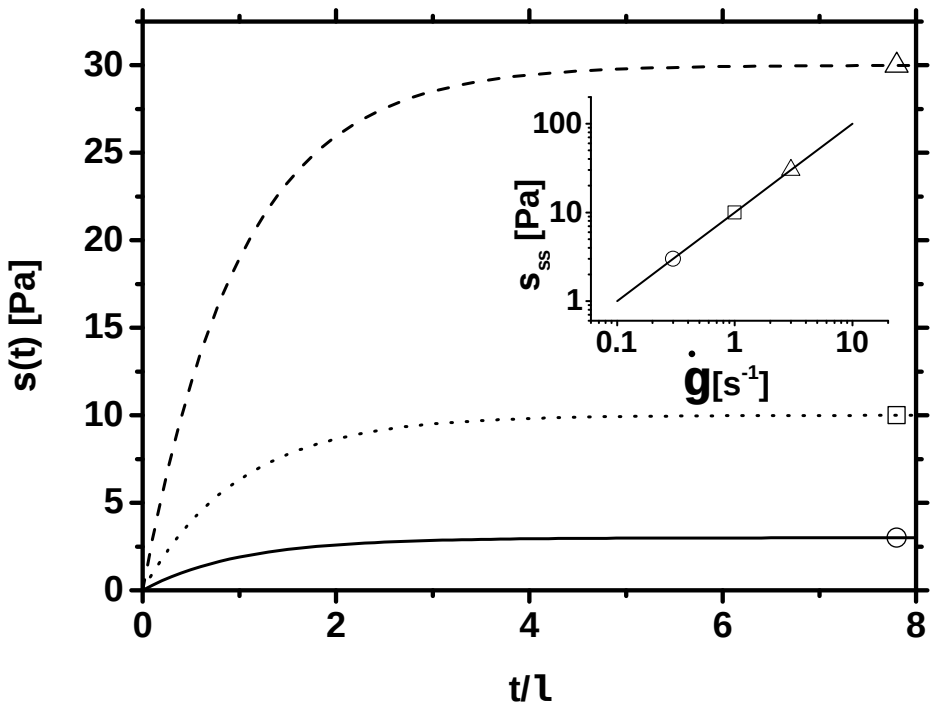


**Figure 2.3:** Start-up behavior of the Maxwell model for $G = 10$ Pa and $\lambda = 1$ s at $\dot{\gamma} = 0.3$, 1 and 3 $s^{-1}$. The steady state stress $\sigma_{ss}$ after start-up (open symbols) still follows Newton's law as shown in the inset.

### 2.1.2 Shear rate dependent viscosity

The steady shear viscosities of many complex materials, in contrast to the assumptions of the Maxwell model (Fig. 2.3), are shear rate dependent due to microstructural rearrangements, orientation effects and, for polymeric systems, chain stretching. Possible shear rate dependencies are depicted in Fig. 2.4 as $\sigma$ vs $\dot{\gamma}$ and $\eta$ vs $\dot{\gamma}$ plots. They include shear

thinning ($\eta$ decreases with increasing $\dot{\gamma}$), shear thickening ($\eta$ increases with increasing $\dot{\gamma}$) as well as the appearance of a high shear rate Newtonian range. In practicem, the most commonly observed dependency is shear thinning, which is prominent for suspensions, emulsions, polymer melts and concentrated polymer solutions, surfactant solutions and many other complex fluids. Due to the complexity of these systems it has not been possible to develop a general microstructural theory to predict shear thinning. Therefore, a variety of empirical functions are used to parametrize experimental results. A simple function to describe shear thinning and shear thickening is given, for example, by the Ostwald-de Waele model (Ostwald 1925), also known as power law model $\sigma = K\dot{\gamma}^c$. Shear thinning is captured for $c < 1$, shear thickening for $c > 1$. Note that since $c$ does not have to be an integer, the units of the consistency $K$ have to be $[\mathrm{s}^{1-c}]$. Models that include a high shear plateau viscosity $\eta_\infty$ are for example the Cross model (Cross 1968) or the Carreau-Yasuda model (Eq. 2.12, Yasuda et al. 1981). The exact shape of the curve in the transition region from $\eta_0$ to $\eta_\infty$ in the Carreau-Yasuda model is determined by the exponents $a$ and $c$. The shear rate at which this transition occurs is set by a relaxation time $\lambda$. Additionally, the Bingham (Eq. 2.13) and the Herschel-Bulkley model (Eq. 2.14) are shown in Fig. 2.4, which are discussed in the next section.

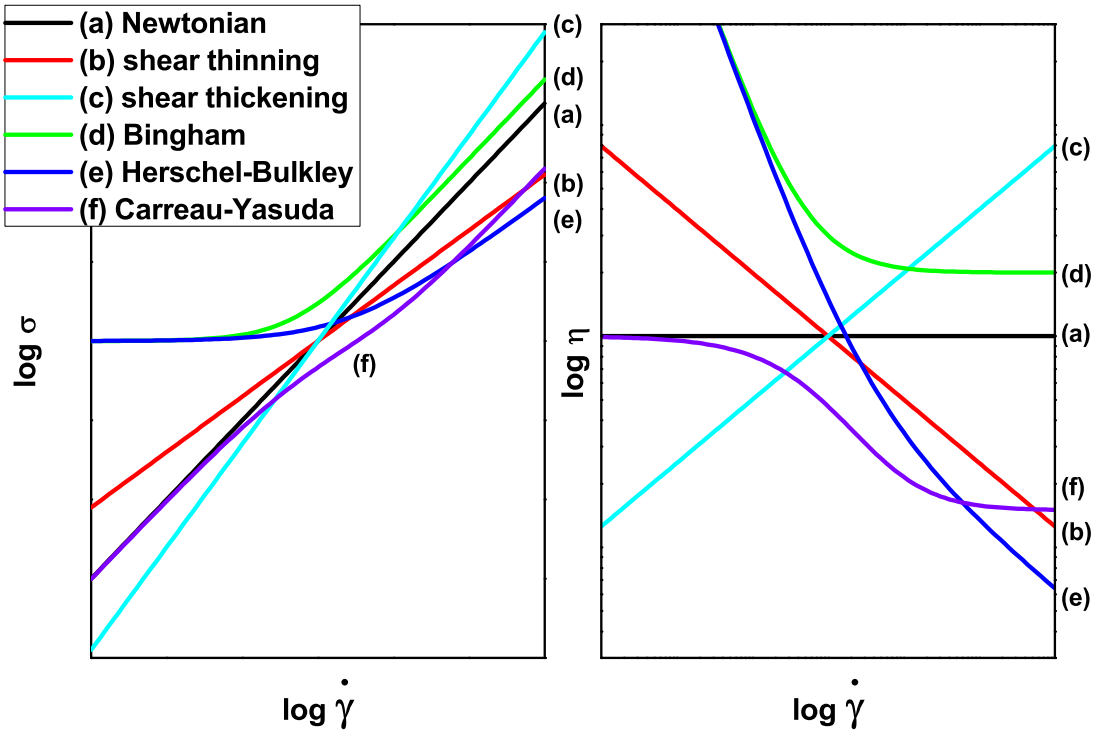


**Figure 2.4:** Possible shear rate dependencies in steady shear experiments in comparison to Newtonian behavior (a), shown as flow curves (left panel, $\sigma$ vs $\dot{\gamma}$) and viscosity curves (right panel, $\eta$ vs $\dot{\gamma}$) : shear thinning (b) and shear thickening (c) according to a power law, $\sigma = K\dot{\gamma}^c$; yield stress models: Bingham (d), Eq. 2.13, Hershel-Bulkley (e), Eq. 2.14); (f) occurence of zero shear and high shear viscosity plateaus (e.g. Carreau-Yasuda model, Eq. 2.12).

$$\sigma_{CY}(\dot{\gamma}) = \dot{\gamma}\left(\eta_\infty + (\eta_0 - \eta_\infty)[1 + (\lambda\dot{\gamma})^a]^{\frac{c-1}{a}}\right) \tag{2.12}$$

$$\sigma_B(\dot{\gamma}) = \sigma_c^B + \eta\dot{\gamma} \tag{2.13}$$

$$\sigma_{HB}(\dot{\gamma}) = \sigma_c^{HB} + \eta\dot{\gamma}^c \tag{2.14}$$

### 2.1.3 Yielding

Especially for high volume fraction dispersions and gelled systems in stress controlled steady shear experiments it has been observed that below a certain stress the samples do not flow but instead behave like a solid. Above this threshold stress, flow is possible that can be Newtonian or non-Newtonian, that is displaying a shear rate dependent viscosity. The solid to liquid transition is termed yielding and the critical stress at which it occurs, defines the yield stress $\sigma_c$. Phenomenological models that include a yield stress are for example the Bingham model (Eq. 2.13) and the Herschel-Bulkley model (Eq. 2.14, Herschel and Bulkley 1926). In the Bingham model the flow after yielding is Newtonian (Bingham 1916), whereas in the Herschel-Bulkley model a power law behavior similar to the Ostwald-de Waele model is assumed for the flowing portion.

### 2.1.4 Small Amplitude Oscillatory Shear (SAOS)

Relaxation times as introduced in the Maxwell model in Section 2.1.1 can be conveniently probed by an oscillatory experiment, where the sample is subjected to a sinusoidal strain input $\gamma(t) = \gamma_0 \sin(\omega_1 t)$ with a strain amplitude $\gamma_0$ at an angular frequency $\omega$. In this time dependent flow, a material's stress response is an oscillating function $\sigma(t) = \sigma_0 \sin(\omega_1 t + \delta)$ with the amplitude $\sigma_0$ and a phase angle $\delta$ relative to the input $\gamma(t)$ as shown in Fig. 2.5. In experiments this linearity is only valid for sufficiently small strain amplitudes, which are material dependent. The solution of the Maxwell model for small amplitude oscillatory shear flow can be described by either shear modulus and viscosity or the fundamental frequency moduli of the stress wave, the storage modulus $G'$ and the loss modulus $G''$ that are defined in Eqs. 2.15 and 2.16 for any periodic signal. The storage modulus, $G'$, is the real component as it produces stress in phase with the input $\gamma$, representing an ideal solid. The loss modulus, $G''$, is the imaginary component as it gives rise to a stress signal in phase with the shear rate $\dot{\gamma}(t)$, therefore phase shifted by 90° to the strain $\gamma(t)$. The loss modulus then characterizes the viscous contribution in the viscoelastic material.

$$G' = \frac{\sigma_0}{\gamma_0} \cos\delta \tag{2.15}$$

$$G'' = \frac{\sigma_0}{\gamma_0} \sin\delta \tag{2.16}$$

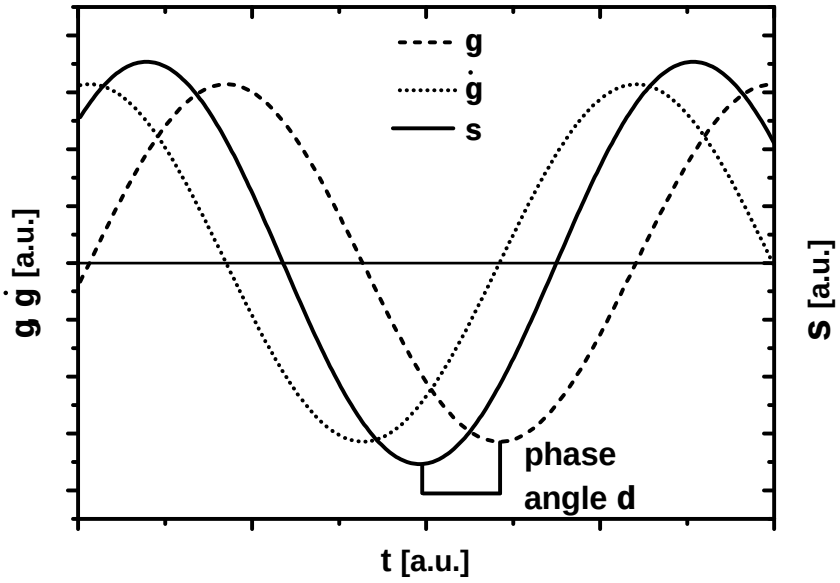


**Figure 2.5:** Strain excitation $\gamma(t)$, its derivative the shear rate $\dot{\gamma}(t)$ and the stress response of the Maxwell element $\sigma(t)$ under oscillatory shear.

Solving the Maxwell model yields explicit expressions for $G'$ and $G''$ as a function of $G$, $\lambda$ and $\omega$ (Eqs. 2.17 and 2.18, Morrison 2001). Their frequency dependence is plotted in Fig. 2.6. For low $\omega$, viscous behavior dominates, $G'' > G'$, power law exponents of 1 and 2 for $G''$ and $G'$ are the limits as $\omega$ approaches zero. At $\omega\lambda = 1$ the storage and loss moduli are equal. For higher frequencies, elastic behavior dominates, evident in $G' > G''$. Furthermore, $G'$ saturates whereas $G''$ declines proportional to $\omega^{-1}$. Together $G'$ and $G''$ result in the complex modulus $G^* = G' + iG''$.

$$G' = G\frac{\lambda^2\omega^2}{1+\lambda^2\omega^2} \tag{2.17}$$

$$G'' = G\frac{\lambda\omega}{1+\lambda^2\omega^2} \tag{2.18}$$

The Maxwell model is a linear model in a sense that the stress amplitude of the signal

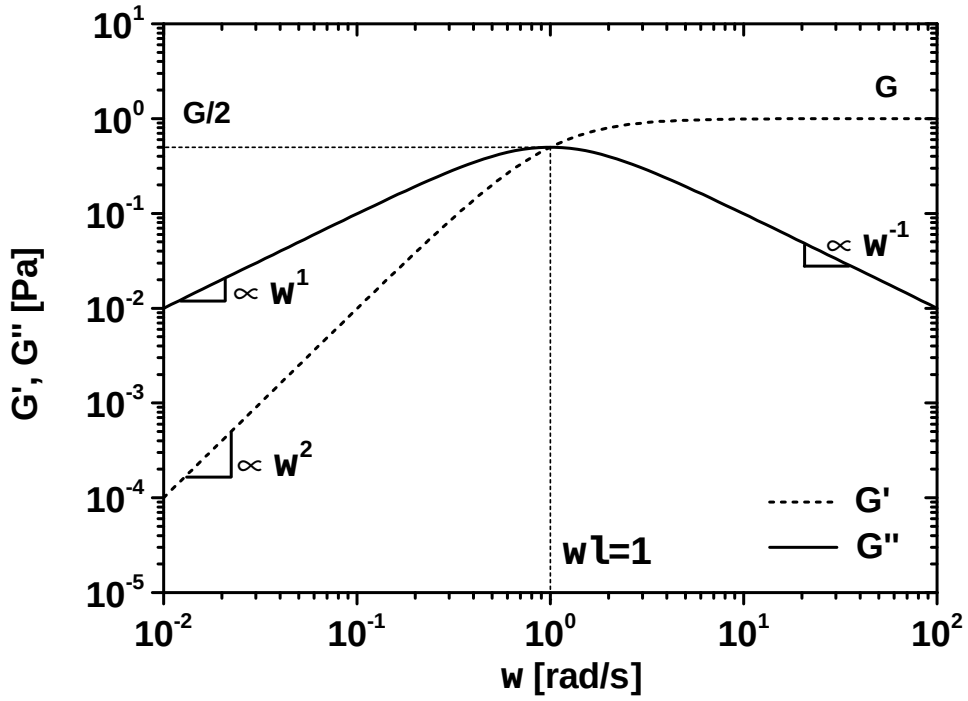


**Figure 2.6:** Angular frequency dependence of $G'$ and $G''$ for the Maxwell model according to Eqs. 2.17 and 2.18, $G = 1$ Pa and $\lambda = 1$ s. The cross-over of storage and loss modulus, $G' = G'' = G/2$ is at $\omega\lambda$=1 and the high frequency limit for $G'$ is $G$.

is a linear function of the strain amplitude. Therefore, $G'$ and $G''$ are independent of $\gamma_0$. Additionally, the Maxwell model is the mechanical analogon to the resistor-capacitor circuit in electrodynamics where the resistor is the analogon of the viscosity and the capacitor is the analogon of the spring. In fact the formalism used in electrodynamics inspired Andrew Gemant (Gemant 1935; Bird and Giacomin 2012) to define the complex viscosity $\eta^*$ which is related to the complex modulus $G^*$ as in Eq. 2.19.

$$i\eta^* = \eta' - i\eta'' = G^*/\omega \tag{2.19}$$

$$\eta' = G''/\omega = G\lambda\frac{1}{1+\lambda^2\omega^2} \tag{2.20}$$

$$\eta'' = G'/\omega = G\lambda\frac{\lambda\omega}{1+\lambda^2\omega^2} \tag{2.21}$$

Note that Gemant initially defined the complex viscosity using a slightly more complicated model, consisting of a dashpot in series with a parallel set-up of a second dashpot and a spring, which became known as the Jeffreys model. Therefore, his complex viscosity has a different frequency dependence than the one of the Maxwell model.
The formalism established so far defines a complex material function $G^*(\omega)$ that describes

the linear response. It will form the basis for the modeling approach presented in chapter 5, where the Maxwell model is extended in order to describe nonlinear effects in the stress response $\sigma(t)$. These nonlinearities manifest in $\gamma_0$ dependencies of $G'$ and $G''$ and deviations from the pure sinusoidal form.

## 2.2 Large Amplitude Oscillatory Shear (LAOS)

If the strain amplitude $\gamma_0$ exceeds a material and frequency dependent limit, deviations from the simple linear behavior described in Section 2.1.4 occur. This is the Large Amplitude Oscillatory Shear (LAOS) experiment. The rheological response becomes nonlinear in the sense that the stress amplitude $\sigma_0$ is not linear in $\gamma_0$. Additionally, the wave form cannot be described by a single sinusoidal wave. The amount of nonlinearity can be conveniently analyzed using the meanwhile well established Fourier-Transform-Rheology protocols (Wilhelm 2002; Hyun et al. 2011). Furthermore, many alternative methods have emerged which are presented in Section 2.2.2.

### 2.2.1 Fourier transform analysis in LAOS

#### Fundamentals

An example of a nonlinear but still periodic stress wave that results from a strain controlled LAOS experiment is shown in Fig. 2.7 (a). It can be described as a superposition of the angular frequency of excitation $\omega_1$ and its higher harmonics $n\omega_1$.
To obtain information on the higher harmonic content, a Fourier transform according to Eq. 2.22 is performed, which results in a complex spectrum $S^*(\omega)$. The complex spectrum consists of either real $\Re(\omega)$ and imaginary spectrum $\Im(\omega)$ or intensity $I(\omega)$ (Eq. 2.23) and phase spectrum $\delta(\omega)$ (Eq. 2.24). For technical aspects of discrete Fourier transforms, the reader is referenced to work of Wilhelm et al. (1999) and Ewoldt (2013). The two important parameters of discretization are the sampling rate $t_s$ and the acquisition time $t_{AQ}$ (total length of the signal). Their product determines the point number in the discrete signal, the complex spectrum then has half this point number. Decreasing $t_s$ allows the detection of increasing number of higher harmonics, $n_{max} = \frac{1}{2t_s}$ . Increasing $t_{AQ}$ leads to a higher frequency resolution in the spectra, $\Delta f = 1/t_{AQ}$. For example, sampling 10 cycles at $\omega/2\pi = f = 1$ Hz with 200 points per cycle ($t_s = 0.005$ s) means $t_{AQ} = 10$ s, and a maximum detectable harmonic of 100 with $\Delta f = 0.1$ s$^{-1}$. A Fourier transform is defined as follows:

$$S^*(\omega) = \int_{-\infty}^{\infty} \sigma(t) e^{-i\omega t} \mathrm{d}t = \Re(\omega) + i\Im(\omega) = I(\omega) e^{i\delta(\omega)} \tag{2.22}$$

$$I(\omega) = [\Re(\omega)^2 + \Im(\omega)^2]^{\frac{1}{2}} \tag{2.23}$$

$$\delta(\omega) = \arctan\left(\frac{\Im(\omega)}{\Re(\omega)}\right) \tag{2.24}$$

After Fourier analysis, the nonlinear shear stress can be expressed by Eq. 2.25 using the intensities $I_n$ and phases $\delta_n$ of the integer numbered harmonics (Wilhelm 2002; Dusschoten and Wilhelm 2001; Hyun and Wilhelm 2009). $I_n$ and $\delta_n$ are taken from the intensity and

phase spectra, $I(\omega)$ and $\delta(\omega)$ (Eqs. 2.23 and 2.24), at integer multiples of the applied fundamental frequency $\omega_1$:

$$\sigma(t) = \sum_{n\in\mathbb{N}} I_n \sin(n\omega_1 t + \delta_n) \tag{2.25}$$

$$I_n = I(n\omega_1) \tag{2.26}$$

$$\delta_n = \delta(n\omega_1) \tag{2.27}$$

Figure 2.7 (b) shows the normalized intensity spectrum of the respective stress signal in panel (a). For a symmetrical flow response, the signal contains only odd harmonics (Pearson and Rochefort 1982; Wilhelm et al. 1999), but even harmonics can appear if the symmetry is broken by an eccentricity of the measuring geometry or if the sample's structure is anisotropic (Sagis et al. 2001). Other sources for the occurrence of even harmonics can be stick-slip artifacts (Klein et al. 2007) or certain combinations of elasticity and shear thinning (Atalik and Keunings 2004).
Using trigonometric identities, Eq. 2.25 can be rewritten as Eq. 2.28 with $I_n \cos\delta_n/\gamma_0 = G'_n$ and $I_n \sin\delta_n/\gamma_0 = G''_n$ giving the familiar storage and loss modulus for $n = 1$ (Eq. 2.29) and the higher order terms for $n > 1$ that account for the deviation from pure sinusoidal response. In Eq. 2.29, $G'_n$ and $G'_n$ are $\gamma_0$ dependent. According to Pearson and Rochefort (1982), this $\gamma_0$-dependence can be approximated by a power series resulting in a double series description (Eq. 2.30), where $m$ refers to the $\gamma_0$ power and $n$ to the harmonic number.

$$\sigma(t) = \sum_n I_n \cos\delta_n \sin(n\omega_1 t) + I_n \sin\delta_n \cos(n\omega_1 t) \tag{2.28}$$

$$\sigma(t) = \sum_n \gamma_0 G'_n \sin(n\omega_1 t) + \gamma_0 G''_n \cos(n\omega_1 t) \tag{2.29}$$

$$\sigma(t) = \sum_{m,odd} \sum_{n,odd}^{m} \gamma_0^m \left[G'_{mn}(\omega_1)\sin(n\omega_1 t) + G''_{mn}(\omega_1)\cos(n\omega_1 t)\right] \tag{2.30}$$

$$I_{n/1} = \frac{I_n}{I_1} = \frac{\sqrt{G'^2_n + G''^2_n}}{\sqrt{G'^2_1 + G''^2_1}} = \frac{\sqrt{(\sum_m \gamma_0^m G'_{mn})^2 + (\sum_m \gamma_0^m G''_{mn})^2}}{\sqrt{(\sum_m \gamma_0^m G'_{m1})^2 + (\sum_m \gamma_0^m G''_{m1})^2}} \tag{2.31}$$

Usually for reasons of higher reproducibility and to compare different samples of varying moduli, the intensities of the higher harmonics are normalized to the intensity of the fundamental wave (Eq. 2.31). In the experimental chapters of the thesis, results of $\gamma_0$-dependent measurements will be usually compared using the storage and loss moduli $G'_1$ and $G''_1$, where the index 1 will be dropped because higher harmonics will be compared on the basis of $I_{n/1}$. This is shown in Fig. 2.7 (c). For increasing strain amplitude $\gamma_0$, the

transition from linear to nonlinear behavior can be followed by either a decrease of the moduli $G'$ and $G''$ or by the emergence of higher harmonic intensities. One advantage of analyzing the higher harmonic content is the dynamic range: When the moduli for example change by only 10%, in the same strain amplitude range (indicated by arrows in Fig. 2.7 (c)), $I_{3/1}$ increases by a factor of over 300.

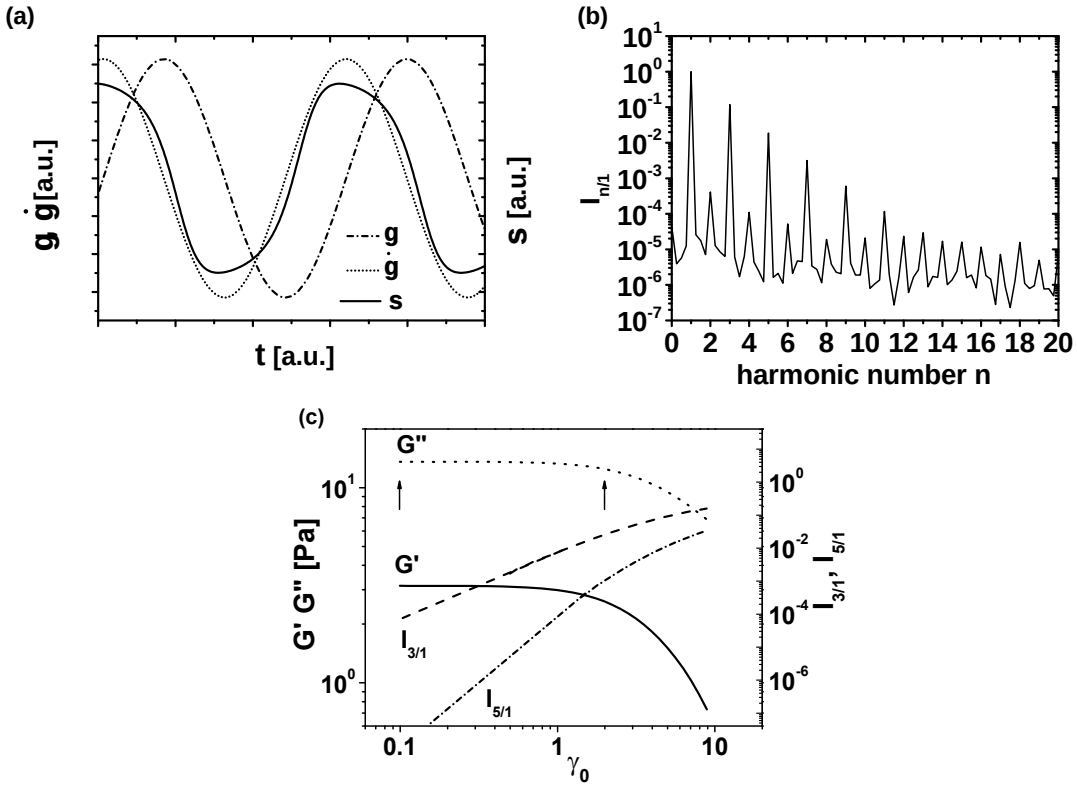


**Figure 2.7:** Schematic depiction of the procedure for conducting LAOS experiments and analysis using FT-rheology. (a) Application of sinusoidal strain (and shear rate) and measurement of shear stress response in the time domain. (b) Normalized frequency spectra after the Fourier transformation of the shear stress exhibit the fundamental peak at the angular frequency $\omega$. Higher harmonics $I_{n/1}$ with $n$ being a positive integer are detected for a periodic nonlinear shear stress wave. (c) By variation of $\gamma_0$ the transition from linear to nonlinear mechanical behavior can be observed in the increase of $I_{n/1}$ or the change of the storage and loss moduli from their respective plateau values.

A simple argument for the occurrence of only odd harmonics in the ideal case (symmetric flow, no shear banding, no stick-slip) can be made by assuming a viscosity that is nonlinear in the shear rate, as shown by Wilhelm et al. (2000), where the authors used a polynomial expansion for the viscosity function (Eq. 2.32). They concluded that the absolute intensity of a higher harmonic $I_n$ ought to scale with the $n$th power of the strain amplitude for small enough deviation from the linear regime, as shown by Eq. 2.34. Therefore, a normalized intensity is expected to scale as $I_{n/1} \propto \gamma_0^{n-1}$ in the transition region between linear and nonlinear regime (Fig 2.7 (c)).

$$\eta(\gamma, t) = \eta_0^* + a^* \dot{\gamma}^2 + b^* \dot{\gamma}^4 + \cdots \tag{2.32}$$

$$\dot{\gamma} = \frac{\mathrm{d}\gamma}{\mathrm{d}t} = \frac{\mathrm{d}(\gamma_0 \cdot e^{i\omega t})}{\mathrm{d}t} = i\omega\gamma_0 \cdot e^{i\omega t} \tag{2.33}$$

$$\begin{aligned} \sigma(\gamma, t) &= (\eta_0 + a^* \cdot i^2\omega^2\gamma_0^2 e^{i2\omega t} + b^* \cdot i^4\omega^4\gamma_0^4 e^{i4\omega t} + \cdots) i\omega\gamma_0 e^{i\omega t} \\ &= \underbrace{\eta_0 \cdot i\omega\gamma_0}_{I_1} e^{i\omega t} - \underbrace{a^* \cdot i\omega^3\gamma_0^3}_{I_3} e^{i3\omega t} + \underbrace{b^* \cdot i\omega^5\gamma_0^5}_{I_5} e^{i5\omega t} + \cdots \end{aligned} \tag{2.34}$$

It is worth noting that the description of a nonlinear viscosity using Taylor expansions has an analogon in nonlinear optics (Boyd 2008), where the polarization of a molecule $P(t)$ in an oscillating electrical field $E(t)$ can be represented by the product of the permittivity of free space $\epsilon_0$, the electrical field $E(t) = E_0 \sin(\omega t)$ and the nonlinear susceptibility $\chi$ (Eq. 2.35). Therefore, it is not surprising that dielectric spectroscopy has also been extended to the nonlinear range (Schiener et al. 1996; Bauer et al. 2013; Bauer and Loidl 2015).

$$P(t) = \epsilon_0 \chi(E(t)) E(t) \tag{2.35}$$

$$= \epsilon_0 \left[ \chi_1 E(t) + \chi_2 E^2(t) + \chi_3 E^3(t) + ... \right] \tag{2.36}$$

The scaling behavior for the mechanical higher harmonics has been verified experimentally by Hyun and Wilhelm (2009) and Reinheimer et al. (2011). Subsequently, for every harmonic an intrinsic nonlinear parameter ${}^nQ(\gamma_0, \omega)$ was introduced, together with the intrinsic nonlinearity at low strain amplitude, ${}^nQ_0(\omega)$. Through this reduction a single, only frequency dependent, quantity for every harmonic was obtained (Eq. 2.37):

$${}^nQ(\gamma_0, \omega) = \frac{I_{n/1}}{\gamma_0^{n-1}} \quad \text{with} \quad {}^nQ_0(\omega) = \lim_{\gamma_0 \to 0} {}^nQ(\omega) \tag{2.37}$$

${}^nQ_0(\omega)$ can be used to infer the inherent nonlinear material properties of a sample as the trivial scaling $I_{n/1} \propto \gamma_0^{n-1}$ is eliminated. The intrinsic nonlinearity parameter ${}^3Q$, that is derived from the third harmonic, has been shown to be useful in evaluating the topology of polymer melts (Hyun and Wilhelm 2009), in investigating the droplet size distribution of emulsions (Reinheimer et al. 2011; Reinheimer et al. 2012) and has also been evaluated

for the Pom-Pom model (Hyun et al. 2013; Hoyle et al. 2014).
In first approximation, only the first nonlinear term is considered when using the FT framework (Hyun and Wilhelm 2009; Wagner et al. 2011; Merger and Wilhelm 2014). In this case, $n$ equals three and ${}^3Q_0$ is written as $Q_0$. This nomenclature will be adopted for the rest of the thesis. Even higher harmonics (fifth, seventh, ...) increase in a similar fashion to $I_{3/1}$, albeit with different scaling exponents, but have overall smaller intensities. Since the harmonic intensities are not increasing independently of each other, only the third harmonic will be used as a representative quantity for the nonlinearity.

$$ {}^3Q(\gamma_0, \omega) = \frac{I_{3/1}}{\gamma_0^2} \quad \text{with} \quad \lim_{\gamma_0 \to 0} {}^3Q(\omega) = Q_0(\omega) \tag{2.38} $$

The intrinsic concept implies that in principle no linear viscoelastic range (LVR) exists, since at any combination of $\gamma_0$ and $\omega$ finite values of higher harmonic intensities exist. Nevertheless, it is useful to define a threshold below which contributions $I_{n/1}$ can be neglected and the response is treated as linear. The choice is somewhat arbitrary and ultimately up to the user of the method (Ewoldt and Bharadwaj 2013) but the current experimental detection limit for the most intensive higher harmonic, $I_{3/1}^{\min} = 10^{-4} - 10^{-5}$ (Wilhelm et al. 2012), is a reasonable choice. In practice oftentimes the end of LVR is taken to be at the strain amplitude where the moduli $G'$ and $G''$ deviate more than 10% from their plateau values (Mezger 2006).

**Overview of nonlinear shear rheology**

Nonlinear shear rheology, performed in steady shear or in oscillatory shear (Dealy and Larson 2006; Morrison 2001; Macosko 1994), can be used to probe different time scales of a material's mechanical behavior. Figure 2.8 shows an overview of six characteristic cases where the complexity of the rheological response increases due to increasing nonlinear effects.
Case (a) is the standard small amplitude oscillatory shear experiment, where the amplitude is sufficiently small, therefore no significant structural changes can be induced and only an equilibrium structure is probed. This results in linear behavior, meaning the stress amplitude is a linear function of the strain amplitude. Furthermore, the stress amplitude is constant in time.
In the nonlinear steady shear experiment (case (b)), sufficiently high shear rates lead to nonlinear behavior: the viscosity $\eta$ becomes a function of the shear rate $\dot{\gamma}$. The shear rate dependency is captured by models such as the Carreau-Model (a special case of the Carreau-Yasuda model with $\eta_\infty = 0$ and $a = 2$, Section 2.1.2). Although the measurement is nonlinear, it is still time stationary, as every point in the curve represents a steady state value of $\eta$ at the specific $\dot{\gamma}$.
LAOS experiments probe nonlinear behavior at a certain angular frequency $\omega$ (case (c)). The structural changes responsible for the nonlinear behavior take place on roughly the

time scale as the inverse of $\omega$, therefore the structure follows the strain excitation. An example for such a structural change is the deformation of the droplet surface in emulsions (Reinheimer et al. 2011; Reinheimer et al. 2012). The nonlinear behavior is quantified by higher harmonic intensities, which stay constant over time, since no irreversible change of the structure occur.

If additional shear induced modification of the structure (often accompanied by a change of the stress amplitude) occurs on a time scale much longer than the length of an oscillation, this results in a time dependence of the measured harmonic intensities, as indicated in Fig. 2.8 (d). The harmonic peaks have been shifted in $\omega$ for clarity. Such long time structure modification can be monitored by measuring harmonic intensities as a function of time, as has been done for the orientation of block-co-polymer domains (Langela et al. 2002; Oelschlaeger et al. 2007; Meins et al. 2012).

Such large scale structural changes can be much faster for colloidal systems, where thixotropy, is commonly observed (Mewis and Wagner 2012; Mewis and Wagner 2009). Thixotropy, is defined as a continuous decrease of the viscosity during flow, and a subsequent recovery during rest. In contrast to start-up behavior of shear thinning samples, in thixotropic systems no steady state of the viscosity can be reached even after long times. If the characteristic time of this change $\tau_c$ approaches the duration of one oscillation cycle $T_a$, the peaks in the intensity spectra broaden (case (e)) and the $S/N$ decreases. Quantification of the peak broadening can then provide information about the rate of the structural change.

The last case (f) illustrates a chaotic material response in spectral form. If the excitation is much faster than the material's ability to respond, the stress signal is random and not correlated to the excitation anymore. In this case no distinct peaks in the spectrum are observable, instead the intensity decreases inversely proportional to the frequency $I_{n,1} \propto 1/\omega$. Investigation of nonlinear behavior by LAOS experiments is not possible at such extreme conditions.

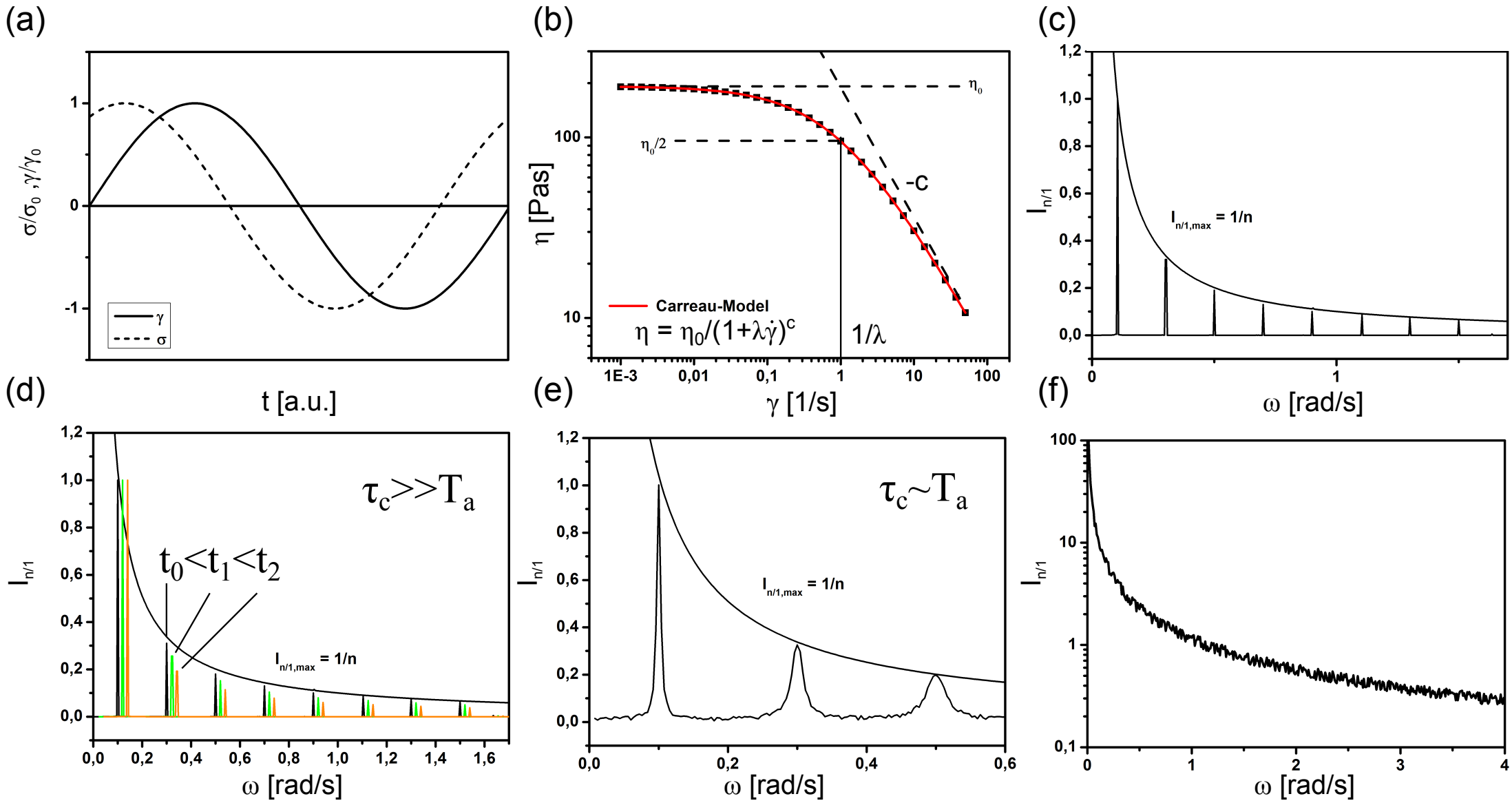
(a)
σ/σ0 ,γ/γ0
1
0
-1
γ
σ
t [a.u.]
(b)
η [Pas]
100
10
η0
η0/2
-C
Carreau-Model
η = η0/(1+λγ̇)c
1/λ
1E-3
0,01
0,1
1
10
100
γ [1/s]
(c)
In/1
In/1,max = 1/n
ω [rad/s]
(d)
τc>>Ta
t0<t1<t2
In/1,max = 1/n
In/1
ω [rad/s]
(e)
τc~Ta
In/1,max = 1/n
In/1
ω [rad/s]
(f)
In/1
ω [rad/s]

**Figure 2.8:** Overview of shear rheology tests in steady shear and oscillatory shear. (a) SAOS experiment, (b) nonlinear steady shear experiments, (c) LAOS experiment, (d) LAOS experiment with slow shear induced changes in the structure, (e) LAOS experiment with fast shear induced changes in the structure, (f) no correlation between strain input and stress output signals. $\tau_c$ is the characteristic time of the shear induced structural change, $T_a$ is the length of an oscillation period.

### Pipkin space

The different regimes of material behavior discussed so far, i.e. linear and nonlinear regime, oscillatory and steady shear, can be summarized in a so called Pipkin diagram (Pipkin 1972). When using oscillatory shear one can vary the strain amplitude $\gamma_0$ and angular frequency $\omega$ independently and therefore investigate different regions of a materials behavior in the Pipkin space as shown in Fig. 2.9. At this point it is useful to reiterate the definitions of two commonly used dimensionless numbers to describe flow, the Deborah number $De = \lambda\omega$ and the Weissenberg number $Wi = \lambda\omega\gamma_0 = \lambda\dot{\gamma}$.
The Deborah number is defined as the ratio of a characteristic relaxation time of the material $\lambda$ and a characteristic time of observation $\tau_o$, which is inverse of the angular frequency $\tau_o = 1/\omega$ for oscillatory shear. It measures to what degree elastic effects influence the overall mechanical response. For example in the Maxwell model, if $De < 1$ then viscous behavior dominates, $G'' > G'$, whereas for $De > 1$, the response is predominantly elastic, $G' > G''$. The Weissenberg number, is the ratio of $\lambda$ and a characteristic time $\tau_d$ of the deformation. $\tau_d$ is the inverse of the shear rate $\tau_d = 1/\dot{\gamma}$ for steady shear or $\tau_d = 1/\dot{\gamma_0} = 1/(\omega\gamma_0)$ for oscillatory shear (Dealy 2010). The Weissenberg number can be seen as a dimensionless shear rate that indicates the importance of nonlinear behavior.
In Fig. 2.9 at sufficiently low $De$ a viscoelastic material has enough time to relax and behaves like a Newtonian liquid for small $Wi$. Increasing $Wi$ at constant $De$ means applying higher shear rates that result in nonlinear effects such as shear thinning, which can be modeled by a generalized Newtonian fluid model (Macosko 1994). If $De$ is varied at small $Wi$ the experiment represents the common frequency sweep in the linear visco-elastic region (LVR) with $G'$ and $G''$ being only dependent on the frequency. The test the gives information about the balance of viscous and elastic effects. Increasing $Wi$ at higher (but constant) $De$ drives the material first into the instrinsic LAOS region (where the scaling laws of Eq. 2.37 for the departure from linearity apply) and finally even beyond. Thus a Large Amplitude Oscillatory Shear experiment is not an additional, different test among steady shear and the classic dynamic measurements in the LVR, but it is a logical combination for the two tests and covers smoothly the transition between the limiting cases.

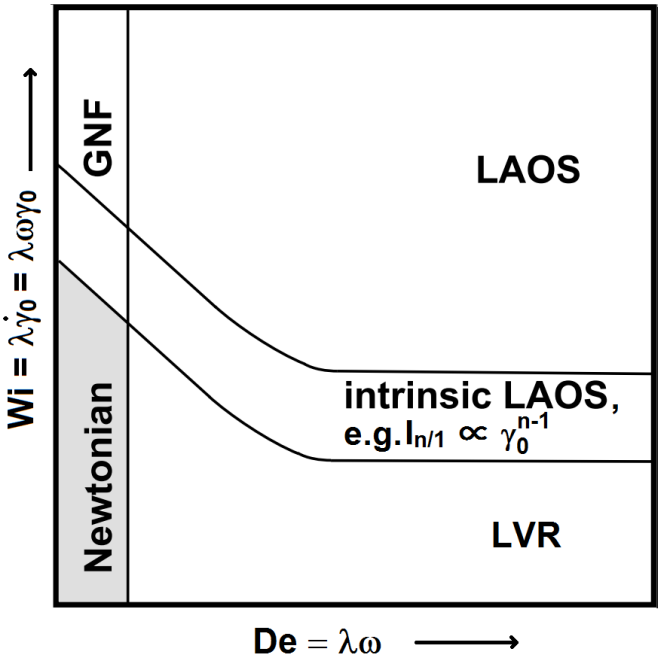


**Figure 2.9:** Schematic map of nonlinear rheology as a function of angular frequency $\omega$ and strain amplitude $\gamma_0$, known as the Pipkin diagramm (reproduced after Pipkin (1972) and Ewoldt and Bharadwaj (2013)). Simple Newtonian and generalized Newtonian fluid behavior (GNF) are observed for small $\omega$. For higher $\omega$ linear viscoelastic (LVR) properties are probed, which become nonlinear with increasing $Wi = \lambda\omega\gamma_0$ (LAOS). For intermediate $Wi$ an intrinsic LAOS regime can be defined. In this range scaling laws (Eq. 2.37) for the departure from linearity can be applied.

### 2.2.2 Alternative analysis methods for LAOS

Plenty of other methods besides the formalism using Fourier intensities to quantify and to interpret the shear stress in LAOS experiments or model predictions have been proposed. They are summarized in Fig. 2.10. The starting point in this diagram is the measured stress signal $\sigma(t)$ on the left. At small enough strain amplitudes (Small Amplitude Oscillatory Shear, SAOS), the stress wave is a pure sine with a phase shift relative to the input and plotting $\sigma(t)$ vs $\gamma(t)$ or vs $\dot{\gamma}(t)$ gives Lissajous figures that are ellipses (upper left corner). Storage and loss modulus, $G'$ and $G''$, are sufficient to completely describe the signal. Increasing $\gamma_0$ leads to the occurrence of nonlinearities (LAOS). The nonlinearity is quantified by a Fourier transform, where an intensity and a phase spectrum is generated for each stress wave. The nonlinear analysis frameworks will be introduced clockwise. Nonlinear waveforms can be analyzed directly by a geometric interpretation following Cho et al. (2005), where $\sigma(t)$ is decomposed into an elastic contribution, $\sigma'(t)$, and a viscous contribution, $\sigma''(t)$. They are drawn as black lines going through the origin in the upper central Lissajous curves. By describing $\sigma'(t)$ and $\sigma''(t)$ as a series of Chebishev polynomials (Ewoldt et al. 2008; Ewoldt and Bharadwaj 2013), shown in the upper right corner, many wave forms for increasing $\gamma_0$ can be compared with a relatively small amount of quantities, the elastic and viscous Chebishev coefficients.

Furthermore, the waveform can be interpreted as a sequence of physical processes (SPP) of elastic straining, yielding and viscous or plastic flow (Rogers et al. 2011b). The extension of the SPP to time dependent moduli $R'(t)$ and $R''(t)$ is based on a 3D interpretation of the $\sigma(t)$ vs $\gamma(t)$ vs $\dot{\gamma}(t)$ curves as shown in the lower right corner. It will be introduced in detail in Section 2.2.4.

The majority of LAOS studies so far have compared nonlinear data using the intensities and phases of higher harmonics obtained directly from the Fourier transform (Section 2.2.1) as depicted in the lower central portion of the diagram.

Anharmonic moduli can be used to contrast fundamental frequency behavior to all higher harmonic content (Poulos et al. 2013; Laurati et al. 2014). They are obtained by subtracting the fundamental wave $\sigma_1(t)$ from the nonlinear wave $\sigma(t)$ and analyzing the resulting anharmonic stress wave $\sigma_{anh}(t) = \sigma(t) - \sigma_1(t)$ at the peak strain and at zero strain, $\gamma = \gamma_0$ and $\gamma = 0$. The anharmonic storage and loss modulus are then defined as $G'_{anh} = \sigma_{anh}(\gamma = \gamma_0)/\gamma_0$ and $G''_{anh} = \sigma_{anh}(\gamma = 0)/\gamma_0$, respectively.

Alternatively, a superposition of the sine wave with other characteristic functions, such as rectangle, triangle and sawtooth waves can be used to describe the nonlinear stress wave in LAOS experiments (Klein et al. 2007). The additional, inherently nonlinear, functions account for effects such as shear thinning (square), shear thickening (triangle) and stick-slip artifacts (sawtooth). The individual contributions of rectangle, triangle and sawtooth waves are determined in Fourier space by matching intensity and phase spectra of the characteristic functions to experimentally determined spectra.

Although all these possible frameworks seem to be quite different from the basic harmonic

analysis, they mostly rely on the Fourier transform for direct calculation of their own nonlinear parameters or at least use the FT as comb filter to smooth experimental data and reduce noise. This is indicated by additional arrows going from the spectrum in the middle of the diagram to the individual frameworks. Already in SAOS the original stress signal can be reconstructed from $G'$ and $G''$. For the anharmonic moduli the fundamental wave $\sigma_1(t)$ is calculated similarly. $\sigma'(t)$ and $\sigma''(t)$ in the stress decomposition method as well as the Chebishev coefficients can be computed from higher harmonic moduli $G'_n$ and $G''_n$ according to Eqs. 2.39 and 2.40, respectively (Cho et al. 2005; Ewoldt et al. 2008).

$$\begin{aligned}\sigma'(t) &= \frac{\sigma(\gamma,\dot{\gamma}) - \sigma(-\gamma,\dot{\gamma})}{2} = \gamma_0 \sum_{n,odd} G'_n \sin(n\omega t) \\ \sigma''(t) &= \frac{\sigma(\gamma,\dot{\gamma}) - \sigma(\gamma,-\dot{\gamma})}{2} = \gamma_0 \sum_{n,odd} G''_n \cos(n\omega t)\end{aligned} \tag{2.39}$$

$$\begin{aligned}e_n &= G'_n(-1)^{(n-1)/2} \\ v_n &= \frac{G''_n}{\omega}\end{aligned} \tag{2.40}$$

For the sequence of physical processes framework (SPP), which uses local measures in the Lissajous curves, the stress data is usually reconstructed from the spectra using only odd harmonic intensities and phases (Rogers et al. 2011b). This effectively removes random noise. In the generalized version of the SPP, which uses the time dependent moduli $R'(t)$ and $R''(t)$, the essential quantity, the binomial vector $\mathbf{B}(t)$, is also available from $G'_n$ and $G''_n$ (see Eq. 2.41).

In conclusion, there is hardly an analysis framework that does not employ FT as part of its data treatment procedure. As FT of any signal is a linear and invertible operation it has the great advantage that most of the quantities of those frameworks can be recalculated into the others through the Fourier coefficients. The two approaches known as 'sequence of physical processes' developed by Rogers et al. (2011b) are discussed in detail in the next section, due to their relevance in Chapter 7.

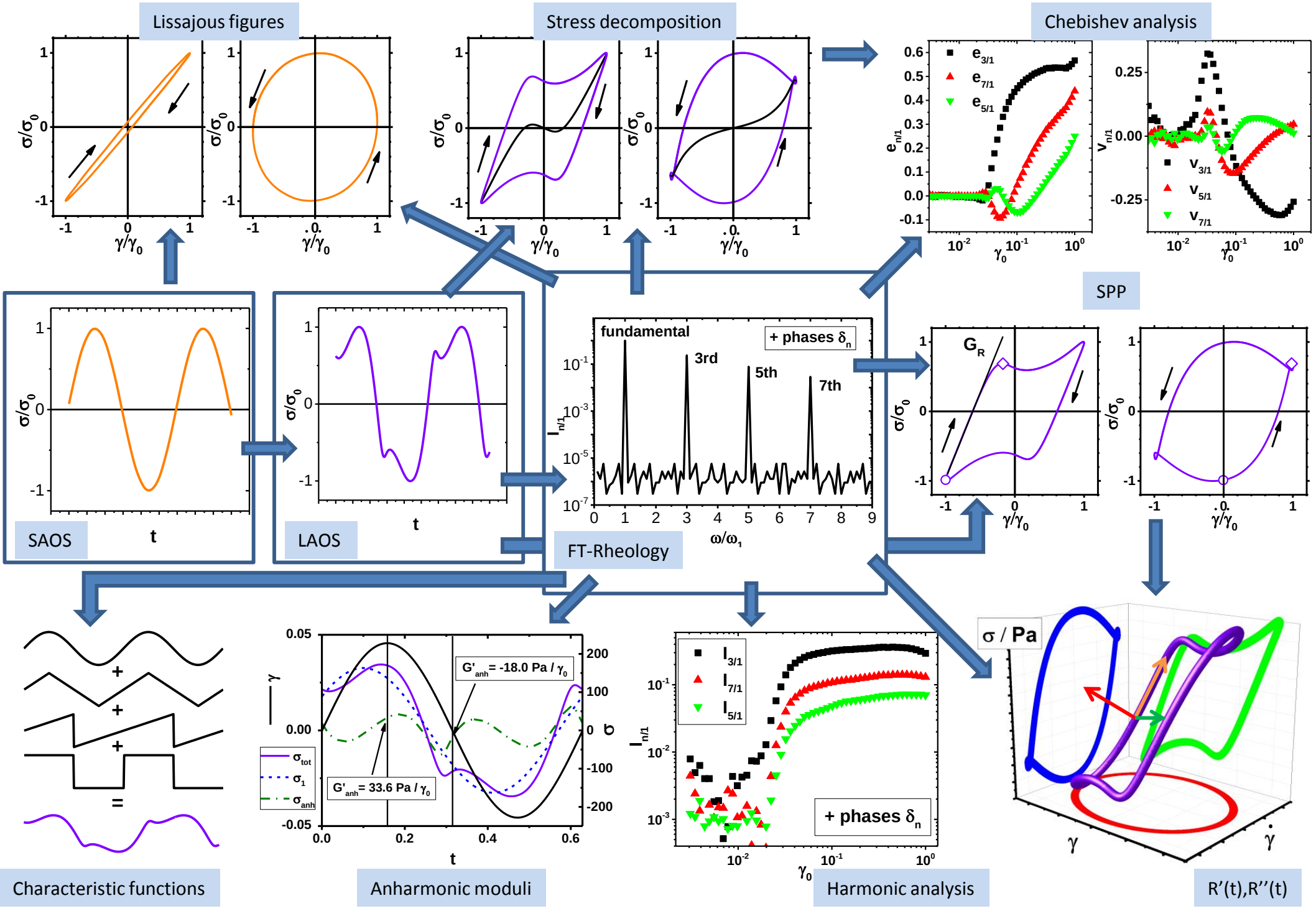
Lissajous figures
Stress decomposition
Chebishev analysis
SPP
SAOS
LAOS
FT-Rheology
fundamental
3rd
5th
7th
+ phases δn
Characteristic functions
Anharmonic moduli
Harmonic analysis
R'(t),R''(t)
σ / Pa

**Figure 2.10:** Overview of the most common LAOS analysis methods. Starting point is the measured stress signal $\sigma(t)$. From there, the possibilities are Fourier transform, geometric stress decomposition, Chebishev polynomial analysis, the sequence of physical processes (SPP), the anharmonic moduli analysis and decomposition to characteristic functions. After the FT, higher harmonic intensities and phases can be analyzed for varying strain amplitudes and angular frequencies. Based on the stress decomposition method, Chebishev analysis can be performed, although the Chebishev coefficients are also directly computable from the Fourier coefficients. As an extension of the SPP framework, time dependent moduli $R'(t)$ and $R''(t)$ can be analyzed, which are also accessible from the Fourier coefficients (see Section 2.2.4). The anharmonic moduli analysis and the description using characteristic function rely on the FT as well. In the former case the fundamental wave $\sigma_1$ is calculated from $G'$ and $G''$, in the latter case the intensities of the characteristic function are optimized such that they reproduce the experimental Fourier spectra. Therefore, all frameworks shown here rely on FT to either calculate their own parameters from Fourier coefficients directly or use it as a comb filter when waveform data is reconstructed to reduce experimental noise.

### 2.2.3 Sequence of physical processes (SPP)

A conceptually different approach to analyze temporal stress signals obtained from LAOS experiments that will be used for the investigation of the yielding behavior of a colloidal gel (see Chapter 7), is the sequence of physical processes as it has been established by Rogers et al. (2011b). Instead of describing the stress wave as an infinite series of basis functions with their respective intensities and phases, here Lissajous figures, i.e. stress vs. strain or stress vs. strain rate curves, are directly interpreted as shown in Fig. 2.11. That means the analysis moves from the time/frequency domain to the deformation/shear rate domain. Specific parts of the Lissajous curve are associated with certain physical processes, that follow a sequence that is repeated twice per oscillation cycle. The SPP approach is especially useful to describe waveforms of yield stress fluids under LAOS, as for example glassy suspensions (Rogers et al. 2011b; Vaart et al. 2013) or colloidal gels (Kim, Merger, et al. 2014). It has also been applied to constitutive models such as the Bingham and the Giesekus model (Rogers and Lettinga 2012). In all these studies the different physical processes are elastic straining, yielding, plastic and/or viscous flow. These processes can be quantified with the following parameters that are extracted from elastic Lissajous (stress vs. strain) plots, see Fig. 2.11. The sequence starts at the point of maximum strain and flow reversal (circle symbol) and progresses clockwise in the Lissajous loop:

- The cage modulus or residual modulus $G_R = \frac{d\sigma}{d\gamma}|_{\sigma=0}$ quantifies the strength of the residual elasticity that is recovered in every cycle. It approximates the linear region of the stress strain curve after reversal of flow direction (circle symbol). For small deformations, that is in the linear viscoelastic regime, $G_R$ is equal to the storage modulus $G'$.

- The yield stress $\sigma_c$ measures the maximum stress that can be stored in the system before yielding (diamond symbol in Fig 2.11).

- The yield strain $\gamma_c$ measures the maximum strain that is accumulated from the point of flow reversal at $\gamma = -\gamma_0$ (circle symbol in Fig 2.11) to the point of yielding designated by a local maximum in the stress after the linear region (diamond symbol).

- The instantaneous viscosity at maximum shear rate $\eta_L = \frac{\sigma(t)}{\dot{\gamma}(t)}|_{\gamma=0}$ (square symbol) that characterized the flowing portion of the half-cycle.

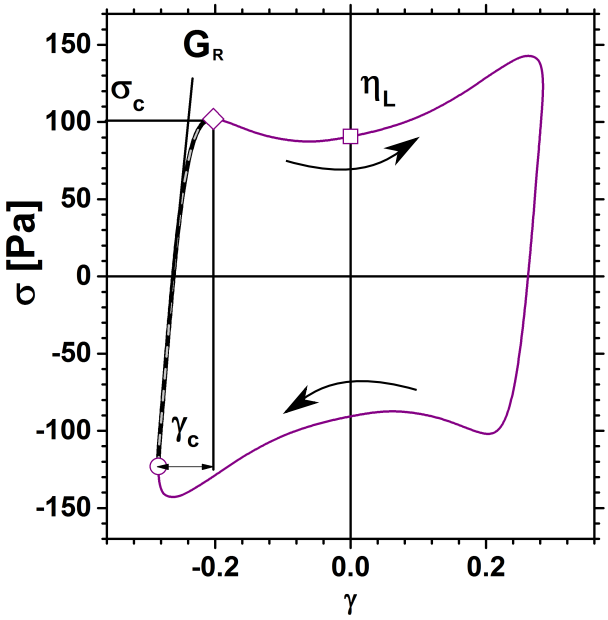


**Figure 2.11:** Elastic Lissajous plot (stress vs strain) for a colloidal gel (33 vol.-% PDMS droplets in an aqueous continous phase containing 33 vol.-% of bridging polymer and 230 mM sodium dodecyl sulfate) at $\omega = 10$ rad/s and $\gamma_0 = 0.284$. Arrows indicate the reading direction for the interpretation according to the SPP framework. The local waveform parameters $G_R$, $\gamma_c$ and $\sigma_c$ have been defined by (Rogers et al. 2011b).

When analyzing a set of LAOS experiments, the proposed quantities can be tracked as a function of increasing $\gamma_0$ and provide useful insight into the yielding behavior of the investigated materials. This approach could distinguish clearly between a hard sphere and a soft sphere suspension and showed that the soft sphere suspension yields more gradually in comparison to the hard sphere suspension due to the particle softness (Vaart et al. 2013).

### 2.2.4 Time dependent moduli $R'(t)$ and $R''(t)$

The semi-quantitative framework in section 2.2.3 has been extended by Rogers (2012) to a fully quantitative level. Rogers described the periodic stress signal with two time dependent modulus functions, $R'(t)$ and $R''(t)$, which in the LVE correspond to elastic and viscous behavior measured by the storage and loss modulus (Section 2.1.4). In the nonlinear case they are allowed to change in magnitude over the duration of the oscillation cycle. To arrive at $R'(t)$ and $R''(t)$, one first has to apply the concept of the Frenet-Serret frame (Frenet 1852; Serret 1851) to the three dimensional loop in a $\sigma$ vs $\gamma$ vs $\dot{\gamma}$ representation of the LAOS data for a fixed pair of $\omega$ and $\gamma_0$ as shown in Fig. 2.12. The data can be represented by a three dimensional vector $\mathbf{r}(t) = [\gamma(t) \quad \dot{\gamma}(t) \quad \sigma(t)]$. At every point in time a set of three mutually orthogonal vectors can be defined to describe the curvature of the loop in three dimensions. The tangential vector $\mathbf{T}(t)$ traces the movement along the curve and is defined as $\mathbf{T}(t) = \dot{\mathbf{r}}(t)/|\dot{\mathbf{r}}(t)|$. The normal vector $\mathbf{N}(t) = \dot{\mathbf{T}}(t)/|\dot{\mathbf{T}}(t)|$ points towards

the local center of rotation. The binormal vector $\mathbf{B}(t)$ is orthogonal to the tangential and to the normal vector $\mathbf{N}(t)$ ($\mathbf{B}(t) = \mathbf{T}(t) \times \mathbf{N}(t)$) and contains information about the elastic and the viscous response.

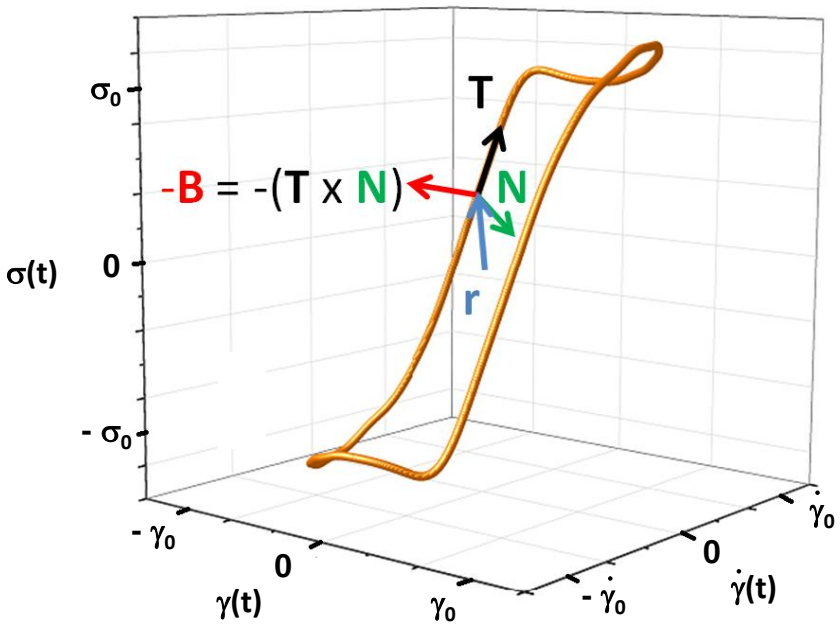


**Figure 2.12:** Nonlinear stress $\sigma(t)$ vs strain $\gamma(t)$ vs shear rate $\dot{\gamma}(t)$ plot with representations of the binormal vector $\mathbf{B}(t)$, the tangential vector $\mathbf{T}(t)$ and the normal vector $\mathbf{N}(t)$. The three mutually orthogonal and time dependent vectors define the Frenet-Serret frame (Frenet 1852; Serret 1851).

For analytical models, if $\mathbf{r}(t)$ and its higher derivatives $\dot{\mathbf{r}}(t)$ and $\ddot{\mathbf{r}}(t)$ can be represented by explicit expressions, then $\mathbf{B}(t)$ can be calculated as $\mathbf{B}(t) = \frac{\dot{\mathbf{r}}(t)\times\ddot{\mathbf{r}}(t)}{|\dot{\mathbf{r}}(t)\times\ddot{\mathbf{r}}(t)|}$. For experimental data or numerical solutions of models $\mathbf{r}(t)$ is discrete in time. Then, $\mathbf{B}(t)$ has to be approximated using a Taylor expansion of $\mathbf{r}(t)$ by $\mathbf{B}(t) \approx \frac{1}{\mathrm{d}t^3}\mathbf{r}(t+\mathrm{d}t) \times [\mathbf{r}(t-\mathrm{d}t) + [\mathbf{r}(t-\mathrm{d}t) - \mathbf{r}(t+\mathrm{d}t)] \times \mathbf{r}(t)] + \mathcal{O}(\mathrm{d}t^3)$.
If the frequency spectrum is known, then $\mathbf{B}(t)$ can be easily calculated by Eq. 2.41 from the series of $G'_n$ and $G''_n$, that have been defined in in Eq. 2.29 in section 2.2.

$$\begin{aligned}\mathbf{B}(t) = \boldsymbol{\gamma} \sum_{n,odd} \Big[ \{n^2 G'_n \sin\omega t - nG''_n \cos\omega t\} \sin n\omega t + \{n^2 G''_n \sin\omega t + nG'_n \cos\omega t\} \cos n\omega t \Big] + \\ + \dot{\boldsymbol{\gamma}} \sum_{n,odd} \Big[ \{n^2 G'_n \frac{\cos\omega t}{\omega} + nG''_n \frac{\sin\omega t}{\omega}\} \sin n\omega t + \{n^2 G''_n \frac{\cos\omega t}{\omega} - nG'_n \frac{\sin\omega t}{\omega}\} \cos n\omega t \Big] \\ + \boldsymbol{\sigma}\,[-1]\end{aligned} \tag{2.41}$$

The phase angle $\delta(t)$ and the absolute values of the time dependent complex modulus $|G^*(t)|$ can be calculated from $\mathbf{B}(t)$ using Eqs. 2.42 and 2.43. In these equations, $B_\gamma(t)$ and $B_\sigma(t)$ are the strain and stress vector components, respectively, and $\mathbf{B}_p(t)$ is the projection of $\mathbf{B}_\omega(t) = [B_\gamma \quad \omega B_{\dot{\gamma}} \quad B_\sigma]$ onto the $\gamma$ - $\dot{\gamma}$ plane and $\beta$ is the angle between $-\mathbf{B}(t)$ and

the vector [0 0 1], that points along the $\sigma$ axis.

$$\cos\delta = \frac{B_\gamma(t)}{|\mathbf{B}_p(t)|} \tag{2.42}$$

$$|G^*(t)| = \tan\beta = \tan\left[\cos^{-1}\left(\frac{B_\sigma(t)}{|\mathbf{B}(t)|}\right)\right] \tag{2.43}$$

Finally $R'(t)$ and $R''(t)$ can be obtained from Eqs. 2.44 and 2.45.

$$R'(\gamma_0,\omega,t) = |G^*(\gamma_0,\omega,t)|\cos\delta \tag{2.44}$$

$$R''(\gamma_0,\omega,t) = |G^*(\gamma_0,\omega,t)|\sin\delta \tag{2.45}$$

The time dependent moduli $R'(t)$ and $R''(t)$ have been effectively applied in a recent study on a hyualuronic acid solution. The solution was used as a model system for synovial fluid in human joints (Zhang and Christopher 2015). The study revealed that under LAOS, in the yielded state, elastic behavior of the fluid is still present within an oscillation cycle at times where the strain is close to its maximum $\gamma_0$, although the overall behavior was predominantly viscous. The authors proposed that this prevailing intracycle elasticity is responsible for the shock absorbing properties of the synovial fluid in the joint.
The $R'(t)$ and $R''(t)$ framework has also recently been extended to the LAOStress experiment, where the excitation is a sinusoidal stress signal and therefore the response $\mathbf{r}(t)$ is defined in the coordinates of $\boldsymbol{\sigma}(t)$, $\dot{\boldsymbol{\sigma}}(t)$ and $\dot{\boldsymbol{\gamma}}(t)$ (Thompson et al. 2015).

### 2.2.5 Strain dependent LAOS vs stress dependent LAOS

So far only strain input has been considered and the stress response has been analyzed using different methods, which is often called LAOStrain (Ewoldt 2013). There is of course the possibility of conducting a stress controlled experiment and analyzing nonlinearities in the strain response, which in turn is termed LAOStress. A priori, there is no reason to expect the ratios of harmonics in the shear stress response in LAOStrain to agree with the ratios of harmonics in the shear strain response in LAOStress. The two experiments give different results and are therefore complementary (Läuger and Stettin 2010). Currently, literature on LAOStress is still scarce although a theoretical framework has been laid out (Ewoldt 2013) and first experimental results have been published recently (Läuger and Stettin 2010; Dimitriou et al. 2013; Bae et al. 2013; Souza Mendes et al. 2014). However, technical difficulties regarding the excitation using a sinusoidal stress wave have been reported. Läuger and Stettin (2010) noted that in the LAOStress experiments they conducted the input stress wave contained up to 1% of relative third harmonic intensity. In contrast LAOStrain experiments can be performed with a strain excitation that contains $I_{3/1}$ lower than $10^{-5}$ as will be shown in Chapter 4. Since the analysis frameworks of LAOStrain are further evolved, more published experimental data for comparison is available and the

LAOStress excitation is comparatively less accurate, LAOS experiments in this thesis will be restricted to the LAOStrain kind. Henceforth, all experiments called LAOS will refer to sinusoidal strain excitation.

# Chapter 3

# Structure and rheology of the investigated materials

The range of materials that can be classified as *soft matter* comprises the following classes (Gompper et al. 2003; Larson 1999):

- Dispersions (suspensions, emulsions, foams)
- Gels
- Polymer melts
- Polymer solutions
- Surfactant solutions
- Elastomers
- Liquid crystals
- Polyelectrolytes

These materials cannot be described as ideal elastic nor as ideal viscous bodies, they all show visco-elastic behavior which is caused by their microstructure and how the microstructure reacts to external mechanical fields. Within this thesis special interest was taken in the classes 'dispersions', 'gels', 'polymer melts', 'polymer solutions' and 'surfactant solutions'. In the following some fundamental textbook knowledge on the systems under investigation will be reviewed with an emphasis on their structures and the interactions of their constituents. The structure which results from interactions is ultimately responsible for the viscoelastic properties in the linear as well as the nonlinear regime.

## 3.1 Suspensions

Suspensions are heterogeneous systems, comprised of solid particles in a liquid medium. Important quantities characterizing a suspension are particle concentration or volume

fraction, particle size distribution and shape, but also particle surface properties such as the charge density or the thickness of a stabilizing layer. This multitude of variables makes suspensions a complex system with various structures: fluid, glassy crystalline and gel-like states are possible.

### Noncolloidal hard sphere suspensions

The most basic model system for real life suspensions is an ensemble of identical spheres of radius $a$ suspended in a Newtonian medium of viscosity $\eta_s$ with no other interactions than repulsion at contact. Structure and mechanical properties then depend on the particle number density $n$ or rather the volume fraction $\phi$ occupied by the particles.

$$\phi = \frac{V_{\text{particle}}}{V_{\text{solvent}} + V_{\text{particle}}} = \frac{4\pi a^3}{3} n \tag{3.1}$$

The phase diagram of a hard sphere suspension is only a function of the volume fraction $\phi$ as depicted in Fig. 3.1. Below $\phi_{\text{f}} = 0.495$ the sample is a disordered fluid, for $\phi_c < \phi < \phi_f$ there is a coexistence region of fluid and crystalline phases. Upon further increasing the volume fraction a fully crystalline sample is expected if enough time for the crystallization has passed. In practice such high order can be impeded by the slow crystallization kinetics. Therefore, above $\phi_g = 0.58$ one often finds a solid disordered state, that is termed the glass state. The glass state can exist only up to the maximum volume fraction of random close packing $\phi_{\text{rcp}} = 0.638$. If even higher volume fractions are to be achieved, crystallization is necessary, an ideal face centered cubic (fcc) lattice of spheres in direct contact would have the maximum volume fraction of $\phi_{\text{fcc}} = 0.74$.

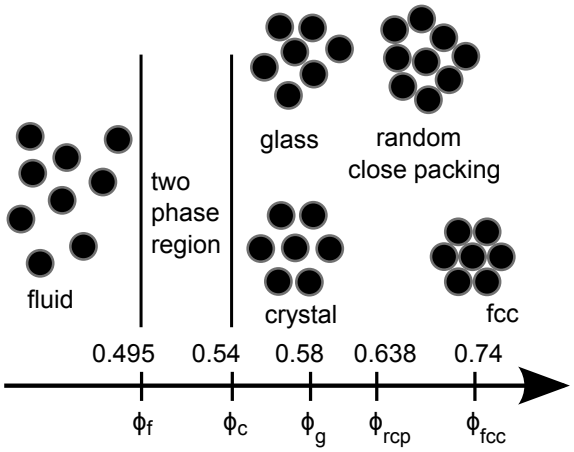


**Figure 3.1:** Phase diagram of a hard sphere suspension depending on the volume fraction $\phi$. See text for detailed description.

For polydisperse samples the crystallization can be avoided if the polydispersity of the particle radius exceeds approximately 12% (Phan et al. 1998) and the phase diagram simplifies to only one phase transition from the fluid to the glass. Experimental observations show that at this transition the relative zero shear viscosity $\eta_r$ diverges, at the same time a

yield stress emerges and the suspension becomes viscoelastic. All these rheological effects at the glass transition can be explained theoretically by the mode coupling theory (Fuchs 1995; Kob 2002; Brader et al. 2012; Brader et al. 2010; Siebenbürger et al. 2009). A simple local picture for the glassy system is that of the observed particle trapped in a cage of its neighbors as shown in the phase diagram in Fig. 3.1 for the glass. The escape of a particle from the cage can only happen by collective movement of several particles. The mode coupling theory will be introduced in more detail in Chapter 6, where its predictions for LAOS flow will be compared to experimental data measured on a concentrated suspension of PS/Pnipam particles (for experimental details see Chapter 8).
The relative zero shear viscosity $\eta_r = \eta(\phi)/\eta_s$ of a hard sphere suspension as a function of $\phi$ can be described by several relationships depending on the value of $\phi$ (Rutgers 1962):

- dilute range ($\phi < 0.05$)

  In the dilute range particles do not interact with each other, solving the flow problem around one particle suffices to describe the viscosity of the system. $\eta_r$ is linear in volume fraction as described by Einstein's law (Einstein 1906; Einstein 1911):

$$\eta_r(\phi) = 1 + 2.5\phi \tag{3.2}$$

- semidilute range ($0.05 < \phi < 0.15$)

  For increasing $\phi$ particle interactions cannot be neglected, then Einsteins equation can be extended by a quadratic term in $\phi$ to account for pair interaction:

$$\eta_r(\phi) = 1 + 2.5\phi + c_2\phi^2 \tag{3.3}$$

  The second order coefficient $c_2$ incorporates hydrodynamic effects as well as particle collisions and has been determined to be between 5 and 6 depending on the initial microstructure (Mewis and Wagner 2012).

- concentrated range ($\phi > 0.15$)

  For even higher volume fractions incremental addition of higher order terms in $\phi$ is not useful anymore, instead effective medium approaches are employed to correlate $\eta_r$ and $\phi$. A widely known relationship (Eq. 3.4) was proposed by Krieger and Dougherty (1959) and is depicted in Fig. 3.4. As soon as the volume fraction approaches the maximum value for a random close packing structure $\phi_{\mathrm{rcp}} = 0.64$, the relative viscosity diverges due to the increase of many body interactions.

$$\eta_r(\phi) = \left(1 - \frac{\phi}{\phi_{\max}}\right)^{-2.5\phi_{\max}} \tag{3.4}$$

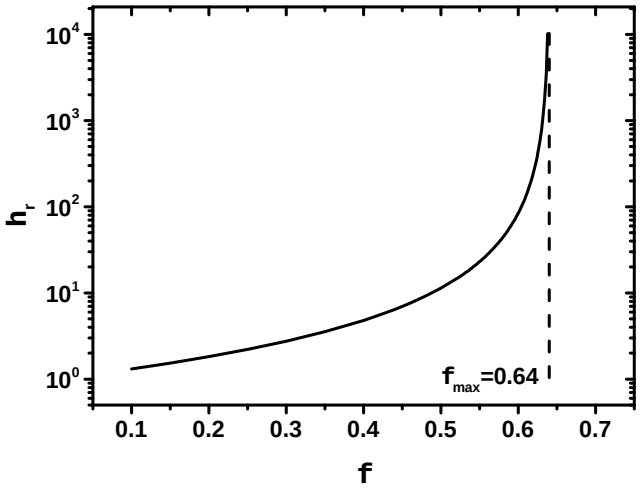


**Figure 3.2:** The relative zero shear viscosity $\eta_r = \eta_0/\eta_s$ as a function of the volume fraction according to Eq. 3.4 by Krieger and Dougherty (1959). The maximum packing fraction is taken to be that of the random close packing structure $\phi_{\mathrm{rcp}} = 0.64$.

### Brownian suspensions

For submicron sized particles ($a < 1\ \mu$m), thermal motion of the solvent molecules introduces an effective force acting on the suspended particles. This leads to Brownian diffusion with a characteristic time scale of $a^2/D_0$. The Einstein-Smoluchowski diffusivity $D_0$ can be calculated by Eq. 3.5, where $k_B$ is the Boltzmann constant and $T$ the temperature (Einstein 1905). Diffusion maintains an equilibrium structure in the suspension given enough time. In shear experiments the modification of the suspensions structure by the external forces is contested by Brownian diffusion which results in shear thinning, relaxation behavior and viscoelasticity (Larson 1999).

$$D_0 = \frac{k_B T}{6\pi\eta_s a} \tag{3.5}$$

It is advantageous to introduce the dimensionless shear rate $Pe$ (Eq. 3.6), known as Péclet number and the reduced stress $\sigma_{red}$ (Eq. 3.7) to compare suspensions of differently sized particles. $Pe$ is the ratio of advection by the flow, $\dot{\gamma}$ measured by to the rate of diffusion by Brownian motion. The reduced stress is the ratio of the measured stress to the natural energy scale per volume of a particle, $k_B T/a^3$ (Mewis and Wagner 2012). These dimensionless numbers will be used in Chapter 6, where nonlinear viscoelastic properties of a suspension of thermoresponsive particles that change their diameter with $T$ will be measured.

$$Pe = \frac{\dot{\gamma}}{D_0/a^2} = \frac{6\pi\eta_s\dot{\gamma}a^3}{k_B T} \tag{3.6}$$

$$\sigma_{red} = \frac{\sigma}{k_B T/a^3} \tag{3.7}$$

In the high frequency limit of an oscillatory shear experiment the particles response is dominated by hydrodynamic forces. Lionberger and Russel (1994) have developed an expression for the real part of the limiting high frequency viscosity $\eta'_{r,\infty}$ of hard spheres, see Eq. 3.8. It is a relative quantity normalized to the solvent viscosity and is therefore indexed with an $r$. The function diverges when the volume fraction is approaching $\phi = 0.64$. The expression can be used to infer $\phi$ by measuring $\eta'_{r,\infty}$.

$$\eta'_{r,\infty} = \frac{1 + 1.5\phi(1 + \phi - 0.189\phi^2)}{1 - \phi(1 + \phi - 0.189\phi^2)} \tag{3.8}$$

**Charged suspensions**

Pure hard sphere interactions are difficult to realize in practice. Charges covalently attached to the suspended particles and solubilized in the dispersant often remain from the synthesis and are notoriously difficult to remove. One possibility is extensive dialysis (Sirota et al. 1989; Hellweg et al. 2000). Therefore, interactions other than pure hard sphere repulsion must be considered. These can be of electrostatic or sterical nature.

Electrostatic stabilization is the most common case. Charges of the same sign attached to the particles form a repulsive layer. Its thickness decreases with increasing ionic strength ultimately leading to aggregation if the repulsion is screened entirely. The theory of Derjaguin, Landau, Verwey and Overbeek, which describes the interface as an electrical double layer, provides reasonable predictions for the dependence of the interaction potential on the ionic strength (Dörfler 2002; Mewis and Wagner 2012; Isrealachvili 1997).

Steric stabilization can be induced by grafting and/or adsorption of polymers onto the particle surface. A polymeric shell of sufficient density and molecular weight can prevent particles from aggregation by an entropic effect: If two particles approach each other, their polymeric shells start to penetrate each other. The resulting reduction of the conformational freedom of the individual polymer coils is unfavorable, hence the interaction is repulsive (Dörfler 2002).

The effects of a stabilizing layer can be qualitatively understood by assuming an effective radius which is larger than the core radius and consequently calculating an effective volume fraction $\phi_{\text{eff}}$. In doing so, mapping of rheological data of stabilized dispersions to data of hard spheres using $\phi_{\text{eff}}$ can be performed.

Electrostatic repulsion gives an additional contribution to the zero shear viscosity $\eta_{r,0}$ leading to its divergence at smaller nominal values of $\phi$. Steric stabilizing layers contribute to both, $\eta_{r,0}$ and $\eta'_{r,\infty}$, due to the increased hydrodynamic drag of the shell.

## 3.2 Colloidal gels

### 3.2.1 Fundamentals of colloidal gels

Colloidal gels are formed from attractive particles that build up a network as depicted in figure 3.5. Attractive interactions can be realized by screening the electrostatic repulsion until only van der Waals forces remain (Shao et al. 2013), by addition of a bridging agent (Kim, Merger, et al. 2014) or by depletion forces (Koumakis and Petekidis 2011). Sterical stabilization can be removed by changing the solvent quality for the stabilizing layer, for example by a change of temperature (Helden et al. 1981), and thus lead to gelation. The interaction is oftentimes modeled by square well potentials (Mewis and Wagner 2012). described by Eqs. 3.9, where $\Delta$ defines the width of the well. For distances ($r$) smaller that the diameter of the spheres $2ar$ the interaction is hard sphere repulsion, for $2a < r < 2(a + \Delta)$ attraction of $\epsilon$ is present, for even larger $r$ no interaction exists.

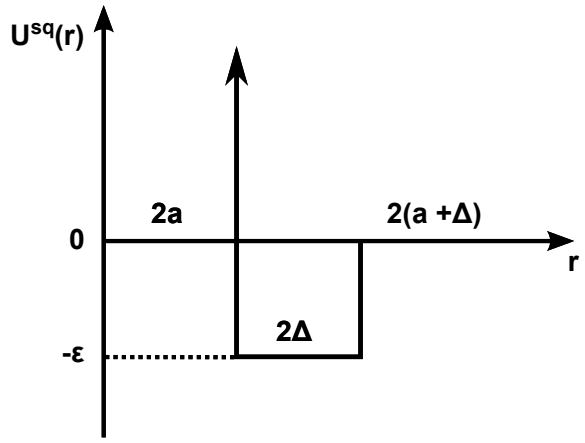


**Figure 3.3:** Square well potential which combines hard sphere repulsion for distances $r$ smaller than $2a$ and an attractive interaction for $2a < r < 2(a + \Delta)$.

$$U^{sq}(r) = \begin{cases} \infty, & r < 2a \\ -\epsilon, & 2a < r < 2(a + \Delta) \\ 0, & r > 2(a + \Delta) \end{cases} \tag{3.9}$$

The rich phase behavior that can be observed in a suspension of interacting spheres is shown schematically in Fig. 3.4. The upper part, where interactions are repulsive, resembles the phase diagram of hard spheres shown in Fig. 3.1, whereas the lower part contains additional phases, the gel and the attractive driven glass. Increasing $\phi$ at constant interaction strength leads to formation of particle clusters that eventually cross a percolation threshold and build a sample spanning network, which is then called a gel. At very high volume fractions and attractive interactions also a so-called attractive driven glass (ADG) state exists. The ADG differs from the repulsive glass (RDG) in the structure: since the particles are sticking to each other, the cage trapping an observed particle is much tighter. This results in qualitatively different dynamics as particle movements are more localized (Kaufmann and Weitz 2006). It has also an effect on the rheological properties, for example ADG systems

exhibit higher moduli than respective RDG systems (Mewis and Wagner 2012).

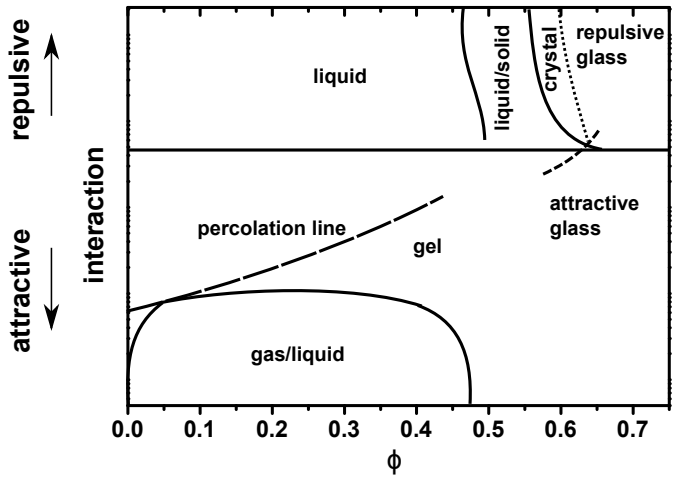


**Figure 3.4:** Schematic phase diagram for a suspension of interacting spheres, reproduced after Mewis and Wagner (2012).

In the presence of attractive forces the suspended particles stick to each other and initially form dimers, trimers and so forth. These early aggregates, called flocs, have a fractal structure, that means they are self-similar on multiple length scales ranging from the particle radius $a$ to the radius of gyration of the floc $R_g$. The radius of gyration is defined as the averaged particle distance to the center of mass, $R_g = 1/N \sum_{i=1}^{N} |\mathbf{r}_i - \mathbf{r}_{cm}|^2$, where $\mathbf{r}_i$ and $\mathbf{r}_{cm}$ are the vectors defining the position of the individual particles and the center of mass for the floc (Larson 1999).

**Figure 3.5:** Schematic structure of a fractal floc formed by attractive spheres. If this structure spans the entire sample, the system is called a gel.

The density distribution of fractal structures can be characterized by relating the number of particles $N$ with $R_g$ as in Eq. 3.10. The limits for the fractal dimension are $1 \leq D_f \leq 3$. For $D_f = 1$ the aggregates are chainlike, for $D_f = 3$ they are dense spheres (Mewis and Wagner 2012). Typical values for real systems are for example $D_f = 1.7 - 1.8$ for gold

particles or $D_f = 2.0 - 2.2$ for silica particles (Larson 1999). Gaussian polymer coils have a fractal dimension of 2 (Beaucage 1996).

$$N \propto \left(\frac{R_g}{a}\right)^{D_f} \tag{3.10}$$

With increasing $\phi$ the flocs eventually become so large that they connect and form a sample spanning mechanical network, which is called percolation. The percolation concept is also applied to other physical phenomena such as electrical conductivity of composite materials. At the percolation point the rheological properties change drastically, in a narrow $\phi$ range the material turns from a liquid to a viscoelastic solid with a yield stress. An important rheological criterion for determining the critical gel state has been established by Chambon and Winter (1987): at the liquid-solid transition the linear moduli follow a power law behavior, $G'(\omega) \propto \omega^n$ and $G''(\omega) \propto \omega^n$, which originates from a power law distribution of relaxation times corresponding to a distribution of length scales. The exponent $n$ is between 0.5 and 1, usually close to 0.5 (Mewis and Wagner 2012). Measuring a full frequency spectrum depending on the floc volume fraction can be difficult in cases where the gelation process is time dependent. This is the case for gelations induced by a chemical reaction or by physical adsorption. Therefore, the simple criterion $G' = G''$ measured at a single frequency is oftentimes preferred instead. This however, is only correct for gels where the powerlaw exponents for $G'(\omega)$ and $G''(\omega)$ are exactly 0.5 (Winter 1987).
The elastic properties of the resulting gels depend in a complicated way on the inter-particle potential $U(r)$. Nevertheless, some simple scaling relationships can be provided by theory for the storage modulus $G'$ and the yield stress $\sigma_c$. Based on mode coupling theory (MCT) predictions, Eq. 3.11 has been used to scale $G'$ with the particle radius $a$, volume fraction $\phi$ and inter particles potential $U(r)$, which enters into the localization length $r_{loc}$ (Chen and Schweizer 2004). An introduction to MCT will be given in Chapter 6, page 105.

$$\frac{G'a^3}{k_BT} = 0.29\frac{\phi a^2}{r_{loc}^2} \tag{3.11}$$

Within mode coupling theory, $r_{loc}$ is a finite mean-square displacement of the particles at long times and serves as a structural characteristic of the gel on a smaller length scale than the previously introduced radius of gyration of the flocs. Larger scale structures are considered indirectly through modification of $r_{loc}$ (Mewis and Wagner 2012).
The yield stress is assumed to be proportional to the number of particle contacts in the system and the force required to break the contacts. The breaking force is given by the maximum of the first derivative of the potential. Therefore, a relation according to Eq. 3.12 can be used to rescale experimental yield stress data for different concentrations and potentials (Larson 1999).

$$\sigma_c \propto \frac{\phi^2}{a^2}\left(\frac{\mathrm{d}U}{\mathrm{d}t}\right)_{max} \tag{3.12}$$

Structural heterogeneity in colloidal gels can strongly influence the rheological properties,

for example Wyss et al. (2004) found that heterogeneous gels of attractive silica particles exhibit much higher elastic and yield properties than homogeneous gels at the same volume fraction. In Chapter 7, the nonlinear viscoelastic behavior of a heterogeneous gel under LAOS will be addressed.

### 3.2.2 Small angle scattering of fractal gel systems

The fractal structure of colloidal gels can be investigated by scattering methods (Mewis and Wagner 2012). If the primary particles and the agglomerates are on the nanometer scale, small angle X-ray and neutron scattering are well established methods to provide information on structural parameters such as the fractal dimension (Teixeira 1988; Bushel et al. 2002; Bhatia 2005). In Fig. 3.6 the small angle scattering experiment is shown schematically.

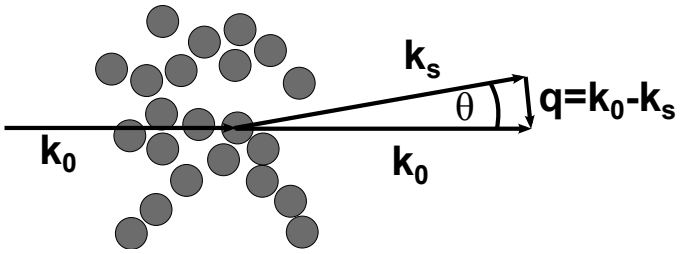


**Figure 3.6:** Schematic depiction of the small angle scattering experiment on a fractal arrangement of spheres.

If the incident beam, described by the vector $\mathbf{k}_0$, is scattered by interaction with a particle, the resulting scattered beam $\mathbf{k}_s$ has a scattering angle of $\theta$ to $\mathbf{k}_0$. The difference $\mathbf{q} = \mathbf{k}_0 - \mathbf{k}_s$ is called scattering wave vector and is connected to $\theta$ by $\mathbf{q} = 2\mathbf{k}_0 \sin(\theta/2) = 4\pi/\lambda \sin(\theta/2)$, where $\lambda$ is the wave length. The inverse $\mathbf{q}^{-1}$ represents the length scale which is probed in the scattering experiment. For crystalline structures, Bragg's law of diffraction (Eq. 3.13, Bragg and Bragg 1913) relates the plane distance $D$ of the lattice with the magnitude of the scattering wave vector $q = |\mathbf{q}|$.

$$q = \frac{n2\pi}{D} \qquad \text{or} \qquad n\lambda = 2D\sin(\theta/2) \tag{3.13}$$

For less ordered structures (fluids, amorphous solids, fractals), Bragg reflexes are not observed, however the interpretation of $q$ as a measure for the probed length scale can still be applied. For example values in the range $0.063\ \text{nm}^{-1} < q < 0.63\ \text{nm}^{-1}$ correspond to probed lengths in the range $10\ \text{nm} < D < 100\ \text{nm}$.

The $\mathbf{q}$ dependent scattering intensity $I(\mathbf{q})$ of a system of scatterers with the number density $N$ can be described as the product of the scattering produced by an individual scatterer, the form factor $P(\mathbf{q})$, and the scattering due to the arrangement of the particles, the structure factor $S(\mathbf{q})$ (Eq. 3.14).

$$S(\mathbf{q}) = NP(\mathbf{q})S(\mathbf{q}) \tag{3.14}$$

For isotropic scattering, the form factor of a sphere of radius $a$ of uniform density $\rho$ is described by Eq. 3.15, where $V$ is the volume and $\rho_0$ is the density of the dispersant. The form factors of other simple geometrical objects such as rods or ellipsoids can be found in Guinier and Fournet (1955).

$$P(q) = V^2(\rho - \rho_0)^2[3\sin(qa) - qa\cos\left(\frac{qa}{(qa)^3}\right)]^2 \tag{3.15}$$

The most challenging part of interpreting scattering curves is the appropriate modeling of the structure factor $S(q)$. For isotropic systems, $S(q)$ can be written explicitly in terms of the pair distribution function $g(r)$ (Eq. 3.16).

$$S(q) = 1 + N\int[g(r) - 1]r^2\frac{\sin(qr)}{qr}\mathrm{d}r \tag{3.16}$$

For fractal systems with a fractal dimension $D_f$ (Eq. 3.10), $g(r)$ can be written as in Eq. 3.17. The parameter $\xi$ is introduced as a cut-off length above which the structure of the system is not fractal but homogeneous (Teixeira 1988).

$$N[g(r) - 1] = \frac{D_f}{4\pi a^{D_f}}r^{D_f-3}\exp(-r/\xi) \tag{3.17}$$

Fourier transform of Eq. 3.17 and substitution in Eq. 3.16 gives $S(q)$, where $\Gamma$ denotes the Gamma function:

$$S(q) = 1 + \frac{1}{(qa)^{D_f}}\frac{D_f\Gamma(D_f - 1)}{\left[1 + \frac{1}{q^2\xi^2}\right]^{\frac{D_f-1}{2}}}\sin[(D_f - 1)\arctan(q\xi)] \tag{3.18}$$

At small values of $q$ the scattering is dominated by the large scale structure, whereas at large $q$ the individual particles form factor dominates (Teixeira 1988). Usually one measures the form factor independently on a diluted sample, subsequently divides the total scattering intensity by $P(q)$. The resulting $S(q)$ is then modeled by equations such as Eq. 3.18 to extract the fractal dimension (Courtens and Vacher 1987).

## 3.3 Polymer melts and polymer solutions

Polymers consist of covalently bonded molecules that assume a coiled conformation due to their many rotational degrees of freedom. In an ideal solution, Gaussian statistics of a 'random walk' in 3 dimensions is an adequate formalism to describe the dimension of the coil. This gives the average end-to-end distance $\langle R^2\rangle = Nl^2$, where $N$ is the number of segments (proportional to the molecular weight $M$) and $l$ is the length of the segment (Dealy and Larson 2006).

In dilute solutions ($\phi < 0.01$) the polymer coils swell in the solvent filling a larger volume than they would in the melt. Their conformation is not perturbed by the neighboring chains and the ensemble of coils is essentially a dispersion of soft spherical particles. Steady shear viscosities for a specific molecular weight are linear in concentration in this regime (Einstein

1906; Einstein 1911). The dependence on molecular weight can be described by the intrinsic viscosity $[\eta]$, as defined in Eq. 3.19, where the solvent contribution $\eta_s$ is subtracted and the resulting relative viscosity has been extrapolated to vanishing concentrations. The intrinsic viscosity $[\eta]$ shows then a power law dependence on the viscosity averaged molecular weight $M_v$. The powerlaw exponent $f$ depends on the solvent quality and the proportionality constant $K_c$ depends on the chemistry of the polymer. The parameters $K_c$ and $f$ are known as the Mark-Houwink parameters (Young and Lovell 2011) and have been determined experimentally for many combinations of polymers and solvents (Mark 2007). The intrinsic concept of extrapolation to vanishing concentration is similar to the definition of nonlinear parameters like $Q_0$ (Hyun and Wilhelm 2009) or intrinsic Chebishev coefficients, which are extrapolated to zero strain amplitude (Ewoldt and Bharadwaj 2013), see Chapter 2 for more details.

$$[\eta] = \lim_{c\to 0} (\eta_0 - \eta_s)/\eta_s c = K_c M_v^f \tag{3.19}$$

Microscopic theory predicts that even dilute solutions are already viscoelastic (Ferry 1980). The source of viscoelasticity lies in the orientational degrees of freedom and the possibility to stretch the polymer chain by the flow. Many models of different complexity ranging from rigid dumbbells to bead spring models exist for the linear properties and give expressions for the intrinsic storage and loss moduli $[G'] = \lim_{c\to 0} G'/c$ and $[G''] = \lim_{c\to 0} (G'' - \omega\eta_s)/c$ of polymer solutions (Bird et al. 1987). Viscoelastic behavior of dilute solutions plays a crucial role for drag reduction (Ting and Hunston 1977) and vortex inhibition in turbulent flow (Gordon and Balakrishnan 1972).

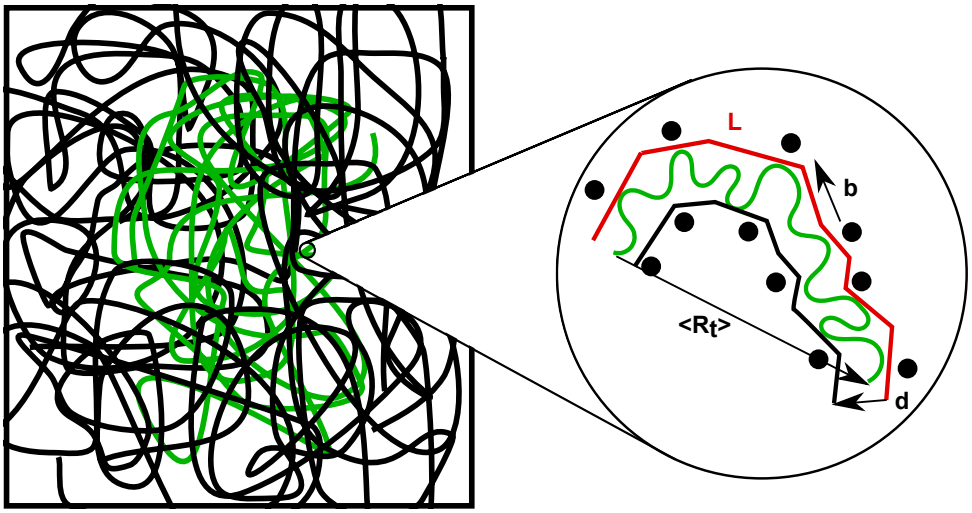


**Figure 3.7:** Structure of a polymer melt or a concentrated solution: The macromolecules are disordered coils that overlap and are entangled. Neighbor chains restrict the movement of the observed chain, therefore it can only diffuse along a tube shaped path. This mean field approach is the basis of the Doi-Edwards theory.

Typically, for volume fraction above 0.1 the polymer coils overlap and therefore assume dimensions that are identical to those in the melt (Graessley 2008). Thus, many of the

theoretical predictions derived for the melt are also applicable for the concentrated solution. Figure 3.7 depicts the structure of such a concentrated solution or melt. If the chains have a higher molecular weight than some critical entanglement molecular weight, $M_e$, they intertwine and form entanglements. These non-permanent crosslinks are responsible for elastic effects in polymer melts. The entanglement molecular weight $M_e$ decreases for increasing chain stiffness, which means stiffer chains are more entangled (Heymans 2000). A typical value for $M_e$ of for example a cis 1-4 polyisoprene is 4000 g/mol (Mark 2007). However, around 3 entanglement per chain are necessary to significantly change the rheological properties. For $M > 3M_e$ the experimentally observed $M$-dependence of the zero shear viscosity (Eq. 3.20) in a melt changes from approximately linear to a power law with an exponent $n = 3.4$.

$$\eta_0 = KM^n \tag{3.20}$$

The dynamics of an entangled polymer system can be effectively modeled by a mean field approach where a single chain is described in a matrix of the remaining chains, as shown in Fig. 3.7. The other chains form a constraint that is shaped like a tube in which the observed chain can diffuse along its contour and to some extent sidewise. This picture has become the basis for the widely known 'tube theory' or Doi-Edwards theory named after its original proposers (Doi and Edwards 1986). Important results of their work are expressions for the tube dimensions: the tube diameter $d$ (Eq. 3.21), end-to-end distance of the tube $\langle R_t \rangle$, the segment length $b = \langle R \rangle / N$ and the contour length $L = d \cdot M/M_e$, where $\rho$ is the polymer density.

$$d^2 = \frac{4}{5}\frac{M_e}{M_0}b^2 = \frac{4}{5}\frac{\rho RTb^2}{M_0 G_N^0} \tag{3.21}$$

Based on the tube dimensions and a monomeric friction coefficient $\xi_f$ the time needed for a chain to diffuse from its initial tube ($\tau_d$), which is the longest relaxation time, can be expressed by Eq. 3.22.

$$\tau_d = \frac{\xi_f N^3 b^4}{\pi^2 k_B T d^2} \tag{3.22}$$

Furthermore, the plateau modulus $G_N^0$ (Eq. 3.23) and the molecular weight dependence of the zero shear viscosity (Eq. 3.24) can be obtained.

$$G_N^0 = \frac{4}{5}\frac{\rho RT}{M_e} \tag{3.23}$$

$$\eta_0 = 0.822 G_N^0 \tau_d \tag{3.24}$$

As the reptation time $\tau_d$, according to Eq. 3.22, scales cubic with the molecular weight $M$ (or $N$), the exponent $n$ for the general molecular weight dependence in Eq. 3.20 is predicted to be 3 by the tube model, which is very close to the experimentally observed

3.4 (Graessley 2008).
Although the tube model takes entanglements into account it does describe them explicitly as point contacts of two chains, that is why some experimental effects are not accounted for by the tube model. An example is the relaxation behavior after large strain steps, where the relaxation mechanisms covered by the tube theory, chain retraction and chain stretching (Dealy and Larson 2006), are not suffiecient to describe recent experimental data (Boukany et al. 2009). Wang (2015) discusses this problem and contrasts the tube idea to more detailed molecular entanglement theories.

## 3.4 Wormlike micelle surfactant solutions

Surfactants are amphiphilic molecules with a polar head and a nonpolar tail, which are widely used as detergents in home and personal care or as stabilizers for colloidal dispersions. In solution they form aggregates above a certain concentration, the critical micelle concentration (CMC) (Dörfler 2002). Depending on physico-chemical conditions like concentration, temperature and ionic strength, these aggregates, most commonly called micelles. They can have a variety of shapes: spheres, rods, lamellae (Rehage and Hoffmann 1991; Dörfler 2002). Furthermore, liquid crystalline phases can be obtained at even higher concentrations (Cappelaere et al. 1995). Surfactant molecules with relatively small head group areas tend to pack in elongated, rodlike aggregates (Isrealachvili 1997). This phase where the micelles attain a wormlike shape has attracted considerable research interest, because if the micelles become long enough to entangle, a viscoelastic fluid forms. The wormlike micelle solution has many structural features that are similar to polymer melts as shown in Fig. 3.8. The long cylindrical aggregates can be linear or branched (Rogers et al. 2014). As for polymers longer chains lead to overall higher viscosities of the solution. The difference to polymeric systems is that the molecules in wormlike micelles (WLMs) are not covalently bound to each other, therefore breaking and reformation is taking place continuously.
Typical surfactant systems that form WLMs are depicted in Fig. 3.9: cetylpyridinium chloride, cetyltrimethylammonium bromide (CTAB), sodium dodecylbenzenesulfonate or dimethyl(tetradecyl)amine oxide. Additionally, various salts and co-surfactants can be added to promote chain growth. Salt addition induces chain growth due to enhanced screening of interactions (Isrealachvili 1997), for WLMs based on CTAB for example potassium bromide can be used (Khatory et al. 1993). However, at higher concentrations salt is also known to induce branching of the micelles (Rogers et al. 2014).
Added co-ions, a widely known example is salicylate, interfere with the structure of the micelles through adsorption and therefore modify the chain length (Rehage and Hoffmann 1991). The effect of the co-ion concentration on the chain length, and therefore the rheological properties, is non-monotonic. Oftentimes plots of viscosity versus co-ion concentration exhibit several maxima and minima (Rehage and Hoffmann 1991).
WLMs are widely used as rheological modifiers and as detergents in home and personal

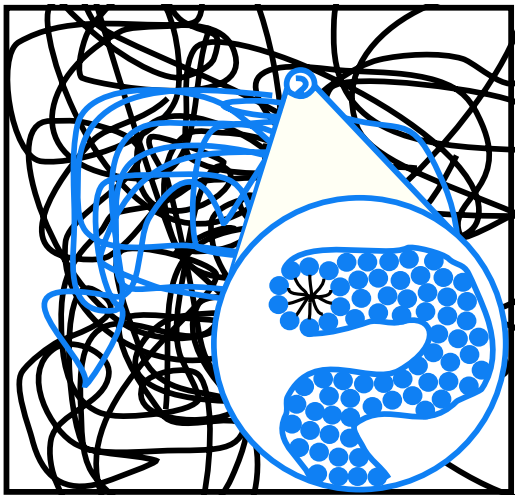

**Figure 3.8:** Structure of a solution of wormlike micelles: Amphiphilic surfactant molecules (examples are shown in Fig. 3.9) assemble into long tube-like micelles that entangle similarly to macromolecules in a polymer melt (compare to Fig. 3.7).

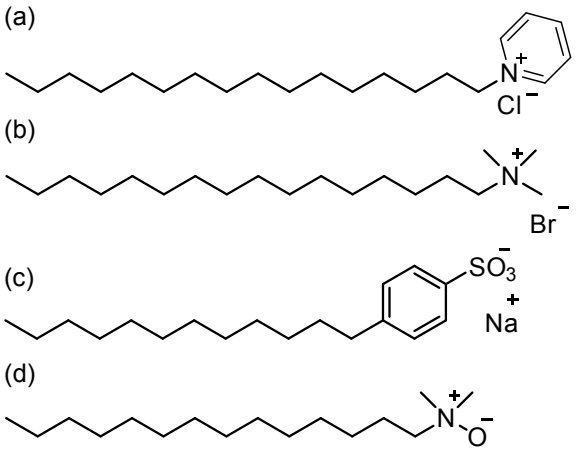


**Figure 3.9:** Chemical structures of some common surfactant systems known to form wormlike micelles: (a) Cetylpyridinium chloride, (b) Cetyltrimethylammonium bromide, (c) sodium dodecylbenzenesulfonate, (d) Dimethyl(tetradecyl)amine oxide.

care products (Yang 2002). Another field of application is fluid fracturing in oil drilling, where WLMs are superior to conventional polymer solutions. Their main advantage is that clogging as it happens with polymer residue can be avoided since WLM can be reversibly broken down to the small molecular size of their surfactant constituents (Chase et al. 1997). WLMs can also serve as drag reducing agents in pumping processes, similar to water soluble polymers, but with the advantage that chain degradation is countered by their spontaneous restoration (Rodrigues et al. 2008).

The continuous presence of scission and reformation events in the elongated cylinders leads to surprisingly simple rheological behavior under small amplitude oscillatory shear: As long as the chain scission occurs fast enough compared to the observation time of the experiment, the chain contour is renewed by breaking and recombination (Rogers et al. 2014) and not by reptation as is the case for linear entangled polymers. Therefore, only

a single relaxation time is present despite the chains having different lengths. A single relaxation time leads to Maxwell behavior as pointed out in Chapter 2. Experimentally determined storage and loss moduli, $G'$ and $G''$, can be easily fitted with Eqs. 2.17 and 2.17, subsequently the model parameters elastic modulus $G$ and relaxation time $\lambda$ can be extracted with high precision. More detailed modeling of $G'$ and $G''$ has been used recently to extract characteristic length and time scales such as average micelle length, breakage rate, entanglement and persistence lengths (Zou et al. 2015).

The specific microstucture of WLMs is also responsible for their rich nonlinear behavior. In steady shear experiments, after an initial shear thinning region, a plateau in the stress versus shear rate curves has been observed (Helgeson, Vasquez, et al. 2009). This has been explained by shear banding, an instability where the symmetry of the simple shear flow field is broken and two bands with two different shear rates appear. The cause of this instability has been attributed to an isotropic-nematic transition (Helgeson, Reichert, et al. 2009) similar to that in liquid crystals.

The particularly simple linear rheological properties of WLMs, especially the Maxwellian behavior under small amplitude oscillatory shear, make them an ideal model system for studies of nonlinear viscoelasticity. This will be the subject of Chapter 5, where a simple extension of the Maxwell model will be verified experimentally using a CTAB sample.

# Chapter 4

# Current limits of detection and reproducibility in LAOS experiments for stress and strain controlled rheometers

Early Large Amplitude Oscillatory Shear experiments have been conducted by Dodge and Krieger (1971); Krieger and Niu (1973) using a modified Weissenberg Rheogoniometer. At that time Fourier Analysis was performed by an oscilloscope. When employing harmonic intensity analysis, the signal-to-noise ratio ($S/N$), that is the ratio of an intensity of a harmonic to the intensity at a point in the spectrum where it is known that no peak is present, are crucial to estimate the limit of detection. The signal-to-noise ratio in the spectra of Krieger and Niu (1973) were claimed to be high but no actual numbers were specified. Excessive LAOS investigations were hampered by the rheometer's accuracy and too tedious data acquisition and processing for that time. Later, LAOS measurement on polymeric samples were made using sliding plate rheometers (Giacomin et al. 1989). Mostly, Lissajous figures were analyzed by fitting constitutive model predictions to experimental data (Jeyaseelan and Giacomin 1993; Yosick et al. 1997). However, Fourier Transform was also employed and $S/N \approx 300$ were achieved (Giacomin and Dealy 1998).

Wilhelm et al. (1998) introduced a simple setup that coupled a commercial rheometer to an analog-to-digital converter, which made the deflection angle and torque data easy to sample for post-processing on a personal computer. This step was crucial for the increased availability of LAOS capable instruments. Before that, LAOS tests could still be performed on commercial rheometers but only $G'$ and $G''$ could be analyzed because the full waveform data was discarded after calculation of $G'$ and $G''$ to free up memory. With the set-up of a commercial instrument and custom data processing, which also included oversampling (Dusschoten and Wilhelm 2001), $S/N$ of up $10^5$ to were possible (Wilhelm 2002).

Nowadays several commercial instruments are available that include at least some forms

of LAOS analysis routines in their software but the exact data treatment is confidential. Nevertheless, optimized measuring procedures using commercial routines led to $S/N$ of over $10^7$ (Wilhelm et al. 2012). However, the instruments $S/N$ is not the only limiting factor in harmonic intensity detection. If the sample's rheological properties slowly change over time or sample loading procedures are inconsistent, exact reproduction of harmonic intensities can be difficult. In this thesis an assessment of the repeatability and reproducibility of LAOS experiments on different instruments has been performed. The results have been previously published in references (Merger and Wilhelm 2014) and (Giacomin et al. 2015), therefore this chapter contains passages and figures which are very similar the ones in the articles. Specifically, it was investigated if different instruments measure the same values for $I_{3/1}$ over a range of $\gamma_0$ and $\omega$ for a given sample. For this purpose, three polymeric samples were chosen because they are easy to handle, their composition stays constant over time and they reproducibly showed the expected square scaling of $I_{3/1}$ with the strain amplitude on the ARES-G2 rheometer. The samples were an anionically synthesized 1,4-cis-polyisoprene melt (abbreviated: PI-84k, $M_w$ = 84000 g/mol, PDI = 1.04) and two 10 wt.-% solutions of polyisobutylene (PIB, $M_w = 1.1{\cdot}10^6$ g/mol and PIB-2, $M_w = 4.8{\cdot}10^6$ g/mol). More details on the systems can be found in Chapter 8.

## 4.1 Strain controlled and stress controlled rheometers

Currently, two general rotational rheometer types (Macosko 1994) are commercially available that can be used for LAOS experiments: controlled strain rheometers and controlled stress rheometers. Apart from the rotational rheometers, custom built instruments, such as the sliding plate rheometer by Giacomin et al. (1989) are also suitable, but will not be discussed here, as they are less common. Furthermore, there are rotational rheometers available that use closed, pressurized measuring geometries. The LAOS capabilities of these instruments have been investigated by Debbaut and Burhin (2002). The two common rotational rheometer types differ slightly in their design and are depicted schematically in Fig. 4.1. In Fig. 4.1 (a), the setup of a strain-controlled or separated motor-transducer (SMT) rheometer is shown. Here the sample follows the lower plate that performs a set deformation profile, so that strain is the input variable and stress is the output variable (strictly the instruments apply a certain angular displacement that is related to the strain and measure a torque that is related to the stress, the conversion constants depend on the geometry type being used). The stress is determined from the electrical voltage and current that are needed to keep the upper geometry in a fixed position by a second motor, the transducer. The voltage is directly related to the torque generated by the sample which is again proportional to the stress. This measuring principle is known as a force rebalance transducer (FRT). The advantage of the SMT design is that the torque measurement is completely decoupled from the torque that is applied by the rheometer in order to deform the sample.

Figure 4.1 (b) shows the basic principle of the stress-controlled rheometer, also known as a

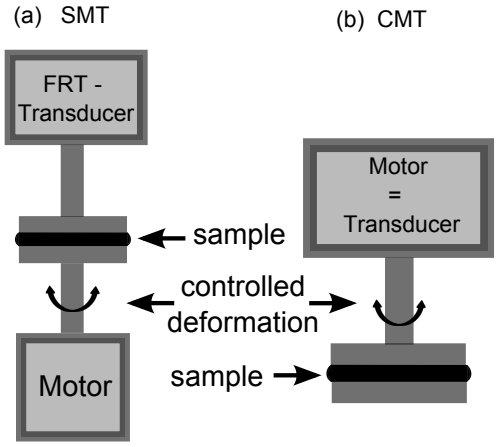


**Figure 4.1:** Typical design of an (a) separated motor-transducer (SMT) rheometer and (b) combined motor-transducer (CMT) rheometer. The SMT instrument uses a force rebalance transducer (FRT) for torque detection, whereas in the CMT instrument the drag cup motor itself is the torque transducer.

combined motor-transducer (CMT) rheometer. The lower geometry part is fixed to the frame of the instrument and the upper geometry part can be rotated by controlling the torque produced by the motor. In this case, the torque transducer is the motor itself, the input signal is the stress and the output signal is the strain (Macosko 1994). The software of these instruments allows for running an experiment at variable strain amplitudes. When using this operation mode several, iterative cycles have to be measured before the actual measurement. During these iterations, the applied torque is adjusted to produce the desired strain amplitude (Läuger et al. 2002). In contrast to the classical way of amplitude adjustment, new operating modes of CMT-Rheometers (termed *Direct Strain Oscillation* or *Continuous Oscillation*) use a feedback control to compare the current strain signal $\gamma(t)$ at time $t$ to the desired pure sinusoidal signal $\gamma_d(t) = \gamma_{d0} \sin(\omega_1 t)$. The control loop then adjusts the torque accordingly in order to minimize the difference $|\gamma_d(t + \Delta t) - \gamma(t + \Delta t)|$ for the next step at $t + \Delta t$. This deformation control enables a CMT-Rheometer to mimic a strain controlled experiment (Läuger et al. 2002). This holds true even beyond the linear regime where nonlinear contributions to the strain wave are compensated for and are then transferred into the stress wave, as the control loop tries to make the appropriate adjustments to the torque within minimum time.

## 4.2 Temperature effects

Before one starts to compare reproducibility of LAOS experiments it is important to have some knowledge on the material's linear properties and if they are measured correctly by all instruments. Viscoelastic properties have a significant temperature dependence which is described by the Williams-Landel-Ferry (WLF) equation and the Time-Temperature-Superposition principle (TTS) (Macosko 1994; Shaw 2012). According to the TTS principle, when measuring the frequency behavior of a polymeric sample in a SAOS test, instead

of increasing the frequency for measuring larger $De$, alternatively one can lower the temperature, thus increasing the relaxation times of the polymer. The TTS principle is therefore used to measure mechanical spectra over a wider range in angular frequency than it is instrumentally possible. Usually shear rheometers cannot exceed $\omega$ higher than $\approx$ 100 rad/s. Higher frequencies are accessed by cooling the molten sample and shifting the measured $G'$ and $G''$ curves to higher frequencies, thus creating a master curve (Dealy and Larson 2006).

It is important to confirm that all investigated instruments control the temperature equally well. For this purpose frequency dependent tests were made for PI-84k and PIB. The data is displayed in Fig. 4.2 and shows good agreement (less that 12% deviation) for the moduli and $\tan\delta$ measured on all instruments with one exception: When using the ARES-LS, the temperature was controlled with a forced convection oven (FCO) in contrast to the Peltier plate that was used for the other three instruments. This had a severe effect on both the linear and the nonlinear measurements. With FCO temperature control the values for moduli and $I_{3/1}$ were around 30% smaller than those measured on the other instruments due to the different thermal conditions of the sample. A direct comparison on a single instrument between the FCO and Peltier plate heating methods as measured on the ARES-G2 is shown in Fig. 4.3. Here, it is evident that the moduli differ by the same horizontal factor across the measured frequencies. The reason for this is assumed to be a temperature gradient due to the fact that a Peltier plate is heating only the bottom part of the sample whereas the FCO is assumed to produce a more homogeneous temperature field. The frequency dependent linear data can be matched by shifting the Peltier data to higher frequencies using a factor of 1.39, which corresponds to setting the Peltier plate to 57°C instead of 52.8°C. The same shift factor was consequently applied to all nonlinear measurements of the PI-84k sample that were made using Peltier plates at $T = 52.8$°C.

For the PIB polymer solution, the results for the moduli and the loss tangent measured with the different instruments agreed within a range of $\pm$ 15%. At angular frequencies below 5 rad/s the ARES-LS was not able to reliably determine the phase angle, therefore the loss tangent and the storage modulus scattered strongly. This can be attributed to the lower instrument sensitivity of ARES-LS relative to the ARES-G2 and DHR. The results from the MCR 501 show a similar deviation in $\tan\delta$ and in $G'$ for angular frequencies lower than 3 rad/s. In this case the deviation can not be explained by reaching the sensitivity limit, as the minimum measurable torque for the MCR 501 is comparable to the one of the DHR-3 instrument (see table 8.2). However, the sensitivity issue plays no role in the LAOS tests, since at larger amplitudes, the measured torques are sufficiently large to ensure a precise determination of the nonlinear parameters. Since the PIB measurements were performed at 25°C the possible discrepancies between Peltier and oven temperature control were small enough (the moduli varied by less than 6%) to be neglected and no shift in the frequency was necessary for the ARES-LS data.

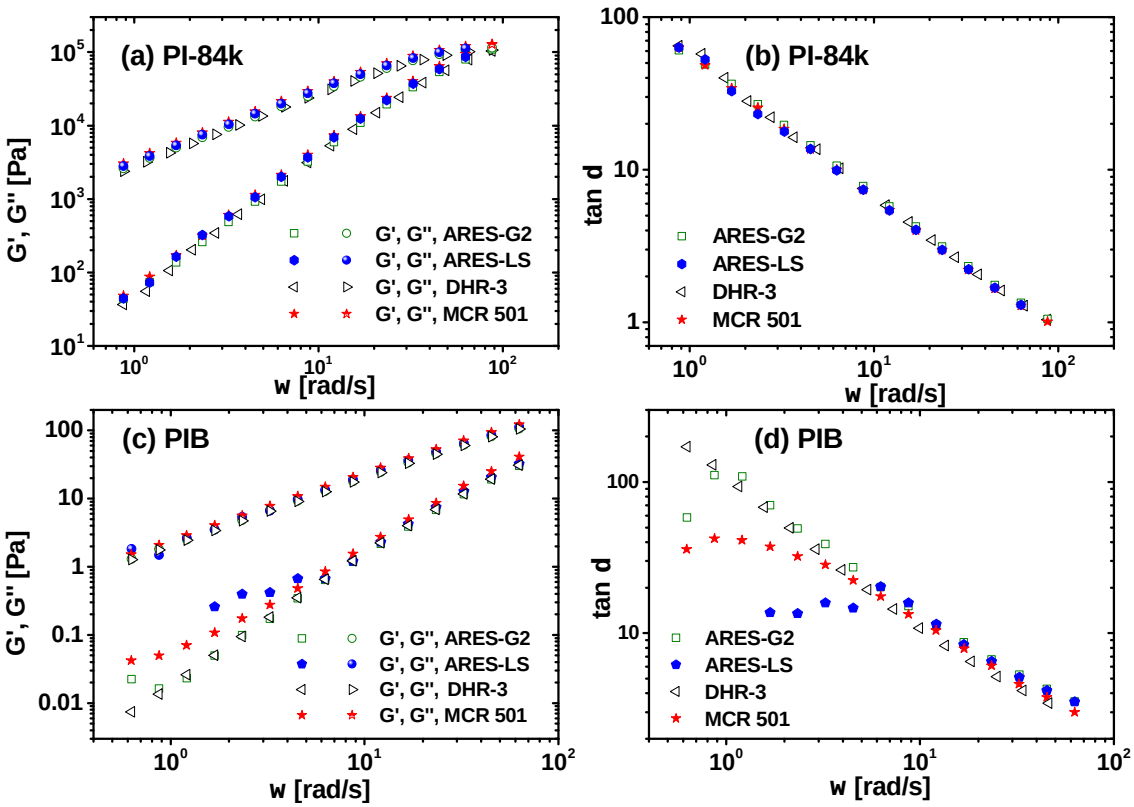


**Figure 4.2:** Storage and loss moduli ($G'$ and $G''$) (a) and $\tan\delta$ (b) for PI-84k and for the PIB solution, (c) and (d), measured at a strain amplitude of 0.01 for PI-84k and 0.1 for PIB on the four indicated instruments. The measuring temperatures were 52.8°C for PI-84k and 25°C for PIB. Note that for PI-84k the ARES-G2, DHR-3 and MCR 501 data was horizontally shifted to higher frequencies with the factor $\alpha = 1.39$ in order to account for using a Peltier plate for temperature control instead of forced convection oven heating.

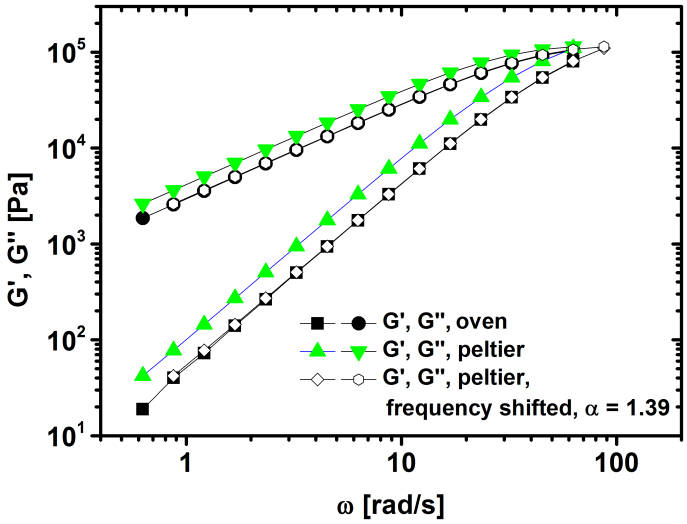


**Figure 4.3:** Storage and loss moduli of PI-84k measured at a strain amplitude of 0.01 on the ARES-G2 using either Peltier plate or a forced convection oven for temperature control. The temperature was set to 52.8°C . The data obtained using the Peltier plate can be matched to the oven data by multiplying the frequency axis by $\alpha = 1.39$.

## 4.3 Geometry effects

When performing LAOS experiments on samples with appreciable viscosities (larger than $\eta \approx 100$ Pas) using parallel disks or cone and plate geometry is preferable to a concentric cylinders (Couette) geometry due to easier loading procedures. Furthermore smaller sample amounts are needed than for concenctric cylinders. When deciding between parallel disks and cone and plate one has to acknowledge the inhomogeneous flow field in the parallel disks geometry: As the plate distance is constant the strain and the shear rate increases linearly along the radius (Macosko 1994; Giacomin and Dealy 1998). This has an impact for linear measurement of $G'$ and $G''$ already. In general, for parallel disks flow the stress $\sigma$ can be calculated from the torque $M$ by using Eq. 4.1 with $R$ being the radius of the disks and $\theta_0$ the deflection angle amplitude. However, as the derivative $\mathrm{d}M/\mathrm{d}\theta_0$ enters into the calculation, a series of narrowly spaced measurements for varying $\theta_0$ (therefore varying $\gamma_0$) and subsequent numerical differentiation are always needed to calculate $\sigma$ from $M$. This procedure has been used successfully by MacSporran and Spiers (1984) and recently by Fahimi et al. (2014) for LAOS measurements.

$$\sigma = \frac{1}{2\pi R^3}\left(\theta_0 \frac{\mathrm{d}M}{\mathrm{d}\theta_0} + 3M\right) \tag{4.1}$$

Wilhelm et al. (1999) measured differences between cone/plate and parallel disks geometries and adjusted by multiplying by the strain amplitude values of the parallel disk experiments by 0.75 to match parallel disk results to data from cone and plate experiments. This was done based on the idea of an 'equivalent radius'. This radius is smaller than the actual disk radius so that the average strain amplitude in parallel disks equals the one from the cone and plate geometry. This procedure was used successfully to correct $I_{3/1}$ for solutions of polyisobutylene. Wagner et al. (2011) corrected using a multiplication factor of 3/2 to convert $M_{3/1}$ from parallel disk experiments to $I_{3/1}$ measured on polystyrene melts. This procedure was crucial to reach agreement of their experiments with the model predictions of the molecular stress function model.

Giacomin et al. (2015) used a detailed analysis of the corotational Maxwell model to derive an analytical expression for the conversion of the relative intensity of the third harmonic as measured in a parallel disks geometry to the true intensities as they would be measured in cone and plate geometry. The corotational Maxwell model is a differential, tensorial model which can be written as Eq. 4.2 (Giacomin et al. 2011; Saengow et al. 2015).

$$\boldsymbol{\sigma} + \lambda \frac{\mathscr{D}\boldsymbol{\sigma}}{\mathscr{D}t} = -\eta_0 \dot{\boldsymbol{\gamma}} \tag{4.2}$$

In Eq. 4.2, $\dot{\boldsymbol{\gamma}} = \nabla \mathbf{v} + (\nabla \mathbf{v})^{\dagger}$ denotes the rate of deformation tensor (Bird et al. 1987). The difference to the standard Maxwell model (Chapter 2.1.1, page 16) is the use of the

Jaumann derivative which includes the material derivative $\mathrm{D}\boldsymbol{\sigma}/\mathrm{D}t = \partial\boldsymbol{\sigma}/\partial t + \mathbf{v}\cdot\nabla\boldsymbol{\sigma}$:

$$\frac{\mathscr{D}\boldsymbol{\sigma}}{\mathscr{D}t} = \frac{\mathrm{D}\boldsymbol{\sigma}}{\mathrm{D}t} + \frac{1}{2}[\boldsymbol{\omega}\cdot\boldsymbol{\sigma} - \boldsymbol{\sigma}\cdot\boldsymbol{\omega}] \tag{4.3}$$

$$= \frac{\partial\boldsymbol{\sigma}}{\partial t} + \mathbf{v}\cdot\nabla\boldsymbol{\sigma} + \frac{1}{2}[\boldsymbol{\omega}\cdot\boldsymbol{\sigma} - \boldsymbol{\sigma}\cdot\boldsymbol{\omega}] \tag{4.4}$$

The Jaumann derivative is also known as the corotational derivative because it measures rates of changes of the stress tensor $\boldsymbol{\sigma}$ with respect to a coordinate frame that both translates and rotates with the fluid (Saengow et al. 2015). The rotation invariance is ensured by using the vorticity tensor which is defined as $\boldsymbol{\omega} = \nabla\mathbf{v} - (\nabla\mathbf{v})^{\dagger}$.
In (Giacomin et al. 2015) approximate expressions for the third and fifth relative harmonic arising in the torque signal when measuring with parallel disks were derived, they are denoted as $M_{3/1}$ and $M_{5/1}$ (Eqs. 4.5 and 4.6, respectively). The expressions are only approximations as they are Taylor series truncated at fifth order in $Wi$ and the representation of $M_{3/1}$ and $M_{5/1}$ is analogous to the series representation in Eq. 2.31. The Deborah number ($De = \lambda\omega$) dependent coefficients $A_{mn}$ and $B_{mn}$ are collected in Table 8.3 in the Appendix.

$$M_{3/1} = \frac{\sqrt{[Wi^2A_{33} + Wi^4A_{53} + \cdots]^2 + [Wi^2B_{33} + Wi^4B_{53} + \cdots]^2}}{\sqrt{[-1 + Wi^2A_{31} + Wi^4A_{51} + \cdots]^2 + [-De + Wi^2B_{31} + Wi^4B_{51} + \cdots]^2}} \tag{4.5}$$

$$M_{5/1} = \frac{\sqrt{[Wi^4A_{55} + \cdots]^2 + [Wi^4B_{55} + \cdots]^2}}{\sqrt{[-1 + Wi^2A_{31} + Wi^4A_{51} + \cdots]^2 + [-De + Wi^2B_{31} + Wi^4B_{51} + \cdots]^2}} \tag{4.6}$$

Similarly, expressions for third and fifth relative harmonic present in the torque signal when measuring with a cone and plate geometry were derived. Since they are identical to the stress harmonic ratios and therefore represent the undisturbed nonlinear parameters they are denoted as $I_{3/1}$ and $I_{5/1}$ (Eqs. 4.7 and 4.8). The coefficients $C_{mn}$ and $D_{mn}$ can be found in Table 8.3 in the Appendix.

$$I_{3/1} = \frac{\sqrt{[Wi^2C_{33} + Wi^4C_{53} + \cdots]^2 + [Wi^2D_{33} + Wi^4D_{53} + \cdots]^2}}{\sqrt{[-1 + Wi^2C_{31} + Wi^4C_{51} + \cdots]^2 + [-De + Wi^2D_{31} + Wi^4D_{51} + \cdots]^2}} \tag{4.7}$$

$$I_{5/1} = \frac{\sqrt{[Wi^4C_{55} + \cdots]^2 + [Wi^4D_{55} + \cdots]^2}}{\sqrt{[-1 + Wi^2C_{31} + Wi^4C_{51} + \cdots]^2 + [-De + Wi^2D_{31} + Wi^4D_{51} + \cdots]^2}} \tag{4.8}$$

Taking the ratios of Eqs. 4.7 and 4.5, $\frac{I_{3/1}}{M_{3/1}}$, and Eqs. 4.8 and 4.6, $\frac{I_{5/1}}{M_{5/1}}$, produces corrections for the third and firth harmonic. These corrections (Eqs. 4.9 and 4.10) have to be multiplied

with harmonic ratios measured in a parallel disks geometry, $M_{3/1}$ and $M_{5/1}$, to convert them to the true nonlinear parameters, which would be measured in a cone and plate geometry, $I_{3/1}$ and $I_{5/1}$. In first approximation they are 3/2 and 5 for the third and the fifth harmonic, respectively. Therefore the approach of Wagner et al. (2011) was corroborated based on a specific constitutive model.

$$\frac{I_{3/1}}{M_{3/1}} = \frac{3}{2} + \frac{3}{8}Wi^2\left[\frac{De(2De+1)}{(De^2+1)(1+4De^2)}\right] - ... \tag{4.9}$$

$$\frac{I_{5/1}}{M_{5/1}} = 2 + Wi^2\frac{2De^2+1}{2(De^2+1)(1+4De^2)} - ... \tag{4.10}$$

In this work, the correction factors have been verified experimentally with the following LAOS tests using the PI-84k sample (experimental details are in Chapter 8, page 141). In Fig. 4.4 a fit of the true nonlinear parameters $I_{3/1}$ and $I_{5/1}$ with the corotational Maxwell model is shown. Although the corotational Maxwell model underestimates the magnitude of $I_{5/1}$, the scaling law $I_{5/1} \propto \gamma_0^4$ holds. The fitted relaxation time $\lambda$ was 0.0158 s. Figure 4.5 shows a comparison of $M_{3/1}$, $M_{5/1}$ and $I_{3/1}$, $I_{3/1}$, confirming the viability of this correction method. If $M_{3/1}$ and $M_{5/1}$ are multiplied with 3/2 and 2, respectively, they are matching $I_{3/1}$ and $I_{5/1}$ for larger $Wi$ ($Wi > 0.05$ for $I_{3/1}$ and $Wi > 0.164$ for $I_{5/1}$). At smaller values of $Wi$, the intensities are dominated by noise.

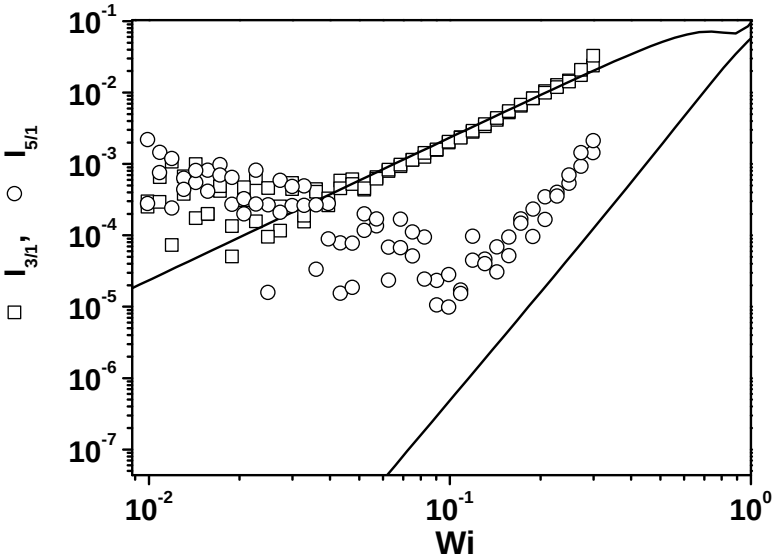


**Figure 4.4:** $I_{3/1}$ and $I_{5/1}$ vs $Wi = \lambda\omega\gamma_0 = 0.0158\text{s}\cdot 6.3\text{rad/s}\cdot\gamma_0$ for the PI-84k sample measured in a cone and plate geometry at T = 52.8°C. Lines are model predictions using Eqs. 4.7 and 4.8.

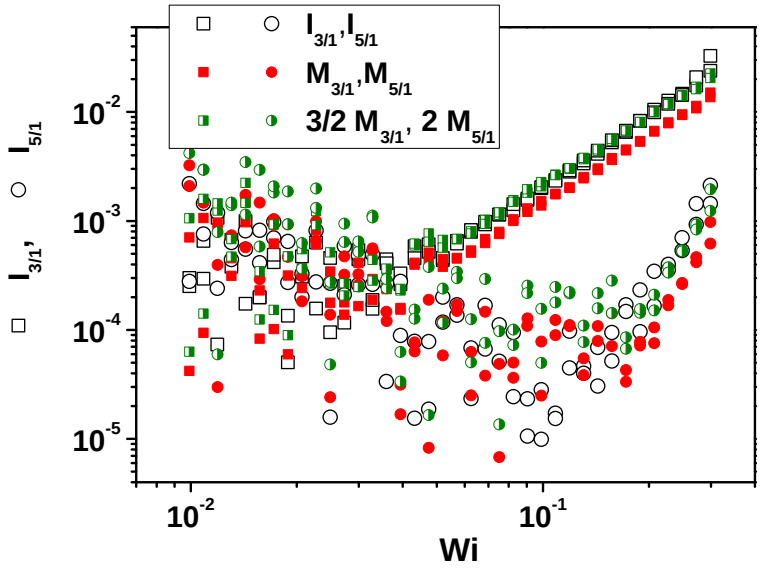


**Figure 4.5:** $I_{3/1}$ and $I_{5/1}$ measured in the cone/plate geometry, $M_{3/1}$ and $M_{5/1}$ from the parallel disks geometry vs $Wi = \lambda\omega\gamma_0$ = 0.0158s·6.3rad/s·$\gamma_0$ at T = 52.8°C. The correction using a factor of 3/2 is sufficient to map $M_{3/1}$ onto $I_{3/1}$. $M_{5/1}$ is converted to $I_{5/1}$ by multiplying with a factor of 2.

## 4.4 LAOStrain experiments on SMT and CMT rheometers

### 4.4.1 Nonlinear measurements on PI-84k

#### Transient Data and FT-Spectra

In the case of small deviations from linear behavior, as for a LAOS test on PI-84k at $\omega = 6.3$ rad/s and $\gamma_0 = 1$, the distorted stress wave cannot be directly distinguished from the pure sinusoidal wave in the linear representation of stress versus time, as shown in Fig. 4.6. However, in the frequency domain the deviations are easily detectable and can be quantified by the intensities of the odd harmonics. In the example shown in Fig. 4.6 the stress wave contains a relative contribution of 0.188% from the third harmonic.

For the four investigated instruments, ARES-G2, ARES-LS, DHR-3 and MCR 501, normalized magnitude spectra of the torque waves were obtained by Fourier transforming 15 oscillation cycles (Fig. 4.7). The angular frequency was 6.3 rad/s and the strain amplitude was set to $\gamma_0$ =1. The signal-to-noise ($S/N$) - ratio was calculated from the normalized spectra as $S/N$, with $S$=1 and $N$ being the noise level in the spectra, as determined by the mean values of data averaged in the region $17.07 < \omega/\omega < 18.3$. In this region no peaks should be present. Since the transient torque data showed a small decay of the amplitude (few percent over the course of 15 cycles), the data was additionally fitted with a decaying sinusoidal wave $M = M_0 \cdot \exp(-t/\tau)\cos(\omega t + \phi)$ to determine the characteristic decay time $\tau$. Subsequently the decay was corrected for by multiplying the transient wave with $\exp(t/\tau)$ prior to performing the Fourier transform. The values of $\tau$ were of the order of $10^3 - 10^4$ s. This procedure increased the $S/N$-ratio typically by a factor of 2

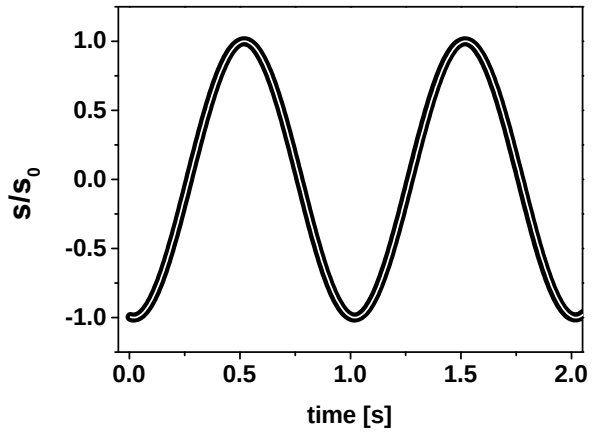


**Figure 4.6:** Normalized stress wave from a LAOS measurement conducted on PI-84 at $\omega = 6.3$ rad/s and $\gamma_0 = 1$ using the ARES-G2 (thick black line). The stress wave contains 0.188% contribution from the third harmonic relative to a pure sine wave $\sigma = \sigma_0 \sin(\omega t + \delta)$ (white line). Typically contributions of up to few percents of $I_{3/1}$ can not be detected if viewed in the time domain.

to 8, depending on the instrument, narrowed the peaks and also slightly increased $I_{3/1}$. The actual values are summarized in Table 4.1. Note that the decay correction will not be employed in the subsequent sections because the decay occurred only at amplitudes above $\gamma_0$ =1 for PI-84k, its effect on $I_{3/1}$ was monotonous on the four instruments and is therefore not significant for the comparison presented here. However, this form of decay correction can be used to enhance the $S/N$-ratio, when necessary, for example to determine the intensities of harmonics higher than the third.

The ARES-LS instrument showed a slightly lower $S/N = 9.5{\cdot}10^4$ in comparison to that for ARES-G2, which was equal to $1.6{\cdot}10^5$ under these conditions. For the DHR-3 it was higher at $6.4{\cdot}10^5$ whereas for the MCR 501 it was lower ($5.2{\cdot}10^4$) relative to the two SMT-rheometers. The lower value for the MCR 501 can be attributed to the fact that for this instrument a smaller diameter parallel plate geometry was used, 8 mm instead of 13 mm, because the latter was not available. As the measured torque has a cubic dependence on the plate diameter, decreasing the plate diameter from 13 mm to 8 mm should decrease the $S/N$-ratio of the MCR 501 by a factor of $(8/13)^3 = 0.233$ compared to the other instruments if similar sensitivities are assumed. The actual decrease in $S/N$ for the MCR 501 caused by a smaller plate diameter is 0.325, which suggest that its sensitivity is comparable to the ARES-G2. From these results it can be concluded that the $S/N$ ratio for all instruments, is sufficiently high to reliably detect harmonic intensities down to $1{\cdot}10^{-4}$. Note that by using larger geometries and averaging more oscillation cycles even higher $S/N$ ratios of up to $10^7$ can be reached, as shown for example for aqueous foams (Wilhelm et al. 2012). The actual measured intensities for the third harmonic differ slightly for PI-84k when measured on different rheometers. In this case the MCR 501 measured a value for $I_{3/1}$ that is higher by a factor of 1.8 compared those measured on the ARES-G2, ARES-LS and DHR-3. The latter three intensities agree with each other within

an uncertainty of 13%. The exact values are shown in Table 4.1.

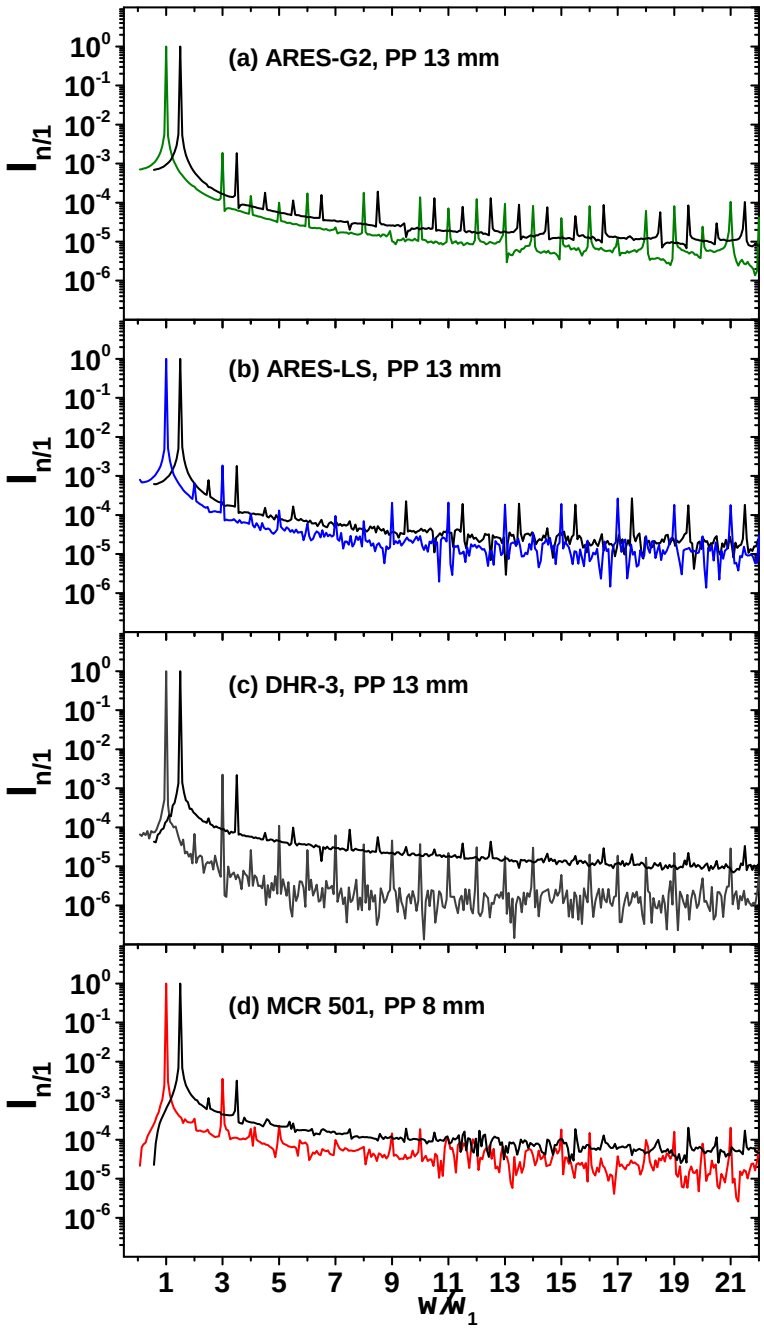


**Figure 4.7:** Normalized magnitude spectra of the torque waves for PI-84k (colored lines) measured on the investigated instruments: (a) ARES-G2, (b) ARES-LS, (c) DHR-3 and (d) MCR 501. For the DHR-3 the *stiff* motor setting was used (for details see Section 8.2). In order to account for the temporal decay of the torque signal a correction was made by multiplying the transient wave with $\exp(t/\tau_i)$ prior to the Fourier transform. The uncorrected spectra are also shown (black lines) and were shifted with respect to the relative frequency by + 0.5 for clarity. The angular frequency was 6.3 rad/s, the strain amplitude was set equal to 1, $T = 52.8°\mathrm{C}$ . Fifteen cycles were recorded with the TRIOS software for the ARES-G2 and the DHR-3 whereas, for the ARES-LS and the MCR 501, the custom written LabView routine (see Section 8.2) was used.

| Instrument | $S/N^u$ | $S/N$ | $I^u_{3/1}$ | $I_{3/1}$ |
|---|---|---|---|---|
| ARES-G2 | $8.1{\cdot}10^4$ | $1.6{\cdot}10^5$ | $1.85{\cdot}10^{-3}$ | $1.88{\cdot}10^{-3}$ |
| ARES-LS | $5.3{\cdot}10^4$ | $9.5{\cdot}10^4$ | $1.80{\cdot}10^{-3}$ | $1.86{\cdot}10^{-3}$ |
| DHR-3 | $8.9{\cdot}10^4$ | $6.4{\cdot}10^5$ | $2.18{\cdot}10^{-3}$ | $2.24{\cdot}10^{-3}$ |
| MCR 501 | $1.7{\cdot}10^4$ | $5.2{\cdot}10^4$ | $3.22{\cdot}10^{-3}$ | $3.62{\cdot}10^{-3}$ |

**Table 4.1:** Signal to noise ratio $S/N$ and normalized intensity of the third harmonic $I_{3/1}$ for the spectra shown in Fig. 4.7 for the PI-84k sample measured at $T = 52.8°$C and $\gamma$=1. In order to account for the decay of the torque signal a correction was made by multiplying the transient wave with $\exp(t/\tau_i)$ prior to the Fourier transform. The uncorrected results for $S/N$ and $I_{3/1}$ are marked with the superscript $u$.

### Intensities of the third harmonic $I_{3/1}$

The third harmonic $I_{3/1}$ is the first nonlinear contribution to appear in the transition from the linear to the nonlinear regime and has the highest intensity of all higher harmonics. Since it is also the only harmonic that can be reliably measured for both samples in the investigated amplitude range, further discussion will be limited to $I_{3/1}$ and the quantities derived from it. Fig. 4.8 shows the strain amplitude dependence of $I_{3/1}$ for PI-84k at $\omega =$ 6.3 rad/s. Note that for the ARES-LS, the displayed data was measured at a temperature of 48°C instead of the usual 52.8°C, as for the other three instruments in order to account for the inherent differences when using an oven instead of a Peltier plate for temperature control, see section 4.2.

In addition to $I_{3/1}$ from the stress wave (open symbols), Fig. 4.8 shows $I_{3/1}$ from the input strain wave (closed symbols). For the ARES-G2, $I_{3/1}$ present in the strain, $I^\gamma_{3/1}$ is more than three decades smaller than corresponding values from the stress, $I^\sigma_{3/1}$, and are therefore outside the range shown here. Not that here we use $\sigma$ and $\gamma$ as superscripts, not as exponents. For the ARES-LS, $I^\gamma_{3/1}$ is around $2{\cdot}10^{-4}$ and approximately independent of the amplitude. The larger $I^\gamma_{3/1}$ might be attributed to higher friction in comparison to the ARES-G2 caused by the brushes of the motor.

A correlation between $I^\gamma_{3/1}$ and $I^\sigma_{3/1}$ can be seen for measurements made on the two CMT-rheometer DHR-3 and MCR 501 and shows that the deformation control is not able to completely compensate for all the nonlinearity present in the strain. However, $I^\gamma_{3/1}$ was at least one decade smaller than $I^\sigma_{3/1}$ for all measurements. The fact that the deformation control of the CMT - instruments is not able to reduce nonlinear contributions in the strain wave as effectively as it is done in the case of the ARES-G2 is due to the compromise between controlling the strain through adjustment of the torque and the same time, maintaining a certain torque resolution for the measurement. In this respect, the DHR-3 seems to be more effective than the MCR 501, since for the DHR-3 the ratio of $I^\gamma_{3/1}/I^\sigma_{3/1}$ was smaller with $\sim 0.02$ compared to a ratio of roughly 0.1 for the MCR 501, where in the ideal case this ratio's limit would be zero.

The $I_{3/1}$ values for PI-84k measured on the MCR 501 were consistently larger than the ones on the other instruments for all strain amplitudes above the detection limit $\gamma_d$. The detection limit was determined from the minimum in the fitted curve to the data of the amplitude dependent $I_{3/1}$ using the function shown Eq. 4.11. This function combines the

theoretically predicted quadratic amplitude dependence for $I_{3/1}$ at medium amplitudes (Pearson and Rochefort 1982) with a scaling of $\gamma_0^{-1}$ in the linear regime (Reinheimer et al. 2012). This scaling of $\gamma_0^{-1}$ originates from the consideration that the values for $I_3$ reflect only the noise level $N$ for $\gamma_0 < \gamma_d$. Therefore $I_3 \approx N$ for $\gamma_0 < \gamma_d$ and $I_{3/1}$ is consequently inverse proportional to $I_1$, since $I_1 \propto \gamma_0$.

$$I_{3/1} = A\gamma_0^{-1} + Q_0\gamma_0^2 \tag{4.11}$$

The parameter $A$ depends on the instrument and should decrease with increasing sensitivity that causes $\gamma_d$ to decrease and thus enables the measurement of $I_{3/1}$ down to smaller amplitudes. The fitting parameters for the strain sweeps at $\omega = 6.3$ rad/s are shown in Table 4.2. Very similar values were found for ARES-G2, ARES-LS and DHR-3, which is surprising since these instruments significantly differ in their minimum detectable torques (50, 400 and 0.5 nNm, respectively, as specified by the manufacturers). Apparently, an overall higher sensitivity does not necessarily lead to an improved detection of $I_{3/1}$.
The detection limits $\gamma_d$ for the ARES-G2, ARES-LS and DHR-3 are also very similar (see Table 4.2), whereas, for MCR 501, $\gamma_d$ is lower, due to the fact that for this instrument the complete $I_{3/1}$-curve is shifted to smaller amplitudes. In addition to the determination of $\gamma_d$, the fitted curve also determines the intrinsic nonlinearity $Q_0$. The variations in $Q_0$ are a consequence of the differences in $I_{3/1}$ that were shown for $\omega = 6.3$ rad/s in the previous section.

| Instrument | $A$ | $Q_0$ | $\gamma_d$ |
|---|---|---|---|
| ARES-G2 | $9.79{\cdot}10^{-5}$ | $1.89{\cdot}10^{-3}$ | 0.30 |
| ARES-LS | $1.1{\cdot}10^{-4}$ | $1.64{\cdot}10^{-3}$ | 0.32 |
| DHR-3 | $1.17{\cdot}10^{-4}$ | $1.97{\cdot}10^{-3}$ | 0.30 |
| MCR 501 | $1.24{\cdot}10^{-5}$ | $3.22{\cdot}10^{-3}$ | 0.12 |

**Table 4.2:** Fitting parameters $A$, $Q_0$ from Eq. 4.11 and the calculated detection limit $\gamma_d$, which is the minimum of the curve for the data shown in Fig. 4.8. For the MCR 501 the complete $I_{3/1}$-curve seems to be shifted to smaller amplitudes, which leads to an artificially low $A$ and $\gamma_d$ as well as a too large $Q_0$ in comparison to the other instruments.

When using the DHR-3 rheometer, the motor mode setting gives the user the ability to adjust the gain for the active deformation control and thus to define how strong this control is applied to correct nonlinearities in the strain. This feature has been created by the manufacturers to optimize the torque resolution and smoothness. The possible settings are *auto*, *soft*, *medium* or *stiff*. When performing LAOS experiments one would prefer to set the setting to *stiff*, since in that case the suppression of nonlinearities in the strain wave is most effective. The disadvantage is that a stiffer setting of the motor mode results in a lower torque sensitivity. Fig. 4.9 shows a comparison of measurements of $I_{3/1}$ as a function of the strain amplitude at 6.3 rad/s in the *stiff* and the *auto* setting. In addition, $I_{3/1}$ for the strain signal is also displayed. Using the correct setting *stiff* leads to very good agreement of the $I_{3/1}$-contributions present in the stress wave, $I_{3/1}^{\sigma}$, when compared to data collected on the SMT-instrument ARES-G2. In contrast, if the *auto* setting is used,

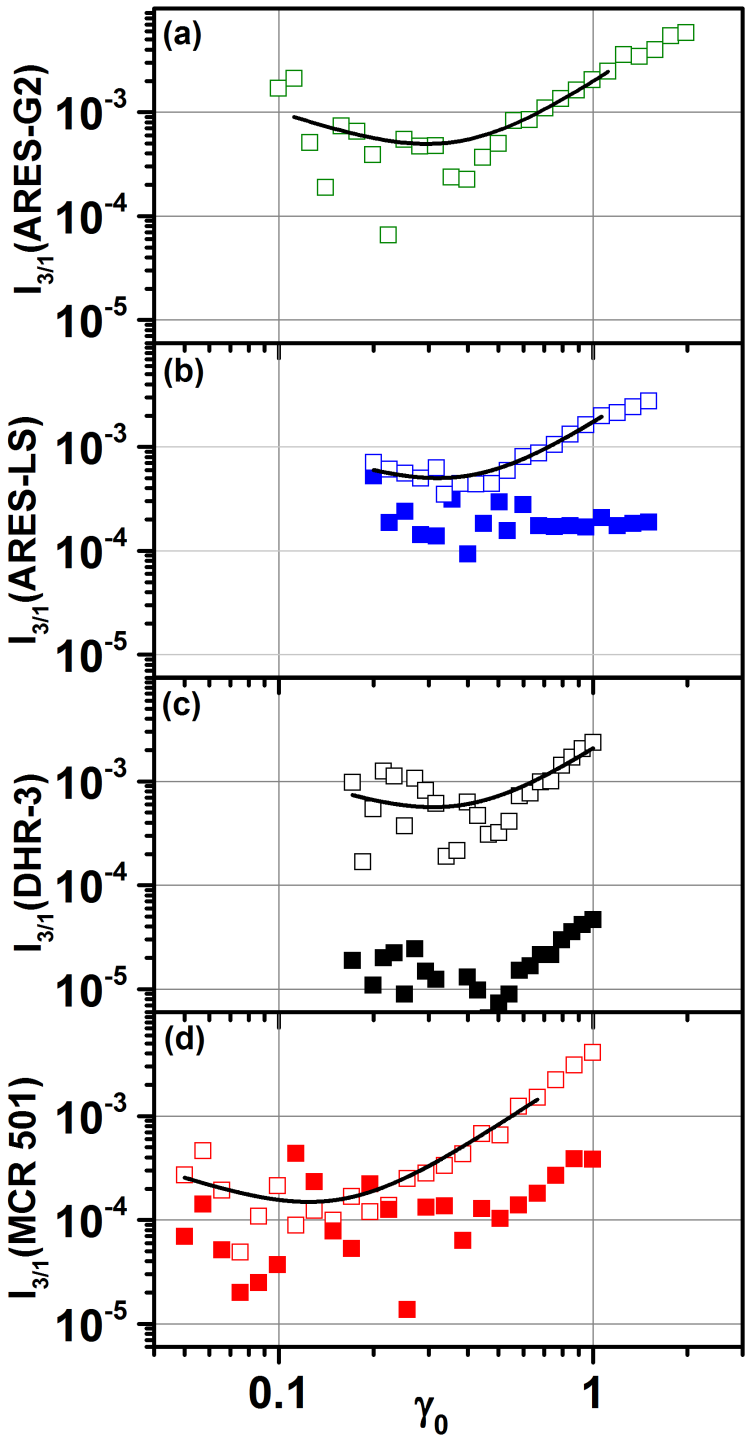


**Figure 4.8:** Results for $I_{3/1}$ as a function of the strain amplitude at $\omega = 6.3$ rad/s for PI-84k on the investigated instruments: (a) ARES-G2, (b)ARES-LS, (c)DHR-3 and (d) MCR 501. Open symbols represent $I_{3/1}$ from the stress wave, closed symbols $I_{3/1}$ from the strain wave. The black lines are fitted curves using Eq. 4.11. The ARES-LS data was measured at a temperature of 48°C instead of 52.8°C as for the other three instruments to account for the differences introduced by using an oven instead of a Peltier plate for temperature control, see section 4.2.

nonlinearities in the strain wave, $I^{\gamma}_{3/1}$, are not suppressed efficiently enough and therefore the determined $I^{\sigma}_{3/1}$-values are too small. Hence, for all further DHR-3 measurements on PI-84k the motor mode setting was set to *stiff*.

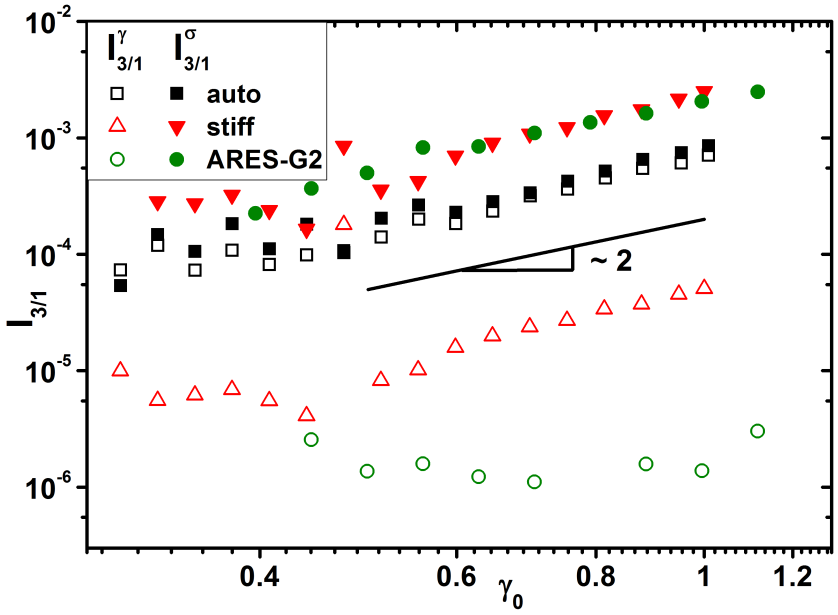


**Figure 4.9:** Results for $I_{3/1}$ in the strain, $I^{\gamma}_{3/1}$, and the stress wave, $I^{\sigma}_{3/1}$, as a function of the strain amplitude at $\omega = 6.3$ rad/s and $T = 52.8°$C for PI-84k on the DHR-3 using the different motor modes *auto* and *stiff* compared to ARES-G2 data.

Another interesting observation concerns the scaling of $I_{3/1}(\gamma_0)$ with the strain amplitude as measured on the DHR-3 rheometer. For this instrument, measurements on PI-84k consistently and independent of the motor mode setting, gave slightly larger scaling exponents that were around 2.5 instead of the expected value of 2 (see Eq. 2.34) as determined on the other three instruments. A comparison with ARES-G2 and MCR501 data for the frequencies 1.3, 6.3 and 10 rad/s is shown in Fig. 4.10. The deviations in the scaling exponents lead to the consequence that the data used for the determination of $Q_0$ had to be restricted to a smaller strain amplitude range where a slope of 2 was still found. Although this reduction of data points in principle makes the $Q_0$-determination less reliable for the DHR-3, the values that were extracted were still within a reasonable range as will be discussed in the subsequent section. Although this is a minor implication for the current framework of analysis, it can become a serious source of error when using alternative LAOS analysis methods (see Chapter 2, page 32) where a wider range of $\gamma_0$ needs to be taken into account.

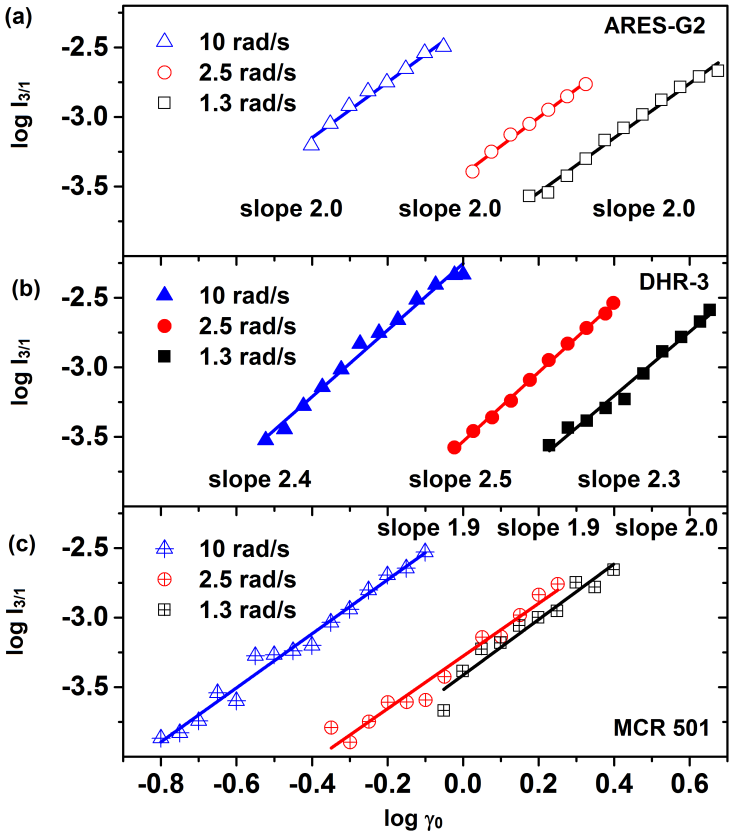


**Figure 4.10:** Strain amplitude dependence of $I_{3/1}$ at $\omega = 1.3$, 2.5 and 10 rad/s. The slope are determined by a linear regression with $\log I_{3/1} = a \log \gamma_0 + b$ for PI-84k from the ARES-G2, (a), compared to DHR-3 and MCR 501 data, (b) and (c).

### $Q$-coefficient

A plot of the $Q$-coefficient $Q = I_{3/1}/\gamma_0^2$ as a function of $\gamma_0$ is shown in Fig. 4.11 (see Chapter 2, page 26 for details on the scaling laws). Here, the data points below the detection limit have been omitted because they are dominated by noise. At sufficiently low strain amplitudes, the $Q$-coefficient is scattered around a plateau value, $Q_0$. Instead of using the fit function from Eq. 4.11, all values for $Q_0$ were determined by averaging 5-10 points in the plateau regime. This approach proved to give more reliable results in those cases where only few points below the detection limit were gathered. Deviations from the square scaling of $I_{3/1}$ for DHR-3, as previously discussed, caused $Q$ to increase (Fig. 4.11). Therefore, in this case only the first 5 plotted data points were averaged in order to determine $Q_0$. Apart from this, the data agreed reasonably well as shown in Fig. 4.11. For the specific angular frequency of 6.3 rad/s the data from the MCR 501 led to an approximately 60% larger value for $Q_0$ compared to the other three instruments, among which the deviations in $Q_0$ were less than 10%.

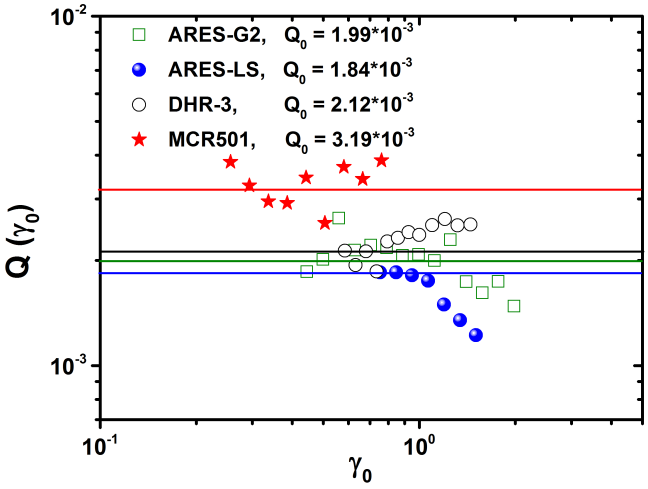


**Figure 4.11:** $Q$-coefficient as a function of $\gamma_0$, defined as $Q = I_{3/1}/\gamma_0^2$, for PI-84k measured on the investigated instruments at $\omega = 6.3$ rad/s at $T$=52.8°C . Data points which were dominated by noise have bee omitted.

### Intrinsic nonlinearity $Q_0$

Frequency dependent measurements of the $Q$-coefficient were performed to analyze if the agreement between the investigated instruments shown in the previous section can also be observed at other angular frequencies $\omega$. The results are displayed in Fig. 4.12. Since instruments using a Peltier plate had different temperature settings (see section 4.2), the data from ARES-G2, DHR-3 and MCR 501 were shifted to higher frequencies using a factor of 1.39 when compared to the data from ARES LS that used a force convection oven. Note also that all previously shown results of $I_{3/1}$ and $Q$ were measured in parallel plates geometries. In the following, the correction from Section 4.3 has been applied, so all presented $Q_0$ values for the PI-84k and PIB samples have been corrected for the inhomogeneous strain field in the parallel plates geometry by multiplying with 3/2, and therefore represent values that would be measured in a cone and plate geometry. The intensities $I_{3/1}$ reported in the previous sections, however, are not corrected for the inhomogeneous strain field.

The frequency dependence of $Q_0$ for an entangled polymer was predicted to be quadratic (Hyun and Wilhelm 2009) at low enough frequencies, therefore, for the data in Fig. 4.12, a linear regression according to $\log(Q_0) = c + 2\log(\omega/(\text{rad/s}))$ was used to determine the intercepts in a plot on logarithmized axes. The intercepts are shown in Table 4.3 and were used to calculate the relative deviations between the instruments for the whole $Q_0(\omega)$ curve. The ratio $\overline{Q}_0 = 10^{c(\text{i})}/10^{c(\text{ARES-G2})}$ shows that ARES-LS and ARES-G2 deliver very similar results, which was expected, since both are SMT-rheometers, the former being an older generation of the latter.

To demonstrate the substantial effect of the deformation control setting on the DHR-3 results (previously mentioned in Section 4.4.1), data from measurements using the *stiff*

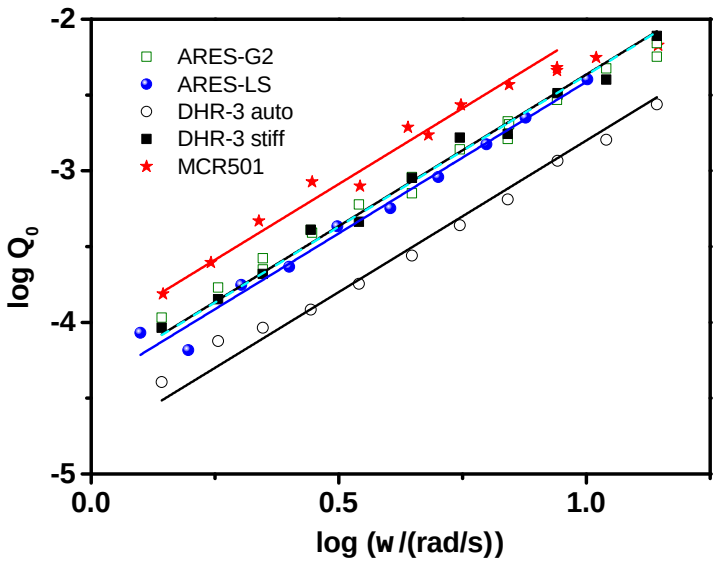


**Figure 4.12:** Frequency dependence of $Q_0$ for PI-84k at $T = 52.8°C$ , $Q_0$ is defined as the plateau value of $Q$ at small strain amplitudes (Eq. 2.38). All values of $Q_0$ have been corrected for the inhomogeneous strain field in the parallel plates geometry by multiplying with 3/2, and therefore represent values that would be measured in a cone and plate geometry. The data measured on the ARES-G2, DHR-3 and MCR 501 were shifted to higher frequencies with a factor of 1.39 to account for the difference in temperature control when using the Peltier plates instead of the forced convection oven (ARES-LS). The lines are linear regressions with a fixed slope of 2. The line for the ARES-G2 (black) and the DHR-3 (light and dashed) overlap. The DHR-3 data match only if the motor mode is set to *stiff*. However, setting the motor mode to *auto* for the DHR-3 caused severe deviations as shown by the open symbols.

and the *auto* setting are shown. The results obtained on the DHR-3 match remarkably well with the ones from the SMT instruments but only if the correct setting for the motor mode in the deformation control is used, which was the *stiff* setting for PI-84k. Other settings resulted in $Q_0$-values that are smaller by a factor of up to three as shown by the measurement using the *auto* setting.

With proper precautions the results for ARES-G2, ARES-LS and DHR-3 agreed well and the differences are only slightly larger than the reproducibility range of measurements on a single instrument, which was determined to be in the range 4-8% (relative standard deviation of three independent measurements).

The MCR 501 delivers $Q_0$-values that are in general larger by a factor of 1.92 for PI-84 when compared to the ones from the SMT-rheometers. The reason for this deviation is assumed to be connected to the deformation control. The fact that the values were consistently larger relative to the other instruments suggests that the deformation control introduces additional nonlinearities into the stress signal. The ultimate source of this deviation remains unclear and might be sample dependent, but we can exclude several possible sources. First, the deviation cannot be caused by the use of the smaller diameter parallel plate geometry and therefore smaller sensitivity in terms of signal to noise ratio, see section 4.4.1, as in an additional measurement with a 25 mm diameter plate identical results

were obtained. Furthermore the result was confirmed on an additional measurement using a different MCR 501, suggesting that the deviation is not a technical problem of the specific instrument used so far. At last, the relatively large amount of nonlinear contribution that is still present in the strain wave as evident from Fig. 4.8 d (the ratio of $I_{3/1}$ in the strain to $I_{3/1}$ in the stress is roughly 1/10), can not be responsible for the large deviations in $Q_0$ because these would transfer into the stress wave linearly and therefore would cause an error on the order of 10% but not 192% of the measured values.
Note that changes of several percent in $Q_0(\omega)$ seem to be of minor significance, since this parameter can vary over two to three decades of magnitude (Hyun et al. 2011), but a factor of two might not be negligible.

| Instrument | Intercept $c$ | $10^c \cdot 10^5$ | $\overline{Q}_0$ |
|---|---|---|---|
| ARES-G2 | –4.365±0.018 | 4.32 | 1 |
| ARES-LS | –4.413±0.025 | 3.86 | 0.90 |
| DHR-3 stiff | –4.368±0.019 | 4.29 | 0.99 |
| DHR-3 auto | –4.800±0.025 | 1.56 | 0.37 |
| MCR 501 | -4.081±0.028 | 8.30 | 1.92 |

**Table 4.3:** Intercepts $c$ from linear regression on the PI-84k data in Fig. 4.12 using a fixed slope of 2 and the ratio $\overline{Q}_0 = 10^{c(\mathrm{i})}/10^{c(\text{ARES-G2})}$, which shows the deviations between the instruments using the ARES-G2 data as the reference.

### 4.4.2 Nonlinear measurements on PIB

Similar measurements to those on PI-84k were done on a polyisobutylene solution (PIB), for sample details see experimental Chapter 8, page 141 . Since the measuring temperature was 25°C a temperature gradient effect when using a Peltier plate was not observed. Therefore, in contrast to the PI-84k measurements the following data had not be shifted with respect to the frequency to compensate for temperature gradients.
Moreover, the different motor mode settings of the DHR-3 produced very similar results for $I_{3/1}$, except when the *stiff* setting was used. Using the *stiff* setting here instead introduced additional noise in the torque signal and led to a strong scattering in the $I_{3/1}$ measurements that made the determination of $Q_0$ impossible. Therefore the *medium*-setting was used, since it reduced the nonlinearity in the strain to a minimum and still gave reliable $Q_0$ values. Therefore, it is not possible to know a priori which setting of the DHR-3 motor mode will be optimal for an unknown sample. On one hand a stiffer setting of the deformation control reduces nonlinearities in the strain wave more efficiently, but on the other hand it introduces additional noise in the torque signal when applied on samples of lower viscosity. Consequently, we would recommend to set the mode to as stiff as possible as long as the results for $I_{3/1}$ are not significantly altered by the additional noise introduced by the deformation control.
Furthermore, as already shown for PI-84, deviations from the square scaling of $I_{3/1}$ were observed when using the DHR-3. In this case, the scaling exponents were usually around 1.5 at intermediate frequencies of $\omega$ = 3 - 20 rad/s, whereas at higher and lower frequencies

slopes equal to 2 were found as expected from theory (Eq. 2.34). This again reduced the strain amplitude range that was used for the determination of $Q_0$, nevertheless $Q_0$ still could be extracted.

The frequency dependence of $Q_0$ for the PIB sample is shown in Fig. 4.13. The results for the two SMT-rheometers and MCR 501 agreed reasonably well, as the relative standard deviation for specific $Q_0(\omega)$ values from different instruments was below 25% at most frequencies, in contrast to the PI-84k sample, where a much stronger deviation was found for the MCR 501. At low frequencies $Q_0$ shows a quadratic dependance on the angular frequency $\omega$. Therefore, a similar linear regression as shown for PI-84k in section 4.4.1 was performed on the data in the range -0.06 < log($\omega$/(rad/s)) < 0.654 in Fig. 4.13. A comparison of the intercepts (see Table 4.4) reveals that the average deviation between the instruments is below 12% in this region.

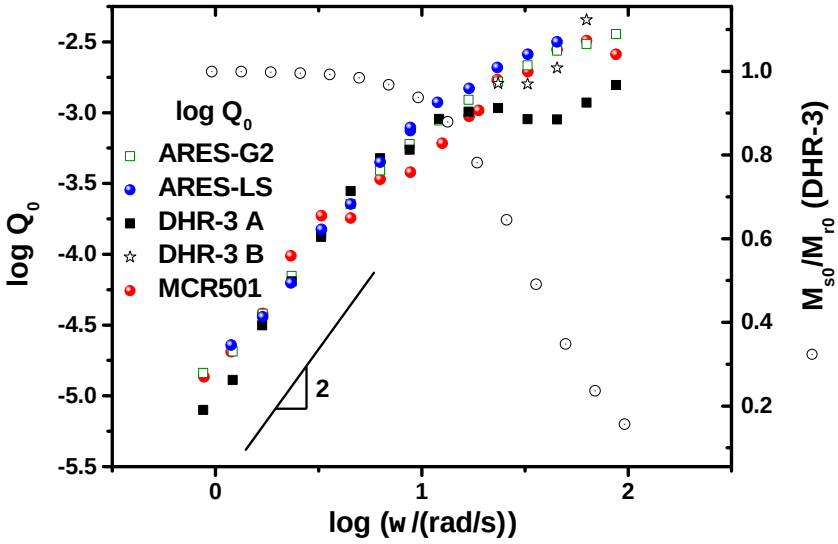


**Figure 4.13:** Frequency dependence of $Q_0$, defined as the plateau value of $Q$ at small strain amplitudes (Eq. 2.38), for PIB. All values of $Q_0$ have been corrected for the inhomogeneous strain field in the parallel plates geometry by multiplying with 3/2, and therefore represent values that would be measured in a cone and plate geometry. The DHR-3 A data was recorded using the correlation acquisition mode, whereas for the DHR-3 B-data, the transient acquisition mode was used. At low angular frequencies $Q_0$ is proportional to $\omega^2$. Additionally, the ratio of the sample torque amplitude to the raw torque amplitude $M_{s0}/M_{r0}$ for the DHR-3 A data is shown. When $M_{s0}/M_{r0}$ reaches approximately 0.8, i.e. the inertia contribution makes up 20% of the total torque, pronounced deviations in $Q_0$ are observed when no inertia correction is applied.

For the DHR-3, an apparent maximum in the $Q_0(\omega)$-curve was observed at 23 rad/s (Fig. 4.13). This maximum is caused by instrument inertia effects. When using the DHR-3 in the correlation acquisition mode, the transient data that is Fourier-transformed by the software is the raw torque data. For a CMT-rheometer the raw torque $\mathbf{M}_r$ is the sum of the sample torque $\mathbf{M}_s$ and an additional contribution caused by instrument inertia $\mathbf{M}_I$ (Franck 2003) as shown in Eq. 4.12.

| Instrument | Intercept $c$ | $10^c \cdot 10^6$ | $\overline{Q}_0$ |
|---|---|---|---|
| ARES-G2 | -4.882±0.033 | 1.32 | 1.03 |
| ARES-LS | –4.898±0.026 | 1.27 | 0.99 |
| DHR-3 | –4.945±0.023 | 1.14 | 0.89 |
| MCR 501 | -4.861±0.056 | 1.38 | 1.08 |

**Table 4.4:** Intercepts $c$ from linear regression on the PIB data in Fig. 4.13 in the range -0.06 < $\log(\omega/(\mathrm{rad/s})) < 0.654$ using a fixed slope of 2. The ratio $\overline{Q}_0 = 10^{c(\mathrm{i})}/10^{\overline{c}}$ shows the deviations between the instruments using the mean of the four intercepts, $\overline{c}$, as the reference.

$$\mathbf{M}_r(t) = \mathbf{M}_s(t) + \mathbf{M}_I(t) \tag{4.12}$$

$$= \sigma(t)/K_\sigma + I\ddot{\theta}(t) \tag{4.13}$$

$$= \sigma(t)/K_\sigma - I\omega^2\theta_0 \sin(\omega t) \tag{4.14}$$

$\mathbf{M}_I$ increases quadratically with the frequency due to the second time derivative of the deflection angle $\ddot{\theta}$, $I$ represents the instrument inertia constant and is calibrated for every geometry, $K_\sigma$ is the geometry constant for the torque-to-stress conversion. Due to the relationship $\mathbf{M}_I \propto \omega^2$, $\mathbf{M}_I$ can dominate over the sample torque for low viscosity materials and high frequencies. Since the DHR-3 software gives the amplitudes for the raw torque $M_{r0}$ and the sample torque $M_{s0}$, the ratio of $M_{s0}/M_{r0}$ was calculated to monitor the frequency at which the inertia contribution starts to dominate the total torque. The decrease in $Q_0$ began at a frequency of around 23 rad/s and, at these conditions, the $M_{s0}/M_{r0}$ ratio is roughly 0.8, meaning that the inertia contribution makes up 20% of the total torque. If this inertia contribution is assumed to be free of nonlinearity, normalization leads to erroneous values for $I_{3/1}$ and, consequently, for $Q_0$. It can therefore be concluded that when conducting LAOS experiments at different frequencies using a CMT-rheometer, one has to ensure that the inertia effects are negligible by avoiding both high frequencies and low viscosities. Alternatively, it is possible to transform inertia corrected torque data, which is the sample torque $M_s(t)$, when using the transient acquisition mode. This was done for the frequencies above 23 rad/s and is shown by the data points named DHR-3 B in Fig. 4.13. These values agree better with the data from the other instruments. Although this acquisition mode is more tedious than the correlation acquisition because the Fourier transform step is no longer done automatically by the software, it is necessary when working with low viscosities and high frequencies where instrument inertia contributions become relevant.

For MCR 501 the software applied an inertia correction, so the sample torque $M_s(t)$ could be analyzed directly and instrument inertia effects were corrected in the investigated frequency range.

### 4.4.3 Evaluation of the MCR 702 rheometer

In addition to the previously investigated instruments a new controlled strain rheometer, the MCR 702 (Anton Paar), became available at a late stage of the thesis. The MCR 702 instrument employs two identical motors, one of them can be used for the excitation, the other motor acts as an FRT-transducer measuring the torque in the sample, resulting in a truly separated motor-transducer instrument. Since the specific instrument that was available could not provide any temperature control system, direct comparison to the previous measurements in Sections 4.4.2 and 4.4.1 were not possible. Therefore, a new test series was performed on the samples PI-84k and PIB-2. PIB-2 was used instead of PIB because the specific batch of the latter was not available in sufficient amounts anymore. PIB-2 ($M_w = 4.8 \cdot 10^6$ g/mol) differs from PIB ($M_w = 1.1 \cdot 10^6$ g/mol) in the molecular weight, and therefore has a higher zero shear viscosity and a longer relaxation time, see Table 8.1, page 142. The MCR 702 results are compared to identical measurements on the ARES G2.

First, the linear viscoelastic properties are compared. In Fig. 4.14 the angular frequency dependence of $G'$ and $G''$ for the PI-84k and the PIB-2 sample at $T$ =20.4°C is shown. Good agreement (less than 10% variation) confirms that each sample has the same dynamics in the linear regime on both rheometers.

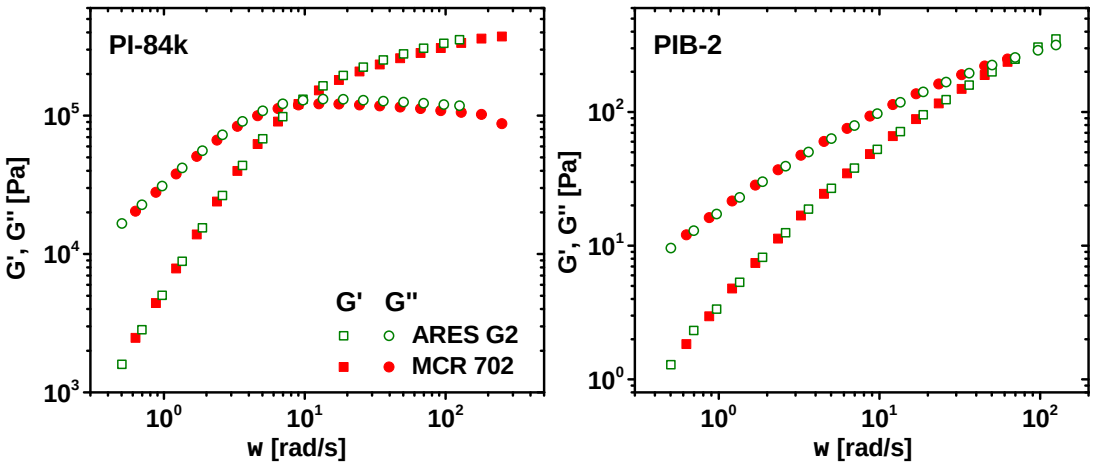


**Figure 4.14:** Frequency dependence of $G'$ and $G''$ for the PI-84k and the PIB-2 sample at $T = 20.4$°C confirming identical dynamics in the samples for both rheometers, the ARES G2 and the MCR 702.

The MCR 702 software does not provide the actually measured raw data, but instead gives data that has been reconstructed using only odd harmonics. This is evident when stress data from the software is Fourier transformed. A spectrum of the signal from a measurement of PIB-2 at $\omega = 2\pi$ rad/s, $\gamma_0 = 0.1$ and $T = 20.4$°C is shown in Fig. 4.15. Since only one cycle is provided by the software, it was copied seven times to generate a total signal of eight cycles for sufficient frequency resolution in the spectrum. The odd harmonic intensities are scattered around an intensity of $N = 1.61 \cdot 10^{-3}$. Inbetween points have intensities $< 10^{-16}$ and represent the numerical noise of the FT. Therefore, the signal

provided by the software must have been reconstructed using only odd harmonics. Since at $\gamma_0 = 0.1$ the PIB-2 sample is still in the LVR, vanishing harmonic intensities should be present, that are caused by the sample. Consequently, the determined intensities represent a measure of the noise in the stress wave. The $S/N$ for this measurement is 621, whereas for the ARES G2 measurements it is 2900. These values are significantly smaller than the ones presented in Section 4.4.1, due to lower torques. However, the ratio of $S/N$ of the two instruments, $\frac{S/N_{\text{ARES G2}}}{S/N_{\text{MCR 702}}} \approx 4.7$, is close to the one found previously for the comparison of the ARES G2 instrument with the MCR 501 (Table 4.1), which was 4.8. This suggests that using the two motor SMT setup of the MCR 702 does not provide improved LAOS sensitivity.

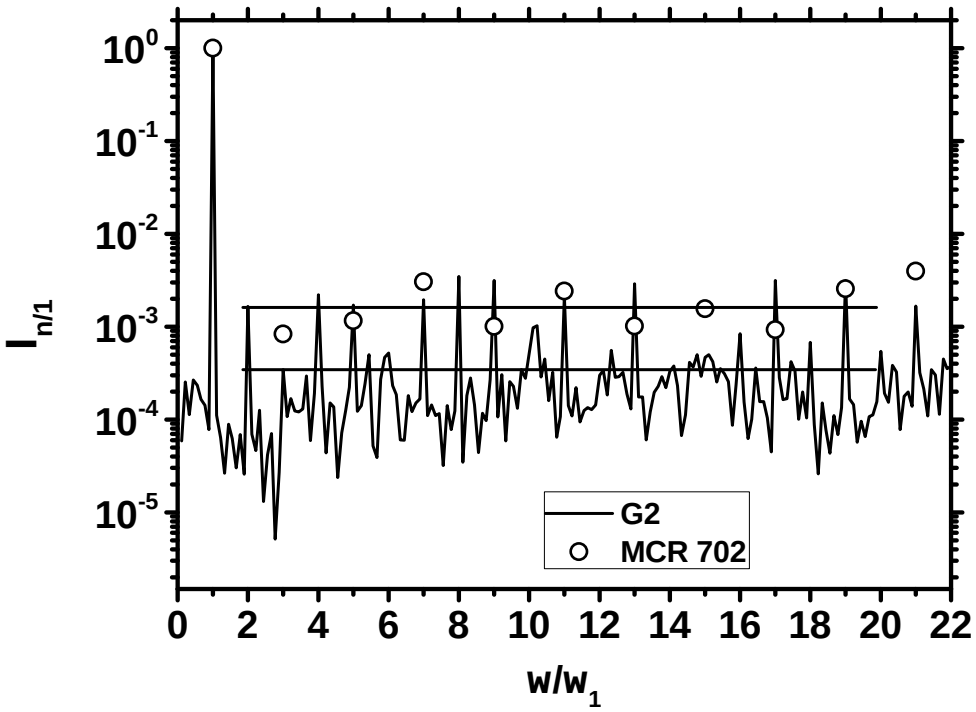


**Figure 4.15:** Fourier spectra of the stress signal measured on the PIB-2 sample at $\omega = 2\pi$ rad/s, $\gamma_0 = 0.1$ and $T = 20.4°\text{C}$ . Lines indicate the noise levels, $1.61 \cdot 10^{-3}$ ($S/N = 621$) and $3.44 \cdot 10^{-4}$ (($S/N = 2900$)), for MCR 702 and ARES G2, respectively. In the MCR 702 spectrum intensities occur only at odd multiples of the excitation frequency (circles), all inbetween points have intensities $< 10^{-16}$ and represent the numerical noise of the FT. Therefore, the signal provided by the software must have been reconstructed using only odd harmonics.

As for the previous comparisons, $\gamma_0$ dependent measurements were performed, $I_{3/1}$ was determined and converted to the intrinsic nonlinearity $Q_0$. Measurements of $Q_0$ at three different $\omega/2\pi = 0.1, 1$ and $10\ \text{s}^{-1}$ are shown in Fig. 4.16. $Q_0$ values for PIB-2 from both rheometer agree well, whereas for the PI-84k sample, a systematic deviation for all three angular frequencies is evident. The MCR 702 measures values that are twice as large as the ARES G2, which is the same deviation as already found for the MCR 501 for the PI-84k sample. This result suggests that the source of the deviation is not the CMT design

but rather a general problem of the MCR series, which occurs only for samples of higher viscosities, corresponding to higher torques.

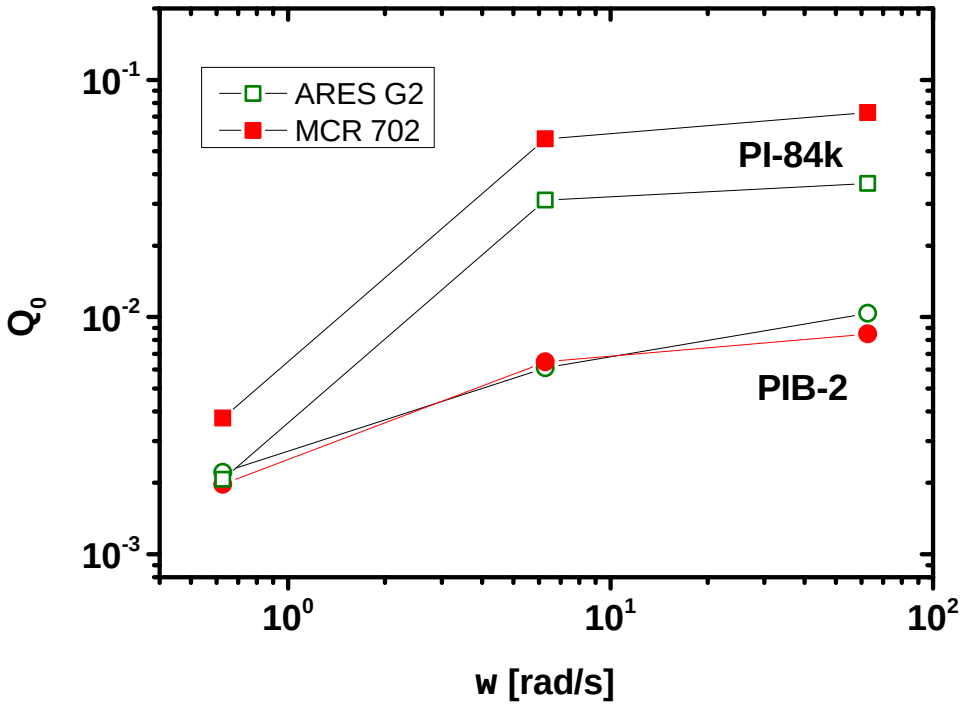


**Figure 4.16:** Comparison of $Q_0$ for the PI-84k and the PIB-2 sample, $T = 20.4°C$ , measured using the MCR 702 and the ARES G2 rheometer. The PI-84k data has been multiplied with 3/2 to correct for the inhomogeneous strain field in parallel plates geometry (Section 4.3). This was not necessary for the PIB-2 data, since cone and plate geometry was used.

## 4.5 Summary

This chapter deals with the technical aspects of conducting LAOStrain experiments on stress controlled and strain controlled rheometers. Data from LAOStrain experiments on a polyisoprene melt and polyisobutylene solutions measured on five different rheometers is compared to point out experimental details that need to be considered in order to achieve a reasonable agreement of the measured nonlinear quantities. The instruments under investigation were: ARES-G2 (TA Instruments), ARES-LS (TA Instruments), MCR 702 (Antron Paar), all three are separated motor-transducer rheometers, DHR-3 (TA Instruments) and MCR 501 (Anton Paar), which are combined motor-transducer rheometers. The data was analyzed using the framework of FT-Rheology as introduced in chapter 2 to obtain the normalized intensity of the third harmonic $I_{3/1}$ of the stress wave and the zero-strain nonlinearity $Q_0$ derived from it.

Although the general behavior of $I_{3/1}(\gamma_0)$ was qualitatively the same on all rheometers for both materials, the absolute values varied. The method of temperature control has an

important effect on the results when measuring above ambient temperature. Deviations of up to 30% in $Q_0$ were observed for the polyisoprene melt when a Peltier plate was used instead of a forced convection oven, but this deviation could be corrected by simply applying time temperature superposition.
Differences in harmonic intensities arising from using parallel disks geometry due to its inhomogeneous flow field were addressed. A correction factor of 3/2, that when multiplied with intensities from parallel disks, converts them to cone and plate intensities, was derived by A. J. Giacomin using the corotational Maxwell model. This factor could be confirmed experimentally with LAOS measurements on the polyisoprene sample.
Another instrument control parameter that had a large impact on the results was the setting for the deformation control on the DHR-3 (*motor mode*). This setting had to be chosen correctly in order to mimic a real LAOStrain experiment on a CMT-Rheometer. Only with the optimal setting could nonlinearities in the strain be sufficiently suppressed to achieve a good agreement between the measured $Q_0$-values and the results from the SMT-instruments. Otherwise, nonlinearities were distributed between strain and stress, which led to smaller $Q_0$-values. As for an unknown sample the optimal setting is not known a priori, this is a disadvantage of the DHR-3 instrument. Furthermore, measurements on the DHR-3 resulted in scaling exponents for $I_{3/1}$ in the range of 2.3 to 2.5 instead of the theoretically expected values of 2, which might be caused by the deformation control.
The results for $I_{3/1}$ and consequently also for $Q_0$-values obtained from the MCR 501 and the MCR702 proved to be larger by a factor of approximately two, which suggests that, in these cases, the active deformation control may introduce additional nonlinearities in the stress signal. This deviation occurred only for the polyisoprene sample and so far its ultimate source could not be elucidated. Further investigations, also in collaboration with the instrument manufacturer, would be required.
For polyisobutylene, the results for $Q_0$ from all the investigated instruments were found to be within a reproducibility range of 12%. When using the CMT-rheometer DHR-3, effects caused by the instrument inertia became noticeable for measurements at frequencies above 23 rad/s leading to an apparent maximum in the frequency dependence of $Q_0$. This artifact can be avoided by measuring in the transient mode since the inertia corrected stress of the sample can be Fourier-transformed instead.
Although it was found that the two CMT-instruments, when running a LAOStrain experiment, were not able to reduce the nonlinearity in the strain input wave, $I^{\gamma}_{3/1}$, to a level as low as that of an SMT-instrument, the measured nonlinearities in the stress, $I^{\sigma}_{3/1}$, were close enough to results from the SMT-instruments to suggest that the residual nonlinearity in the strain is negligible.
In summary, if certain precautions, such as careful temperature control, appropriate settings for the gain of the active deformation control and avoidance or correction of instrument inertia effects, are taken, then the relative deviations of the measured nonlinear quantities $I_{3/1}$ and $Q_0$ for a LAOStrain experiment on different rheometers can be expected to be below 12%.

# Chapter 5

# Simple theoretical predictions for LAOS using an extended 1D Maxwell model

Constitutive modeling has accompanied the development of the LAOS technique from a early point on (Bird et al. 1987; Macosko 1994; Morrison 2001; Giacomin et al. 2011). Even analytical solutions are available in rare cases (Saengow et al. 2015; Boisly et al. 2014). However, the complexity of most models naturally limits their application. Very general models that can predict arbitrary flows, such as the Oldroyd 8 parameter model (Bird et al. 1987), require many parameters that are difficult to determine experimentally.
Therefore, in this chapter a simple LAOS model is presented, that contains only the most necessary effects that are typical for polymeric substances and dispersions. The first is viscoelasticity, which will be incorporated by the linear Maxwell model (Chapter 2). The second is shear thinning behavior, which will be introduced by the Cox-Merz rule (Cox and Merz 1958). The two parameters that are used are already known from the Maxwell model, the elastic modulus $G$ and a relaxation time $\lambda$. The model is a scalar, 1-D model, therefore normal forces are neglected as well.

## 5.1 Modification of the Maxwell model

### 5.1.1 Differential equation

Starting from the scalar Maxwell model, which is a linear combination of a Hookean spring and a Newtonian dashpot (Dealy and Larson 2006; Morrison 2001), a simple way to generate nonlinear behavior is to introduce nonlinear building blocks in the model. As the viscosity is known to be very much shear rate dependent for many complex fluids (Dealy and Larson 2006; Morrison 2001; Malkin 2013), the dashpot is described by a function $\eta(\dot{\gamma})$ instead of a constant material parameter $\eta$. The exact function $\eta(\dot{\gamma})$ will be specified later. Previous work by Zacharatos and Kontou (2015) focused on modeling of strain stress

curves and start-up of steady shear behavior using a nonlinear phenomenological model based on the standard solid model (a spring parallel with a Maxwell element). They used an Eyring type (Bird et al. 1987) nonlinear dashpot as well as a nonlinear spring which followed a power law. LAOS flow, however, was not modeled. Similarly, but based on the Maxwell model, Monsia (2011) calculated stress build up with a model consisting of a generalized spring and generalized dashpot. Both elements were modeled by power laws. To set up the differential equation for the serial combination of the linear spring with a nonlinear dashpot as depicted in Fig. 5.1, the same procedure as for the Maxwell model is used.

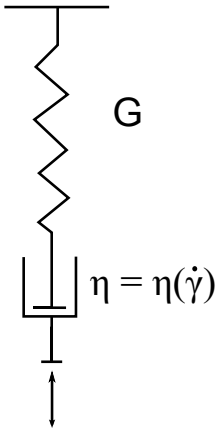


**Figure 5.1:** Phenomenological model consisting of a linear spring and a nonlinear dashpot in series. The introduction of a nonlinear dashpot is a simple way to introduce nonlinearity into the Maxwell model.

Both elements, spring and dashpot, have the same stress $\sigma$ and the sum of the individual strains in the spring and the dashpot, $\gamma_s$ and $\gamma_d$, equals the total strain $\gamma_t$. Also the sum of the individual shear rates equals the total shear rate.

$$\sigma_s = \sigma_d \tag{5.1}$$

$$\gamma_t = \gamma_s + \gamma_d \tag{5.2}$$

$$\dot{\gamma}_t = \dot{\gamma}_s + \dot{\gamma}_d \tag{5.3}$$

Assuming linear behavior of the spring, $\dot{\gamma}_s$ can be replaced by $\dot{\sigma}/G$ using Hooke's law, for the dashpot shear rate, $\dot{\gamma}_d = \sigma/\eta(\dot{\gamma}_d)$ will be used. This leads to the first order ordinary differential equation (Eq.5.5), which is the scalar expression for the shear stress of the White-Metzner model (White and Metzner 1963).

$$\dot{\gamma}_t = \frac{\dot{\sigma}}{G} + \frac{\sigma}{\eta(\dot{\gamma}_d)} \tag{5.4}$$

$$\dot{\sigma} = G\left(\dot{\gamma}_t - \frac{\sigma}{\eta(\dot{\gamma}_d)}\right) \tag{5.5}$$

### 5.1.2 Choice of the shear rate dependent viscosity function

When specifying the shear rate dependent viscosity function of a polymer, two major features are important: a finite zero shear viscosity $\eta_0$ and shear thinning. Many empirical viscosity functions have been proposed which capture these two features (Bird et al. 1987), well known examples are the Carreau-Yasuda (Yasuda et al. 1981) and the Cross model (Cross 1968). In this work a two parameter viscosity function will be used, that can be derived from the Maxwell-Model using the Cox-Merz rule (Cox and Merz 1958). This empirical rule states that for simple viscoelastic materials the angular frequency dependent complex shear viscosity in a small amplitude oscillatory test equals the shear rate dependent viscosity in a steady shear experiment, $|\eta^*(\omega)| = \eta(\dot{\gamma})$, where $\omega$ is expressed in units of rad/s and $\dot{\gamma}$ in $s^{-1}$. Snijkers and Vlassopoulos (2014) have evaluated this rule recently for a variety of polymer melts including linear and branched polymers as well as blends of linear polymers of the same chemistry. Although the Cox-Merz rule generally lacks a physical explanation, it is applied frequently in both, academic and industrial research. Its main use is to easily determine the steady shear viscosity function by measuring the linear viscoelastic properties using a small amplitude oscillatory shear (SAOS) experiment. This is advantageous because the SAOS experiment is more robust and more reproducible than the steady shear experiment. Moreover, higher peak shear rates can be reached without sample failure and less sample is needed because a rotational rheometer can be used instead of a capillary rheometer. Especially using Time-Temperature-Superposition (Morrison 2001; Dealy and Larson 2006) allows to measure $|\eta^*(\omega)|$ over many decades in $\omega$, which then can be converted to $\eta(\dot{\gamma})$.

In the Maxwell model the storage and loss moduli $G'$ and $G''$ are frequency dependent functions according to Eq. 5.6. The absolute value of complex shear viscosity is connected to $G'$ and $G''$ by Eq. 5.7 (Bird et al. 1987). Inserting Eq. 5.6 into Eq. 5.7 and simplifying yields Eq. 5.9 . Applying the Cox-Merz rule, $|\eta^*(\omega)|$ is replaced by $\eta(\dot{\gamma})$ and the angular frequency dependence is changed to a shear rate dependence, which results in Eq. 5.10.

$$G'(\omega) = G\frac{\lambda^2\omega^2}{1+\lambda^2\omega^2} \quad ; \quad G''(\omega) = G\frac{\lambda\omega}{1+\lambda^2\omega^2} \tag{5.6}$$

$$|\eta^*(\omega)| = \sqrt{\eta'^2(\omega) + \eta''^2(\omega)} = \sqrt{(G''/\omega)^2 + (G'/\omega)^2} \tag{5.7}$$

$$= G\lambda\sqrt{\left(\frac{1}{1+\lambda^2\omega^2}\right)^2 + \left(\frac{\lambda\omega}{1+\lambda^2\omega^2}\right)^2} \tag{5.8}$$

$$= G\lambda\sqrt{\frac{1+\lambda^2\omega^2}{1+2\lambda^2\omega^2+\lambda^4\omega^4}} = G\lambda\sqrt{\frac{1}{1+\lambda^2\omega^2}} \tag{5.9}$$

$$\eta(\dot\gamma) = G\lambda\sqrt{\frac{1}{1+\lambda^2\dot\gamma^2}} \tag{5.10}$$

Thus the zero shear viscosity in Eq. 5.10 is $\eta_0 = G\lambda$ and the square root term causes shear thinning behavior for high shear rates. The form of Eq. 5.10 is a particular case of the Carreau model (Eq. 5.11, Yasuda et al. 1981) with $c = 0$ and $\eta_\infty$=0.

$$\eta(\dot\gamma) = \frac{\eta_0 - \eta_\infty}{(1+\lambda^2\dot\gamma^2)^{(1-c)/2}} + \eta_\infty \tag{5.11}$$

Using Eq. 5.10 in Eq. 5.5 results in a differential equation according to Eq. 5.12. The specific choice of $\eta(\dot\gamma)$ keeps the number of parameters for the whole model minimal, using only a single elastic modulus $G$ and a single relaxation time $\lambda$.

$$\dot\sigma = G\dot\gamma - \frac{\sigma}{\lambda}\sqrt{1+\lambda^2\dot\gamma^2} \tag{5.12}$$

In the presented model the relaxation time $\lambda$ defines the balance between elastic and viscous behavior for a fixed frequency and the nonlinearity of the viscosity function at the same time, whereas the modulus $G$ sets only the stress scale. In Fig. 5.2 a plot of the storage and loss moduli as well as the steady shear and the complex viscosity functions for the Maxwell model are shown. The Maxwell model predicts a constant steady state viscosity for steady shear (see Fig. 2.3), whereas the complex viscosity is a function of $\omega$. By incorporating the Cox-Merz rule with the specific choice of the shear rate dependent viscosity (Eq. 5.10), Maxwellian behavior for the linear oscillatory case is combined with shear thinning in steady shear, thus enabling the Maxwell model to predict a LAOS response. Therefore, both steady shear behavior and oscillatory shear for arbitrary strain amplitudes can be described.

## 5.2 Model calculations

The numerical solution of the presented model gives an oscillatory stress signal $\sigma(t)$ for an applied oscillatory strain input of $\gamma(t) = \gamma_0 \sin\omega t$. The relaxation modulus $G$ linearly determines the stress scale of the results and was arbitrarily set to 10 Pa in all calculations. Exemplary results of the waveforms for $G = 10$ Pa, $\lambda = 1$ s, $\omega = 1$ rad/s are shown in Figs. 5.3 for three different strain amplitudes. Only the steady state solutions after all transients have decayed are shown. The elastic ($\sigma$ vs $\gamma$, panel (a)) and viscous ($\sigma$ vs $\dot\gamma$, panel (b))

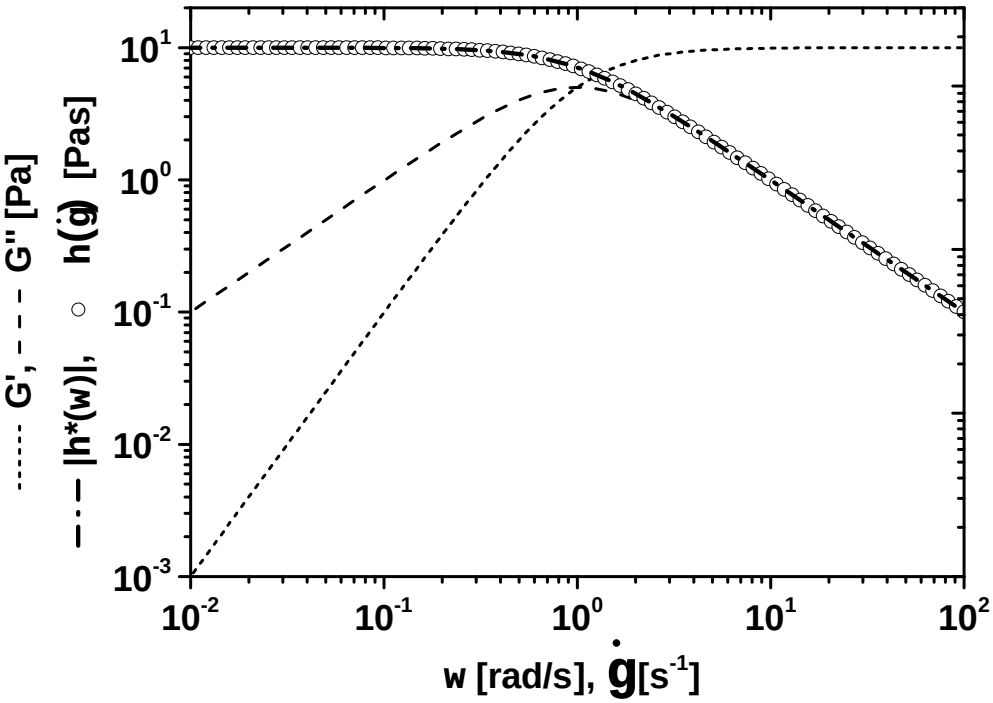


**Figure 5.2:** The frequency dependence of the storage and loss moduli for the presented model is identical to the Maxwell model. Furthermore, in contrast to the Maxwell model, the Cox-Merz rule $|\eta^*(\omega)| = \eta(\dot{\gamma})$ is incorporated. $G = 10$ Pa, $\lambda = 1$ s.

Lissajous plots for a linear response at $\gamma_0 = 0.011$ show an ellipse. In this case $De = 1$ and therefore the phase angle is exactly 45°, thus elastic and viscous behavior are balanced. At larger amplitudes, deviations from the elliptical form are visible. For $\gamma_0 = 1.33$ in panel a), the increased area inside the loop, which is a measure for the dissipated energy in a cycle (Giacomin and Dealy 1998; Ewoldt et al. 2010), suggests that viscous behavior exceeds the elastic behavior in comparison to the case of $\gamma_0 = 0.011$. For $\gamma_0 = 23.7$ pronounced nonlinear effects occur. At higher shear rates ($\dot{\gamma}_{max} = \gamma_0\omega = 23.7$ 1/s) the dashpot is strongly shear thinning within the oscillation cycle (compare the shear rate dependent viscosity in Fig 5.2). This results in behavior reminiscent of an elastoplastic body (Rouyer et al. 2008): as long as the stress is well beyond a yield stress that depends on the magnitude of $G$, the model gives approximately linear elastic behavior. Exceeding this yield stress leads to extreme shear thinning (the viscosity of the dashpot decreases as $\dot{\gamma}^{-1}$), resulting in plastic behavior, that means a stress independent of the strain (or shear rate) for the largest portion of the cycle. At these conditions the model represents a continuous version of the elastoplastic model with smooth transitions from elastic to plastic behavior.

After exploring the waveforms qualitatively, quantitative measures for strain amplitude (or $Wi = \omega\gamma_0\lambda$) dependent calculations are presented. Figure 5.4 displays the $\gamma_0$ dependence of $G'$, $G''$ and $I_{3/1}$ for $G = 10$ Pa, $\lambda = 1$ s, $\omega = 1$ rad/s. For small $\gamma_0$, $G'$ equals $G''$, which is

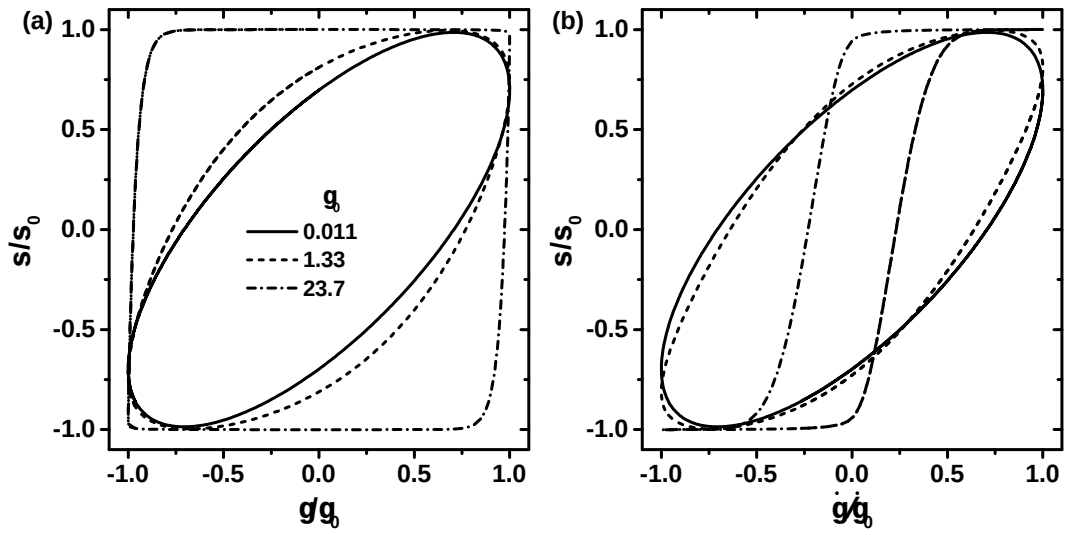


**Figure 5.3:** Waveforms from a numerical solution of the model using $G = 10$ Pa, $\lambda = 1$ s, $\omega = 1$ rad/s, $De = 1$, represented as elastic (a) and viscous (b) Lissajous figures.

consistent with Maxwellian behavior at $De = 1$. With increasing $\gamma_0$ the response becomes increasingly nonlinear: Both $G'$ and $G''$ start decreasing, but $G'$ does so more drastically. $I_{3/1}$ initially displays the power law behavior $I_{3/1} \propto \gamma_0^2$, that is also termed intrinsic LAOS range (Hyun and Wilhelm 2009; Reinheimer et al. 2012; Ewoldt and Bharadwaj 2013) or MAOS (Medium Amplitude Oscillatory Shear, Hyun et al. 2011). Eventually, $I_{3/1}$ levels off at value of 1/3, which is the maximum $I_{3/1}$ for a shear thinning dashpot. The limit of 1/3 results from a shear thinning viscosity that follows a power law with an exponent of -1. This maximum thinning leads to a rectangle wave form for the stress and $I_{3/1}$ of a rectangle wave equals 1/3 (Klein et al. 2007). That means at these high values of $\gamma_0$ (and therefore high shear rates) the effect of the incorporated spring is negligible and the system behaves like a power law shear thinning fluid for the largest portion of the cycle.
Along with the numerical results, asymptotic analytical solutions are plotted as solid lines in Fig. 5.4. The differential equation 5.12 has been solved by Mahdi Abbasi in a slightly generalized form to obtain the first nonlinear terms that scale with $\gamma_0^3$ or $\dot{\gamma}_0^3$, that is the first terms that describe the deviation of $G'$ and $G''$ from their plateau values. Furthermore an asymptotic expression for $I_{3/1}$ (Eq. 5.13) was derived, similar to the one in the work of Giacomin et al. (2015). The coefficients $G'_{mn}$ and $G''_{mn}$ in the nonlinear stress representation according to Eq. 2.30, page 24 for $m = 1, 3$ and $n = 1, 3$ can be found in the appendix.

$$I_{3/1} = \frac{\sqrt{\left(G'_{33}\gamma_0^3 + \cdots\right)^2 + \left(G''_{33}\gamma_0^3 + \cdots\right)^2}}{\sqrt{\left(G'_{11}\gamma_0 + G'_{31}\gamma_0^3 + \cdots\right)^2 + \left(G''_{11}\gamma_0 + G''_{31}\gamma_0^3 + \cdots\right)^2}} \tag{5.13}$$

The asymptotic solutions shown as lines in Fig. 5.4 confirm the numerical results for small deviations from the linear viscoelastic regime. However, already for $\gamma_0 > 1$ (for $De = 1$), the asymptotic predictions fall below the numerical results, because only the 3rd order term in $\gamma_0$ is included. Additionally, $G'$ and $G''$ eventually becoming negative for increasing

$\gamma_0$, which is unphysical, therefore not shown in the log-log plots, as well as the apparent maximum in $I_{3/1}$ around $\gamma_0 = 2.3$ are artifacts caused by the truncation. This shows the limited usability of truncated solutions. In order to reach a description in the full range that is plotted in Fig. 5.4 for the numerical results, the analytic solution would need to include many more higher order terms.

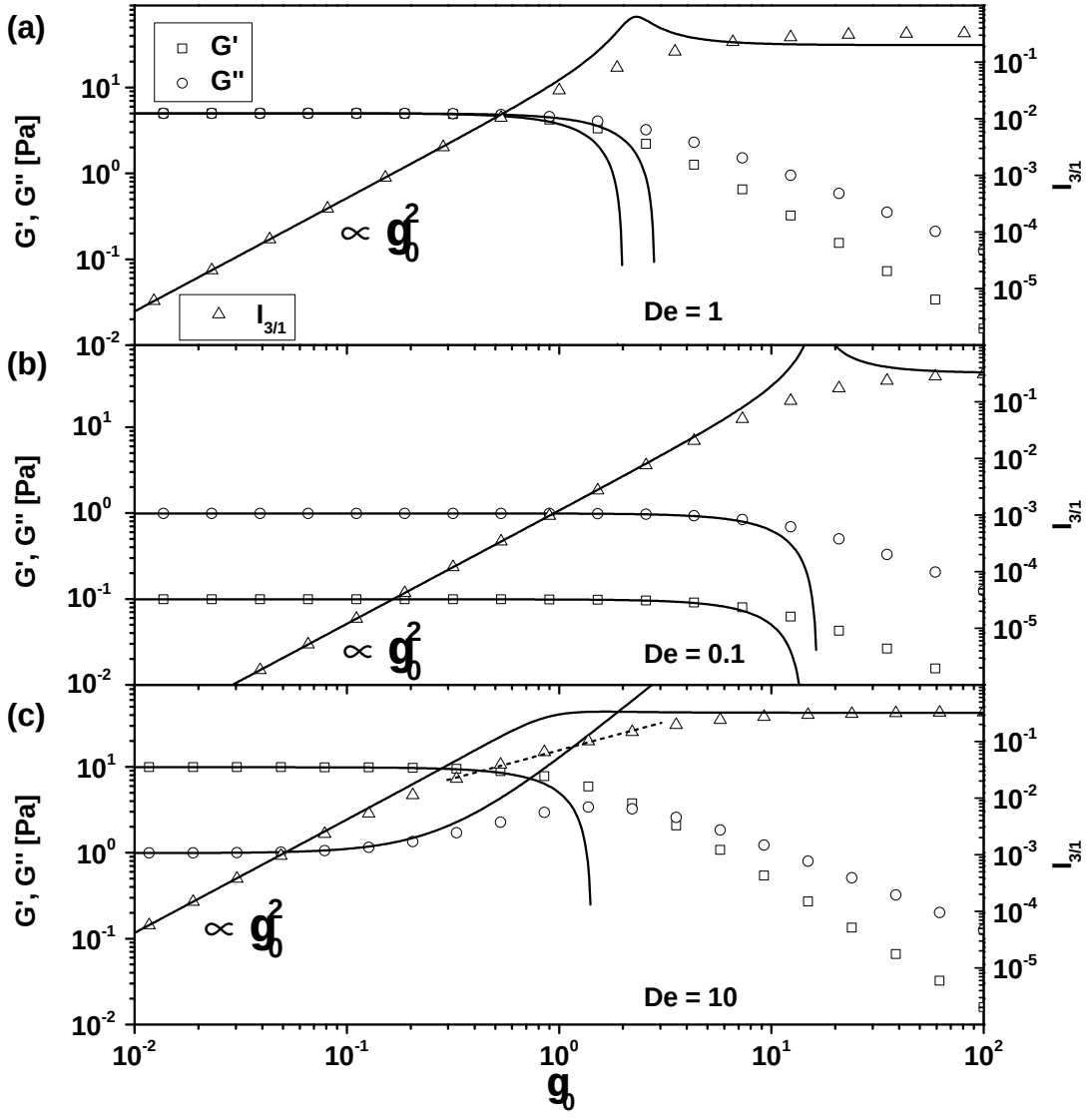


**Figure 5.4:** Symbols show $G', G''$ and $I_{3/1}$ from a numerical solution of the model using $G = 10$ Pa and $\omega = 1$ rad/s. Panel a) limiting case: $\lambda = 1$ s, $De = 1$, panel b) viscous case: $\lambda = 0.1$ s, $De = 0.1$, panel c) elastic case: $\lambda = 10$ s, $De = 10$. Solid lines are asymptotic analytical solutions for the model that are exact only for small enough deformation amplitudes, see the appendix of Merger et al. (2015) for a detailed derivation.

After dealing with the special case of $De = 1$, the representative cases of predominantly viscous ($De = 0.1$) and predominantly elastic behavior ($De = 10$) shown in Fig. 5.4 (b) and (c), respectively, are addressed. The change in $De$ has been made by choosing $\lambda$ accordingly, while keeping $\omega$ constant. For $De = 0.1$ (Fig. 5.4 (b)) in the linear regime $G''$ is 10 times higher than $G'$ and in the nonlinear regime both $G'$ and $G''$ decrease. When

compared to the case of $De = 1$, the overall decrease of nonlinearity is evident in the decrease of the moduli occurring at larger $\gamma_0$. Similarly, $I_{3/1}$, although it has the same functional behavior as in Fig. 5.4 (a), shows smaller values, indicating that the transition from linear to nonlinear behavior occurs at larger $\gamma_0$.

The initial situation for small amplitudes is reversed in the case of $De = 10$ (Fig. 5.4 c), $G'$ is 10 times higher than $G''$, again recovering the results of the Maxwell model for the linear case. Interestingly, for $De > 1$ the model is able to predict an overshoot in $G''$, followed by a cross-over of $G'$ and $G''$. These are common characteristics for yielding under LAOS that have been observed for dense colloidal suspensions, gels and foams (Brader et al. 2010; Kim, Merger, et al. 2014; Rouyer et al. 2008). In filled and vulcanized elastomers this effect has also been observed and is known as the 'Payne' effect (Payne 1962; Allegra et al. 2008). A close inspection of $I_{3/1}$ reveals an intermediate scaling region (broken line in Fig. 5.4 c) where $I_{3/1}$ increases linear with increasing $\gamma_0$, which coincides with the increase in $G''$.

The calculations have been repeated for several other $De$ and the results for $I_{3/1}$ are shown in Fig. 5.5. In all cases an initial power law behavior with $I_{3/1} \propto \gamma_0^2$ can be observed for low $\gamma_0$, which is confirmed by the asymptotic solutions. Furthermore, for $De$>1 , the intermediate scaling region where $I_{3/1}$ is linear in $\gamma_0$ extends over a larger range of strain amplitudes for increasing $De$. Curves of $I_{3/1}$ vs $\gamma_0$ can be superimposed on a master curve for $De < 0.1$ when $I_{3/1}$ is plotted vs $Wi = \omega\gamma_0\lambda$, as shown in the inset of Fig. 5.5. This is not possible for $De > 0.1$ as the functional form of $I_{3/1}$ changes when elastic contributions become important. The influence of the elastic spring also leads to different $De$ scaling behavior of the $I_{3/1}$ curves.

From the regions where $I_{3/1} \propto \gamma_0^2$ holds, the intrinsic nonlinearity $Q_0 = \lim_{\gamma_0 \to 0} \frac{I_{3/1}}{\gamma_0^2}$ (Hyun and Wilhelm 2009) has been determined. It can be interpreted as a measure of how far in strain amplitude the linear range of a sample extends. The definition of 'linear' range is not fixed, because in the intrinsic concept, $I_{3/1}$ actually never equals 0. But one can always assign a range where $I_{3/1}$ is so small that it plays an insignificant role for the overall mechanical behavior of a material. Such a limit could be for example $I_{3/1} = 10^{-4}$, since for all $\gamma_0$ where $I_{3/1}$ is smaller, the deviation of $G'$ and $G''$ from their respective linear values is vanishingly small, compare Figs. 5.4 (a) to (c). With this definition of an apparent linear range in mind, larger $Q_0$, means more narrow apparent linear range, meaning $G'$ and $G''$ decrease from their plateau values at smaller $\gamma_0$.

The dependence of $Q_0$ on $De$ is displayed in Fig. 5.6. For $De << 1$, $Q_0$ increases quadratically with $De$, whereas for $De >> 1$ it is linear in $De$. The quadratic small $De$ behavior is caused by the shear thinning dashpot. This is not surprising as the dashpot is dominating the overall response and any viscosity function that can be represented as an ordered expansion in shear rate leads to $Q_0 \propto De^2$ in the limit of small $De$ (Bharadwaj and Ewoldt 2014). For $De > 1$ the influence of the linear spring becomes evident: Coupling the nonlinear dashpot to a linear spring reduces the increase of $Q_0$ with $De$ from quadratic to linear. The expectation that increasingly dominating elastic behavior would eventually lead to a reduction of nonlinearities for very large $De$ is not met. This is due to only one

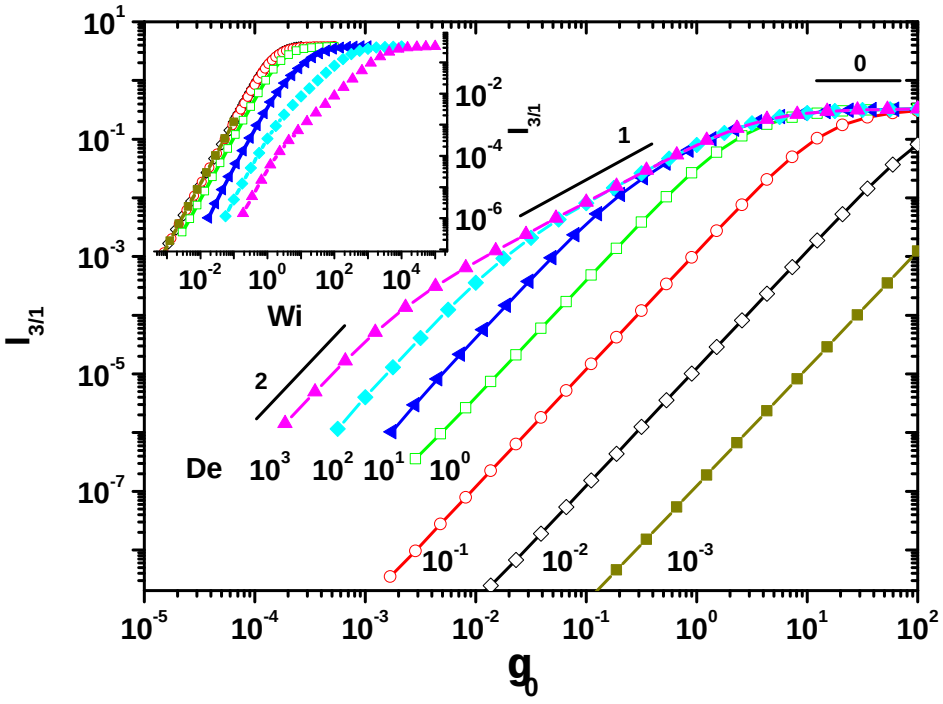


**Figure 5.5:** $I_{3/1}$ for various $De = \lambda\omega$ (by varying $\lambda$) from numerical solutions of the model using $G = 10$ Pa, $\omega = 1$ rad/s, lines indicate scaling regions of $I_{3/1} \propto \gamma_0^2, \gamma_0^1$ and $\gamma_0^0$. Inset shows rescaled curves of $I_{3/1}$ as a function of the Weissenberg number $Wi = \omega\gamma_0\lambda$.

relaxation time $\lambda$ being incorporated in the model. Increasing $\lambda = \eta/G$ at constant $\omega$ makes the material more elastic, but at the same time also shortens the linear range of the dashpot. Therefore in combination this still results in an increase of $Q_0$ with increasing $\lambda$ (and thus increasing $De$ for a fixed $\omega$). Decoupling elasticity from the dashpot nonlinearity by using two relaxation times (Section 5.6), $\lambda_1$ to control the dashpot nonlinearity and $\lambda_2$ for the ratio of $\eta/G$, leads indeed to a decreasing $Q_0$ with increasing $De = \lambda_2\omega$ when elasticity dominates.

When compared to predictions of other available models, the present model predicts very different behavior for the elastic regions (Fig. 5.6). For example, in the corotational Maxwell-Model (CRM) (Giacomin et al. 2015) $Q_0$ plateaus to a value of $\frac{1}{24} \approx 0.0416$. Similarly, a constant value for $Q_0$ is reached in the molecular stress function model for large $De$ [$1/4(\alpha - \beta/10) \approx 0.0345$, for $\alpha = 5/21$ and $\beta = 1$]. The Giesekus and the Pom-Pom model, in contrast, predict a decrease in $Q_0$ for $De > 1$. Which of these different behaviors is more realistic for a simple viscoelastic fluid will be determined in the subsequently presented experiments. Analytical expressions for $Q_0(\omega)$ from different models have been derived by Mahdi Abbasi (Merger et al. 2015) and are summarized in Table 5.1. Along with the full analytical expressions that are shown in the second column, in the third column simplified expressions that capture both limiting behaviors for small and large $De$ are presented. Surprisingly these simplified versions all show a similar functional form that

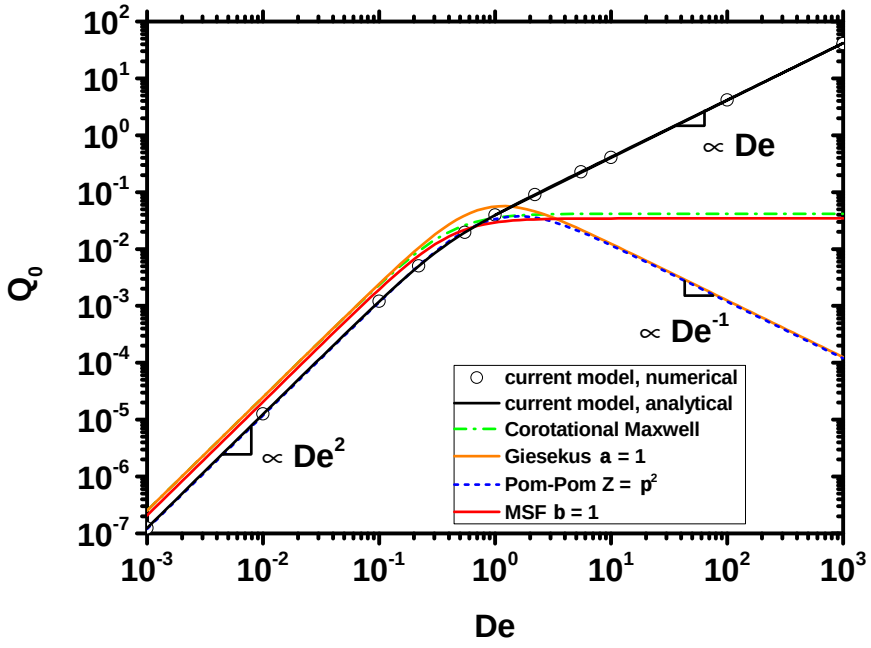


**Figure 5.6:** Intrinsic nonlinearity $Q_0$ versus $De$ for the current model (Eq. 5.12), symbols are extracted from the small $\gamma_0$ range where $I_{3/1} \propto \gamma_0^2$ holds in Fig 5.5. Lines are analytical solutions for the various models collected in Table 5.1.

can be written as Eq. 5.14.

$$Q_0 = a\frac{De^2}{1 + bDe^{2+d}} \tag{5.14}$$

The coefficients are summarized in Table 5.1. This finding is especially intriguing since a similar expression has been proposed by Cziep et al. (2015) based on experimental data covering a range of linear, almost monodisperse homopolymer melts. Therein, the authors provide experimental values for the parameters in Eq. 5.14 $a = 0.32Z^{-0.5}$, $b = 33.75Z^{-1}$ and $d = 0.35$, where $a$ and $b$ are dependent on the number of entanglements $Z = M_w/M_e$. Very recently, a similar procedure has been applied to the corotational Maxwell, Giesekus and MSF model and additionally, to a model for rodlike polymers, an emulsion model as well as the Curtiss-Bird model (Bharadwaj and Ewoldt 2015), where intrinsic nonlinear measures were compared based on Chebishev coefficients (Ewoldt and Bharadwaj 2013).

| Model | $Q_0$ | Asymptotic $Q_0$ for small and large $De$ | $a$ | $b$ | $d$ |
|---|---|---|---|---|---|
| Maxwell with Cox-Merz rule, $\eta(\dot{\gamma}) = \frac{\eta_0}{(1+\lambda^2\dot{\gamma}^2)^{1/2}}$ | $\frac{1}{8}\frac{De^2}{(1+9De^2)^{0.5}}$ | $\frac{1}{8}\frac{De^2}{1+3De}$ | $\frac{1}{8}$ | 3 | -1 |
| Pom-Pom | $\frac{De^2(1-2.5Z_{bb}^{-1})}{2\pi(1+De^2)^{0.5}(1+25De^2Z_{bb}^{-2})^{0.5}(1+4De^2)^{0.5}}$ | $\frac{1}{2\pi}\frac{(1-2.5Z_{bb}^{-1})De^2}{1+10{Z_{bb}}^{-1}De^3}$ | $\frac{1-2.5Z_{bb}^{-1}}{2\pi}$ | $10Z_{bb}^{-1}$ | 1 |
| Molecular stress function (MSF) | $\frac{3}{2}(\alpha-\beta/10)\frac{De^2}{(1+4De^2)^{0.5}(1+9De^2)^{0.5}}$ | $\frac{3}{2}(\alpha-\beta/10)\frac{De^2}{1+6De^2}$ | $\frac{3}{2}(\alpha-\beta/10)$ | 6 | 0 |
| Corotational Maxwell (CRM) | $\frac{1}{4}\frac{De^2}{(1+4De^2)^{0.5}(1+9De^2)^{0.5}}$ | $\frac{1}{4}\frac{De^2}{1+6De^2}$ | $\frac{1}{4}$ | 6 | 0 |
| Giesekus | $\frac{\alpha}{4}\frac{De^2(9De^2+4\alpha^2-12\alpha+9)^{0.5}}{(1+4De^2)^{1.5}(1+9De^2)^{0.5}}$ | $\frac{\alpha}{4}\frac{De^2(4\alpha^2-12\alpha+9)^{0.5}}{1+8(4\alpha^2-12\alpha+9)^{0.5}De^3}$ | $\frac{\alpha(4\alpha^2-12\alpha+9)^{0.5}}{4}$ | $8(4\alpha^2-12\alpha+9)^{0.5}$ | 1 |
| General form for linear monodisperse homopolymers (Cziep et al. 2015) | | $a\frac{De^2}{1+bDe^{2+d}}$ | $0.32Z^{-0.5}$ | $33.75Z^{-1}$ | 0.35 |

**Table 5.1:** Analytical expressions for $Q_0$ for different viscoelastic models. The approximate expressions, which capture the small and large $De$ behavior, in the third column have very similar functional forms, consistent with the general form found for linear monodisperse homopolymers (Cziep et al. 2015). These expressions have been calculated using formulas for $I_{3/1}$ from the following sources: Pom-Pom (Hoyle et al. 2014), MSF (Abbasi et al. 2013), CRM (Giacomin et al. 2015), Giesekus (Gurnon and Wagner 2012). In the Pom-Pom model, $Z_{bb}$ is the number of entanglements that effectively leads to nonlinearities, for this only the backbone entanglements of a branched polymer are considered. It is defined as $Z_{bb} = Z\Phi_{bb}$, where $Z$ is the number of entanglements and $\Phi_{bb} = M_{bb}/M$ is the mass fraction of the backbone.

## 5.3 Comparison to experimental data of wormlike micelles solutions

For the validation of the model predictions a solution of wormlike micelles based on the surfactant cetyl trimethylammonium bromide (CTAB) was chosen as a model system because it is known to exhibit Maxwellian behavior for a wide range of $De$ (Gurnon and Wagner 2012; Khatory et al. 1993; Rehage and Hoffmann 1991). The results of frequency dependent experiments in the linear viscoelastic regime on a 0.15 M aqueous solution of CTAB in the presence of 1.5 M KBr are compared to the model predictions in Fig. 5.7. The model parameters were determined as $G = 68$ Pa and $\lambda = 0.265$ s, respectively using a fit of the Maxwell expressions for $G'$ and $G''$ (Eq. 5.6), as shown in Fig. 5.7. Furthermore, the validity of the Cox-Merz rule can be confirmed for the wormlike micelle solution for a wide range of frequencies/shear rates, as $|\eta^*(\omega)| = \eta(\dot{\gamma})$.

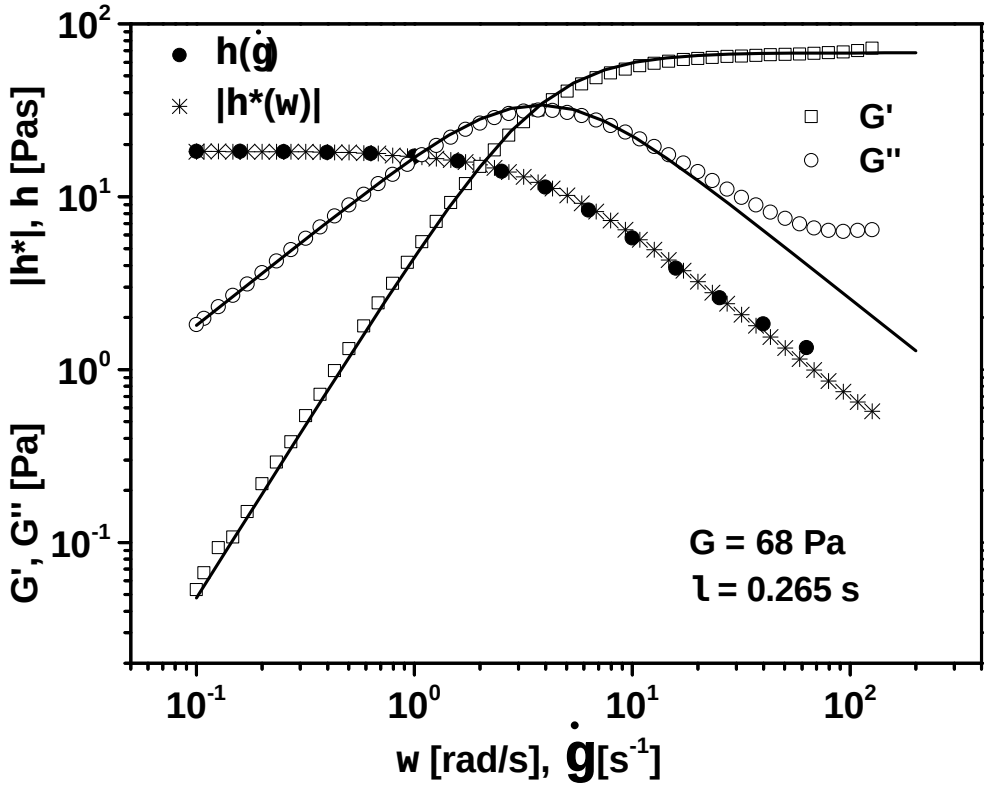


**Figure 5.7:** $G'$ and $G''$ of a 0.15 M aqueous solution of CTAB in the presence of 1.5 M KBr at T = 35°C. Lines are fits of the Maxwell expressions for $G'$ and $G''$ with $G = 68$ Pa and $\lambda = 0.265$ s. Also shown is the validity of the Cox-Merz rule for this sample: The dependence of the absolute value of the complex viscosity $|\eta^*|$ on $\omega$ is the same as the dependence of the steady shear viscosity $\eta$ on $\dot{\gamma}$.

A comparison of the model prediction with experimental LAOS data is shown in the form of Lissajous figures in Fig. 5.8 for three values of $\gamma_0$ at $\omega = 1$ rad/s. The predictions were calculated using $G = 68$ Pa and $\lambda$= 0.265 s which were determined in Fig. 5.7. At $\gamma_0 = 0.0214$, which is considered to be in the LVR (Chapter 2.2.1, page 27), the agreement

is excellent. For $\gamma_0 = 2.92$, where noticeable distortion form an ellipse is evident, prediction and experiment still agree well. Only at very large strain amplitudes, $\gamma_0 = 7.33$, pronounced differences are visible in the Lissajous curves. In the experimental data the stress slightly decreases for $\gamma$ between -2 and 6 and again for $\gamma$ between 2 and -6 in the second half of the cycle, whereas in the prediction the stress is constant in this range. $I_{3/1,m}$, $I_{3/1,e}$ indicate predicted and experimentally determined values, respectively. At $\gamma_0 = 0.214$, $I_{3/1}$ is too small to be detected experimentally.

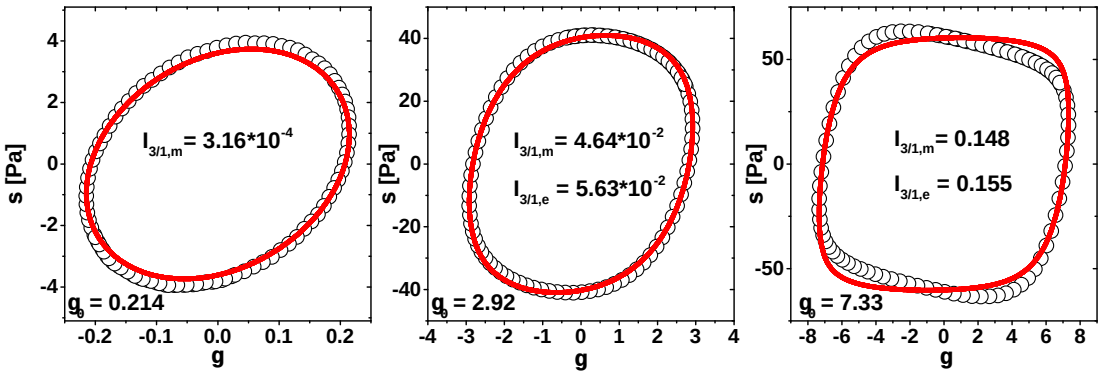


**Figure 5.8:** Lissajous figures for a 0.15 M aqueous solution of CTAB in the presence of 1.5 M KBr at T = 35°C and $\omega = 1$ rad/s. Lines are model calculations (Eq. refdgl3) using $G = 68$ Pa and $\lambda = 0.265$ s, $De = 0.265$. $I_{3/1,m}$, $I_{3/1,e}$ indicate predicted and experimentally determined values, respectively. At $\gamma_0 = 0.214$, $I_{3/1}$ is too small to be detected experimentally.

A quantitative comparison for more narrowly varying strain amplitudes is presented in Fig. 5.9 in terms of $G'$, $G''$ and $I_{3/1}$. As expected from the Lissajous figures, in the LVR the agreement is very good, only small deviations on the order of few percent can be seen in $G'$ and especially $G''$, which result from the good but not perfect fit in Fig. 5.7. For increasing $\gamma$, the model captures the decrease of $G'$ very well, but overestimates values of $G''$, which decrease stronger in the experiment. $I_{3/1}$ values however, are underestimated int the model by approximately 30% in the intrinsic range ($0.5 < \gamma_0 < 2$). The overall agreement is comparable to results of (Nam et al. 2010), who modeled data of poly(ethylene oxide) and poly(acrylic acid) solutions with the more complex multimode Giesekus model.

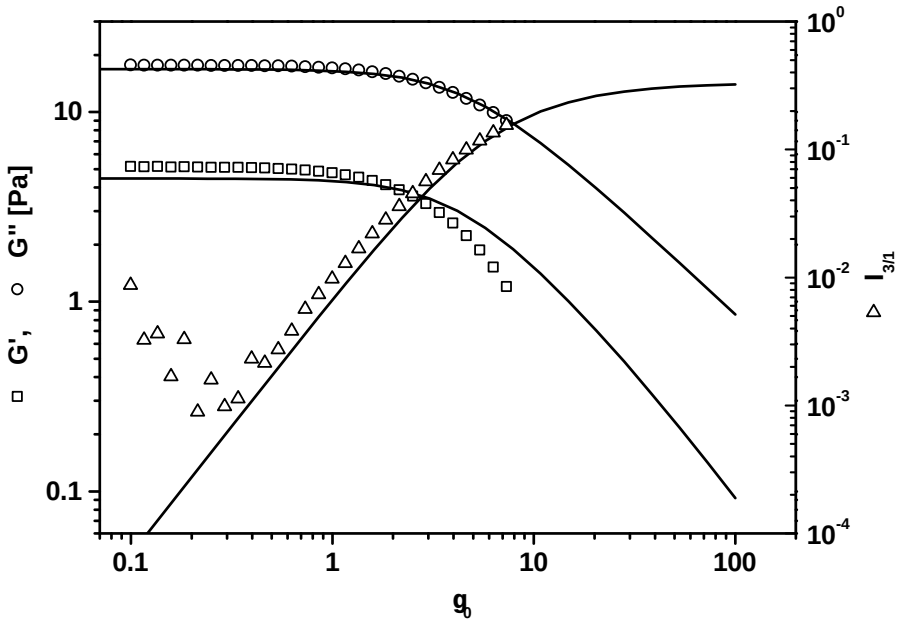


**Figure 5.9:** Strain amplitude dependent $G', G''$ and $I_{3/1}$ for a 0.15 M aqueous solution of CTAB in the presence of 1.5 M KBr at T = 35°C and $\omega = 1$ rad/s. Lines are model calculations (Eq. 5.12) using $G = 68$ Pa and $\lambda = 0.265$ s, $De = 0.265$.

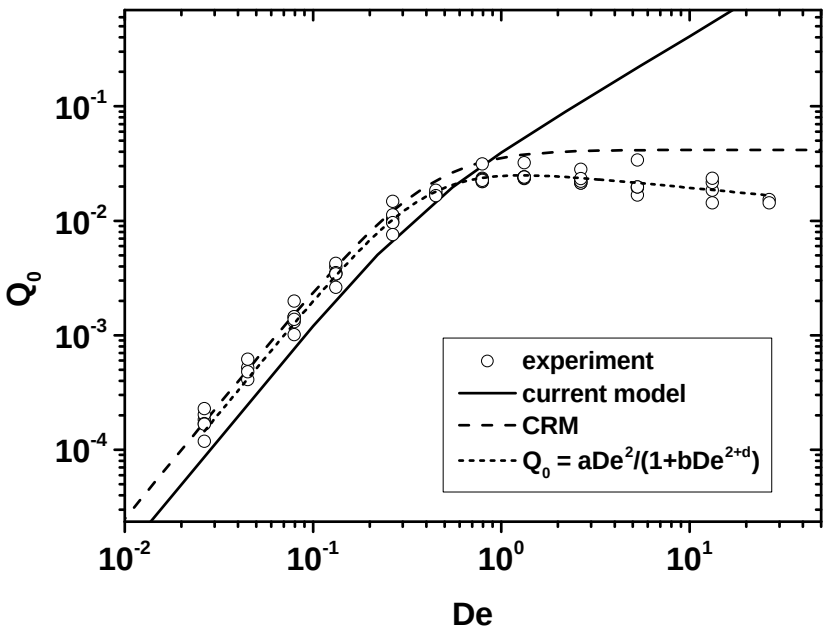


**Figure 5.10:** $Q_0$ of a 0.15 M aqueous solution of CTAB in the presence of 1.5 M KBr at T = 35°C. Repeated measurements with separate loadings give an estimate of the reproducibility. Lines are predictions of the current model (Eq. 5.12) and the corotational Maxwell model (CRM). Additionally, the Eq. 5.14 has been fitted to the data providing $a = 0.2$, $b = 2.53$ and $d = 0.158$.

As shown in Fig. 5.9, $I_{3/1} \propto \gamma_0^2$ for a certain range of $\gamma_0$, therefore the intrinsic nonlinearity $Q_0$ can be determined. Frequency dependent measurements of $Q_0$ of the CTAB sample are shown in Fig. 5.10 along with the predictions of the current model. Repeated measurements with separate loadings give an estimate for the reproducibility of the $Q_0$ values. The corotational Maxwell model has the same model parameters, $G$ and $\lambda$, and therefore is shown as well. In contrast to the current model, in the corotational Maxwell model, nonlinear behavior arises not from assuming a shear rate dependent viscosity but is a consequence of using a corotational derivative in the differential equation (Giacomin et al. 2011). It is a three dimensional, that means tensorial model, where the shear stress is coupled to normal stresses. The corotational derivative ensures frame invariance for rotating coordinate systems and defines the coupling of shear and normal stresses. This coupling allows to predict nonlinear stress signals in LAOS flow. Although generally the modified Maxwell model predictions (Eq. 5.12) fall below the actually measured nonlinearities for $De < 1$, the errors are not too grave, with the predicted values of $Q_0$ being smaller by up to 50%. Although the predictions of the 3D corotational Maxwell model are better, the presented simple modified Maxwell model shows reasonable capability of describing the data for $De < 1$. Its failure for $De > 1$ is not that surprising, as the assumption that the spring is linear and it is only the dashpot that shows nonlinear behavior is not very realistic at conditions where elasticity dominates the material's mechanical properties. The power law exponent for the decrease in the large $De$ range was found to be approximately -0.16 for the specific sample investigated so far. Fitting Eq. 5.14 to the data gives $a = 0.20$, $b$=2.53 and $d$=0.158. In comparison to measurements on linear, narrowly distributed polymer melt by Cziep et al. (2015) where a $d$ value of 0.35 was determined, $Q_0$ decreases weaker for the wormlike micelle solution. It turns out that none of the models shown in Fig. 5.6 is able to predict the large $De$ behavior quantitatively.

## 5.4 Scalar LAOS model with a power law viscosity function

As pointed out in Chapter 2 many different functions can be used to describe the shear rate dependency of the viscosity. The power law model, which is also known as Ostwald-de Waele model, is especially useful due to its simplicity. When Newtonian behavior does not suffice for fluid dynamics calculations it is usually the power law that is employed. In the preceding calculations in Section 5.2, the shear thinning behavior was restricted by the Cox-Merz rule inspired function such that $\eta \propto \dot{\gamma}^{-1}$ for high $\dot{\gamma}$. Now, the shear rate dependent viscosity in the modified Maxwell model is set to follow a powerlaw (Eq. 5.15) allowing different exponents $c$ and resulting in the differential Eq. 5.16. Since the shear rate is oscillating and therefore can also be negative but the viscosity is always positive, the absolute value $|\dot{\gamma}|$ has to be used.

$$\eta(\dot{\gamma}) = K|\dot{\gamma}|^{c-1} \tag{5.15}$$

$$\dot{\sigma} = G\left(\dot{\gamma} - \frac{\sigma}{K|\dot{\gamma}|^{(c-1)}}\right) \tag{5.16}$$

This version of the model, in contrast to the one using the Cox-Merz rule (Section 5.1.2), now lacks a zero shear viscosity but still captures shear thinning. The model parameters are now the elastic modulus $G$, a consistency $K$ and the powerlaw coefficient $c$. Due to the lack of a zero shear viscosity no linear viscoelastic regime exists. Frequency dependencies of the moduli are therefore also strain amplitude dependent. This leads to some interesting effects. For example, keeping $\gamma_0$ constant and decreasing $\omega$ increases nonlinear effects because for decreasing $\omega$, the competition of spring and dashpot is shifted more towards the dashpot, which is inherently nonlinear.

The strain amplitude dependence of $G'$ and $G''$ for different shear thinning coefficients is displayed in Fig. 5.11 (a). The lack of a zero shear viscosity leads to, in comparison to the results in Section 5.2, much simpler behavior of the moduli in $\gamma_0$ dependent calculations. For small $\gamma_0$ elastic properties dominate, $G' > G''$. With increasing $\gamma_0$ the loss modulus increases with a power law exponent that is decreasing with increasing $c$. There is no low $\gamma_0$ plateau for $G''$. The closer $c$ is to 1, which represents Newtonian behavior, the shallower the increase in $G''$. Eventually for further increasing $\gamma_0$, $G'$ starts to decrease, which is followed by a cross-over. Afterwards, both $G'$ and $G''$ decrease but $G'$ does so faster. Again the scaling exponents of the decrease are governed by $c$. Similar trends are evident in $I_{3/1}$ as shown in Fig. 5.11 (b). Here, the numerical solutions showed that $c$ directly translates into the scaling exponent of $I_{3/1}$ that increases proportional to $\gamma_0^{1-c}$. Furthermore, the maximum value of $I_{3/1}$ is decreasing when $c$ goes towards 1.

The fractional scaling of $I_{3/1} \propto \gamma_0^{1-c}$ seems to contradict many other models developed so far (Giacomin et al. 2011; Gurnon and Wagner 2012; Wagner et al. 2011; Reinheimer et al. 2011; Abbasi et al. 2013). All of them predict quadratic scaling of $I_{3/1}$, which is fundamentally linked to a Taylor expansion using only even order terms as shown in Section

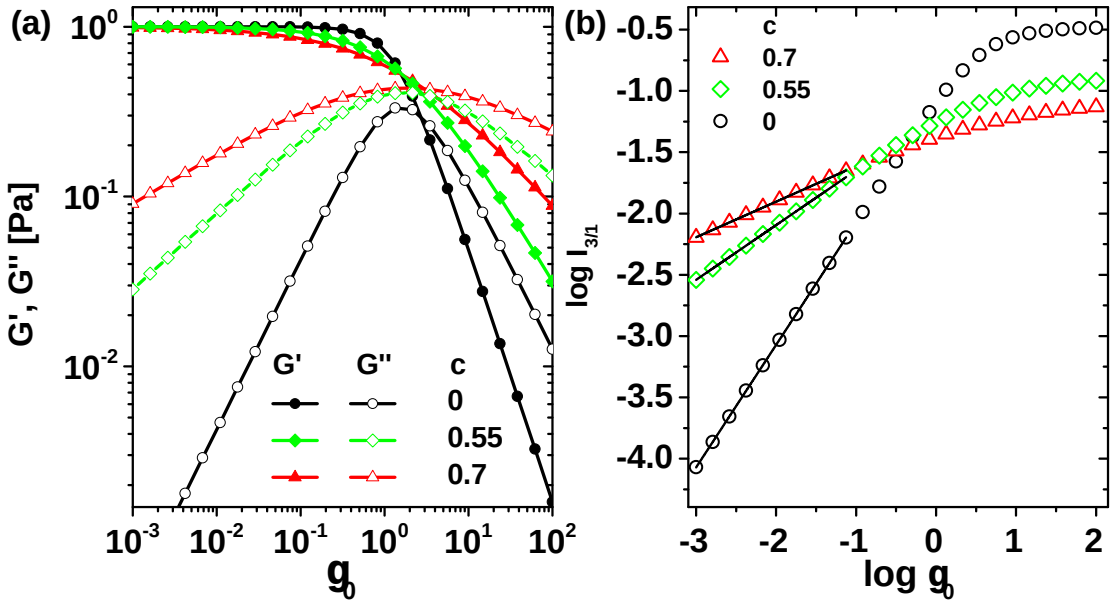


**Figure 5.11:** Strain amplitude dependent storage and loss moduli $G'$ and $G''$ from numerical solutions of the model with a shear rate dependent viscosity according to a power law $\eta(\dot{\gamma}) = K\dot{\gamma}^{c-1}$ for various shear thinning exponents $c$ (a). $K$/Pa·$s^{(1-c)} = 1$, $G = 1$ Pa, $\omega = 1$ rad/s. Corresponding $I_{3/1}$ dependent on $\gamma_0$ (b). The exponent $c$ translates directly into the powerlaw behavior of $I_{3/1} \propto \gamma_0^{(1-c)}$. The regression lines have the slopes 0.3, 0.45 and 1 for $c$=0.7, 0.55 and 0, respectively.

2.2. However, for the power law viscosity function, the Taylor expansion cannot be applied since, $|\dot{\gamma}|^c$ is not continuously differentiable around $\dot{\gamma} = 0$, hence the qualitatively different behavior in comparison to all other models that rely on the Taylor series.

Interestingly, Blackwell and Ewoldt (2014) reported linear scaling for $I_{3/1}$ in their thixotropic Jeffreys model. They used a 3 element model as shown in Fig. 5.12, which is a Maxwell element (for the Maxwell element see Section 2.1.4) arranged parallel to a second dashpot that represents a background viscosity, usually a solvent. Thixotropy was introduced by linking the dashpot and the spring of the Maxwellian part to a scalar structure parameter $\zeta$. The structure parameter $\zeta$ was shear rate and time dependent through Moore's kinetic structure equation 5.17 with two constants gauging the destruction, $\kappa_D$, and rebuilding, $\kappa_A$ of $\zeta$. Appearance of $|\dot{\gamma}|$ in the structure equation ultimately caused $I_{3/1}$ to scale linearly with $\gamma_0$.

$$\frac{\mathrm{d}\zeta}{\mathrm{d}t} = \kappa_A(1-\zeta) - \kappa_D\zeta|\dot{\gamma}| \tag{5.17}$$

The general shape of $G'$ and $G''$ is the same for a chosen $c$, no matter what values the other parameters assume. Varying $K$ moves the curves on the $\gamma_0$-axis as shown in Fig. 5.13. For larger $K$, the solid to fluid transition as evident from a cross-over of the $G'$ and $G''$ delayed to larger $\gamma_0$. Therefore the ratio $K/G$ acts similar to the relaxation time $\lambda$ in the main model that uses the Cox-Merz rule (Section 5.1.2), with the difference that $K/G$ does not have same unit, because the dimension of $K$ changes with $c$.

Analyzing the intrinsic nonlinearity $Q_0$ in this variation of the model first needs an adjusted

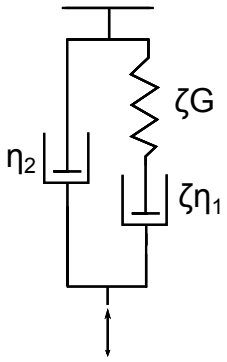


**Figure 5.12:** The thixotropic Jeffreys model by Blackwell and Ewoldt (2014) consists of a Maxwell element (spring with a modulus $G$ and dashpot with a viscosity $\eta_1$) arranged in series to a second dashpot ($\eta_2$) that represents a background viscosity, usually a solvent.

definition, because the quadratic power law that was used previously (see definition in Chapter 2) is now $c$ dependent. Calculations for $c = 0$, which represents the most extreme shear thinning case, and $c = 0.7$, i.e. rather weak shear thinning, show that if the intrinsic nonlinearity is redefined according to Eq. 5.18, ${}^cQ_0$ decreases with $\omega^{-c}$. That means increasing the elasticity in the system by increasing $\omega$ leads to a decrease of overall nonlinearity.

$$ {}^cQ_0(\omega) = \lim_{\gamma_0 \to 0} \frac{I_{3/1}}{\gamma_0^{1-c}} \tag{5.18} $$

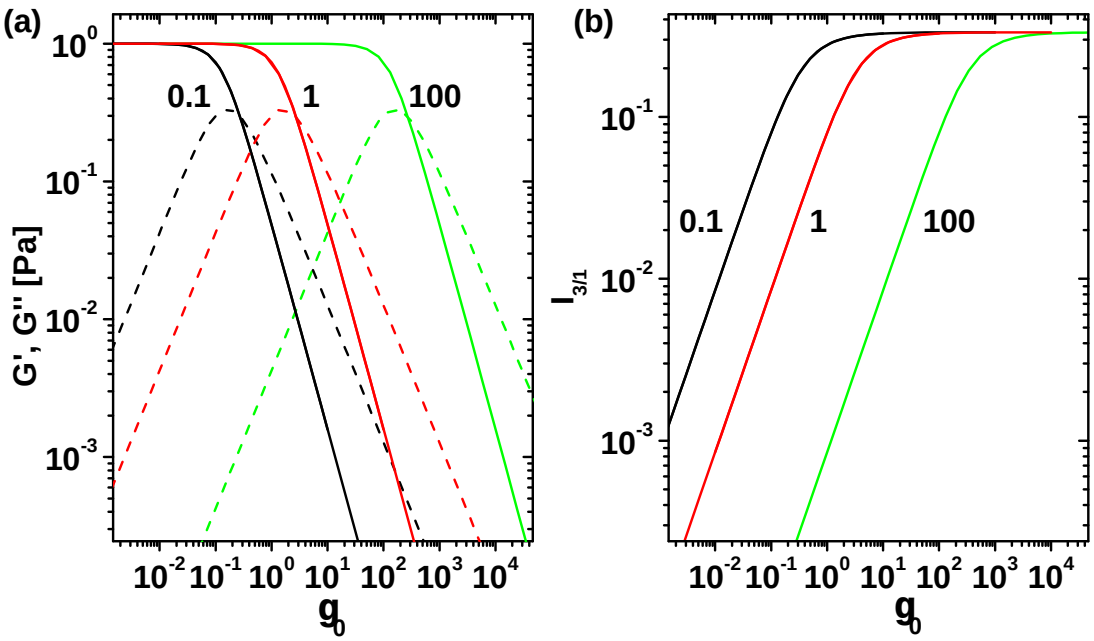


**Figure 5.13:** Influence of the parameter $K/\text{Pa}\cdot s^{(1-c)} = 0.1$, 1 and 100 on the $\gamma_0$ dependent storage and loss moduli (a) and $I_{3/1}$ (b). The parameter $c$ was fixed at 1, $\omega = 1$ rad/s, $G = 1$ Pa. For larger $K$ the solid to fluid transition as evident from a cross-over of the $G'$ and $G''$ is delayed to larger $\gamma_0$.

## 5.5 Scalar LAOS model with a viscosity function including a high shear rate limit

The two modifications of the Maxwell model that were presented so far (Cox-Merz rule based viscosity function and power law viscosity function) predict ever decreasing dynamic moduli ($G'$ and $G''$) and dynamic viscosities ($\eta'$ and $\eta''$) in LAOS for very large $\gamma_0$ and an ever decreasing steady shear viscosity for high shear rates. However, molecular interactions naturally provide a lower limit for the viscosity which is on the order of 0.1-1 mPas for small molecular weight liquids (e.g. $\eta$(water) = 0.89 mPas at $T$=25°C).
Therefore in the next variation of the model, the Cox-Merz rule based viscosity function (Eq. 5.10) is modified to include a high shear rate limiting viscosity $\eta_\infty$ as presented in Eq. 5.19. A limiting viscosity is also oftentimes introduced to empirically account for hydrodynamic interactions in dispersed systems (Mewis and Wagner 2012). Furthermore, if measurements at sufficiently high shear rate are experimentally possible, it is meaningful to restrict the shear thinning behavior, which in the previous model version was infinite. Using Eq. 5.19 in the general differential equation (Eq. 5.12) leads to Eq. 5.20.

$$\eta(\dot{\gamma}) = \eta_\infty + (\eta_0 - \eta_\infty)\sqrt{\frac{1}{1+\lambda^2\dot{\gamma}^2}} \tag{5.19}$$

$$\dot{\sigma} = G\left(\dot{\gamma} - \frac{\sigma}{\eta_\infty + (\eta_0 - \eta_\infty)\sqrt{\frac{1}{1+\lambda^2\dot{\gamma}^2}}}\right) \tag{5.20}$$

Numerical calculations of $G'$, $G''$ and $I_{3/1}$ for $\eta = 1$ Pas, $\eta_\infty = \eta_0/100$ are shown in Fig. 5.14 to demonstrate the effect of incorporating $\eta_\infty$. For small and medium $\gamma_0$ the results are identical to the ones in Fig. 5.13 in Section 5.2. But for further increasing $\gamma_0$ the influence of $\eta_\infty$ sets in, the decreasing moduli eventually level off to plateau values. At large $\gamma_0$, $G''$ is larger that $G'$, that means the model predicts a transition to a viscoelastic but predominantly viscous state. At the same time as $G'$ and $G''$ decrease, $I_{3/1}$, instead of approaching 1/3, decreases linearly.

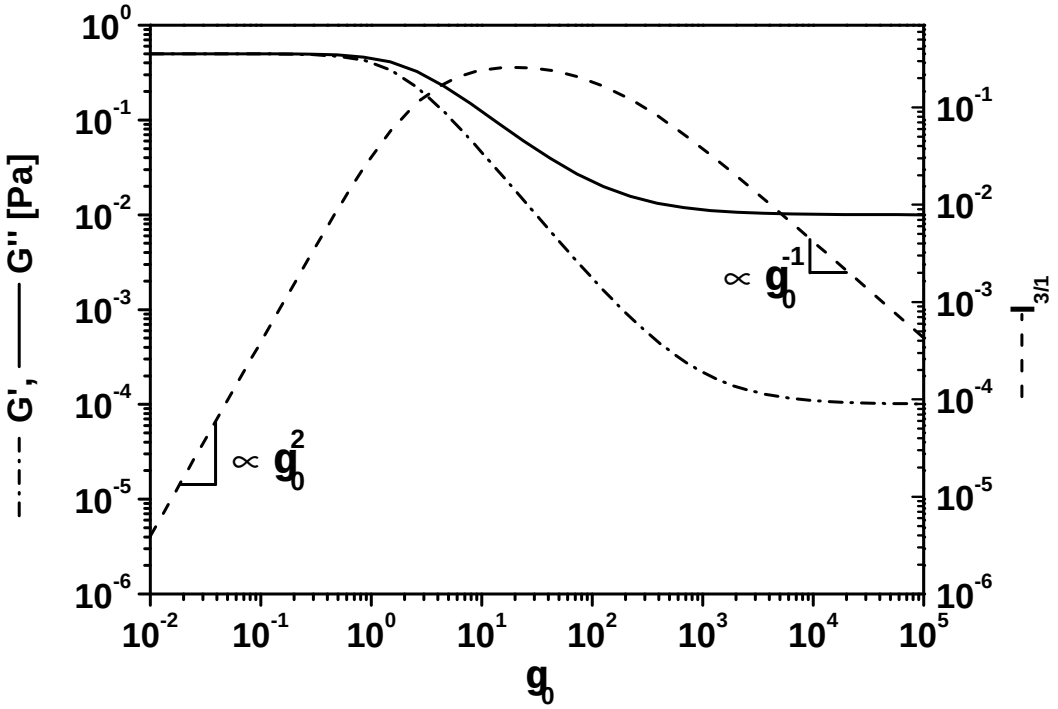


**Figure 5.14:** Effect of including $\eta_\infty$ as in Eq. 5.20 on storage and loss moduli and $I_{3/1}$ for $\omega = 1$ rad/s, $\eta = 1$ Pas, $\eta_\infty = \eta_0/100$, $G = 1$ Pa. For large strain amplitudes the moduli decrease to limiting values, which are set by $\eta_\infty$ and $\eta_0$, at the same time $I_{3/1}$ decreases linearly.

## 5.6 Scalar LAOS model with two relaxation times

The main model in section 5.2 had a single relaxation time (Eq. 5.21) and required the Cox-Merz rule to be valid. There are, however, fluids where the Cox-Merz rule does not apply. Examples for such systems are polymeric fluids which exhibit strong energetic interactions, like strong hydrogen bonds (Kulicke and Porter 1980), WLM systems where shear induces the formation of large scale structures (Kadoma et al. 1997) or some dispersion and emulsion systems (Al-Hadithi et al. 1992). In case of failure of the Cox-Merz rule, the strict condition of the Cox-Merz rule validity in the model can be relaxed by introducing a second relaxation time. The functional form of the shear rate dependent viscosity function $\eta(\dot{\gamma})$ (Eq. 5.22) is retained, such that a zero shear viscosity and shear thinning is predicted. An alternative approach could be the assumption of a Carreau type viscosity (Eq. 5.11) function for the dashpot but in order to stay close to the original model (Eq. 5.21), this approach will not be pursued. In the following modification, the identity of the relaxation time in the Maxwell model, $\lambda_2$, with the relaxation time in $\eta(\dot{\gamma}) = \eta_0\sqrt{\frac{1}{1+\lambda_1^2\dot{\gamma}^2}}$ is not forced, that means $\eta_0/G = \lambda_2 \neq \lambda_1$. This results is the differential equation 5.22, where the first relaxation time $\lambda_1$ sets the nonlinearity of the viscosity curve, whereas the second time, $\lambda_2 = \eta_0/G$, changes the balance of viscous and elastic effects. When the two times are varied independently, this has an interesting effect on the predicted $Q_0$ behavior.

$$\dot{\sigma} = G(\dot{\gamma} - \frac{\sigma}{\lambda}\sqrt{1+\lambda^2\dot{\gamma}^2}) \tag{5.21}$$

$$\dot{\sigma} = G\dot{\gamma} - \frac{\sigma}{\eta_0}\sqrt{1+\lambda_1^2\dot{\gamma}^2} = G(\dot{\gamma} - \frac{\sigma}{\lambda_2}\sqrt{1+\lambda_1^2\dot{\gamma}^2}) \tag{5.22}$$

First, variation of $\lambda_1$ is addressed. The results in Fig. 5.15 show that upon changing $\lambda_1$ the cross-over of storage and modulus can be shifted on the $\gamma_0$ axis, but as $\lambda_2$ is fixed at 100 s the initial values of $G'$ and $G''$ stay unaffected. Thus, the extension of the LVR regime can be varied independently of the elasticity/viscosity balance. This is also evident in $I_{3/1}$ where the functional form is identical, but for the larger $\lambda_1$ the whole curve is shifted to smaller $\gamma_0$, signaling an earlier transition from linear to nonlinear behavior. The inset in Fig. 5.15 shows the dependence of $Q_0$ on $\lambda_1$. Increasing the relaxation time of the dashpot $\lambda_1$ without changing the balance of dashpot and spring (by keeping $\lambda_2$ constant) leads to a quadratic increase in $Q_0$, as it would for a simple nonlinear dashpot without the spring (Bharadwaj and Ewoldt 2014). The spring merely, introduces an off-set as shown by the difference in the $Q_0(\lambda_1)$ dependencies for $\lambda_1 = 1$ and 100 s (inset of Fig. 5.15).
If $\lambda_1$ is fixed and $\lambda_2 = \eta_0/G$ is varied, the balance of viscous and elastic behavior can be changed while at the same time maintaining the nonlinearity level. This, however, is only possible if the viscous behavior is dominating as displayed in Fig. 5.16. For $\lambda_2\omega < 1$ (predominantly viscous behavior), the ratio of starting values of $G'$ and $G''$ can be adjusted by changing $\lambda_2$ as indicated by the arrows, but the transition to nonlinear behavior, marked by a decrease of $G'$ and $G''$, is fixed at, in this case, $\gamma_0 \approx 1$ due to constant $\lambda_1$. For $\lambda_2\omega >$

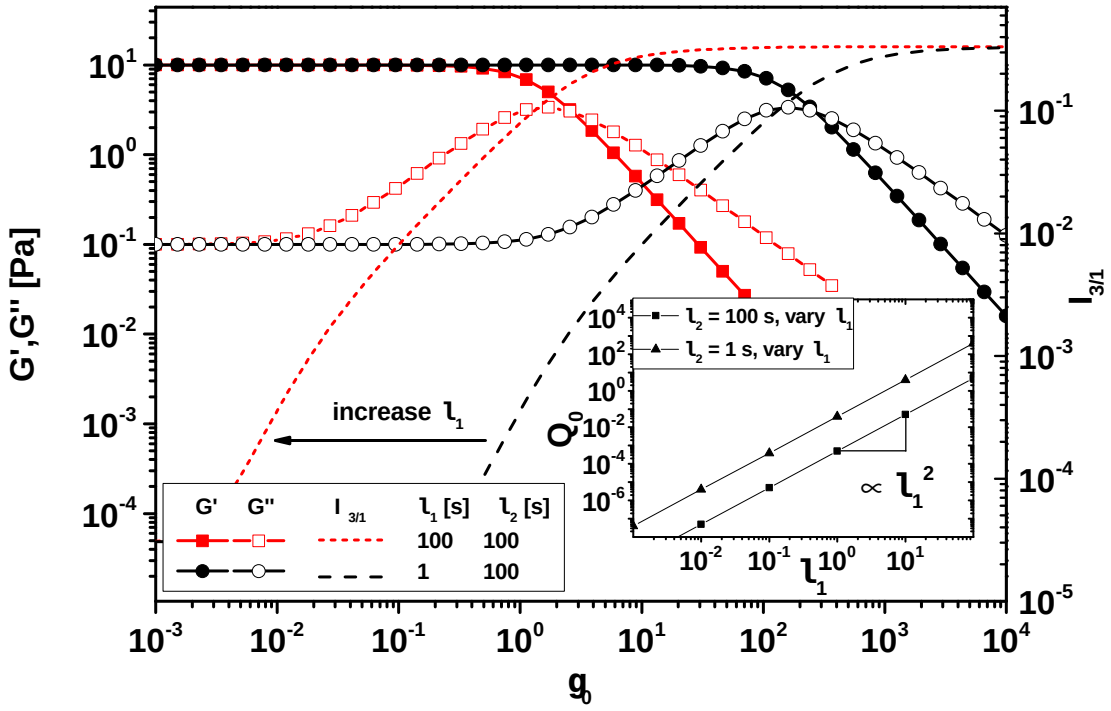


**Figure 5.15:** Influence of the dashpot relaxation time, $\lambda_1$, on the $\gamma_0$ dependent storage and loss moduli and $I_{3/1}$, for the two relaxation time model from Eq. 5.22, $G = 10$ Pa, $\omega = 1$ rad/s. The inset shows the behavior of $Q_0$ for varying $\lambda_1$. A quadratic dependece is found.

1 however (predominantly elastic case, Fig. 5.17), this independence is not found. Here, increasing $\lambda_2$, therefore increasing the initial ratio of $G'/G''$ also shifts the cross-over of $G'/G''$ and the $I_{3/1}$ curve to larger $\gamma_0$, thus increasing the apparent linear range.

Since the Deborah number is supposed to describe the relative importance of elastic effects to purely viscous behavior (Dealy 2010), it is refined for the two relaxation times model as $De = \omega\lambda_2$. Looking at the $Q_0$ behavior for varying $\lambda_2$ (Fig. 5.18), reaveals that if the dashpot nonlinearity is kept constant by fixing $\lambda_1$, changing the balance of spring and dashpot, $\lambda_2$, leads to either constant $Q_0$ when the dashpot is dominating ($De < 1$), or to decreasing $Q_0$ when the spring is dominating ($De > 1$).

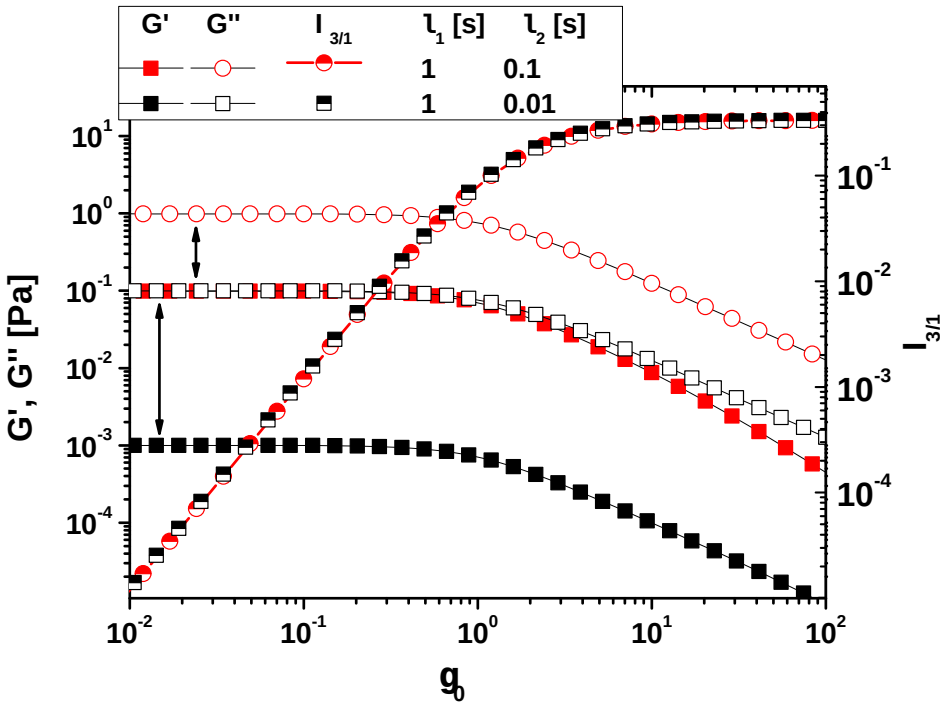


**Figure 5.16:** Influence of $\lambda_2$ on the $\gamma_0$ dependent storage and loss moduli and $I_{3/1}$ for the two relaxation time model from Eq. 5.22 in the predominantly viscous case ($\lambda_2\omega < 1$). Arrows indicate a change of the $G'/G''$ ratio with varying $\lambda_2$, $G = 10$ Pa, $\omega = 1$ rad/s.

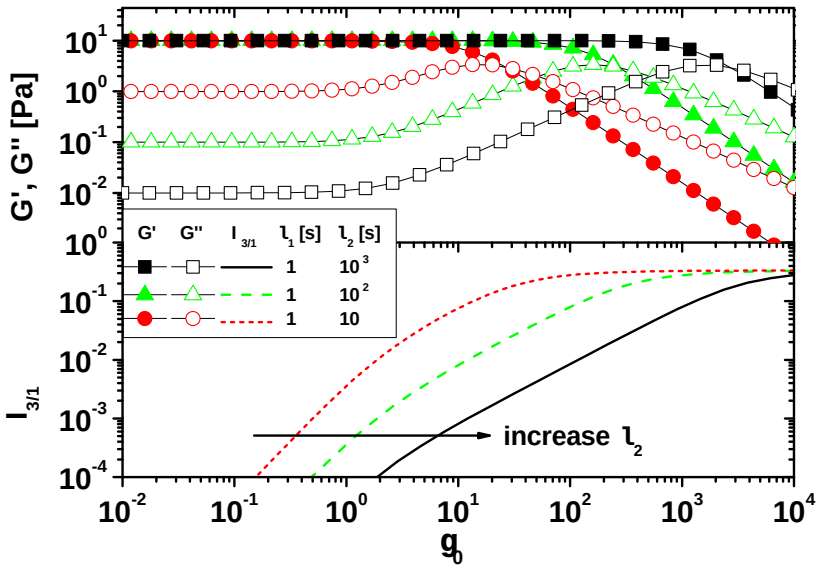


**Figure 5.17:** Influence of $\lambda_2$ on the $\gamma_0$ dependent storage and loss moduli and $I_{3/1}$, for the two relaxation time model from Eq. 5.22 in the predominantly elastic case ($\lambda_2\omega > 1$), $G = 10$ Pa, $\omega = 1$ rad/s.

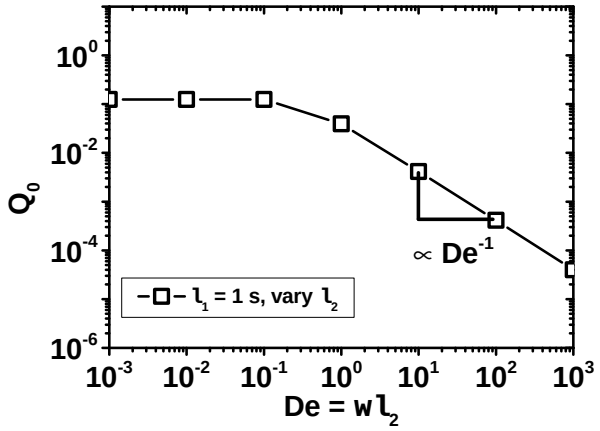


**Figure 5.18:** Dependence of $Q_0$ on $De = \omega\lambda_2$ in the two relaxation time model. The angular frequency $\omega$ was fixed at 1 rad/s.

## 5.7 Summary

In this chapter a simple, scalar, 1D model capable of predicting nonlinearities for the Large Amplitude Oscillatory Shear experiment using only two parameters, a shear modulus and a relaxation time, has been presented. The model was obtained by replacing the linear dashpot in a Maxwell model by a nonlinear function, the spring was kept linear. The specific function for the nonlinear dashpot was chosen by applying the Cox-Merz rule to the expression of complex viscosity from the Maxwell model. The shear modulus sets the stress scale, whereas the relaxation time governs the nonlinearity of the dashpot but also the balance of viscous and elastic effects. The model is a scalar, special case of the White-Metzner model.

Numerical solutions of the model have been calculated for a wide range of frequencies and strain amplitudes. The results analyzed by Fourier transform were presented in terms of the strain amplitude dependencies of the storage and loss moduli, $G'$ and $G''$, the relative intensity of the 3rd harmonic $I_{3/1}$ and the intrinsic nonlinearity $Q_0$. Furthermore, an analytical solution was provided in the form of a truncated power series in strain amplitude. Quadratic scaling laws for $I_{3/1}$ known from previous experiments and predictions of other models were confirmed and the functional form of $Q_0(De)$ was compared to predictions of alternative, more complicated models (corotational Maxwell, Giesekus model, Pom-Pom, molecular stress function).

Furthermore, the model predictions were compared to experimental data on a micellar solution of cetyl trimethylammonium bromide (CTAB). Waveforms were compared using Lissajous figures and good agreement was found. A quantitative comparison was made using $G'$, $G''$ and $I_{3/1}$. It revealed that the model underestimates nonlinear effects as measured by $I_{3/1}$ in the intrinsic LAOS range, typical deviation for $I_{3/1}$ were 30 %. LAOS measurements on CTAB spanning three decades in angular frequency were performed to

determine the intrinsic nonlinearity $Q_0(\omega)$. Agreement of model prediction and experiment for $Q_0(\omega)$ is reasonably good considering the simplicity of the model. Deviations occur for large Deborah numbers (or high angular frequencies), that is when the elastic behavior is dominating.

Moreover, the model was modified by using a powerlaw viscosity function to be able to describe varying shear thinning exponents. This led to deviations from the usually observed square scaling of $I_{3/1}$ with $\gamma_0$.

The inclusion of a high frequency viscosity limit $\eta_\infty$ was investigated. Introducing in the model $\eta_\infty$ had no effect on the intrinsic LAOS region and $Q_0$ but limited the decrease of $G'$ and $G''$ and forced $I_{3/1}$ to decrease linearly for very large $\gamma_0$.

Lastly, the main two parameter model was modified such that the effect of dashpot nonlinearity was decoupled from the balance of elastic and viscous behavior ($\eta_0/G$) by using two relaxation times instead of one. By doing so the validity of the Cox-Merz rule is not a prerequisite anymore, which can be useful for some experimental systems, where the Cox-Merz rule fails. The effects of both times were investigated independently. For increasing dashpot relaxation time $\lambda_1$, $Q_0$ increased quadratically with $\lambda_1$. For increasing $\eta_0/G = \lambda_2$, $Q_0$ was independent of $De = \omega\lambda_2$ if viscous behavior dominated and decreased linearly with $De$ if elastic behavior dominated.

# Chapter 6

# Large Amplitude Oscillatory Shear investigations of dense colloidal suspensions

## 6.1 Introduction to Mode Coupling Theory

In a hard sphere suspension of monodisperse spheres all rheological properties, such as the relative zero shear viscosity or storage and loss moduli, depend only on the volume fraction $\phi$, and not on the size of the particles (Mewis and Wagner 2012). Fundamental rheological properties of hard sphere suspensions have been outlined in Chapter 3, page 40. For investigations at high volume fractions, that means close to the glass transition $\phi_g = 0.58$, one usually prepares a concentrated suspension by centrifugation from which several samples of varying $\phi$ are obtained by dilution. In suspensions of thermo-responsive particles of Polystyrene/poly(N-isopropylacrylamid) (PS/PNipam), which have been prepared by Miriam Siebenbürger in the group of Prof. Ballauff at the Helmholtz-Zentrum Berlin, controlled variations of the volume fraction can be induced by simply changing the temperature, see Chapter 8, page 142 for experimental details on the system. A PS/PNipam suspension is therefore a very convenient system to study the nonlinear rheology of suspensions near the glass transition.

The structure and dynamics in dense suspensions can be described by a fully microscopic theory called mode coupling theory (MCT) that calculates density auto correlation functions $\Phi(t)$ using first principle mechanics (Fuchs and Cates 2012; Brader et al. 2012). The correlator $\Phi_q(t)$ as defined in Eq. 6.1 represents all two body interactions over many decades in time. It is wave vector dependent in the general case, hence the index $\boldsymbol{q}$. $\Phi_q(t)$ is connected to the intermediate scattering function $f(\boldsymbol{q},t) = \Phi_q(t)S_{\boldsymbol{q}}$, which is directly measurable by light scattering experiments (Megen and Pusey 1991; Willenbacher et al. 2011). The structure factor $S_{\boldsymbol{q}}$ contains particle interactions and introduces experimental parameters such as temperature and density (Henrich et al. 2009). The density fluctuation in Eq. 6.1 is taken as $\rho_q(t) = \sum_{j=1}^{N} \exp(i\boldsymbol{q} \cdot \boldsymbol{r}_j(t))$, where $\boldsymbol{r}_j(t)$ is the position vector of the

jth particle and the wave vector $\boldsymbol{q}(t) = (q_x, q_y - \dot{\gamma} t q_x)^T$ introduces a shear rate dependence in the correlator. The equation of motion for $\Phi_{\boldsymbol{q}}(t)$ as expressed in Eq. 6.2 describes the random Brownian motion of the particles as well as their shear induced migration. Equation 6.2 contains an initial decay rate $\Gamma_{\boldsymbol{q}}$ and the memory function $m_{\boldsymbol{q}}(t-t')$, which is not specified as such by the mode coupling theory. Many ansatz functions of varying complexity exist for $m_{\boldsymbol{q}}(t-t')$ that couple flow to $\Phi_{\boldsymbol{q}}(t)$ and introduce various relaxation modes. One possible form for $m_{\boldsymbol{q}}(t-t')$ is Eq. 6.4. Solving Eq. 6.2 for simple shear gives correlators that are depicted schematically in Fig. 6.1.

$$\Phi_{\boldsymbol{q}}(t) = \frac{\langle \rho_{\boldsymbol{q}(t=0)} \rho_{\boldsymbol{q}}(t) \rangle}{N S_{\boldsymbol{q}}} \tag{6.1}$$

$$\dot{\Phi}_{\boldsymbol{q}}(t) + \Gamma_{\boldsymbol{q}} \Big( \Phi_{\boldsymbol{q}}(t) + \int_0^t dt' m_{\boldsymbol{q}}(t-t') \dot{\Phi}_q(t') \Big) = 0 \tag{6.2}$$

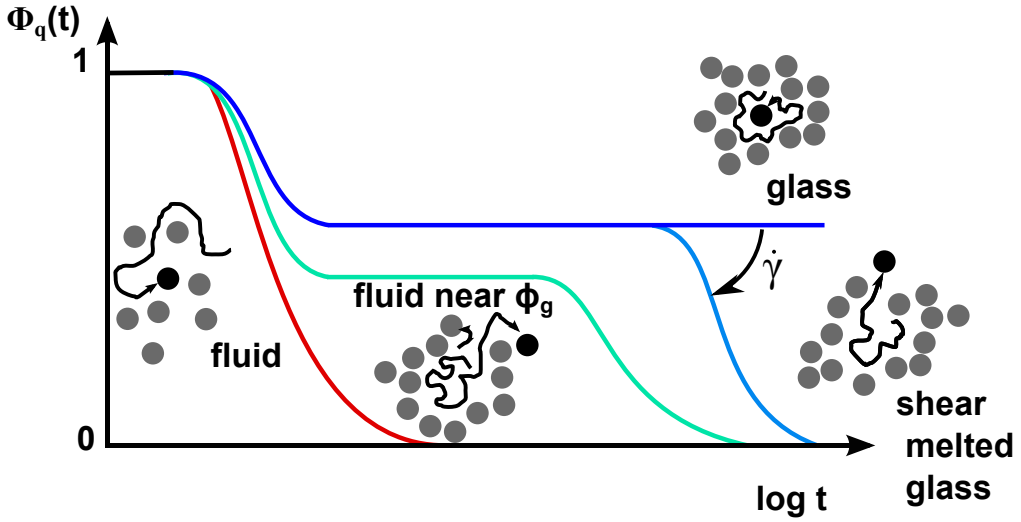


**Figure 6.1:** Schematic depiction of the density correlation function $\Phi(t)$. For fluids far from the glass transition ($\phi << \phi_g$), only one decay is present: the $\alpha$-relaxation that describes random Brownian motion. When the volume fraction is approaching $\phi_g$, $\alpha$-relaxation is preceded by a second relaxation, the $\beta$-relaxation. It describes the limited motion of the particle in a cage of its neighbors. For a glassy system, the correlator does not decay to zero, the particle is fully trapped in the cage. The application of shear, however, melts the glassy sample, therefore a final decay to zero is possible.

In the absence of shear, for fluids far from the glass transition ($\phi << \phi_g$) only one decay is observed in the correlator, the $\alpha$-relaxation. It expresses random particle movement by Brownian motion.

When the volume fraction is increased and comes close to $\phi_g$, the $\alpha$-relaxation is shifted to longer times due to the entrapment of the particles in cages of surrounding neighbors. To escape a cage, collective motion of the neighbor particles is necessary, which is far less probable. Furthermore, a second relaxation, called $\beta$-relaxation, emerges that describes the localized motion of a particle in its cage. For a glassy system ($\phi > \phi_g$), the correlator does not decay to zero because the cages become so tight that escape is not possible anymore. The application of shear increases the decorrelation of the density fluctuations

by additional velocity contributions in the direction of shear. This can be viewed as shear induced melting of the glassy sample, ultimately allowing a final decay of the correlator. As soon as $\Phi_{\boldsymbol{q}}(t)$ is known, mechanical as well as dielectric properties can be calculated (Tarzia et al. 2010). Mode coopling theory has been previously employed to model and predict various other flows than LAOS. Early work dealt with steady shear and predicted flow curves (Fuchs 2003; Fuchs and Cates 2003) as well as small amplitude oscillatory shear, where $G'$ and $G''$ were modeled (Crassous, Siebenbürger, et al. 2008; Siebenbürger et al. 2009). More recent advances led to investigations of steady shear start-up behavior (Amman and Fuchs 2014), that is the transient stress evolution after switching on steady shear. The decay of residual stresses after cessation of steady shear has also been addressed (Ballauff et al. 2013; Fritschi et al. 2014).

LAOS measurements on high volume fraction suspensions can be used to investigate their yielding behavior, that is the transition from a solid to a liquid, under oscillatory and therefore quasistatic conditions. Earlier LAOS studies of suspensions focused on differentiating samples that seemed to have identical steady shear properties (Kallus et al. 2001) or establishing a new LAOS analysis framework (Klein et al. 2007). Oftentimes LAOS was used to induce non-equilibrium structures or crystallize the suspensions (Ackerson 1990; Yan et al. 1994; Panine et al. 2002).

Simultaneously they can be used to test the predictive capabilities of the mode coupling theory. However, solution of the full microscopic (i.e. wave vector dependent) MCT under LAOS flow is currently not possible. Therefore in the work of Brader et al. (2010), a schematic version of the MCT was used, where the main features of the correlator are modeled with a simpler set of equations, that involve model parameters. Schematic here means that although the simplified model is not based on first principle calculations anymore it recovers the important features of the fully microscopic MCT. The parameters of the schematic version cannot be derived from first principles but instead are determined by fitting rheological data, such as flow curves and $G'$ and $G''$. In the schematic model, wave vector invariance is assumed, that means shear induced structures are neglected and the structure stays always isotropic. The argument for this assumption is that flow-induced ordering should be negligible in the range of small Peclet numbers, $Pe_0 \ll 1$. The simplifications in the schematic version allow Eq. 6.2 be solved numerically under oscillatory shear conditions even for large amplitudes.

Within the schematic model, the time dependent density correlator $\Phi(t)$ still remains the essential quantity that describes the structure of the suspension system and its evolution with time, but the wave vector dependence is removed. The correlator can be determined by solving the integro-differential equation (Eq. 6.3).

$$\dot{\Phi}(t) + \Gamma\Big(\Phi(t) + \int_0^t dt' m(t-t')\dot{\Phi}(t')\Big) = 0 \tag{6.3}$$

The memory function in the schematic MCT is approximated with a second order polynomial of the correlator $\Phi$ as shown in Eq. 6.4. In the absence of the memory function the dynamics

is trivial, only one decay is present: $\Phi(t) = \exp(-\Gamma t)$ (Fuchs 2003). The numerator of $m(t)$ describes the slowing down of dynamics caused by increasing particle interactions with increasing volume fraction $\phi$. The denominator controls how strong shear forces accelerate the correlator decay, despite the inhibition of the decay by particle caging. In the limit of vanishing shear disturbance, i.e. when $\gamma_0$ and/or $\omega$ go to zero, the denominator in Eq. 6.4 becomes one.

$$m(t) = \frac{\nu_1\Phi(t) + \nu_2\Phi^2(t)}{1 + (\gamma_0\omega t)^2} \tag{6.4}$$

In the memory function, $\nu_1 = 2(\sqrt{2}-1)+\epsilon/(\sqrt{2}-1)$ and $\nu_2 = 2$. The crucial parameter that describes the state of the system is the distance from the glass transition $\epsilon = (\phi - \phi_g)/\phi_g$. It is positive for a glassy suspension and negative for a flowing suspension. In the schematic MCT all particle interaction effects beyond hard sphere repulsion enter the model only indirectly via a change in the phase diagram, that is by adjusting $\phi$ and $\phi_g$. A suspensions is an ergodic system when observing a specific particle over time leads to the same result as observing many particles, and therefore averaging over the space . Consequently, the fluid suspension is ergodic, whereas the glassy is non-ergodic (Fuchs 2003). Under shear, the model describes two competitive phenomena: On one hand, increasing particle interactions leads to the glass transition and non-ergodicity of the system, which is evident in a plateau of the correlator $\Phi(t)$ for long times. On the other hand, the shear deformation induces an increased decay of $\Phi(t)$, restoring ergodicity.

Solving Eq. 6.2 for the correlator under shear $\Phi(t)$ allows to calculate the time-dependent modulus $G(t)$ according to Eq. 6.5 with $v_\sigma$ as a model parameter that measures the strength of the stress fluctuations. Additionally, hydrodynamic contributions that are not covered by MCT are considered by adding a high frequency viscosity $\eta_\infty$, where $\delta(t-t')$ is the Delta function. Subsequently, $G(t)$ can be used to obtain the shear stress as a function of time by integration of Eq. 6.6.

$$G(t,t') = v_\sigma\Phi^2(t,t') + \eta_\infty\delta(t-t') \tag{6.5}$$

$$\sigma(t) = \int_{-\infty}^{t} dt'\dot{\gamma}(t')G(t,t') \tag{6.6}$$

Numerical solutions of the schematic model for LAOS flow have been performed by Brader et al. (2010) and in first approximation showed good agreement with experimental data of thermo-responsive core-shell particles. In their study the waveforms agreed well, as did the $\gamma_0$ dependencies of $G'$ and $G''$. However, higher harmonic contributions were severely overestimated in the theoretical predictions, for increasing $\gamma_0$, $I_{3/1}$ was initially larger than in the experiments, only for $\gamma_0 > 1$ agreements was good. Furthermore, the experimentally observed quadratic scaling of $I_{3/1}$ at intermediate ranges of $\gamma_0$, that is the intrinsic LAOS region (see Chapter 2), was not confirmed.

Therefore, the theoretical approach changed from full numerical solutions to partially

analytical, asymptotic solutions calculated by Seyboldt (2013). As part of this thesis new LAOS measurements of the thermo-responsive PS/PNipam core-shell particle suspensions, covering over 4 decades in angular frequency (or $Pe_\omega$), have been performed to verify the theoretical advances of the mode coupling theory.
In order to find analytical expressions for the higher harmonics present in the stress wave, that is calculated by the schematic MCT model, Seyboldt (2013) used a Taylor expansion of the density correlator $\Phi$ in even orders of the strain amplitude $\gamma_0$ according to Eq. 6.7. Deriving asymptotic expressions for $I_{3/1}$ requires at least the consideration of a quadratic term, higher order terms are truncated for simplicity.

$$\Phi(t,t') = \Phi_{eq}(t,t') + \gamma_0^2 \Phi_\omega(t,t') + \mathcal{O}(\gamma^4) \tag{6.7}$$

The next order deviations from the equilibrium correlator $\Phi_{eq}(t,t')$, described by $\Phi_\omega(t,t')$, can be further decomposed as in Eq. 6.8, which helps obtaining a solution from the original equation governing the evolution of $\Phi(t,t')$ (Eq. 6.3).

$$\Phi_\omega(t,t') = f_0(t-t') + e^{i\omega(t+t')} f_1'(t-t') + e^{-i\omega(t+t')} f_1''(t-t') \tag{6.8}$$

This ansatz eventually leads to two additional differential equations for $f_0$ and $f_1^* = f_1' + i f_1''$ (Eqs. 6.9 and 6.10, see Seyboldt (2013) for more details), which have the equilibrium correlator $\Phi_{eq}(t,t')$ as input. Unfortunately, due to their complexity, they have to be solved numerically.

$$\begin{aligned}
&f_0'(t) + (1+\nu_1+\nu_2) f_0(t) \\
&+2\int_0^t \mathrm{d}t' f_0(t-t') \dot{\Phi}_{eq}(t') [\nu_1 + \nu_2 \Phi_{eq}(t-t') + \nu_2 \Phi_{eq}(t')] \\
&+(2-\cos(\omega t))[\dot{\Phi}_{eq}(t) + \Phi_{eq}(t)] \\
&+2\int_0^t \mathrm{d}t' \dot{\Phi}_{eq}(t') \cdot m_{eq}(t-t') \cos(\omega(t-t')) = 0
\end{aligned} \tag{6.9}$$

$$\begin{aligned}
&f_1'(t) + (1+\nu_1+\nu_2+i\omega) f_1(t) \\
&+2\int_0^t \mathrm{d}t' f_1(t-t') \dot{\Phi}_{eq}(t') [\nu_1 \cos(\omega t') + \nu_2 e^{i\omega t'} \Phi_{eq}(t-t') + \nu_2 e^{i\omega t'} \Phi_{eq}(t')] \\
&+\tfrac{1}{2}(1-\cos(\omega t))[\dot{\Phi}_{eq}(t) + \Phi_{eq}(t)] \\
&-\tfrac{1}{2}\int_0^t \mathrm{d}t' e^{i\omega t'} \dot{\Phi}_{eq}(t') \cdot m_{eq}(t-t')[1-\cos(\omega(t-t'))] = 0
\end{aligned} \tag{6.10}$$

After solving for $f_0$ and $f_1^*$, the total correlator $\Phi(t,t')$ can be used in Eqs. 6.5 and 6.6 to calculate the stress signal, or directly its Fourier components, $G_1^*$ for the fundamental frequency and $G_3^*$ for the 3rd harmonic (Eqs. 6.11 and 6.12). $F\{\Phi_{eq}(t) \cdot f_0(t)\}(\omega)$ denotes the Fourier transform of $\Phi_{eq}(t) \cdot f_0(t)$ taken at $\omega$. The intrinsic nonlinearity $Q_0$ can then be computed as in Eq. 6.13. The results calculated by Seyboldt are shown in Fig. 6.7, page 116, where they are compared to experimentally determined $Q_0$.

$$
\begin{aligned}
G_1^*(\omega) &= G_{11}^* + \gamma_0^2 G_{31}^* + \mathcal{O}(\gamma^4) \\
&= G_{11}^* + 2v_\sigma \gamma_0^2 i\omega \left[ F\left\{ \Phi_{eq}(t) \cdot f_0(t) \right\}(\omega) + F\left\{ \Phi_{eq}(t) \cdot f_1(t) \right\}(0) \right] \qquad (6.11) \\
G_3^*(\omega) &= \gamma_0^2 G_{33}^* + \mathcal{O}(\gamma^4) \\
&= 2v_\sigma \gamma_0^2 i\omega F\left\{ \Phi_{eq}(t) \cdot f_1(t) \right\}(2\omega) \qquad (6.12)
\end{aligned}
$$

$$
Q_0 = \lim_{\gamma_0 \to 0} \frac{1}{\gamma_0^2} \frac{|G_3^*(\omega)|}{|G_1^*(\omega)|} \qquad (6.13)
$$

## 6.2 Experimental results

Linear and nonlinear shear experiments have been carried out on the CS-80 dispersion kindly provided by Miriam Siebenbürger, HZB Berlin, (see Chapter 8.1.3, page 142 for synthesis and characterization details) in order to investigate the predictive capabilities of the schematic mode coupling theory. Only fluid states very close to the glass were considered, as at the current stage, asymptotic predictions of the schematic MCT cannot be made for glassy states. CS-80 is a polydisperse suspension of thermo-responsive core-shell particles in 0.05 M potassium chloride solution with a solid content of 8.85 wt.-%. The hard sphere core consists of polystyrene and has a diameter of 35 nm, whereas the shell is a network of poly(N-isopropylacrylamide), whose thickness is temperature dependent.

### 6.2.1 Linear viscoelastic properties, flow curves and model fitting

Flow curves and linear viscoelastic moduli of the CS-80 dispersion at the temperatures T = 22, 20, 18 and 15°C are displayed in Figs. 6.2 and 6.3. Dimensionless scales of reduced stress $\sigma_{red} = \sigma R_H^3/(k_B T)$ vs the Péclet number $Pe_0 = \dot{\gamma} R_H^2/D_0$ and reduced moduli $G'_{red} = G' R_H^3/(k_B T)$, $G''_{red} = G'' R_H^3/(k_B T)$ vs $Pe_\omega = \omega R_H^2/D_0$, respectively, are used to allow fitting of MCT predictions to the data. As the temperature is decreasing, the hydrodynamic radius of the thermo-responsive particles increases, which results in a higher volume fraction. Therefore, the viscosity as well as the moduli increase, the Newtonian range in the flow curves shortens and moves outside the experimental window (Fig. 6.2). Similarly, the terminal regime and the cross-over point of the moduli in the frequency dependent tests (Fig. 6.3) moves to smaller $Pe_\omega$ ranges and eventually the cross-over is not measurable anymore.

Since the schematic model does not provide analytical expressions for the viscoelastic moduli and the flow curve depending on the model parameters, the fitting procedure was not as straight forward as for example nonlinear least squares optimization.

For a given set of schematic model parameters, curves for $G'_{red}(Pe_\omega)$, $G''_{red}(Pe_\omega)$ and $\sigma_{red}(Pe_0)$ were calculated numerically using a Python code kindly provided by David Hajnal from the group of Prof. Fuchs in Konstanz. The curves were then fit to the

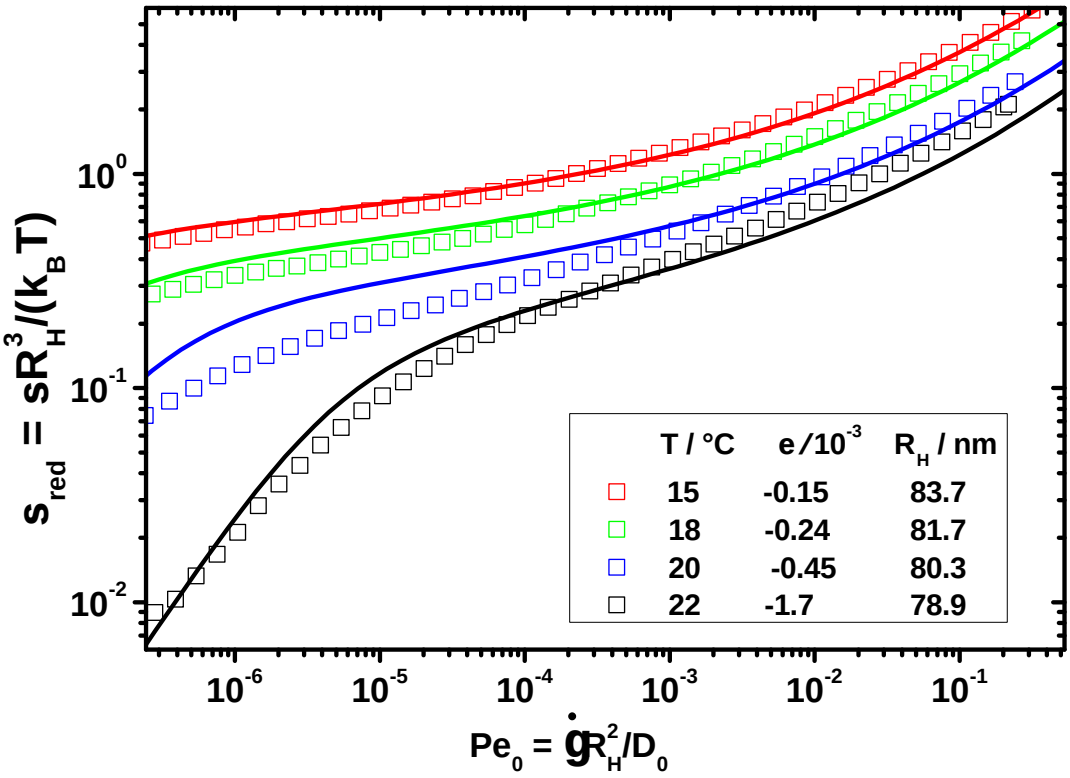


**Figure 6.2:** Symbols represent the experimentally measured flow curves for the CS-80 suspension at four different temperatures, T = 22, 20, 18 and 15°C, $\phi_{\text{eff}} = 0.614$, 0.62, 0.631 and 0.637, lines show fits of the schematic model to the data using the parameters in Table 6.1.

experimental data manually, following the procedure described in detail by Siebenbürger et al. (2009). Briefly, first the separation parameter $\epsilon = (\phi - \phi_g)/\phi_g$, which is the distance from the glass transition, was adjusted to match the cross-over frequency of the experimental data and the prediction. Subsequently, the other parameters were fitted: the initial decay rate, $\Gamma$, was kept constant, $v_\sigma$ set the magnitude of the moduli, the critical strain, $\gamma_c$, was matched using the flow curves and the high frequency limiting viscosity, $\eta_\infty$, was adjusted to the moduli at high $Pe_\omega$. The parameters obtained by the fits are collected in Table 6.1. The overall quality of the fits is good for the flow curves as well as for $G'_{red}(Pe_\omega)$. For low $Pe_\omega$ however, the measured values for $G''_{red}(Pe_\omega)$ are larger than predicted, which is a known problem, see for example the fits in Fig. 5 of Siebenbürger et al. (2009) and Fig. 13 of Brader et al. (2010). This suggests the existence of an additional slow relaxation process that is not covered by the schematic MCT. The discrepancy in $G''_{red}(Pe_\omega)$ caused by this process is even more prominent for glassy samples. In the glassy state, the MCT predicts vanishing $G''_{red}(Pe_\omega)$ as $Pe_\omega$ goes to zero but the experimentally determined $G''_{red}(Pe_\omega)$ increases after a minimum for decreasing $Pe_\omega$ (Crassous, Siebenbürger, et al. 2008; Siebenbürger et al. 2009). Siebenbürger et al. (2009) hypothesized that this slow process develops smoothly and therefore, also exists in the fluid state causing the deviations in $G''_{red}(Pe_\omega)$. Crassous, Siebenbürger, et al. (2008) described this process by modifying the equation of motion for $\Phi(t)$, introducing an additional relaxation time on the order of

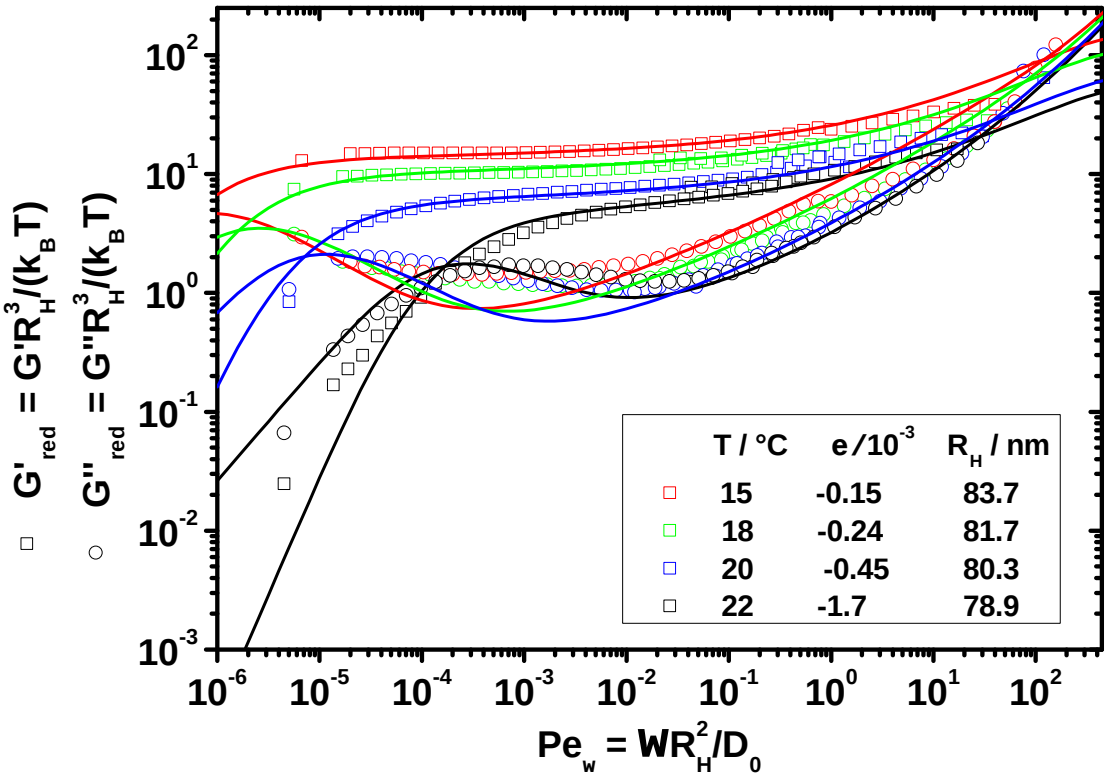


**Figure 6.3:** Symbols represent the experimentally measured storage and loss moduli for the CS-80 suspension at four different temperatures, T = 22, 20, 18 and 15 °C, $\phi_{\text{eff}} = 0.614$, 0.62, 0.631 and 0.637, lines show fits of the schematic model to the data using the parameters in Table 6.1.

$10^4$ s. However, they found that only one extra relaxation time was not sufficient to match $G''_{red}$ at low $Pe_\omega$.

| T [°C] | $\phi_{\text{eff}}$ | $\epsilon$ | $v_\sigma$ $[\frac{k_BT}{R_H^3}]$ | $\Gamma$ $[\frac{D_0}{R_H^2}]$ | $\gamma_c$ | $\eta_\infty$ $[\frac{k_BT}{D_0R_H}]$ |
|---|---|---|---|---|---|---|
| 22 | 0.614 | $-1.7\cdot10^{-3}$ | 60 | 100 | 0.177 | 0.361 |
| 20 | 0.62 | $-4.5\cdot10^{-4}$ | 75 | 100 | 0.213 | 0.375 |
| 18 | 0.631 | $-2.4\cdot10^{-4}$ | 125 | 100 | 0.189 | 0.40 |
| 15 | 0.637 | $-1.5\cdot10^{-4}$ | 167 | 100 | 0.2 | 0.418 |

**Table 6.1:** Fitted model parameters for flow curves and frequency dependent moduli of the thermo-responsive suspension CS-80. The separation parameter $\epsilon = (\phi - \phi_g)/\phi_g$ is a dimensionless distance from the glass transition, the decay rate $\Gamma$ sets the $Pe_\omega$ axis, the stress vertex $v_\sigma$ scales the stress axis, $\gamma_c$ determines the shape of the flow curve, $\eta_\infty$ determines a high frequency limit for the moduli.

### 6.2.2 Lissajous curves

Several earlier LAOS studies on high volume fraction suspensions concentrated on waveform analysis employing Lissajous figures (Brader et al. 2010; Rogers et al. 2011b; Vaart et al. 2013). Therefore, some typical Lissajous figures are presented in Fig. 6.4 as a starting point of the analysis. From measurements of CS-80 suspension at T = 18 °C ($\phi_{\text{eff}} =$

0.631) and $\omega = 4.522$ rad/s ($Pe_\omega = 1.43 \times 10^{-2}$ ) three wave forms are shown. Note that these are reconstructed waveforms which have been calculated from $G'_n$ and $G''_n$ using odd harmonics up to $n$=9. In the linear visco-elastic regime, at $\gamma_0 = 9.45 \times 10^{-3}$ (Fig. 6.4 (a)), the Lissajous figure is an ellipse with a comparatively small area, which is indicative of predominantly elastic behavior. This is even more evident in the $G'$ and $G''$ values shown in Fig. 6.5 (a). For an intermediate strain amplitude, $\gamma_0 = 6.436 \times 10^{-2}$, nonlinear behavior is already evident in the Lissajous curve (Fig. 6.4 (b)), which is not elliptical anymore ($I_{3/1} = 0.024$). For even larger $\gamma_0$, the curves get broader indicating further increasing dissipation (a circle in the Lissajous plot represents an ideal newtonian fluid) and increasing nonlinearity ($I_{3/1} = 0.090$). For $\gamma_0 = 2.4657 \times 10^{-1}$ (Fig. 6.4 (c)), which is larger than the strain amplitude at which $G'$ and $G''$ cross over, the curve approaches the behavior of an idealized Bingham model. The Bingham model is used for yield stress fluids (Bingham 1916; Rogers 2012). The presented waveforms are consistent with previous work (Brader et al. 2010; Rogers et al. 2011b; Vaart et al. 2013). An exception is the stress overshoot that was observed by Brader et al. (2010) for very large strain amplitudes ($\gamma_0 = 5$). However, this range of $\gamma_0$, was not probed in the current study, as the focus lay rather on medium range $\gamma_0$ measurements ($0.01 < \gamma_0 < 0.3$) where the quadratic scaling law for $I_{3/1}$ (Chapter 2, page 27) could be expected.

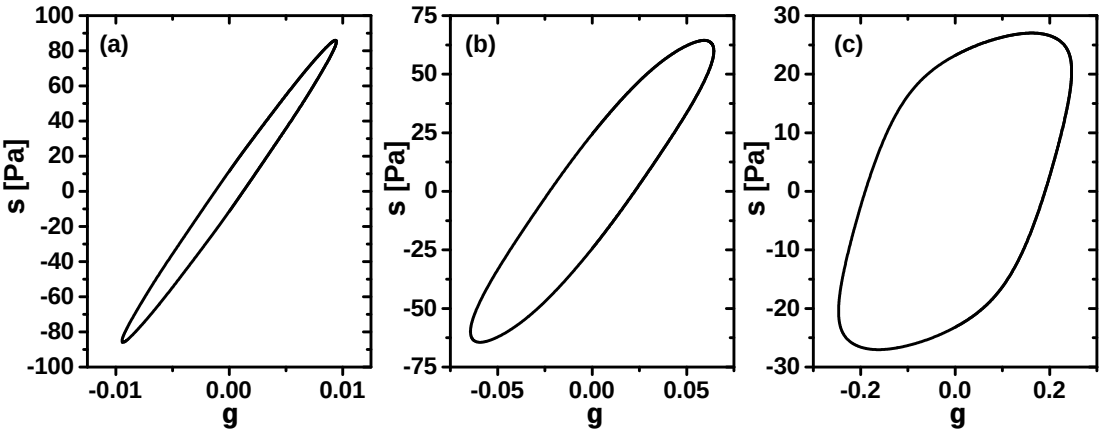


**Figure 6.4:** Representative wave forms as Lissajous plots (strain vs stress) from a LAOS measurement of KS-13 at T = 18 °C ($\phi_{\text{eff}} = 0.631$) and $\omega = 4.522$ rad/s ($Pe_\omega = 1.43 \times 10^{-2}$). a) linear viscoelastic regime, $\gamma_0 = 9.45 \times 10^{-3}$ ; b) intermediate nonlinear range , $\gamma_0 = 6.436 \times 10^{-2}$ ; c) highly nonlinear range, $\gamma_0 = 2.4657 \times 10^{-1}$. Arrows in Fig. 6.5 indicate the position of the wave forms in the $\gamma_0$ dependent measurement. The data were reconstructed from the Fourier moduli including odd higher harmonics up to the 9th.

### 6.2.3 Strain amplitude dependencies of $G'$,$G''$ and $I_{3/1}$

In Fig. 6.5 (a), strain amplitude measurements of the storage and loss moduli at T = 18°C for three different angular frequencies corresponding to different Péclet numbers are presented. As the strain amplitude is increasing, the transition to the nonlinear region can bee seen in the moduli deviating from their plateau values. The reduced storage modulus $G'_{red}$ decreases indicating a weakening of the elastic structure that is originating from the

particles that are jammed in the cages of their neighbors. At the same time, $G''_{red}$ increases and displays a maximum. This is a common feature of jammed colloidal systems, as high volume fraction suspensions (Renou et al. 2010) and colloidal gels (Laurati et al. 2011; Shao et al. 2013; Kim, Merger, et al. 2014). It is also often observed in measurements of rubbers, which are filled elastomers (Payne 1962; Allegra et al. 2008), where it is known as the Payne effect. The increased dissipation signaled by the $G''_{red}$ maximum is usually attributed to breaking of inter-particle bonds that are present in colloidal gels and rubbers. For high volume fraction suspensions, however, no such inter-particle bonds exist. The calculations using a modified Maxwell model in Chapter 5 could reproduce this feature on a continuum level, where no structural features are considered explicitly. However, they enter indirectly by a shear rate dependent viscosity. The requirements for producing this effect in $G''_{red}$ are a shear thinning viscosity in combination with predominantly elastic behavior in the linear visco-elastic regime.

Since storage and loss moduli are not sufficient to describe the material's response beyond the linear visco-elastic region, the next higher order Fourier terms in the form of the relative intensity of the 3rd harmonic in the stress response, $I_{3/1}$, are considered in Fig. 6.5 (b). For increasing $Pe_\omega$, $I_{3/1}$-values are generally lower, indicating that the progression to nonlinear behavior occurs at larger $\gamma_0$. At medium strain amplitudes ($10^{-2} < \gamma_0 < 10^{-1}$), a quadratic dependence of $I_{3/1}$ on $\gamma_0$ is observed, as predicted by various constitutive models [e.g. corotational Maxwell (Giacomin et al. 2015) or Giesekus model (Gurnon and Wagner 2012)] and measured by Hyun and Wilhelm (2009) with polymer melts. Therefore, $I_{3/1}$ is reduced to $Q = I_{3/1}/\gamma_0^2$ as shown in Fig. 6.6. From the plateau in $Q$ the intrinsic nonlinearity, $Q_0$, is determined experimentally by averaging 3-8 points depending on the length of this plateau. The error bars in Fig. 6.6 indicate an estimation for the reproducibility of $Q(\gamma_0)$ from three separate loadings. In contrast to measurements on polymer melts and solutions in Chapter 4, where the error in $Q(\gamma_0)$ (and consequently $Q_0$) was less that 12%, for the suspension it is rather on the order of 20-30%.

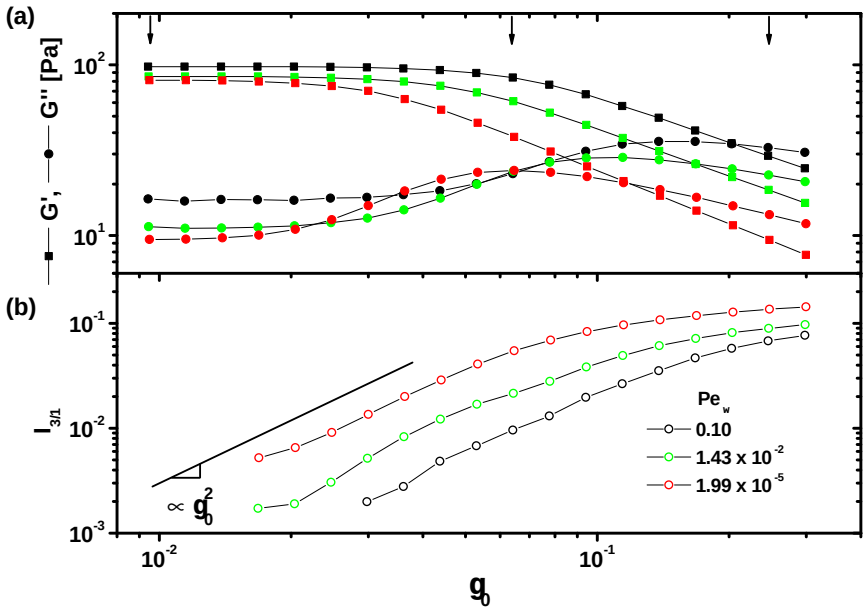


**Figure 6.5:** Strain amplitude dependent measurements of the CS-80 sample at T = 18 °C, $\phi_{\text{eff}} = 0.631$, for different $Pe_\omega = 0.1$, $1.43{\times}10^{-2}$ and $1.99{\times}10^{-5}$ ($\omega$ = 32.5, 4.52 and 0.063 rad/s). Storage moduli, loss moduli (a) and $I_{3/1}$ (b) indicate that the departure from the linear viscoelastic regime is dependent on the Péclet number. Arrows indicate the position of the wave forms from Fig. 6.4 in the measurement at $Pe_\omega = 1.43 \times 10^{-2}$.

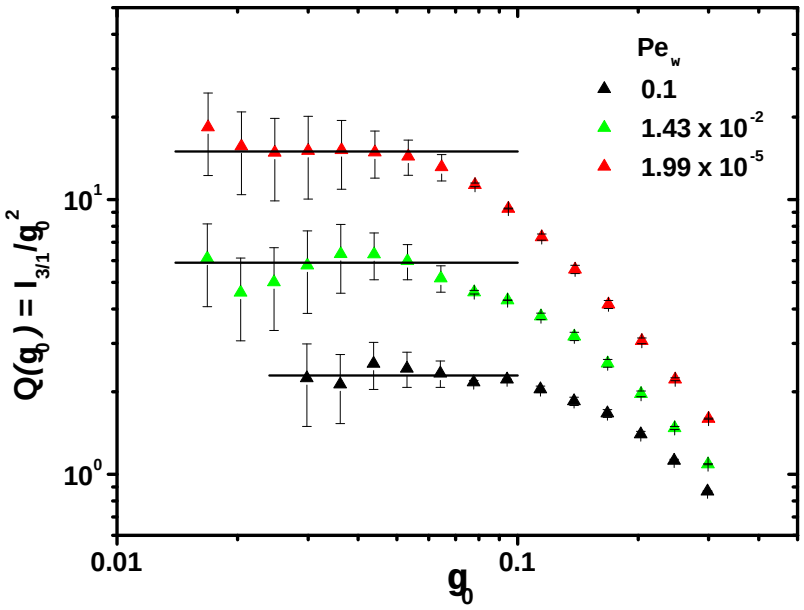


**Figure 6.6:** Strain amplitude dependent measurements of the KS-13 sample at T = 18 °C, $\phi_{\text{eff}} = 0.631$, for different $Pe_\omega = 0.1$, $1.43{\times}10^{-2}$ and $1.99{\times}10^{-5}$ ($\omega$= 32.5, 4.52 and 0.063 rad/s). Determination of the intrinsic nonlinearity $Q_0$ from plateau values at intermediate $\gamma_0$, where the scaling law $I_{3/1} \propto \gamma_0^2$ is applicable. An estimation of reproducibility has been made by averaging three measurements with separate sample loading and is shown as error bars.

### 6.2.4 Intrinsic Nonlinearity $Q_0(\omega)$: Experiment and mode coupling theory prediction

The intrinsic nonlinearity, in theory and experiment, shows a dependence on the angular frequency (or $Pe_\omega$) that depends strongly on the volume fraction (or $\epsilon$ in the MCT). Figure 6.7 shows a comparison of data collected for the CS-80 sample at four temperatures, corresponding to different $\phi_{\text{eff}}$ and $\epsilon$, and the corresponding predictions of the schematic MCT calculated by Seyboldt using the semi-analytical solution outlined in Section 6.1. MCT results predict $Q_0$ curves that show quadratic scaling with $Pe_\omega$ for small $Pe_\omega$, followed by intermediate scaling with an exponent $b \approx 0.69$ at moderate $Pe_\omega$, a maximum and finally $Q_0 \propto Pe_\omega^{-a}$ scaling for large $Pe_\omega$, where $a \approx 0.32$. A similar exponent for the high frequency decrease of $Q_0$ was reported by Cziep et al. (2015) for various linear homopolymer melts. Note that here, $a$ is not the particle radius as used in Chapter 3 and radius dependencies have been rescaled by using the Péclet number. The exponents $a$ and $b$ are not exact numbers but approximate solutions of Gamma functions. Due to the intermediate scaling region with an exponent $b$, a description of the curves using the general $Q_0(\omega) = a\frac{\omega^2}{1+b\omega^{2+d}}$ function (Eq. 5.14) is not possible. This functional form was observed for a variety of other models in Chapter 5 but it is able to describe only two power law regions.

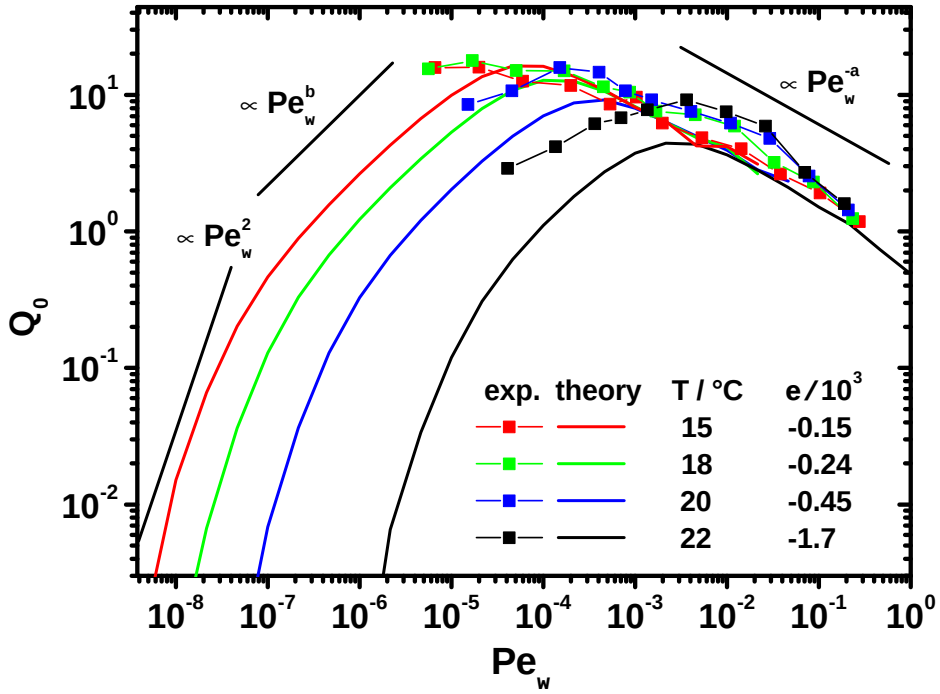


**Figure 6.7:** Comparison of experimental results for $Q_0$ (symbols) of the CS-80 suspension to predictions of the mode coupling theory (lines), calculated by Seyboldt using the Taylor approximation (Section 6.1).

Overall agreement is good, as evident from the experimentally determined exponents $a$ for

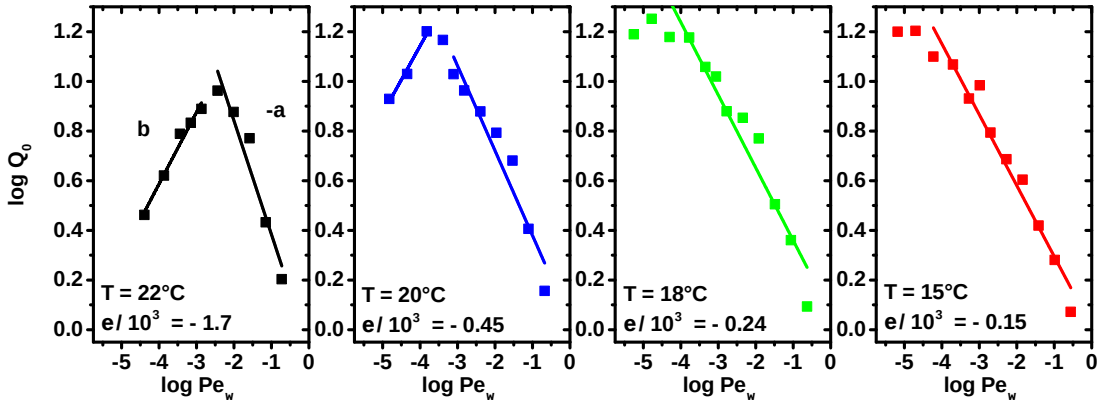


**Figure 6.8:** Linear regressions for $Q_0$ of the CS-80 suspension (data from Fig. 6.7) according to $\log Q_0 = \log A - a \log Pe_\omega$ and $\log Q_0 = \log B + b \log Pe_\omega$ for the determination of the scaling exponents $a$ and $b$ in Table 6.2. For $T = 15$ and 18°C , measurements could not be extended to small enough $Pe_\omega$ to determine $b$.

the large $Pe_\omega$ behavior, which are shown in Table 6.2. The exponents, 0.29< $a$ <0.46, were obtained by a linear regression according to $\log Q_0 = \log A + a \log Pe_\omega$, taking data after the maximum into account as shown in Fig. 6.8. Similar exponents (0.22< $a$ <0.56) were found by Wilhelm et al. (2012) in an investigation on beer foams. From the rheological point of view, foams are somewhat similar to dense suspensions, as the yielding behavior under LAOS looks much alike. For example strain amplitude dependent measurements of $G'$ and $G''$ of foams display the same features as the data shown in Fig. 6.5: a decrease in $G'$ and an overshoot in $G''$, with an eventual cross-over of the two (Rouyer et al. 2008). Further investigations need to clarify if the sublinear decrease of $Q_0(\omega)$ is a general feature of jammed dispersions.

For the two higher temperatures (thus lower volume fractions), $b$ could be determined similarly, but in this case the experimental exponents were half as large as the predicted. The fact that lesser agreement is found at smaller $Pe_\omega$ might be attributable to the previously discussed slow relaxation process which is already evident in the linear moduli (Fig. 6.3).

| T[°C] | $\phi_{\text{eff}}$ | $\epsilon$ | $a$ | $b$ |
|---|---|---|---|---|
| 22 | 0.614 | -1.7·10$^{-3}$ | 0.46 | 0.29 |
| 20 | 0.62 | -4.5·10$^{-4}$ | 0.34 | 0.27 |
| 18 | 0.631 | -2.4·10$^{-4}$ | 0.29 | |
| 15 | 0.637 | -1.5·10$^{-4}$ | 0.29 | |

**Table 6.2:** Experimentally determined intermediate and large $Pe_\omega$ scaling exponents, $Q_0 \propto Pe_\omega^b$ and $Q_0 \propto Pe_\omega^{-a}$, respectively. The theoretically predicted values are $a \approx 0.32$, and $b \approx 0.69$.

As $\epsilon$ is decreasing, that means the system approaches the glass transition, the maximum shifts to smaller $Pe_\omega$ in both, experiment and prediction. For $\epsilon = -1.7 \times 10^{-3}$ and $-0.46 \times 10^{-3}$, the position of the maximum roughly coincides for experiment and prediction. The results are consistent with trends found recently by (Poulos et al. 2015). They investigated the frequency behavior of soft particles of poly(ethylene-alt-propylene)-poly(ethylene

oxide) block copolymers and hard sphere particles of poly-methylmethacrylate in the nonlinear range. For both systems they found that nonlinear behavior as measured by $I_{3/1}$ at a fixed strain amplitude $\gamma_0 = 1$, increased with increasing $\omega$ for $\omega$ lower than the cross-over frequency $\omega_x$, that is when the overall behavior is liquid like. However, for $\omega > \omega_x$ (solid-like behavior), $I_{3/1}$ decreased with increasing $\omega$. They explained this difference arguing that for $\omega < \omega_x$ pronounced shear thinning is responsible for increasing $I_{3/1}$, whereas for $\omega > \omega_x$ viscous behavior over a large portion of the oscillation cycle leads to decreasing $I_{3/1}$ values.

For the smallest $\epsilon$, a decrease of $Q_0$ for decreasing $Pe_\omega$ could not be captured in the experimental window, so the position of the maximum is unclear. Measurements at even lower $Pe_\omega$ are extremely difficult due to low torques and furthermore, they require excessive amounts of time due to very low frequencies. Despite the precautions taken to limit solvent evaporation, measurements longer than three days were not possible on one sample loading. Agreement between experiment and prediction is less for smaller $\epsilon$, where exact determination of $\epsilon$ is more challenging, since the cross-over point of the moduli could not be measured. Therefore, an error in $\epsilon$ might be responsible for the discrepancy.

## 6.3 Summary

In this chapter LAOS measurements on a thermo-responsive suspension of polystyrene-poly(N-isopropylacrylamide) were presented and compared to predictions by the schematic, that means wave vector invariant, version of the mode coupling theory (MCT). The particle radius in the suspension could be changed by variation of the temperature, therefore adjusting the volume fraction. Measurements were conducted on fluid states close to the glass transition. Linear visco-elastic moduli and flow curves were fitted to MCT predictions to obtain model parameters that were used to predict LAOS behavior.

Nonlinear stress wave forms were found to be consistent with previous results on high volume fraction suspensions close to the glass transition. The frequency dependence of the mechanical nonlinearities as quantified by $\gamma_0$-dependent storage and loss moduli and $I_{3/1}$ was investigated for four volume fractions $\phi_{\text{eff}} = 0.614$, 0.62, 0.631 and 0.637. $I_{3/1}$ was found to scale quadratically with $\gamma_0$, therefore the intrinsic nonlinearity $Q_0$ could be determined. Péclet number (or angular frequency) dependent $Q_0$ curves, spanning a range of five decades, were compared to predictions of the mode coupling theory calculated by Rabea Seybold (TU Dresden). The predictions had been obtained by Seyboldt using a Taylor expansion of the density correlator $\Phi$, where the first nonlinear term gave rise to the occurrence of the 3rd harmonic in the resulting stress waves. In the MCT, $Q_0$ was found to scale quadratically with $Pe_\omega$ for very small $Pe_\omega$. This could neither be confirmed nor disproved since this range of $Pe_\omega$ was not accessible experimentally. At intermediate $Pe_\omega$, $Q_0$ is proportional to $Pe_\omega^b$ in the prediction, where $b \approx 0.69$. The experimental result for the exponents, however, were about half as large. The discrepancy might be related to an additional slow relaxation process that is not covered in the schematic MCT. Another possibility is that the available data does not extent to small enough $Pe_\omega$ to determine $b$ quantitatively. For large $Pe_\omega$, the MCT states that $Q_0$ ought to decrease proportional to $Pe_\omega^{-a}$ with $a = 0.32$. This could be confirmed, as the experimental exponents were around 0.3.

# Chapter 7

# Yielding of colloidal gels under Large Amplitude Oscillatory Shear

## 7.1 Introduction

Recently, LAOS measurements have been employed to investigate the yielding in attractive suspensions at moderate volume fractions. Oftentimes, a broadened or so-called "two-step" yielding process is observed, in which the transition from an initially linear, predominantly elastic behavior to viscous flow occurs in a strain amplitude range, that stretches over an order of magnitude or more (Chan and Mohraz 2012; Koumakis and Petekidis 2011; Laurati et al. 2011; Shao et al. 2013). More dilute gels, however, typically exhibit a distinct, unique yield point defined by a simultaneous maximum in the storage modulus, $G''$, and crossover of $G''$ with the loss modulus, $G'$ (Gibaud et al. 2010; Pignon et al. 1997). The two-step process of more concentrated gels is identified by two local maxima in either the strain amplitude dependency of the loss modulus, $G''(\gamma_0)$, or of the average elastic stress, $\sigma' = \gamma_0 G'(\gamma_0)$. Detailed measurements have shown that the strain amplitude at which the local maxima occur are relatively independent of the applied frequency of oscillation. The corresponding values of the stress and moduli, however, can be either frequency dependent or independent, depending on the specific material system (Koumakis and Petekidis 2011; Shao et al. 2013). In some studies, two separate maxima were not distinctly evident, but a rather broad yielding transition was reported (Hsiao et al. 2012; Rajaram and Mohraz 2011). Shao et al. (2013) showed that both behaviors, one-step and two-step yielding, can be found in the same system, depending on whether interparticle repulsions in a jammed suspension are present or screened by addition of salt.

The combination of rheology and (ultra) small angle neutron scattering (Rheo-USANS) allows direct measurement of the microstructural processes that underlie yielding at length scales ranging from one to thousands of primary particles (Porcar et al. 2011; Barker et al. 2005; Kim, Merger, et al. 2014). The LAOS measurements performed in the thesis in combination with Rheo-USANS experiments performed by Juntae Kim and Prof. Matthew E. Helgeson (University of Santa Barbara, California) were used to investigate whether

large-scale heterogeneity in colloidal gels is the fundamental cause for broadened yielding, as suggested by previous experiments from Helgeson et al. (2012). This chapter is essentially a reedited version of the joint paper (Kim, Merger, et al. 2014), therefore, the chapter contains passages and figures similar to the paper, which are not referenced each time.
The gel system under investigation is a well-characterized oil-in-water (O/W) nanoemulsion (Helgeson et al. 2012; Kim et al. 2013) that is gelled by a temperature-responsive bridging polymer, poly(ethylene glycol) diacrylate, in the continuous phase. The systems allows for careful control over interparticle attractions, including the process of gelation, so that it is possible to prepare gels with reproducible microstructure (Helgeson et al. 2012) without the need for shear rejuvenation that is required in many systems. Details on the preparation and characterization of the nanoemulsion system can be found in Section 8.1.4, page 143.

## 7.2 Linear viscoelastic properties and strain amplitude dependence of storage and loss moduli

The gel transition temperature ($T_{gel}$), that is when $G' \approx G''$, was found to be at 45°C. Detailed investigations of the gelation behavior of the system were made by (Helgeson et al. 2014; Helgeson et al. 2012). Their results showed that the so defined $T_{gel}$ is consistent with other measures of the gel point, including the criterion of Winter and Chambon, $G' \approx G'' \propto \omega^{1/2}$, (Chambon and Winter 1987) as well as the point at which the structure becomes percolated. Above $T_{gel}$, the sample exhibits solid-like viscoelasticity with a plateau modulus $G_p \approx 20$ kPa. For the frequency-dependent linear viscoelasticity above $T_{gel}$, a frequency sweep was performed at a fixed temperature of T = 48°C and strain amplitude of $\gamma_0 = 5{\cdot}10^{-3}$ (Fig. 7.1). The dynamic shear moduli depend only mildly on the frequency, in agreement with previous measurements (Helgeson et al. 2012).
The yielding behavior of the nanoemulsion gel was probed at T = 50°C using LAOS experiments at various strain amplitudes and angular frequencies. First the fundamental frequency Fourier coefficients, $G'$ and $G''$, which are displayed in Fig. 7.2, will be analyzed. The storage and loss moduli introduced in Chapter 2 are often used to describe the material's behavior even beyond the linear regime (Kyu et al. 2002). For strain amplitudes $\gamma_0 > 0.01$, $G'$ monotonically decreases from its linear plateau value and shows no frequency dependence within experimental variability. In contrast, $G''$ displays a distinct peak at $\gamma_0 \approx 0.03$. Therefore, according to Hyun et al. (Kyu et al. 2002), it can be classified as a "Type III" material, which displays a strain overshoot. A maximum in $G''$ is known as the "Payne Effect" in the rheology of filled elastomers, where this maximum is associated with bond breaking between load-bearing elements (Allegra et al. 2008). The peak position does not change significantly when the angular frequency is increased, whereas the peak height increases dramatically, as shown more clearly by normalizing $G''$ to its linear value $G''_0$ in Fig. 7.2 (intermediate frequencies have also been measured but are not displayed for clarity). The increasing peak height in $G''$ causes the crossover of $G'$ and $G''$, which is

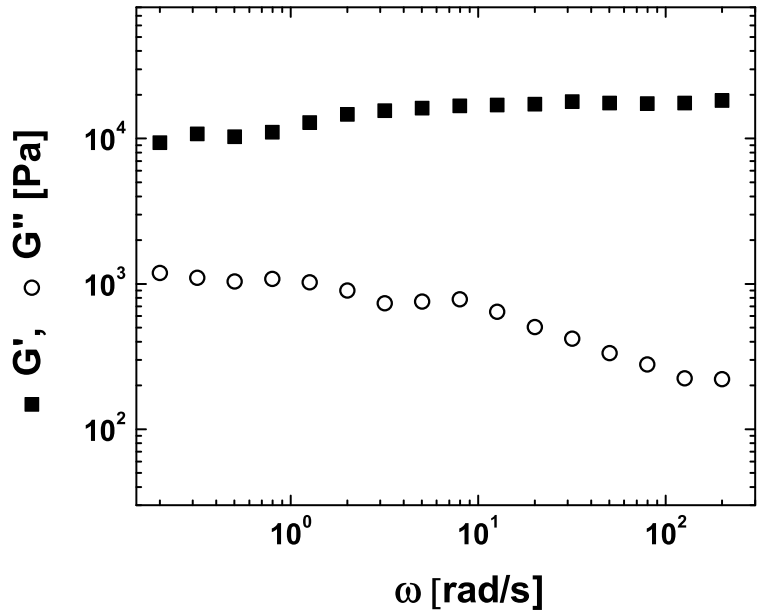


**Figure 7.1:** Frequency sweep of the nanoemulsion gel sample (Section 8.1.4, page 143) from 0.2 to 200 rad/s at 48°C at $\gamma_0 = 5{\cdot}10^{-3}$. The gelation temperature $T_{gel}$ was determined as 45°C.

often regarded as the onset of yielding, to occur at smaller strain amplitudes for increasing $\omega$. The peak heights and the cross-over strains amplitudes are summarized in Fig. 7.2 (c). Interestingly, the observed trend in the peak height is opposite to that reported for glassy microgel suspensions with effective interparticle attractions (Shao et al. 2013), suggesting a qualitatively different yielding behavior.

Three different regimes of yielding, meaning a transition from predominantly elastic behavior of the gel at $\gamma_0$ to viscous flow at large $\gamma_0$, are defined based on the waveform analysis of the nonlinear response (to be discussed subsequently). This definition will aid in the presentation and analysis of the scattering data to follow (Section 7.5). Although the borders of the regions have been defined based on waveform parameters they coincide with characteristic features of $G'$ and $G''$. In Region I, $G'$ exhibits a modest decrease from its value in the linear viscoelastic regime (LVR for the gel is where $I_{3/1} < 5 \cdot 10^{-3}$), whereas $G''$ increases significantly toward its peak value. Region II begins at the maximum in $G''$, and continues through the crossover strain amplitude, ultimately asymptoting to power law behavior of $G'$ and $G''$ with increasing strain amplitude. In Region III, the power law slope of $G''$ exhibits an observable decrease.

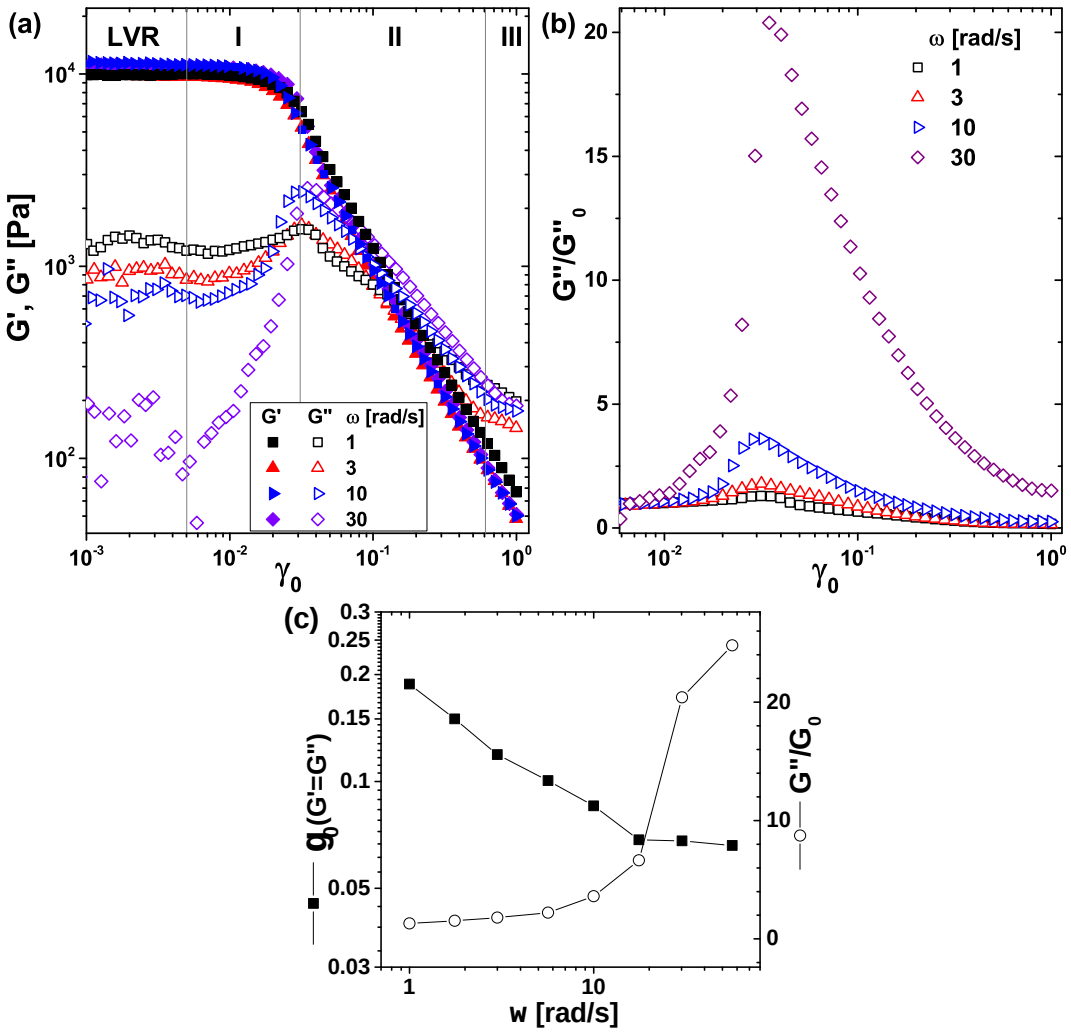


**Figure 7.2:** (a) Strain amplitude dependence of storage and loss moduli at various angular frequencies of deformation, measured at T = 50°C. Lines indicate the linear viscoelastic regime (LVR, for the gel it is where $I_{3/1} < 5 \cdot 10^{-3}$)) and different regions of the yielding stages that will be discussed in Section 7.7. In Region I, $G'$ exhibits a modest decrease from its value in the LVR , whereas $G''$ increases significantly toward its peak value. Region II begins at the maximum in $G''$, and continues through the crossover strain amplitude, ultimately asymptoting to power law behavior of $G'$ and $G''$ with increasing strain amplitude. In Region III, the power law slope of $G''$ exhibits an observable decrease. (b) Increasing peak height in the $G''$ curve with increasing angular frequency as shown by the loss modulus normalized to the plateau value of the linear regime $G''_0$. (c) Cross-over strain amplitudes of $G'$ and $G''$ and normalized peak heights of $G''$ as a function of the angular frequency.

## 7.3 Lissajous curves

In order to gain more insight into the intracycle LAOS behavior of the gel, strain vs stress curves, so called Lissajous figures are analyzed. In Fig. 7.3 an overview of normalized strain vs stress curves of the measurements in Fig. 7.2 (a) is depicted in the form of a Pipkin plot ($\omega$ vs $\gamma_0$).

For small $\omega$ vs $\gamma_0$ the curves are regular ellipses, which means that the sample response is in the linear viscoelastic regime. However, increasing $\gamma_0$ at a fixed value of $\omega$ leads to a qualitative change, where the waveform transforms from a simple ellipse, to a complex nonlinear shape. This transition also reflected in the viscoelastic moduli in Fig. 7.2 (a) by the strong increase of $G''$. Upon further increasing $\gamma_0$ distinct features develop in the Lissajous curves, which persist qualitatively throughout the course of the ongoing strain amplitude sweep (constant $\omega$, increasing $\gamma_0$). These include an approximately linear region after the reversal of shear direction and a local maximum in the instantaneous stress in the upper left quadrant of the elastic representation.

In Fig. 7.4 (a) the stress response is plotted as a function of strain. Note that from now on all strain axes have been rescaled by the value of the strain amplitude where $G''$ is at its maximum ($\gamma_r = \gamma/0.0322$), in order to be able to correlate this data to the data of the sample on which the SANS measurements have been performed (for details see Kim, Merger, et al. (2014)).

The distinct non-ellipsoidal waveforms can be interpreted using the sequence of physical processes approach following Rogers et al. (2011b): Starting at the point where the flow direction is reversed ($\gamma/\gamma_0 = \pm 1$, circle symbol in Fig . 7.4 a) the gel network of agglomerated droplets is strained, and the material initially behaves elastically and therefore the stress increases linearly with the accumulated strain. After the initial linear region, the stress continues to increase until a strain equal to $\gamma_c$ has been accumulated (broken gray line), where it shows a local maximum $\sigma_c$ (diamond symbol in Fig . 7.4 a). This overshoot in the stress curve is due to yielding of the gel network, and afterwards the sample begins to flow. The stress subsequently decreases with further increasing shear rate until a minimum is reached. With further increasing strain, the stress begins to increase again, suggesting thixotropic behavior where the structure gradually rebuilds as the shear rate is decreasing. This continues until the end of the half-cycle ($\gamma = +\gamma_0, \dot{\gamma} = 0$), and subsequently the sequence is repeated in the opposite direction.

The extracted waveform parameters include the residual modulus $G_R$, yield strain $\gamma_c$ and yield stress $\sigma_c$, as well as the instantaneous viscosity $\eta_L$ at peak shear rate, that were introduced in Section 2.2.3, page 35. These parameters show strain amplitude dependencies which are displayed in Fig. 7.4 b, c and d and have been used to define four different regions throughout the strain amplitude sweep experiment. In Section 7.6, these regions will aid the correlation of the nonlinear rheological parameters with the structural parameters from neutron scattering experiments performed by Juntae Kim and Prof. Matthew E. Helgeson.

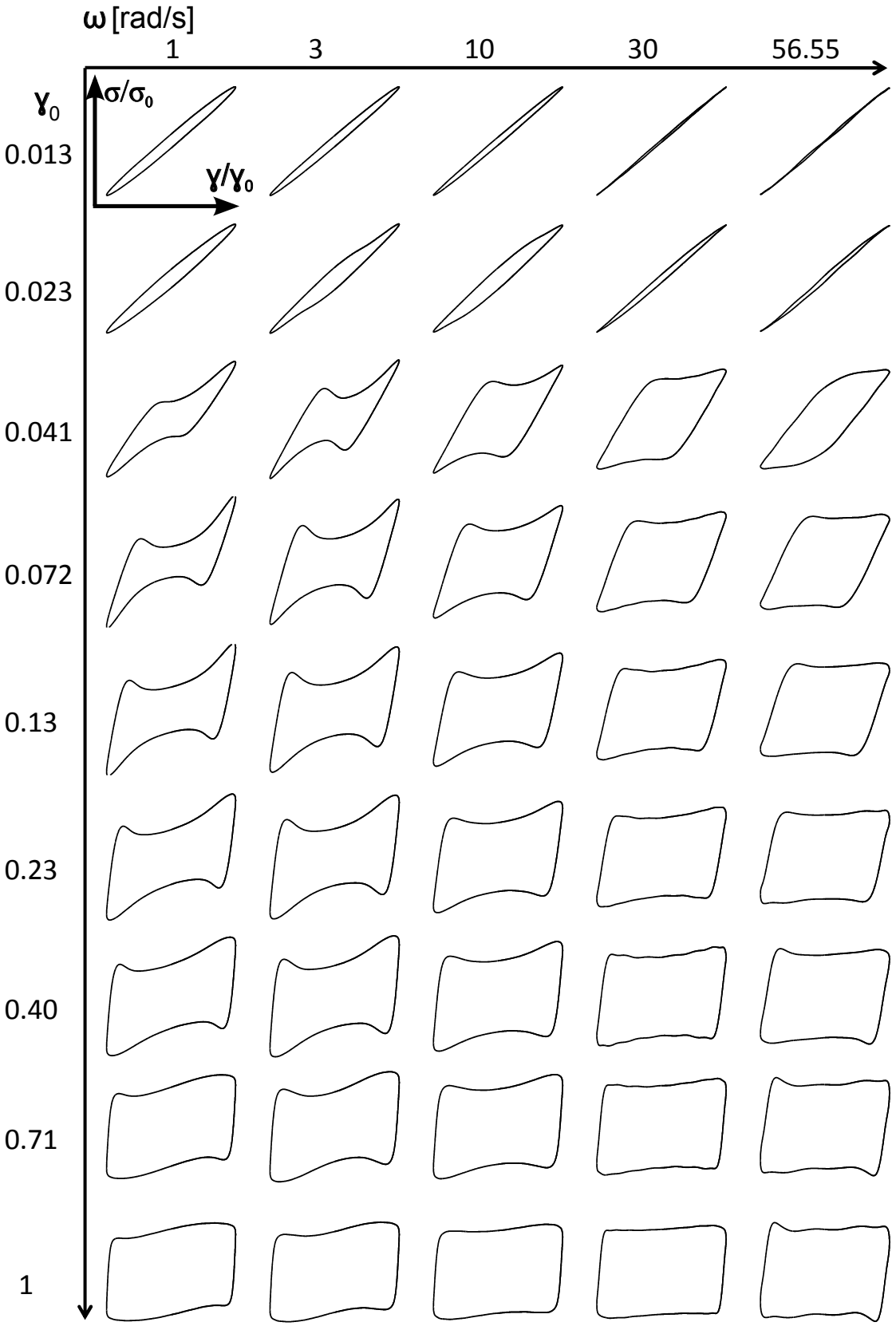


**Figure 7.3:** Selected normalized stress vs strain curves of the measurements in Fig. 7.2 (a), arranged in the Pipkin space ($\omega$ vs $\gamma_0$).

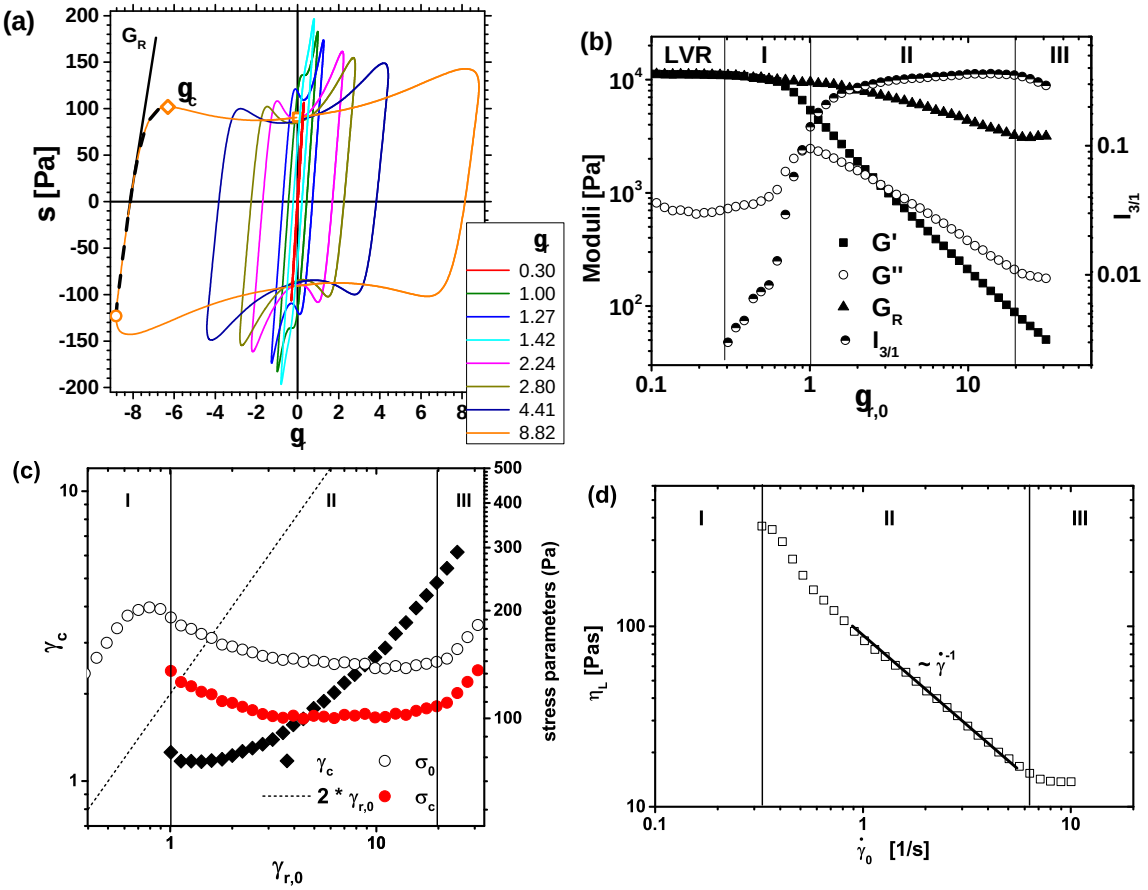


**Figure 7.4:** (a) selected elastic Lissajous plots of a LAOS experiment on a nanoemulsion sample containing a volume fraction of $\phi = 0.33$ PDMS ($\eta_s$ = 5mPas at 25°C ) droplets (radius 21 nm) in an aqueous continuous phase with 33 vol.-% PEGDA ($M_n$ = 700 g/mol) and $c_s$= 230 mM SDS at $\omega = 10$ rad/s. The circle and diamond symbols show the points at flow reversal ($\gamma_r$ = - $\gamma_{r,0}$ and $\dot{\gamma}$= 0) and the following local stress maximum, respectively. The broken black line illustrates the accumulated strain $\gamma_c$ that is necessary to yield the material. The black tangent represents the residual modulus after yielding $G_R$ (equals d$\sigma$/d$\gamma$ at $\sigma = 0$). (b) Residual modulus $G_R$ (equals $\frac{d\sigma}{d\gamma}|_{\sigma=0}$) together with the storage and loss modulus at $\omega$ = 10 rad/s and the relative intensity of the 3rd harmonic $I_{3/1}$. (c) Nonlinear yielding parameters extracted from the waveform data of the LAOS measurements: $\gamma_c$ represents the strain that has been accumulated between the point of flow reversal (circle symbol) and the local stress maximum (diamond) in (a), $\sigma_c$ is the corresponding stress value which is plotted with the stress amplitude $\sigma_0$ as reported by the rheometer software. (d) Instantaneous viscosity at the point of zero strain and maximum shear rate (square symbol), $\eta_L$, as a function of increasing shear rate amplitude. All strain axes have been rescaled by the value of the strain amplitude at which $G''$ is at its maximum ($\gamma_r = \gamma/0.0322$), in order to be able to correlate this data to the data of the sample on which the SANS measurements have been performed.

## 7.4 Time dependent moduli

Based on the work of Rogers (2012), the intracycle yielding is elucidated further by calculating the instantaneous storage $R'(t)$ and loss $R''(t)$ moduli. $R'(t)$ and $R''(t)$ are projections of the binormal vector in a 3D Lissajous plot (stress vs. strain vs. strain rate) onto the strain-stress and shear rate-stress plane. More details can be found in Chapter 2, page 36. These measures can be interpreted as time-dependent analogues of $G'$ and $G''$ and are defined for every point of the response orbit. For brevity the time argument in $R'(t)$ and $R''(t)$ will be omitted and time dependence is implied. Figure 7.5 shows $R'$ and $R''$ for the strain amplitude sweep at $\omega = 10$ rad/s are displayed as surfaces. If viewed in the $R'$, $R''$ versus strain amplitude projection, Fig. 7.5. is reminiscent of the standard representation of a dynamic strain amplitude sweep as in Fig. 7.2 a. In the LVR, $R'$ and $R''$ are constant in time and equal $G'$ and $G''$, respectively. As the strain amplitude increases (moving from the back to the front in Fig. 7.5), the response becomes nonlinear and distinct features develop in the time dependence of both surfaces. Looking at the time dependence at a fixed strain amplitude, the sequence of physical processes that was described previously is evident. However, this analysis reveals additional details about the intracycle yielding that were not evident from the waveform analysis, where yielding was assumed to occur at a single point where the stress shows an overshoot.

The fully nonlinear material behavior can be observed by tracing the intracycle response at a fixed strain amplitude of $\gamma_{r,0} = 0.1$. The starting point of the sequence of processes (i.e. at the point of flow reversal), corresponds in this representation to $t/t_0 = 0.25$ or 0.75. Starting from this point in time, elastic straining is first observed, where $R' > R''$ and both moduli are roughly constant in time. As the cycle proceeds, this gives way to a small region in which $R'$ increases (i.e., strain stiffening occurs). The maximum value of $R'$ for each strain amplitude is larger than $G_R$ by about 30% but has the same strain amplitude dependence. Therefore, only $G_R$ will be used subsequently for the correlation with the scattering data. Shortly after the maximum in $R'$, it abruptly decreases (i.e., strain softening occurs) and $R''$ abruptly increases, until eventually $R''$ exceeds $R'$. Since this portion of the cycle still corresponds to strains in the region of the waveform where the stress is increasing approximately linearly with strain, this behavior is attributed to elastoplastic behavior, in which the deformation is first dominated by softening ($R' > R''$), followed by viscoplastic behavior ($R'' > R'$). After this, a pronounced maximum in $R''$ is observed, which corresponds closely (though not exactly) with the stress maximum in the Lissajous curves used previously to define the yield stress and strain (yellow line in Fig. 7.5). At this point, the material has yielded and begins to flow. Subsequently, both $R'$ and $R''$ decrease dramatically, indicating shear thinning, after which rejuvenation of the structure can be observed as a second crossover in $R'$ and $R''$ that occurs at $t/t_0 < 0.75$, before the end of the half-cycle.

Using the prominent features of the $R'$ and $R''$ landscapes in Fig. 7.5 and the position of the yield point from Fig. 7.4 a), a "phase plot" for the yielding process is produced in Fig.

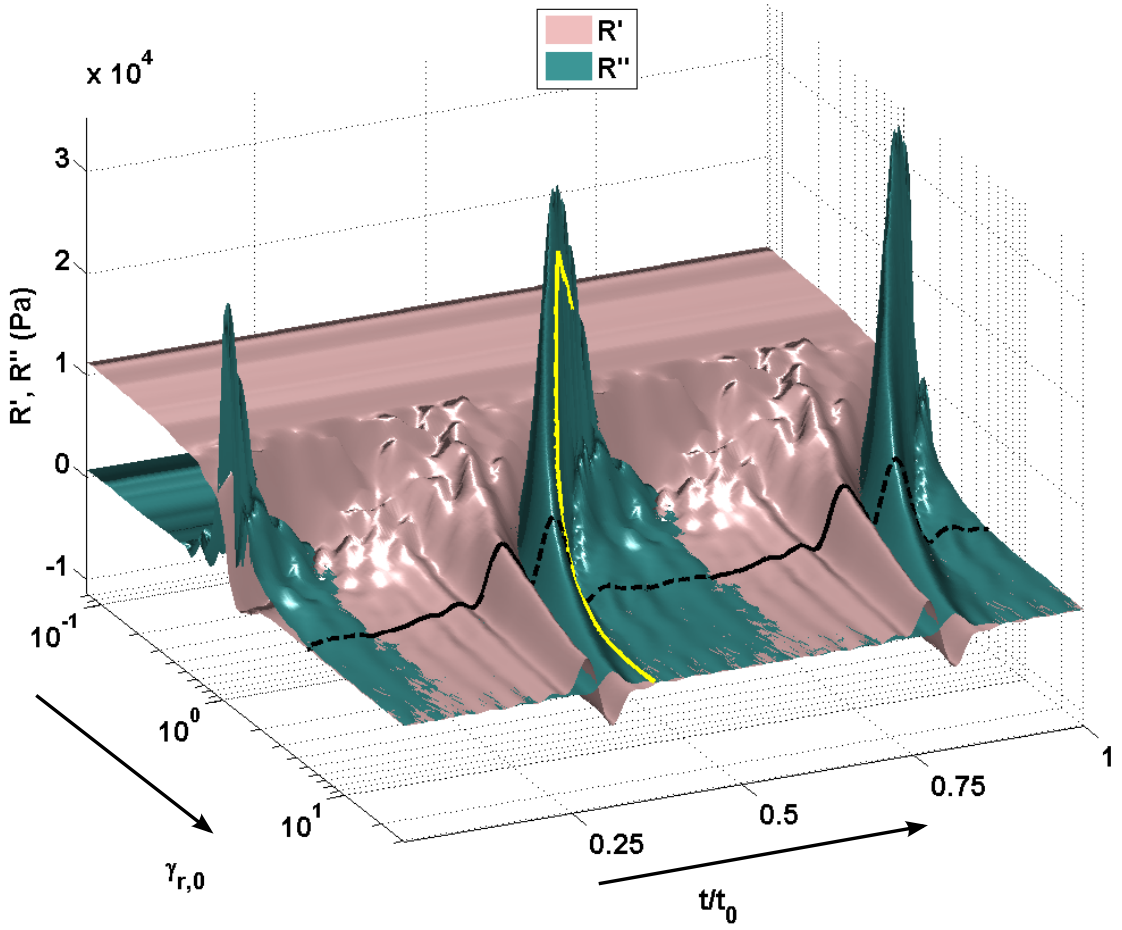


**Figure 7.5:** Surface plot of the instantaneous moduli $R'(t)$ and $R''(t)$ as a function of reduced strain amplitude $\gamma_{r,0}$ and normalized time throughout the oscillation cycle for a fixed frequency of 10 rad/s. A single LAOS cycle corresponds to a portion of the surface at fixed reduced strain amplitude, $\gamma_{r,0}$ and increasing time, $t/t_0$, where $t_0$ is the duration of one cycle. This is indicated by the black line for $\gamma_{r,0} = 5$ (solid line for $R' > R''$ and broken line for $R' < R''$). The yellow line shows the yield point intercycle as determined from the local maximum in the Lissajous curve (diamond symbol in Fig. 7.4).

7.6 in a space of the normalized instantaneous strain (a) or strain rate (b), which represent the time within a cycle, and strain amplitude. Lines have been drawn that represent the various features of $R'$ and $R''$, including the initial maximum in $R'$, followed by the crossover where $R'$=$R''$, and finally the maximum in $R''$. Also shown is the yield point defined by the stress maximum extracted from the Lissajous curves (diamond symbol in Fig. 7.4). The regions in between these curves thus show the boundaries in a nonlinear deformation space between elastic straining (A), elastoplastic softening (B), viscoplastic behavior (C), yielding (D) and flow (E). Note that after yielding only flow and restructuring are present as the shear rate decreases back to zero, and therefore the aforementioned transitions do not occur in the reverse direction. Accordingly, Fig. 7.6 is not a true phase plot as all borders indicate "one-way" transitions. The filled symbols represent borders for the path from $\gamma/\gamma_0$ = - 1 to $\gamma/\gamma_0 = 0$, whereas open symbols show borders for the path from $\gamma/\gamma_0 = 1$ to $\gamma/\gamma_0 = 0$.

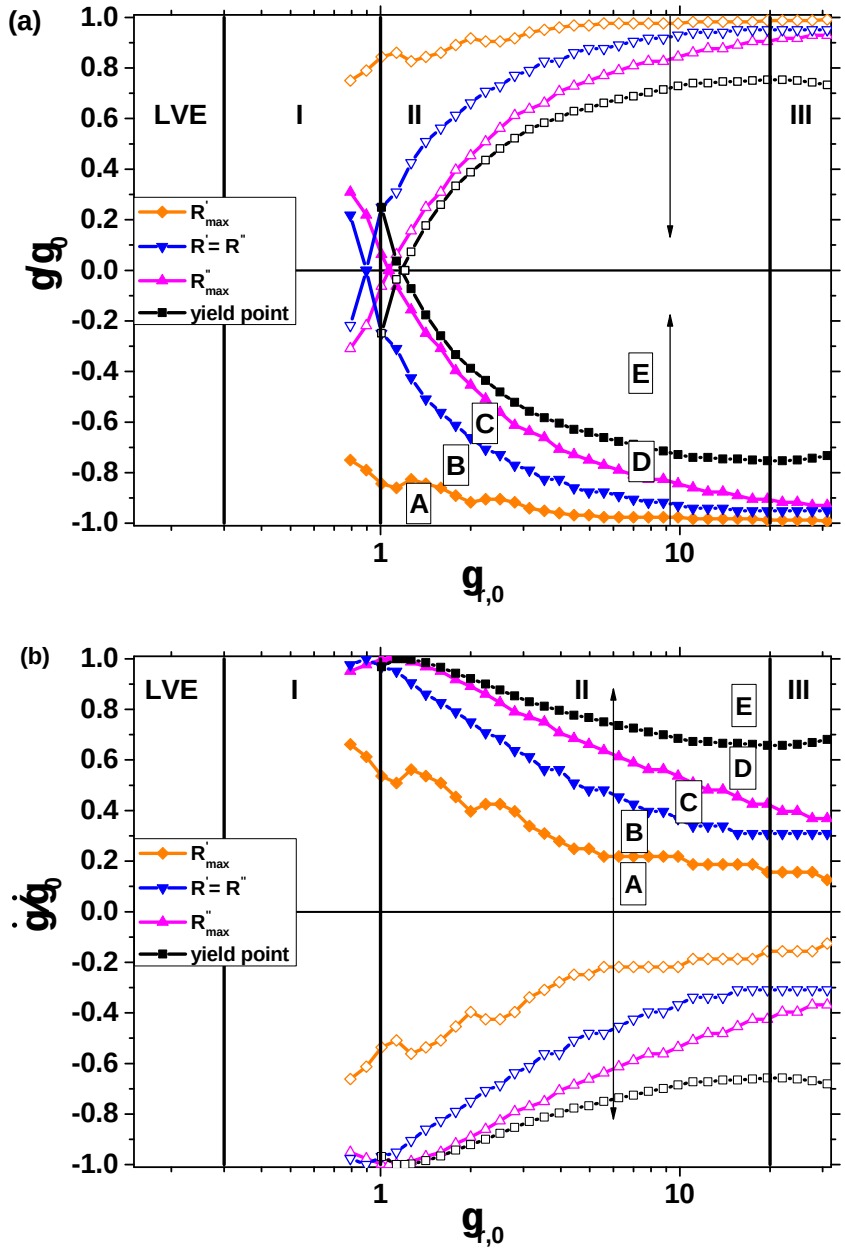


**Figure 7.6:** Phase plot constructed using the various nonlinear parameters from the waveform analysis in the (a) elastic and (b) viscous representations, respectively. Starting from $\gamma/\gamma_0 = 1$ or -1 ($\dot{\gamma}/\dot{\gamma}_0 = 0$) the material's response changes following the arrow through a series of elastic (A), elastoplastic softening (B), viscoplastic responses (C), yielding (D), and finally flow (E). Note that after yielding only flow und restructuring is present, therefore these transitions do not occur in the reverse direction as the shear rate is reduced to zero. Filled symbols represent borders for the path from $\gamma/\gamma_0 = -1$ to $\gamma/\gamma_0 = 0$, and open symbols show borders for the path $\gamma/\gamma_0 = 1$ to $\gamma/\gamma_0 = 0$.

Both the surface plots in Fig. 7.5 and the borders in Fig. 7.6 show that with increasing strain amplitude, the portion of the cycle where the material is yielded (both in time and in shear rate dimension) increases. This supports the idea that information averaged over the entire oscillation cycle with increasing strain amplitude, such as the time-averaged neutron scattering data to follow, increasingly reflects the yielded state. This is shown in

Fig. 7.6 by overlaying the boundaries of Regions I, II and III obtained from intercycle analysis of the waveforms (vertical lines) with the phase plot obtained from intracycle analysis. Doing so, shows that Region I is dominated entirely by elastoplastic softening of the gel network, i.e. the entire cycle is spent in phases A and B. In Region II, the behavior transitions from becoming elastically-dominated to viscous-dominated with increasing strain amplitude, i.e., the fraction of the cycle spent in the flowing state increases with increasing strain amplitude. Finally, in Region III, the fraction of each cycle spent in flow becomes insensitive to the applied strain amplitude.

## 7.5 Scattering under LAOS

Prof. Matthew E. Helgeson and Juntae Kim performed experiments where Small Angle Neutron Scattering (SANS) and Ultra Small Angle Neutron Scattering (USANS) experiments were combined in-situ with oscillatory excitation to probe the gels structure under LAOS. Specifications of the Rheo-SANS setup have been published by Porcar et al. (2011). The specific batch of the nanoemulsion that was used in the Rheo-SANS investigation had nominally the same composition as the batch used for the ex-situ LAOS experiments (Chapter 8.1.4, page 143). Despite the identical composition, deviations in the absolute values of the moduli of approximately 30% were found. The deviations can be explained by a high sensitivity of the moduli to the droplet size distribution (Helgeson et al. 2012). Some variation on the droplet size distribution is unavoidable in the high pressure homogenization process that was used for the preparation of the emulsions. Specifically, the Rheo-SANS batch had an average droplet radius of 17.5 nm which is smaller than the radius of 23 nm for the batch in the ex-situ LAOS experiment. This resulted in $G'$ values of $\approx$ 16 kPa for Rheo-SANS batch in the LVR whereas the ex-situ LAOS batch had $G'$ values of $\approx$ 12 kPa at $\omega = 10$ rad/s (Fig. 7.2). The batch to batch variation led furthermore to a difference of the strain amplitude at which $G''$ has its maximum. This was accounted for by rescaling the respective strain axes to the specific $\gamma_0(G' = G'')$ at $\omega = 10$ rad/s of the Rheo-SANS batch and the ex-situ LAOS batch (Kim, Merger, et al. 2014).
In order to extract structural information from the SANS/USANS spectra (Fig. 7.7 (a)), Helgeson and Kim fitted a model according to Eq. 7.1 to the data.

$$\begin{aligned} I(q) - I_b = \frac{K_1 \xi_{c1}^3}{(1 + (q\xi_{c1})^2)^2} + \frac{K_2\left[\frac{\xi_{c2}}{1+(q-\beta_{max})^2\xi_{c2}^2} - \frac{\xi_{c2}}{1+(q+\beta_{max})^2\xi_{c2}^2}\right]}{\beta_{max} q} \\ + \frac{K_3 \sin[(d_m - d_s + 2)\arctan(\xi_s q)]}{(\xi_s q)[1 + (\xi_s q)^2]^{\frac{d_m - d_s + 2}{2}}} + \frac{K_4 \sin[(d_m - 1)\arctan(\xi_m q)]}{(d_m - 1)(\xi_m q)[1 + (\xi_m q)^2]^{\frac{d_m - 1}{2}}} \end{aligned} \tag{7.1}$$

In contrast to a simple fractal scattering model as outlined in Chapter 3, page 48, Eq. 7.1 comprises four terms that capture the scattering in the various ranges of $q$. At low $q$, the first term, weighed by its intensity $K_1$, is a two-phase Debye-Bueche model (Debye and Bueche 1949) that describes large-scale voids, where $\xi_{c1}$ is their correlation length. The main structural feature of the spectra in Fig. 7.7 (a) is the local maximum around

$qr \approx 0.04$. This maximum is interpreted as a signature of a phase separated system, where the two phases are a droplet rich and a droplet lean phase (Helgeson et al. 2014). The scattering around the maximum is captured by a sum of two Lorentzian terms, weighed by $K_2$, corresponding to correlated density inhomogeneities consistent with phase separation under the Cahn-Hilliard model for spinodal decomposition (Li and Ross 1994). In this term the important parameter is $\beta_{max}$, since its inverse $\beta_{max}^{-1}$ gives a characteristic length scale for the phase separation. The description of the heterogeneous structure as a two phase system is similar to models for structures of demixing quenched binary systems, such as alloys (Gaulin and Spooner 1987) or mixtures of liquids (Gaulin and Spooner 1987). The last two terms with their respective intensities $K_3$ and $K_4$ correspond to a model of combined surface and mass fractal scattering (Wong and Cao 1992), therefore they are similar to Eq. 3.18 in Chapter 3. The relevant parameters are the fractal dimensions of the mass and the surface fractal, $d_m$ and $d_s$, respectively and the corresponding cut-off sizes $\xi_m$ and $\xi_s$. Note that the higher-q scattering due to individual droplets (form factor $P(q)$) was not included. From the multitude of parameters that were published in (Kim, Merger, et al. 2014) only the most relevant are shown in Figures 7.7 (b) and (c). The specific surface of the voids $\Sigma$ is derived from a model-independent asymptotic analysis in the low q limit using Eq. 7.2 (Spalla et al. 2003). This alternative analysis was necessary because the determined void correlation lengths $\xi_{c1}$ were unphysically large (several hunded $\mu$m) due to the absence of any shoulder or plateau in the extremely low-$q$ scattering (Kim, Merger, et al. 2014). In Eq. 7.2, $\Delta\rho$ denotes the difference in scattering density between the void phase (assumed to contain no droplets) and the droplet-rich region. Furthermore, the characteristic length scale of the microphase separation $2\pi/\beta_{max}$ and $\xi_{c2}\beta_{max}$, which is a measure for the peak sharpness, are shown in 7.7 (c).

$$\Sigma = \frac{\lim_{q\to 0} I(q)q^4}{2\pi(\Delta\rho)^2} \tag{7.2}$$

The combined rheo-SANS/USANS measurements (Fig. 7.4 and 7.7) suggest that, as the intracycle mechanical response becomes progressively more dominated by the yielded and flowing states, the microstructure of the gel evolves at progressively smaller length scales (Fig. 7.8). Due to the time-averaged nature of the SANS/USANS measurements, the changes in microstructure observed with increasing strain amplitude represent a moving average over the various dynamic stages of nonlinear behavior. As such, the amount of time per cycle spent in the yielded state will increase with increasing strain amplitude, and thus the measured time-average microstructure will evolve toward the fully flowing state. Therefore, in what follows, it is assumed that the contribution of each of the instantaneous microstructural processes to the overall, time-averaged scattering is proportional to the time per cycle spent in a particular stage of nonlinear behavior.

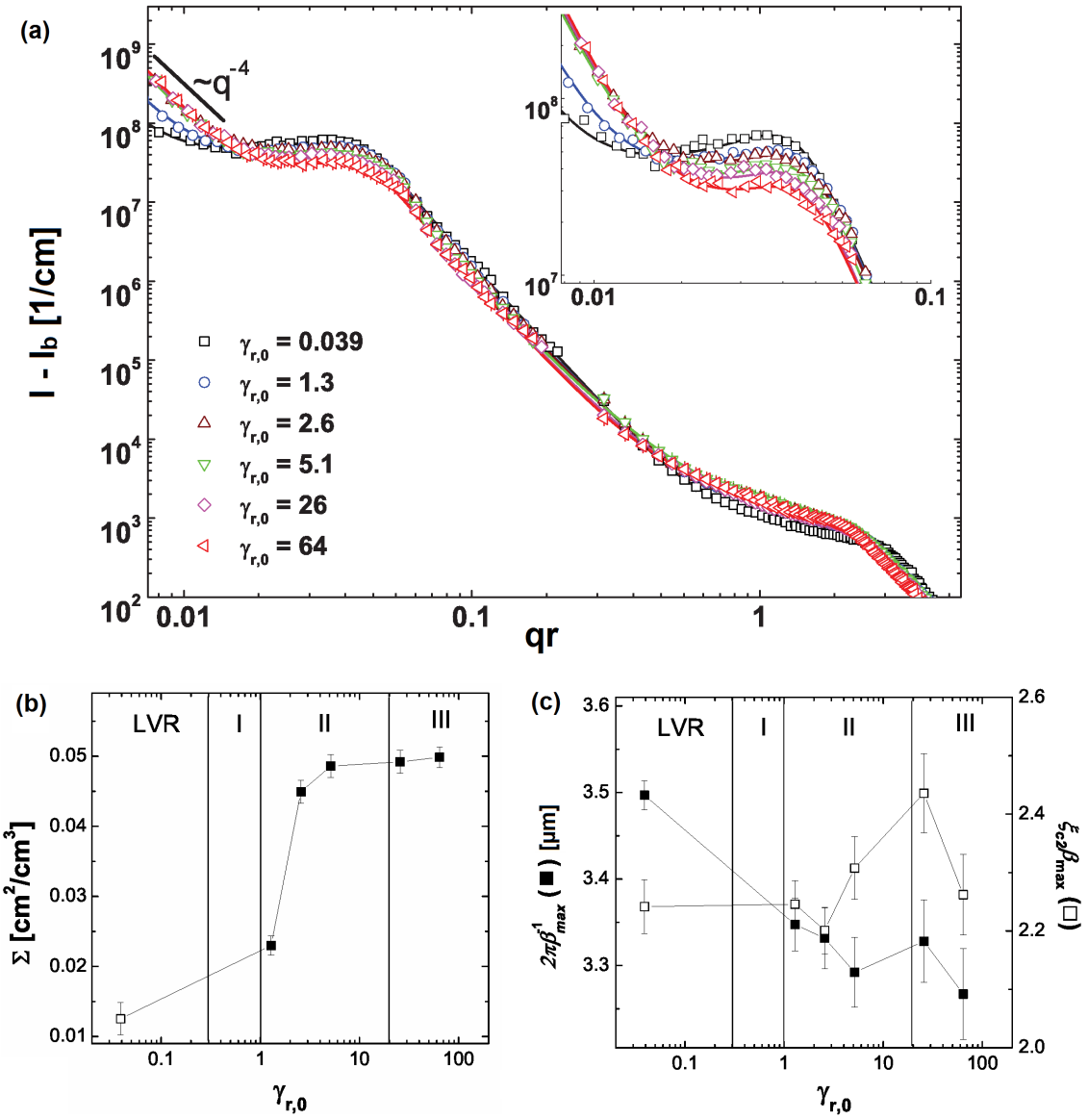


**Figure 7.7:** Combined rheo-USANS and SANS spectra of a nanoemulsion sample containing $\phi = 0.33$ PDMS droplets with P = 0.33 PEGDA and $C_s$= 230 mM SDS in 50/50 (v/v) $H_2O/D_2O$ at the indicated rescaled strain amplitudes. Lines are fits to equation 7.1. Inset: Magnification of low-q portion of USANS data with model fitting. (a) Specific surface area from asymptotic analysis at very low q. (b) Characteristic length scale of the microphase separation (closed squares) and the peak sharpness (open squares) from the model.

## 7.6 Yielding mechanism

The combination of LAOS measurements and neutron scattering allows to propose a mechanism for the yielding behavior of the investigated heterogeneous gel. This and the next section have been reproduced from the joint publication (Kim, Merger, et al. 2014) without much rephrasing, therefore major parts have been originally written by Prof. Helgeson and Juntae Kim. The mechanism is depicted schematically in Fig. 7.8.

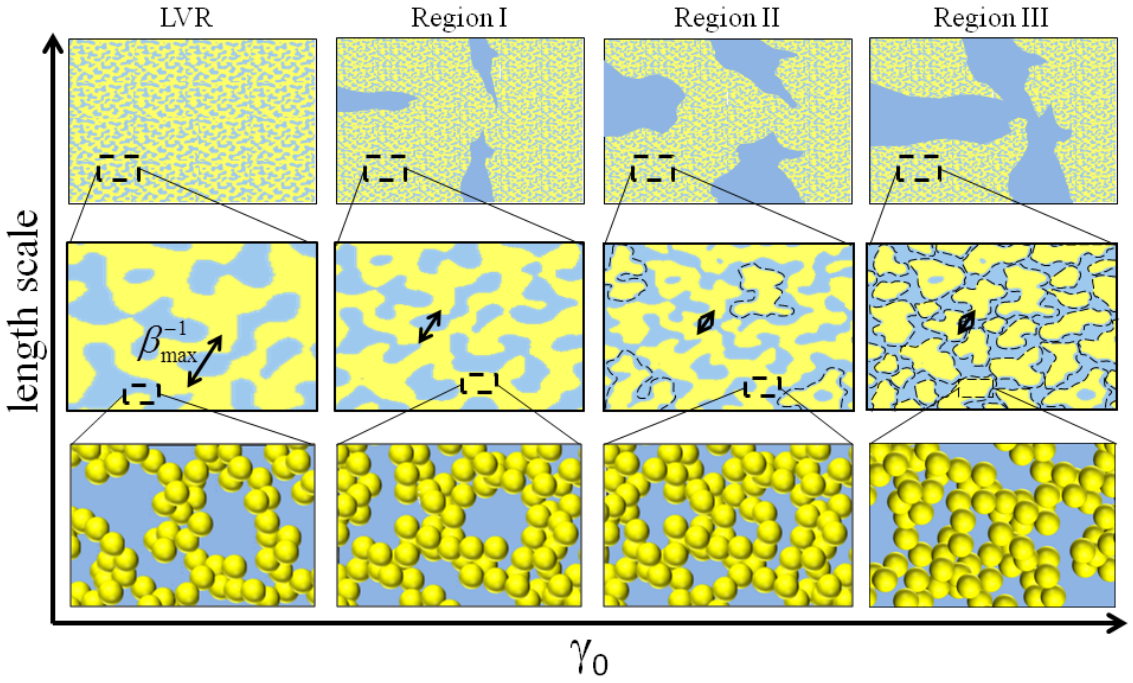


**Figure 7.8:** Schematic of gel microstructure through the yielding transition. (bottom panel) Fractal clusters of droplets (yellow) with diameter D. (middle panel) Bicontinuous network structure consisting of droplet-lean (blue) and droplet-rich (yellow) domains on the length scale of 10-100 times the droplet diameter. (top panel) Macroscopic structure at a length scale of 100-1000 times the droplet diameter, adapted from Kim, Merger, et al. (2014).

In the linear regime, the quiescent microstructure is comprised of a bicontinuous network of droplet-lean "pores" and droplet-rich network strands (middle panel), the latter of which are comprised of fractal clusters of droplets (bottom panel). The bicontinuous structure exhibits a domain size proportional to $1/\beta_{max}$. Upon increasing the strain amplitude into the nonlinear regime, nonlinear deformation causes compression of the network due to compressibility of the droplet-rich domains. This results in the formation of voids, quantified by their specific surface $\Sigma$, at length scales significantly larger than the domain size (top panel). This is evident by the significant low q scattering that develops in Region I, which then saturates in Region II. Such voids are reminiscent of those observed in other gelling systems after yielding under startup of steady shear (Rajaram and Mohraz 2011), and could be a pre-cursor for the shear-induced macroscopic heterogeneities that subsequently develop at large strains. In order to conserve the overall density of droplets, these voids must form at the expense of the bicontinuous structure, resulting in compression of the

network and a decrease in $2\pi/\beta_{max}$ (middle panel). This requires significant compression of the fractal droplet-rich domains relative to the droplet-lean domains (Fig. 7.7 c), which in turn requires yielding of the dense phase. As the strain amplitude is increased further, the compression of the dense network becomes increasingly difficult, resulting in eventual saturation of both the voids as measured by $\Sigma$ and the domain size $2\pi/\beta_{max}$ in Region II. Once the void structures saturate, additional strain input becomes sufficient to rupture the effective "bonds" between network strands, producing discrete agglomerates of fractal clusters (middle panel, dotted lines in Fig. 7.8). The primary signature of this process is the observed increase in the sharpness of the distribution of domain sizes, given by the product $\xi_{c2}\beta_{max}$. This occurs because the most likely size of an agglomerate formed by rupturing of the bicontinuous network will have a characteristic size given by the characteristic domain size. As such, any irregular network strands will be annealed into smaller, disconnected domains with an average size given by $1/\beta_{max}$. This concept could be viewed as similar to that put forth by Hsiao et al. (2012), who proposed that the yielding of shear-rejuvenated colloidal gels under step strain was dominated by the rupture of weak network contacts with a small average contact number. However, it should be noted that in nanoemulsion gel it is rupture of contacts between network strands, rather than individual particles, that is responsible for yielding.

Eventually, at a critically high strain amplitude, enough bonds between domains will be ruptured in order to compromise the integrity of the network, resulting in (on average) a suspension of disconnected domains with a relatively narrow size distribution around $1/\beta_{max}$, similar to what has been observed on colloidal gels at much larger strains after yielding is complete (Rajaram and Mohraz 2011). It is notable that the peak sharpness $\xi_{c2}\beta_{max}$ exhibits a maximum precisely at the onset of Region III, suggesting that the distribution of domain sizes is most homogeneous at the final transition to flow. Previously, a similar maximum during the incipient gelation of bicontinuous nanoemulsion gels was observed that corresponded precisely with the critical gel point measured by rheology Helgeson et al. (2014).

Helgeson et al. (2014) hypothesized that such a maximum in homogeneity is a distinct signature of percolation of heterogeneous gels, and similar observations have been made in other gelling colloidal systems exhibiting phase separated microstructure (Laurati et al. 2011). It is thus tempting to consider that the final stage of yielding in the present study arises from "de-percolation" of the bicontinous gel network into a suspension of disconnected clusters. However, there is the possibility that this common signature, i.e., of a maximum in homogeneity of the network at both the critical gel point and the critical yield point, is merely a coincidence.

Again, it is important to clarify that the preceding is a time-averaged description of the gel microstructure, which is averaged over the sequence of processes (elastic straining, yielding, flow and recovery) comprising one LAOS cycle. In reality, it is reasonable to expect that the intracycle structure will exhibit a continuous transition between the various average microstructures depicted in Regions I-III. Indeed, this will be explicitly considered to be

true in order to rationalize the observed time-dependent nonlinear mechanical response with the observed time-averaged microstructure in what follows.

## 7.7 Relation between microstructure and nonlinear mechanical response

The LAOS measurements have identified three distinct regimes of yielding in heterogeneous colloidal gels, where three qualitatively different intracycle responses are observed. In the following a comprehensive scenario is presented, by which the time-averaged microstructures observed for each of these regions can be reconciled with the nonlinear mechanical signatures observed during LAOS. It is stressed again that this scenario implicitly assumes that the time-averaged microstructure can be seen as a convolution of the instantaneous microstructures during the various intracycle processes (the elastic strain softening, viscoplastic behavior, yielding and flow). As such, in Region I the observed microstructure is dominated by an elastic response, in Region II it evolves from primarily structures dominated by elastoplastic behavior to structures dominated by flow, and finally in Region III it is dominated by flow.

- **Linear viscoelastic region ($\gamma_{r,0} < 0.16$)**

  At sufficiently small strain amplitudes the network structure of the material is only slightly perturbed by the shear forces, such that the gel network remains intact and the imposed strain produces a linear, predominantly elastic stress response, as can be seen by the storage modulus being over an order of magnitude higher than the loss modulus.

- **Region I: onset of nonlinearity and pre-yielding ($0.3 < \gamma_{r,0} < 1$)**

  In this regime, it is the internal rupture and reconfiguration of bonds between clusters within the dense domains (ultimately resulting in compression of the gel network) that weakens the elastic network due to nonlinear plastic deformation, resulting in intracycle strain softening. This is evidenced by a moderate decrease in $G_R$ from its plateau value. Furthermore, $G''$ and $I_{3/1}$ increase strongly with increasing strain amplitude in this regime, signaling the onset of nonlinear behavior, as visible distortions of the waveform from its elliptical shape appear. Moreover, the compression of the dense domains requires the expulsion and drainage of interstitial fluid within the fractal microstructure in order to create additional large voids. This fluid motion causes a strong increase in the dissipated energy, which is evident in both the significant increase in $G''$ as well as the development of significant viscous behavior in the nonlinear waveform. The structural changes which are responsible for the nonlinear mechanical behavior of the gel mark this part of the strain sweep as a transition region to the highly nonlinear region II. It is also in this region that the strain dependent moduli $G'(\gamma_0)$ and $G''(\gamma_0)$ and all other nonlinear parameters

become time dependent. This time dependence is due to a non quasi-static stress signal (see Chapter 8, page 150).

- **Region II: broad yielding transition ($1 < \gamma_{r,0} < 20$)**

  In this region the most important yielding process occurs: the large-scale, dense domains of fractal agglomerates are compressed even stronger than in Region I as evident from a decrease in $1/\beta_{max}$ (Fig. 7.7 c). As the network structure is gradually disintegrated by the breakup of large dense domains during flow, the number of elastic junctions in the percolated structure that can be reformed at the end of a half-cycle is decreasing. This has severe consequences for the rheological properties. Due to the decreasing number of elastic junctions, the amount of elastic strain that the material can accumulate within the oscillation cycle is increasing slower than the applied strain amplitude. This is reflected in a sublinear increase of the yield strain (Fig. 7.4 c). In addition the residual modulus $G_R$ decreases markedly, proving a drastic weakening of the reversible network. In the flowing portion of the cycle, a shear rate amplitude dependent thinning behavior is observed that is caused by the breakage of larger dense domains into smaller ones, resulting in the thixotropic behavior observed during the flowing portion of the intracycle response as a non-monotonicity in the waveform (Fig. 7.4 a). This process homogenizes the domain size distribution and leads to an increase in the peak sharpness $\xi_{c2}\beta_{max}$. As $G'$ and $G''$ measure only the average elastic and viscous contributions to the stress, they obscure the fact that both elastic straining and viscous flow exist well before and after their crossover point. It is important to note that the flowing portion of the response occurs well before the crossover in $G'$ and $G''$, even though this is often used to define the yield point of the gel. This highlights the need for intracycle interpretations of LAOS in order to better characterize the yielding process.

- **Region III: post-yielding flow ($\gamma_{r,0} > 20$)**

  For even higher strain amplitudes, the process of domain rearrangement and breakdown that is predominant in Region II is completed. From this point on, all of the intracycle measures including the transitions between various intracycle process as well as the residual modulus $G_R$ become independent of strain-amplitude, and the intracycle yield strain and stress show a linear increase with strain amplitude. Thus, in every half-cycle only a small fraction of the applied strain is recovered by the elasticity of the network, and the mechanical response in this region is dominated by dissipation of the yielded structure. The remaining strain is acquired through flowing of the now-suspended agglomerated domains. With the number of recoverable bonds between the dense domains minimized, the increasing strain amplitude results in further breaking of cluster-cluster bonds, but now within the suspended domains, and therefore some of the domains decrease in size even further. Thus the domain size distribution is broadened it this region, which is evident from a decrease of $\xi_{c2}\beta_{max}$.

## 7.8 Frequency dependencies under LAOS

The previous sections focused on combining LAOS and neutron scattering to find a correlation of the mechanical behavior with the gels structure for a fixed angular frequency of $\omega = 10$ rad/s. Since Rheo-SANS measurements are very limited due to long measurement times, which are needed for sufficient statistics, other frequencies were investigated in ex-situ LAOS experiments only. To examine the frequency dependence of the yielding processes in the nanoemulsion gel, waveforms at a fixed value of $\gamma_{r,0}$ for varying frequencies in the range from 0.1 to 56.55 rad/s are analyzed. The waveform at a specific amplitude is distinctively frequency dependent, as can be seen in Fig. 7.9, where waveforms for $\gamma_{r,0}$ =1, 2.8, and 20 are shown (corresponding to the beginning, middle and end of region II). With increasing frequency, the Lissajous curves become more box-shaped and the local stress minimum in the vicinity of the shear rate maximum ($\dot{\gamma}_r$=0) becomes less prominent. At the highest amplitudes and frequencies (right panel) a second local minimum in the stress appears which follows the first one. This feature is not an artifact of the data processing as it is present also in the raw data and was furthermore observed by other researchers (Poulos et al. 2013; Renou et al. 2010).

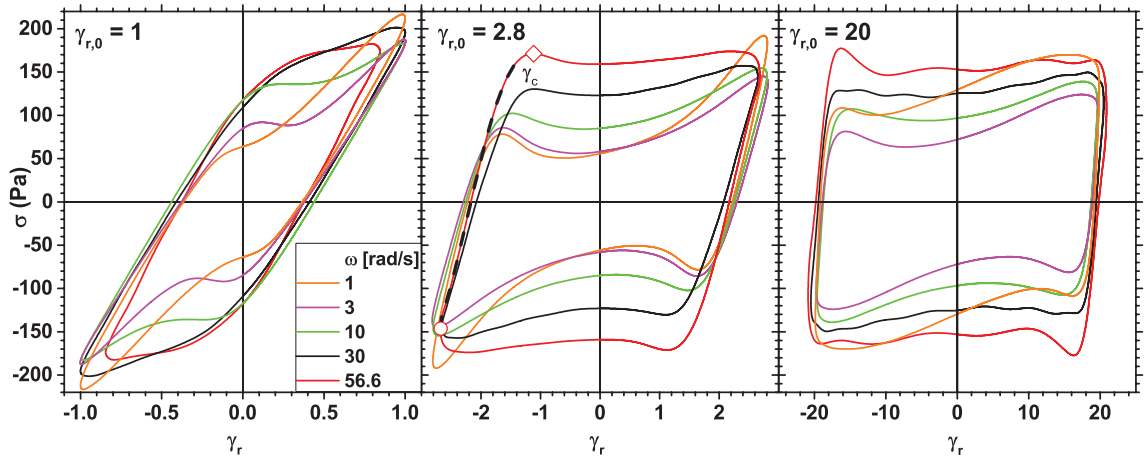


**Figure 7.9:** Elastic Lissajous plot of reconstructed waveforms measured at different angular frequencies at $\gamma_{r,0}$ values of 1, 2.8 and 20. The circle and diamond symbols shown for $\gamma_{r,0} = 2.8$ denote the point of flow reversal ($\gamma = -\gamma_0$ and $\dot{\gamma} = -\dot{\gamma}_0$) and the local stress maximum.

The waveform parameters for $\gamma_{r,0} = 2.8$ are displayed in Fig. 7.10 and show the trends of the waveform evolution more clearly. With increasing $\omega$, the yield stress $\sigma_c$ increases. The accumulated strain at which yielding occurs, $\gamma_c$, first shows a plateau for $\omega < 6$ rad/s and then increases afterward. Figure 7.10 (c) shows the dependence of the instantaneous viscosity $\eta_L$ as function of shear rate. As previously shown in the strain amplitude-dependent waveform analysis, increasing the shear rate leads to shear thinning in the flowing portion of the oscillation cycle ($\eta_L \propto \dot{\gamma}^{-0.8}$). In this case, the strain amplitude is constant and the increasing angular frequency causes higher shear rates. The fact that the shear thinning exponent varies depending on whether the strain amplitude or frequency is varied violates the so-called "Delaware Rutgers rule" (Doraiswamy et al. 1991), further

suggesting thixotropic behavior in the sample. The "Delaware Rutgers rule" is a modification of the Cox-Merz rule (Chapter 5.1.2, page 82) which states that for yield stress fluids, the shear rate dependent viscosity in steady shear is identical to the complex viscosity's dependence on the peak shear rate $\dot{\gamma}_0 = \gamma_0\omega$ in oscillatory shear: $\eta(\dot{\gamma}) = |\eta^*(\gamma_0\omega)|$.

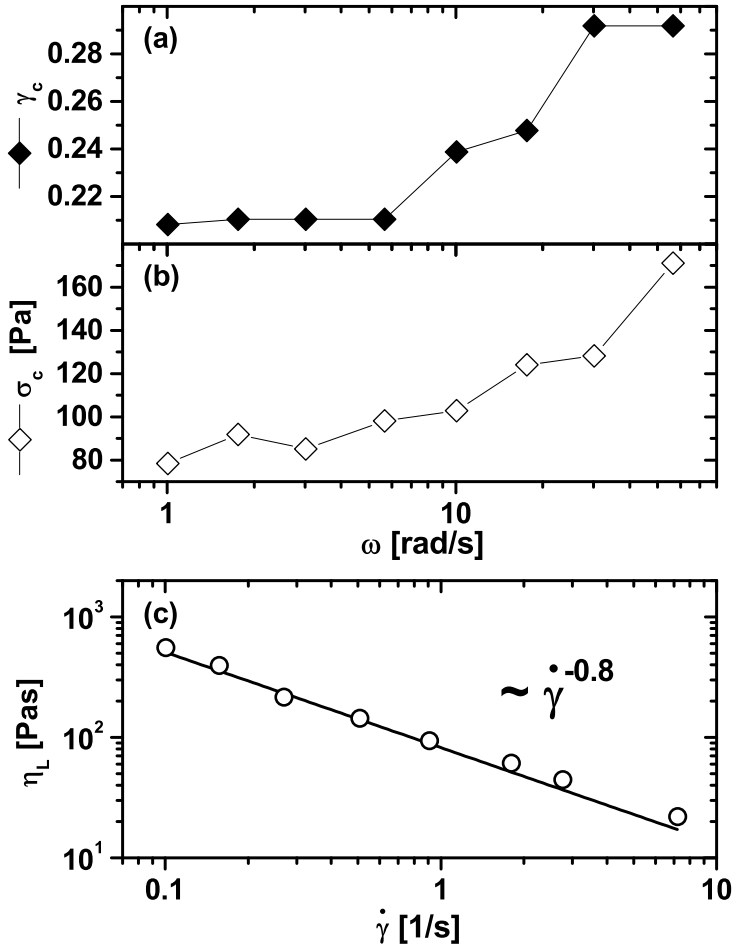


**Figure 7.10:** Nonlinear yielding parameters for the nanoemulsion gel sample at $T = 50°$C as a function of angular frequency at $\gamma_{r,0} = 2.8$ (center panel in Fig. 7.9): (a) $\gamma_c$ is the strain that has been accumulated from flow reversal to the local stress maximum, (b) local stress maximum $\sigma_c$, (c) instantaneous viscosity $\eta_L$ at the point of zero strain and maximum shear rate as a function of the instantaneous shear rate at that point, which is increasing with increasing angular frequency.

The frequency dependent mechanical measurements clearly indicate that the yielding process is not only strain amplitude-dependent but strain rate amplitude-dependent, as the yield strain and yield stress at a fixed strain amplitude increase with increasing frequency. The frequency dependence of the nonlinear waveform measures is is attributed to the dominant structural processes, i.e., the internal rupture and compression of dense fractal domains and the corresponding formation of large fluid voids. As discussed above, these processes require the expulsion of a significant amount of fluid from the interstices of the fractal droplet aggregates. Therefore, it is reasonable to expect poroelastic effects to play a significant role (Showalter and Momken 2002; Song and Huang 2000). Poroelasticity

describes the mechanics of fluid saturated porous media. First described by Biot, the poroelastic theory relies on linear elasticity of the porous matrix and uses Darcy's law for the flow the fluid through the porous matrix (Biot 1942; Whitaker 1986).
The trends that are observed in the LAOS measurements, including the increase in the maximum of $R''(t)$ and the increase in yield stress with increasing frequency are consistent with an increase in the viscous stress due to a resistance to drainage of fluid from the porous gel phase into the void phase under compression (Hong et al. 2001).
Darcy's law states that the volume flux $q$ of a liquid in a porous matrix in one dimension is proportional to the pressure gradient $\Delta p$ and inverse proportional to the liquids viscosity $\eta$, where $k$ is the coefficient of permeability and $L$ is the length of the fluid column (Hunt et al. 2014).

$$q = -\frac{k\Delta p}{\eta L} \tag{7.3}$$

Based on Darcy's law, the time scale for the drainage of the voids was estimated in (Kim, Merger, et al. 2014) to be on the order of 0.01-0.1 s. Thus, at low frequencies, including that probed by rheo-SANS/USANS, the characteristic time for formation and relaxation of voids is much smaller than the cycle time. Consequently, the hydrodynamics arising from drainage of fluid required to form the voids will not contribute significantly to the intracycle response. However, above a critical frequency where $t_{drain}2\pi\omega$ is on the order of 1, the suspending medium will begin to introduce a significant viscous contribution to the stress due to hydrodynamic resistance to drainage during yielding. This is consistent with the observed increase in the yield stress with increasing frequencies above $\sim$20 rad/s, and this frequency is consistent with the preceding argument ($t_{drain}2\pi\omega \sim 0.3$). At high frequencies, these trends ultimately manifest in qualitative changes in the waveform, as the initially pronounced stress overshoot is gradually smoothed out and the waveform becomes box-shaped, similar to the results obtained from experiments on colloidal glasses. This behavior is attributed to the time-averaged structure in region III, i.e., homogenized, suspended domains at relatively high effective volume fraction dominated by the flowing portion of the cycle. It is thus reasonable to expect that the waveform at high frequencies becomes reminiscent of the cage structure in highly concentrated suspensions, since the suspended clusters can experience caging in the same manner as the repulsive particles in the suspension (Chapter 6, page 113), though at a much larger length scale.

## 7.9 Summary

In this chapter detailed nonlinear mechanical measurements were combined with results from neutron scattering performed by the group of Prof. Matthew E. Helgeson in order to elucidate microstructural processes underlying the yielding behavior of a concentrated colloidal gel with heterogeneous microstructure under LAOS. The observed broad yielding, in the concentrated gel can be linked to two dominant microstructural processes. First, the initial yield strain amplitude (at which intracycle flow is initially observed) coincides with internal rupture and compression of dense fractal domains. Second, the strain amplitude signifying the completion of yielding (where the intracycle yielding and flow processes saturate) results from breakage and suspension of dense clusters. At moderate frequencies, this results in three regions of yielding with increasing strain amplitude. In region I, the bicontinuous gel structure is only weakly perturbed, and the nonlinear waveform can be described by an elastoplastic intracycle strain softening of the residual gel network. In region II, the dense phase undergoes significant compression-mediated viscoplastic rupture of fractal domains, resulting eventually in a sequence of intracycle yielding and flow. In this region, significant frequency dependence is also observed, which is hypothesized to be caused by poroelastic flow of fluid from the dense domains into newly formed fluid voids at large length scales. Ultimately, the rupture of fractal domains at sufficiently high strain amplitudes results in degradation of the network, eventually causing suspension of fractal clusters in region III. This results in a relatively "simple" intracycle yielding response in the flowing state, where the residual nonlinear elastic modulus, yield stress, and recoverable strain all become independent of the applied strain amplitude. From the analysis, it is clear that traditional interpretations of the linearized moduli $G'$ and $G'$ are insufficient to describe yielding. Therefore, a number of nonlinear rheological measures have been identified that are relevant to the yielding of colloidal gels, including a "phase map" for intracycle yielding determined by the instantaneous moduli $R'$ and $R''$. This allows for more specific parameterization of the yielding material, including a residual modulus characterizing the remaining elasticity of the network, a yield stress and a yield strain characterizing the intracycle yield point, and a local viscosity during the flowing portion of the strain cycle reminiscent of that observed in steady shear measurements. Such measures could easily be applied to the analysis of LAOS measurements on other colloidal gels, including those with both homogeneous and heterogeneous microstructure. Comparing these measures across different compositions and material systems could provide more complete exploration of the differences between various types of gels (dilute versus concentrated, homogeneous versus heterogeneous, etc.). In the case of the dense, heterogeneous gels formed in the present system, the yielding process is clearly both strain amplitude and shear rate amplitude dependent.

# Chapter 8

# Experimental Details: materials, rheometers, numerical calculations

## 8.1 Materials

### 8.1.1 Polymeric samples

For the comparison of the strain and stress controlled rheometers in chapter 4 three polymeric samples were selected. One was an anionically synthesized 1,4-cis-polyisoprene melt (abbreviated: PI-84k, $M_w$ = 84000 g/mol, PDI = 1.04). It is an entangled ($M_w/M_e$ = 21 entanglements per chain, $M_e$ = 4000 g/mol, Mark 2007), nearly monodisperse, linear homopolymer with a glass transition temperature $T_g$ of -61.7°C as measured by differential scanning calorimetry. The other two samples were 10 wt.-% solutions of polyisobutylene (PIB, $M_w = 1.1{\cdot}10^6$ g/mol and PIB-2, $M_w = 4.8{\cdot}10^6$ g/mol) in oligoisobutylene which had been provided by BASF. The samples were chosen because they are easy to handle, their composition stays constant over time and they reproducibly showed the expected square scaling of $I_{3/1}$ with the strain amplitude on the ARES-G2 rheometer. Their zero shear viscosities and relaxation times are collected in Table 8.1.

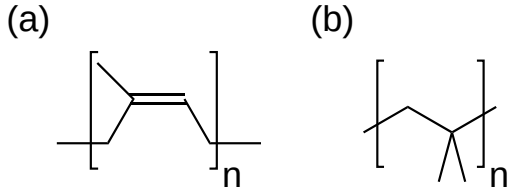


**Figure 8.1:** Polymeric samples used in Chapter 4: (a) 1,4-cis-polyisoprene melt, abbrev. PI-84k, and (b) 10 wt.-% polyisobutylene solution in its oligomer, abbrev. PIB.

| sample | $M_w$ [g/mol] | T [°C] | $\eta_0$ [Pas] | $\lambda$ [s] |
|---|---|---|---|---|
| PI-84k | 84000 | 52.8 | 3990 | $1.1{\cdot}10^{-2}$ |
| | | 20.4 | 33000 | 0.104 |
| PIB | $1.1{\cdot}10^{6}$ | 25 | 3.38 | $4.8{\cdot}10^{-3}$ |
| PIB-2 | $4.8{\cdot}10^{6}$ | 20.4 | 21 | $1.28{\cdot}10^{-2}$ |

**Table 8.1:** Samples used in chapter 4 and their weight averaged molecular weights $M_w$, zero shear viscosities $\eta_0$ and relaxation times $\lambda$. Note that the PIB and PIB-2 samples are 10 wt.-% solutions of the stated molecular weight polymers in oligoisobutylene.

### 8.1.2 Wormlike micelle solutions

LAOS experiments for the validation of the extended Maxwell-Model in Chapter 5 were performed on a 0.15 M aqueous solution of cetyl trimethylammonium bromide (CTAB, obtained from Sigma Aldrich), containing potassium bromide (1.5 M, obtained from Sigma Aldrich) following the recipe of Khatory et al. (1993). At a concentration of 0.15 M, CTAB forms wormlike micelles which become long enough to entangle, resulting in viscoelastic behavior of the solution (Gurnon and Wagner 2012; Khatory et al. 1993; Rehage and Hoffmann 1991). The high concentrations of CTAB and KBr made it necessary to stir the sample at 40°C for 48 hours to ensure complete dissolution of CTAB and KBr. Inbetween measurements the solution was kept at 40°C to prevent precipitation of the solutes.

### 8.1.3 Thermoresponsive suspension

For the rheological experiments in Chapter 6, a polydisperse suspension of thermo-responsive core-shell particles (Siebenbürger et al. 2009) in 0.05 M potassium chloride solution with a solid content of 8.85 wt.-% was used, which is abbreviated CS-80 (core-shell, ≈80 nm radius at 25°C). The core of the particles consists of polystyrene and has a diameter of 35 nm, whereas the shell is a slightly crosslinked network of poly(N-isopropylacrylamide) (PNipam) with a degree of crosslinking of 2.5 mol-%. The crosslinker is N,N'-methylenebisacrylamide. The synthesis is a two step process: in a first step the polystyrene core is synthesized by an emulsion polymerization, onto which in a second step the PNipam shell is added. Since in the second step no surfactant is used, the insoluble Nipam cannot form additional micelles, that is new primary particles, but rather polymerized at the PS core surface, forming a shell (Dingenouts et al. 1998). The crosslinking of the shell ensures that core and shell are linked permanently. The structural, thermal and linear rheological properties of such PS-Pnipam suspensions are well documented (Dingenouts et al. 1998; Crassous, Wittemann, et al. 2008; Siebenbürger et al. 2009). For the specific sample used here the hydrodynamic radius shows a linear dependence on the temperature according to $R_{\mathrm{H}} = -0.6909$ nm/°C $\times T$[°C] + 94.11 nm in a temperature range $10 < \mathrm{T} < 25$ °C , which had been previously determined by Siebenbürger using dynamic light scattering experiments (Siebenbürger 2006). The relative standard deviation of the radius was 14%. The sample was measured at four temperatures, $T = 22$, 20, 18 and 15 °C, which correspond to the effective volume fractions of $\phi_{\mathrm{eff}} = 0.614$, 0.62, 0.631 and 0.637. These volume fractions have been determined by

mapping the parameter $\eta_\infty$, which was obtained from a fit of the high frequency moduli, to the respective volume fractions using the prediction by Lionberger and Russel (1994), Eq. 3.8, and assuming partial draining of the network, as has already been done in previous studies (Siebenbürger et al. 2009; Brader et al. 2010). Note that at these conditions the sample is still in a fluid state. The glass transition volume fraction $\phi_g$ must therefore be significantly higher than it is for monodisperse hard spheres (0.58). This is possible due to the appreciable polydispersity of the particles.

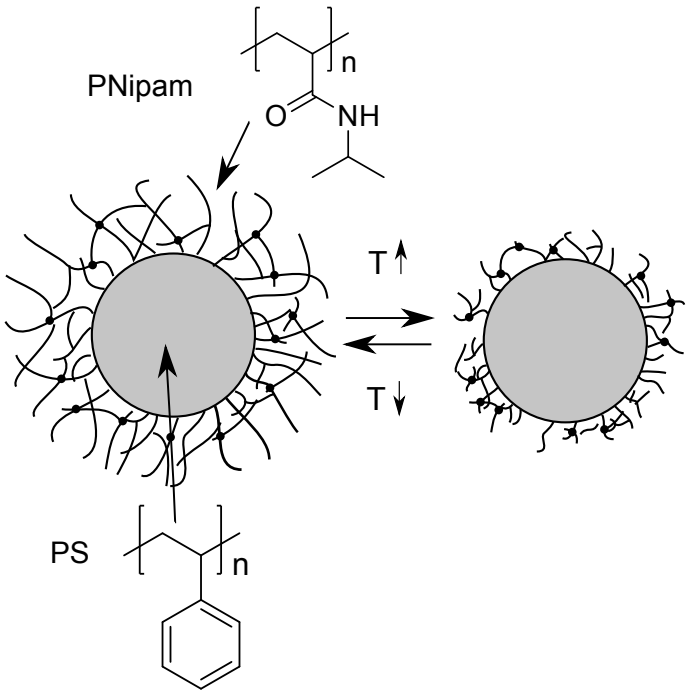


**Figure 8.2:** The hydrodynamic radius $R_H$ of the core-shell particles, consisting of a hard sphere polystyrene core and a slightly cross-linked PNipam shell, decreases upon temperature increase, because the PNipam shell gradually shrinks and collapses (Siebenbürger et al. 2009).

### 8.1.4 Nanoemulsion gel

For the LAOS investigation of colloidal gels in Chapter 7, a gel system based on nanoemulsions was used. Nanoemulsions consist of two immiscible fluid phases, where the droplet size of the dispersed phase is on the order of 20-100 nm (Mason et al. 2006). In contrast to macroemulsions, which have larger droplet sizes (100 nm - 100 µm), nanoemulsions are stable over much longer times due to the small droplet size. As the destabilization rate of an emulsion is linear in the droplet radius (Dörfler 2002), the prolonged stability of nanoemulsions is a purely kinetic effect. Furthermore, they are not to be confused with microemulsions, which have comparable droplet sizes but are thermodynamically stable systems. Microemulsions form spontaneously from a quaternary mixture of water, oil, surfactant and co-surfactant, such as n-Pentanol (Dörfler 2002).
The nanoemulsion system was prepared by Juntae Kim in the group of Prof. Matthew. E. Helgeson at the University of California, Santa Barbara. The preparation and characteri-

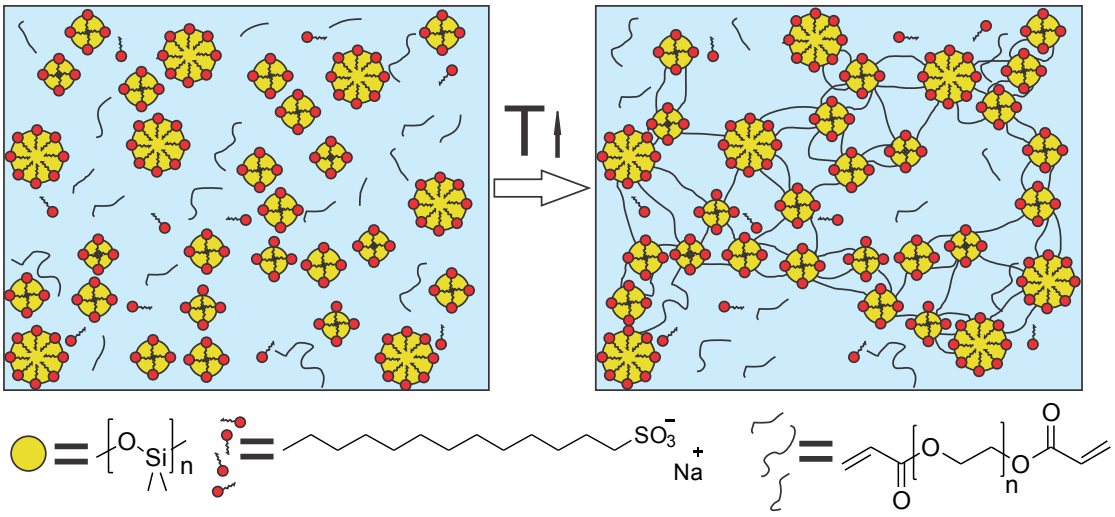


**Figure 8.3:** Schematic gelation mechanism in a oil/water emulsion nanoemulsion. The oil phase consists of polydimethylsiloxane and is stabilized by sodium dodecyl sulfate. Polymeric chains of poly(ethylene glycol) diacrylate from the continuous phase adhere to the oil droplets (average droplet radius 20 nm) and effectively bridge them upon temperature increase. This leads to the formation of a network (Helgeson et al. 2012).

zation procedures are reproduced briefly from the joint publication (Kim, Merger, et al. 2014), further details can be found therein.

Figure 8.3 shows schematicaly the structure and gelation process of the nanoemulsion. Polydimethylsiloxane (PDMS, $\eta = 5$ mPas at 25°C) was used as the dispersed phase for the O/W nanoemulsion sample. The aqueous continuous phase consisted of poly(ethylene glycol) diacrylate (PEGDA, $M_n = 700$ g/mol) and sodium dodecyl sulfate (SDS) dissolved in deionized water. Helgeson et al. (2012) showed that the gelation process depends strongly on the endgroup of the PEG derivative. Only hydrophobic end groups containing an acrylic group led to gelation, whereas nanoemulsions containing hydroxy-terminated PEG did not gel. The gelation mechanism was explained by increased dehydration the acrylic groups at elevated temperatures, which forces the acrylic groups to adhere to the hydrophobic surface of the oil droplets (Helgeson et al. 2012).

All chemicals were purchased from Sigma Aldrich. For USANS/SANS measurements, deuterium oxide (D2O, 99.9%, Cambridge Isotope Laboratories) was used in the aqueous phase to enhance neutron contrast. Nanoemulsions were prepared using a high-pressure homogenization method (Avestin Emulsiflex-C5) following a procedure described by Kim et al. (2013). Dynamic light scattering (DLS) was used to obtain the size distribution of the nanoemulsion droplets. For the DLS experiments, the nanoemulsions were diluted to a volume fraction $\phi = 0.01$ using the continuous phase described before. Intensity autocorrelation measurements were performed at a scattering angle of 90° and a temperature of 25°C. The average hydrodynamic diameter and polydispersity of the nanoemulsion was obtained from a cumulant analysis. The specific sample used is a nanoemulsion containing PDMS with $\phi = 0.33$, the continuous phase containing 230 mM SDS and 33 vol.-% PEGDA. The average droplet radius measured by DLS was $R_H = 21$ nm with a polydispersity of

0.238. The specific volume fraction and concentrations of the other constituents were chosen in order to produce heterogeneous gels with structure resembling arrested phase separation (Helgeson et al. 2014). Note that, the large pressure jump across the oil-water interface due to surface tension renders the droplets essentially undeformable under the conditions measured in the experiment in Chapter 7 (for the most extreme conditions studied here, the capillary number $Ca$ has been estimated to be smaller than $10^{-4}$ (Kim, Merger, et al. 2014)).

## 8.2 Rheological instrumentation

The measurements in Chapter 4 were conducted on five different rheometers. Two were separated motor transducer (SMT)-rheometers, namely the ARES-G2 (TA Instruments) and the ARES-LS (TA Instruments) with a 1KFRTN1 transducer. The ARES-G2 is equipped with a brushless direct current motor (also known as electrically commutated motor), which is used for the excitation of the sample, whereas the ARES-LS employs a DC motor with brushes. Another two instruments were combined motor transducer-rheometers, the DHR-3 (TA Instruments) and the MCR 501 (Anton Paar). The DHR-3 is equipped with a drag cup motor, the MCR 501 uses a brushless DC motor like the ARES-G2. Both the DHR-3 and the MCR501 are in principle stress controlled instruments, but can be used for strain controlled experiments when employing the deformation control feedback option (called *continuous oscillation* for DHR-3 and *direct strain oscillation* for MCR501). Additionally a fifth rheometer became available at a late stage of the thesis, the MCR 702, which employs two identical motors. One of these motors can be used for the excitation, the other motor acts as an FRT-transducer, measuring the torque in the sample. Therefore, the MCR702, in contrast to the earlier model MCR 501, represents a truly separated motor-transducer instrument. Since the specific instrument that was available could not provide any temperature control system, direct comparison to the study of the other four instruments was not possible. Therefore, a new test series was performed on the samples PI-84k and PIB-2. Apart from the fundamental design, SMT or CMT, the instruments also differ slightly in their torque sensitivity, which is represented by the minimum measurable torque according to the manufacturers' specifications, see Table 8.2.

| Instrument | $M_{\min}$ [nNm] | $M_{\max}$ [mNm] | $d$(PI-84k) [mm] | $d$(PIB) [mm] |
|---|---|---|---|---|
| ARES-G2 | 50 | 200 | 13 | 40 |
| ARES-LS | 400 | 100 | 13 | 50 |
| DHR-3 | 0.5 | 200 | 13 | 40 |
| MCR 501 | 100 | 230 | 8 | 50 |
| MCR 702 | 0.5 | 230 | 8 | 25* |

**Table 8.2:** Minimum and maximum torques (as specified by the manufacturers) and diameters $d$ for the parallel plate geometries used for the different samples on the five instruments. * for the comparison of the ARES G2 with the MCR702 using the PIB-2 sample, a 25 mm cone and plate geometry (cone angle 0.1 rad) was used.

Measurements for Chapters 5 and 6 were performed on the ARES G2. The LAOS behavior of the nanoemulsion gel from Chapter 7 was investigated using an ARES-LS at the University of California, Santa Barbara. This instrument had the same specifications as the one in Chapter 4. In the gel study the temperature was controlled by a jacket of circulating water in the lower plate geometry. In order to minimize solvent evaporation, a solvent trap was used. In-situ Rheo-SANS experiments performed by Helgeson and Kim were made on an MCR 501 at the NG7 30 m SANS instrument (National Institute of Standards and Technology, Gaithersburg, Maryland, USA). The sample was measured in a quartz Couette geometry (50 mm outer diameter and 49 mm inner diameter). The temperature was controlled by a heated and cooled double air jacket.

## 8.3 Rheological measurement protocols

### 8.3.1 Polymeric samples

For the rheometer evaluation in Chapter 4, frequency dependent measurements in the linear regime were made to test if the four instruments deliver the same results for the linear viscoelastic moduli $G'(\omega)$ and $G''(\omega)$. The angular frequency range was 0.63 to 63 rad/s and the tested strain amplitudes were 0.01 and 0.1 for the PI-84k and the PIB samples, respectively. Furthermore, strain amplitude-dependent LAOS tests were run at different frequencies in the range of 1 to 10 rad/s for PI-84k and 0.63 to 63 rad/s for PIB to measure the frequency dependence of the intrinsic nonlinearity $Q_0$. For the experiments on the CMT-rheometers (DHR-3 and MCR 501), the active deformation control was used. For the DHR-3 rheometer, this setting is called *continuous oscillation-mode*; for the MCR 501, the corresponding term is *direct strain oscillation*. Both are feedback control loops that are employed to produce, in the ideal case, a pure sinusoidal deformation, as mentioned in Section 4.1. The *continuous oscillation-mode* of the DHR-3 allows the user to set the gain of the deformation control thus varying how fast it reacts to nonlinearities in the strain. This option is called 'motor mode' and can be set to *auto*, *soft*, *medium* or *stiff*. The motor mode was set to *stiff* for the PI-84k sample and to *medium* for the PIB sample. The reasons for these choices are discussed in Section 4.4.1 as the setting has a substantial effect for the quantitative analysis. The optimal setting for an unknown sample is not known.

Torque and deflection angle data collected on the ARES-G2 and the DHR-3 was internally Fourier-transformed by the TRIOS software to give the linear viscoelastic parameters and the intensities as well as the phases of the higher harmonics present in the response signal. On both instruments the software routinely transforms only the torque signal but not the stress signal. This is viable for the ARES-G2 since, for an SMT-rheometer, torque and stress are in general proportional and only normalized quantities like $I_{3/1}$ are investigated within this article. For the DHR-3, the transformation of the torque instead of the stress can have an effect on the result due to instrument inertia effects, which are discussed in

Section 4.4.2. Additionally, transient oscillatory data at $\omega = 6.3$ rad/s and $\gamma_0 = 1$ for PI-84k was recorded using oversampling and Fourier-transformed using either the TRIOS software or custom MATLAB routines.
For the ARES-LS, transient torque and deflection angle data was recorded manually using the 2 analog outputs, an 16-bit analog-to-digital converter (ADC) and custom written LabView routine (Wilhelm 2002). Oversampling was used to enhance sensitivity to its maximum and reduce the data amount to a sampling rate of 200 points per oscillation cycle (Dusschoten and Wilhelm 2001). With the frequency increasing from 0.63 to 87 rad/s, the number of recorded cycles per strain amplitude was increased from 6 to 25. For the extraction of the intensities of the higher harmonics a home-written MATLAB routine was used that employed a half-sided, discrete, complex, magnitude Fourier transform (Wilhelm 2002).
Measurements on the MCR 501 were performed using the LAOS-Package of the commercial RheoPlus software, provided by Anton Paar. Depending on the frequency, 6 to 25, oscillation cycles per amplitude were carried out. Out of these cycles, the software gave the time data for only the last cycle, which consisted of 257 data points and was already corrected for instrument inertia. The first and the last point were identical, as only 256 were used for the Fourier transform. In order to check the signal to noise ratio of the spectra, additional sampling of the raw data with an ADC was required. This sampling as well as the data analysis was done with the same parameters as for the ARES-LS data.
For the validation of the correction factors based on the corotational Maxwell model in Section 4.3, measurements of the PI-84k sample had to be extended to strain amplitudes as large as $\gamma_0 = 3$. Since at such large amplitudes edge fracture artifacts, where sample is expelled from the geometry, hamper the measurements (Schweizer 2003), special partitioned geometries according to the design of Schweizer (2003) were used. The diameters of the parallel disks were 10 mm, for the cone and plate set-up, the diameter was 10 mm as well, the cone angle was 0.099 rad. LAOS tests were run at $\omega = 6.3$rad/s and $T = 52.8°$C. For each amplitude, 25 cycles were recorded in the time domain using the commercial TRIOS software provided by TA Instruments. The first two cycles of the sampled time data for each strain amplitude were discarded, to ensure a quasi-static stress signal, so that cycles 3 through 27 were then analyzed. For the Fourier transform of the time data, a custom MATLAB code was used and subsequently harmonic intensities were extracted from the spectra.

### 8.3.2 Wormlike micelle solution

Measurements of the linear dynamic moduli ($G'$ and $G''$), flow curve measurements ($\sigma(\dot{\gamma})$) and LAOS experiments were performed using an ARES-G2 strain controlled rheometer (TA Instruments), equipped with a concentric cylinders geometry ($r_1 = 18.6$ mm and $r_2 = 20$ mm) and a Peltier temperature control system. The measurement temperature was T = 35°C. The stress signals were recorded using the commercial rheometer software

TRIOS. For a given strain amplitude 8 cycles were recorded, the first 3 of which were discarded to ensure a quasi-stationary signal. Data recorded in TRIOS was analyzed using the same MATLAB code that was employed for the analysis of the numerical solutions. Repeated measurements were analyzed using the TRIOS software after confirmation that both analysis routines give identical results.

### 8.3.3 Thermoresponsive suspension

The rheological experiments on CS-80 were conducted on a ARES-G2 (TA Instruments) strain controlled rheometer using a Couette geometry (bob diameter 18.6 mm, cup diameter 20.0 mm) with a Peltier temperature control system. The same dispersion was measured at four temperatures, corresponding to different volume fractions. Each experiment was preceded by a pre-shear step at a shear rate of 50 1/s for 200 seconds in order to erase the previous shear history. A solvent trap was used to minimize water evaporation and allowed experiment durations of up to 3 days. Flow curves were recorded at shear rates in the range of $1 \cdot 10^{-4}$ 1/s $< \dot{\gamma} <$ 100 1/s, linear viscoelastic moduli were measured at a strain amplitude of $\gamma_0 = 0.01$ in the angular frequency range of 2.1 $\times 10^{-3}$ rad/s $< \omega <$ 250 rad/s. Additional high frequency measurements of the linear viscoelastic moduli in the range 60 rad/s $< \omega <$ 12500 rad/s were made using a piezo-axial vibrator (PAV) (Crassous et al. 2005). The PAV is a dynamic press (Fig. 8.4) that is used as a squeeze-flow rheometer. The gap was adjusted using a 50 mm spacer ring.

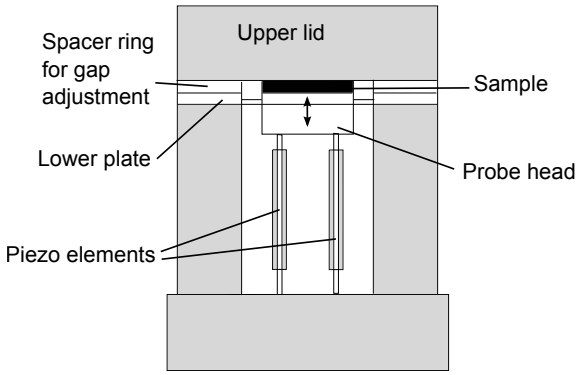


**Figure 8.4:** The piezoaxial vibrator is a squeeze flow rheometer that can used to measure linear high frequency behavior (10 and 3000 HZ) of low viscosity fluids. Redrawn after Crassous et al. (2005).

Large amplitude oscillatory shear experiments were carried out on the ARES-G2 rheometer using the same geometry and preshear protocol as in the shear rate dependent and linear oscillatory experiments. Strain amplitude sweeps ($0.001 < \gamma_0 < 0.3$) at different angular frequencies were conducted to obtain the strain amplitude dependent relative intensity of the third harmonic $I_{3/1}(\gamma_0, \omega)$ from which the intrinsic nonlinearity $Q_0(\omega) = \lim_{\gamma_0 \to 0} I_{3/1}/\gamma_0^2(\omega)$ was deduced. All LAOS measurements were performed in the correlation mode, where stress data was internally Fourier transformed by the instruments software TRIOS.

### 8.3.4 Nanoemulsion gel

**Wall slip of nanoemulsion gels under LAOS**

Wall slip artifacts, that is when the sample loses contact with the geometry surface, are known to severely complicate measurements of soft elastic samples like microgel suspensions (Dimitriou et al. 2013) and colloidal gels (Laurati et al. 2011). In Chapter 7 this artifact was prevented by attaching 600 grit sandpaper to the 50 mm cone and plate geometries (cone angle 0.04 rad) using double sided adhesive tape, following a the procedure reported by Dimitriou et al. (2013). A recent study by Carotenuto and Minale (2013) showed that using a rough geometry cannot effectively prevent wall slip even for Newtonian liquids, since the investigated fluid does not adhere to the rough geometry surface but rather flows through it.

However, within the thesis the sand paper procedure was tested on a Newtonian fluid and gave reasonable agreement for the complex viscosity of a visco-elastic silicone oil ($|\eta^*|$ = 17 Pas at T = 25°C) with and without the sandpaper, see inset in Fig. 8.5. Therefore, possible errors caused by the sandpaper (e.g. through a larger gap error or the sandpaper peeling off during the experiment) could be excluded.

In Fig. 8.5 the effect of using roughened surfaces is shown for a nanoemulsion gel sample. When smooth geometries are used, $G'$ and $G''$ seems to decrease in two steps. The reproducibility of the apparent two step yielding with the smooth geometries was poor and in some measurements $G'$ and $G''$ even displayed a local minimum in the strain amplitude range $0.01 < \gamma_0 < 0.1$. Roughened geometries eliminated slip artifacts and led to reproducible results with a monotonic decrease for $G'$ as well as for $G''$ after its maximum.

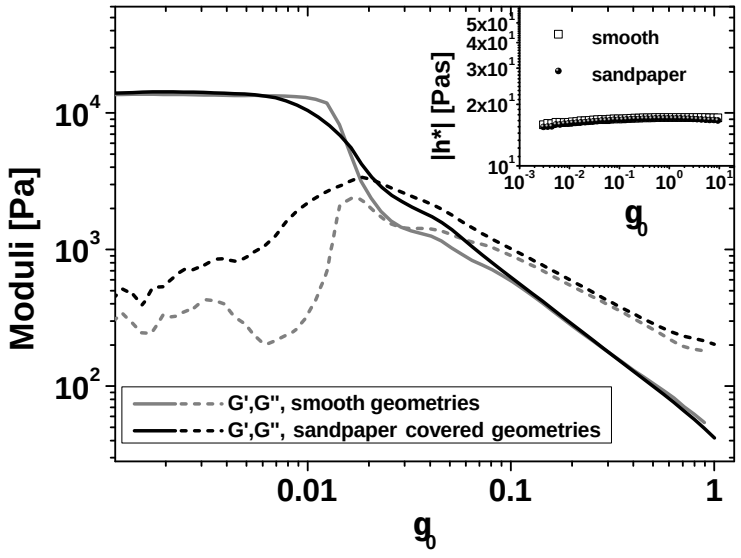


**Figure 8.5:** Comparison of LAOS tests using smooth geometries and geometries covered with sandpaper to prevent wall slip. Inset: Measurement of the complex viscosity $|\eta^*|$ as function of strain amplitude for the validation of the sandpaper procedure using a silicone oil ($\eta$ = 17 Pas at T = 25°C).

**Thixotropic effects in nanoemulsion gels under LAOS**

In all LAOS measurements of the nanoemulsion gel, the raw stress signal started to show a transient decay in amplitude as soon as the linear visco-elastic regime was exceeded ($\gamma_0$>0.01). This decay corresponds to slow intercycle thixotropic behavior or aging, and prevents the Lissajous-Bowditch curves from forming closed loops. Thixotropic behavior, is defined as a continuous decrease of the viscosity during flow, and a subsequent recovery during rest (Mewis and Wagner 2012). In contrast to start-up behavior of shear thinning samples, in thixotropic systems no steady state of the viscosity can be reached even after long times. Thixotropy is a common nonlinear rheological feature of gel-like systems (Mewis and Wagner 2009) and is therefore also present in LAOS experiments, in contrast to colloidal glasses, where a quasistationary state under LAOS can be reached almost immediately (Rogers et al. 2011a). Quasistationary refers to a state in which the harmonic intensities and phases do not change as a function of time. Since the gel measurements did not reach a quasistationary state even after over 100 oscillation cycles for a specific set of $\omega$ and $\gamma_0$, data from only the first 8 cycles for each amplitude were used for the analysis. The 8 cycles per amplitude have been decomposed to Fourier coefficients according to Eq. 2.29. Each representative cycle was then reconstructed in the time domain using only odd harmonics up to $n = 21$. Since each odd harmonic with $n$ >21 displayed relative intensities smaller than 0.1%, all significant contributions to the stress have been taken into account. Even harmonics were negligible as $I_{2/1}$, which is the most prominent of them, was always below 0.3% of the total signal and showed no time dependence. The reconstruction procedure is essentially a comb filter and all waveform data for the nanoemulsion gel represent an average over the intracycle transient behavior during a strain amplitude sweep. This procedure renders the later extracted nonlinear parameters to be time-dependent to some extent. However, the alternative of waiting for the sample to reach a stationary oscillatory state is unfeasible due to the long measuring times, especially at low frequencies.

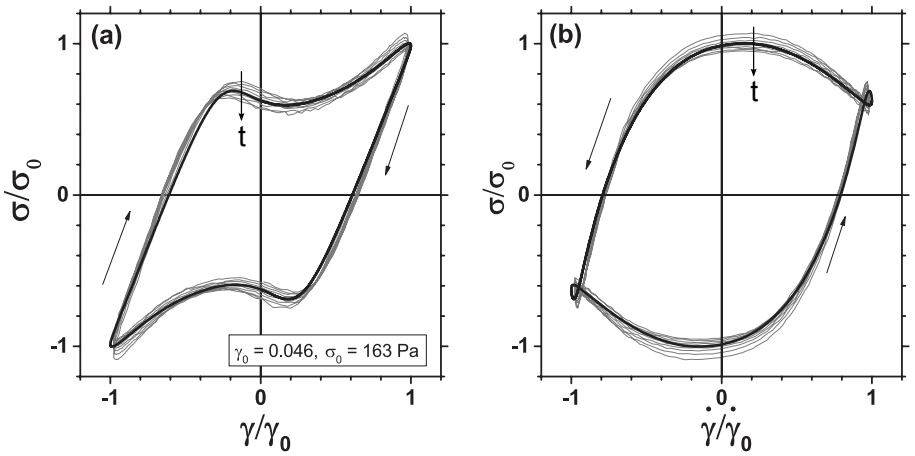


**Figure 8.6:** Normalized plots of stress versus (a) strain (elastic projection), and (b) shear rate (viscous projection) recorded at $\omega = 10$ rad/s and $\gamma_0 = 0.046$ for the nanoemulsion gel sample (Section 8.1.4). The gray line represents the raw signal, whereas the black line shows the reconstructed signal from an average over eight cycles. Arrows indicate the reading direction for the Lissajous curves. The overall stress signal decays over time as indicated by the additional arrows.

## 8.4 Numerical methods

The model calculation in Chapter 5 were performed using a custom-written code in MATLAB, which employed a 4th order Runge-Kutta solution scheme (ode45 solver) in order to solve the differential equations 5.12, 5.16, 5.20 and 5.22. For this 512 equally spaced points per oscillation cycle were calculated, which is a typical sampling rate in an experiment. For a set of $G$ and $\lambda$ the initial value problem was solved for varying strain amplitudes at a fixed angular frequency, thus varying $Wi = \omega\gamma_0\lambda$ while keeping $De = \lambda\omega$ fixed.

Any time dependent model with a memory has its own start-up behavior, as for example the scalar Maxwell or the corotational Maxwell model (Giacomin et al. 2011). In Fig. 8.7 this start-up behavior is shown for a numerical solution of Eq. 5.12 using the parameters $G = 1$ Pa and $\lambda = 1$ s at $\omega = 1$ rad/s and $\gamma_0 = 0.329$. In the time plot left, only upon

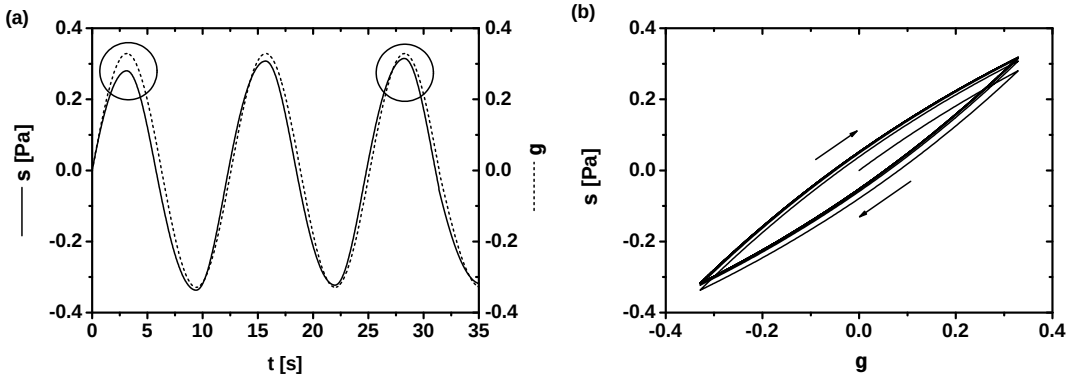


**Figure 8.7:** Start-up behavior of numerical solutions of the modified Maxwell model (Eq. 5.12) presented as time evolution of the stress (a) and as Lissajous figure (b), $G = 1$ Pa and $\lambda = 1$ s at $\omega = 1$ rad/s and $\gamma_0 = 0.329$.

close inspection of the maxima in the circles, one can see differences between the first few oscillations. A Lissajous plot (right) shows the start-up behavior more clearly, as the initial curves shape does not coincide with the quasi-stationary shape at later times. This behavior was most pronounced for $De > 1$ in a $\gamma_0$ range where $G'$ was already decreasing and $G''$ was still increasing to its local maximum.
Therefore, for every pair of $[\gamma_0, \omega]$ coordinates in the Pipkin space 55 oscillation cycles were calculated from which the first 50 were discarded to eliminate the start-up behavior. Cycle 51 through 55 were Fourier-transformed using MATLAB and $G'$, $G''$ and $I_{3/1}$ were calculated from the spectra (Eq. 2.23). Weissenberg number dependent calculations were repeated for various $De$.

# Conclusion

In this thesis, Large Amplitude Oscillatory Shear (LAOS) experiments were employed to characterize the nonlinear viscoelastic behavior of colloidal suspensions and colloidal gels based on nanoemulsions. Results for the suspensions were compared to Mode Coupling Theory (MCT) predictions. LAOS measurements on the gels were correlated to a structural investigation by neutron scattering performed by the group of Prof. Matthew Helgeson to elucidate the changing structure during yielding. Furthermore, a simple modeling approach based on a modification of the Maxwell model was developed and validated with LAOS measurements on an aqueous solution of cetyl trimethylammonium bromide that forms a viscoelastic fluid. Moreover, LAOS experiments on model materials, a polyisoprene melt and polyisobutulene solutions, were performed on five different instruments for an assessment of reproducibility of LAOS parameters, such as the relative intensity of the third harmonic $I_{3/1}$ and the intrinsic nonlinearity $Q_0$.

Chapter 4 focused on the technical aspects of conducting strain controlled LAOS experiments on stress controlled and strain controlled rheometers and reproducibility of LAOS quantities. Nonlinear data in terms of $I_{3/1}$ and $Q_0$ from a polyisoprene melt and polyisobutylene solutions measured on five different rheometers was compared to point out important experimental precautions that need to be considered in order to achieve a reasonable agreement of the measured nonlinear quantities. The instruments under investigation were: ARES-G2, ARES-LS, MCR 702, (separated motor-transducer rheometers) and DHR-3 and MCR 501, which are combined motor-transducer rheometers (CMT). The method of temperature control (Peltier element or convection oven) was found to cause deviations of up to 30% in $Q_0$ for the polyisoprene melt even at moderate temperatures ($T = 52.8°\mathrm{C}$ ) when a Peltier plate was used instead of a forced convection oven due to inhomogeneous heating. Differences in $I_{3/1}$ arising from using parallel disks geometry due to its inhomogeneous flow field can be corrected by multiplying torque intensity ratios by a factor of 3/2 to convert them to stress intensity ratios as measured by the cone and plate geometry. The deformation control on the DHR-3 (called *motor mode*) had to be chosen such that the CMT-rheometer closely mimics a LAOStrain experiment by producing a strain excitation as free of nonlinearities as possible. Using the wrong setting of the *motor mode*, led to occurrence of nonlinearities in both strain and stress signal of approximately equal intensities, which resulted in smaller $Q_0$-values in comparison to strain controlled

instruments. As for an unknown sample the optimal setting is not known a priori, this is a disadvantage of the DHR-3 instrument.
The results for $Q_0$-values of the polyisoprene sample obtained from the MCR 501 and the MCR702 was determined to be larger by a factor of approximately two in comparison to the other instruments, which suggests that, in these cases, the active deformation control introduces additional nonlinearities in the stress signal.
For polyisobutylene, the results for $Q_0$ from all the investigated instruments were found to be within a relative reproducibility range of 12%. When using the CMT-rheometer DHR-3, effects caused by the instrument inertia became noticeable for measurements at frequencies above 23 rad/s leading to an apparent maximum in the frequency dependence of $Q_0$.
If temperature control, excitation control and instrument inertia are considered and corrected for, the relative deviations of the measured nonlinear quantities $I_{3/1}$ and $Q_0$ for a LAOS experiment on different rheometers can be expected to be below 12%.
In Chapter, 5 a simple scalar model, capable of predicting nonlinear response for LAOS experiments using only two parameters (a shear modulus $G$ and a relaxation time $\lambda$) has been presented. The model was obtained by assigning a shear rate dependent viscosity to the dashpot in a Maxwell model while the spring was kept linear. The shear rate dependence was introduced by applying the Cox-Merz rule to the expression of complex viscosity from the Maxwell model. In this model $G$ sets the stress scale, whereas $\lambda$ governs the nonlinearity of the dashpot but also the balance of viscous and elastic effects. The model is a scalar, one dimensional, special case of the tensorial White-Metzner model. It was solved numerically, the resulting stress signals were analyzed by a Fourier transform. The results agreed well to an approximate analytical solution derived by Mahdi Abbasi (KIT) that was valid for small deviations from linear behavior. At intermediate strain ampltiudes $\gamma_0$, a quadratic $\gamma_0$ dependence for $I_{3/1}$ was found (intrinsic LAOS range), subsequently the frequency dependence of $Q_0$ was determined for the model and the functional form of $Q_0(\omega)$ was compared to predictions of other models, such as corotational Maxwell, Giesekus, Pom-Pom and MSF.
Furthermore, the model predictions were compared to experimental data on a micellar solution of cetyl trimethylammonium bromide (CTAB). CTAB was chosen as a model system because it displays Maxwellian linear viscoelastic behavior with a single relaxation time and also the Cox-Merz rule can be applied. The model parameters, $G = 68$ Pa and $\lambda = 0.265$ s, were determined by a fit of the Maxwell model to $G'$ and $G''$ data and the validity of the Cox-Merz rule could be confirmed for the CTAB sample. Predicted and measured waveforms were in good agreement. However, the quantitative comparison based on $G'$, $G''$ and $I_{3/1}$ revealed that the model underestimates nonlinear effects in the intrinsic LAOS range, typical deviation were on the order of 30 % in $I_{3/1}$. LAOS measurements on CTAB spanning three decades in angular frequency were performed to determine the intrinsic nonlinearity $Q_0(\omega)$. Agreement of model prediction and experiment for $Q_0(\omega)$ is reasonably good considering the simplicity of the model. Quadratic scaling of $Q_0(\omega)$ predicted by the model for the viscous regime is in agreement with the experiments, but

the absolute $Q_0(\omega)$ values of the prediction were about 50 % smaller than the measured values. Qualitative deviations occur when the elastic behavior is dominating, that means for high angular frequencies (or large Deborah numbers).
Lastly, several modifications were explored to broaden the flexibility of the model. The modifications included the use of a power law viscosity function instead of the Cox-Merz rule related function, which led to non quadratic scaling of $I_{3/1}$ with strain amplitude. Moreover, the inclusion of a high frequency viscosity limit $\eta_\infty$ was investigated as well as employing two relaxation times in order to investigate the effect of dashpot nonlinearity separately from the viscosity/elasticity balance.

In Chapter 6, LAOS measurements on a polydisperse, thermo-responsive suspension of polystyrene-poly(N-isopropylacrylamide) particles were presented and compared to predictions by the schematic version of MCT. Measurements were conducted on fluid states close to the glass transition, four effective volume fractions $\phi_{\text{eff}} = 0.614$, 0.62, 0.631 and 0.637 were investigated. Linear viscoelastic moduli and flow curves were fitted to MCT predictions to obtain model parameters, which were used to predict LAOS behavior.
Nonlinear stress wave forms agreed with previous results on high volume fraction suspensions close to the glass transition. The frequency dependence, or in nondimensionalized form, the Péclet number dependence, of the mechanical nonlinearities as quantified by $\gamma_0$-dependent $G'$, $G''$ and $I_{3/1}$ was investigated. Quadratic scaling $I_{3/1}(\gamma_0)$ allowed to determine $Q_0$. Péclet number dependent $Q_0$ curves, spanning a range of five decades, were compared to MCT predictions calculated by Rabea Seybold (TU Dresden). The predictions had been obtained by Seyboldt using a Taylor expansion of the density correlator $\Phi$. Its first nonlinear term was used calculate $I_{3/1}$ in the resulting stress waves. Since the first nonlinear term in the expansion of $\Phi$ was quadratic, this led to $I_{3/1} \propto \gamma_0^2$ scaling. MCT predicts $Q_0$ to scale quadratically with $Pe_\omega$ for very small $Pe_\omega$, which could neither be confirmed nor disproved since this range of $Pe_\omega$ was not accessible experimentally. At intermediate $Pe_\omega$, $Q_0$ is proportional to $Pe_\omega^b$ in the prediction, where $b \approx 0.69$, experimentally determined exponents, however, were about half as large. The discrepancy might be related to an additional slow relaxation process that is not covered in the schematic MCT. For large $Pe_\omega$, MCT states that $Q_0$ ought to decrease proportional to $Pe_\omega^{-a}$ with $a = 0.32$. This could be confirmed, with experimental exponents close to 0.3.

In Chapter 7, LAOS measurements were correlated to results from neutron scattering experiments performed by the group of Prof. Matthew E. Helgeson (University of Santa Barbara, California) in order to investigate microstructural processes during the yielding transition of a colloidal gel with heterogeneous microstructure. The gel consisted of nanosized ($R_H = 21$ nm) droplets of uncrosslinked polydimethylsiloxane in water ($\phi = 0.33$), bridged by polyethylene glycol diacrylate molecules. The structure of the gel can be described as a two phase system of droplet rich and droplet lean domains reminiscent of spinodal decomposition in quenched mixtures. The yielding process occured over a $\gamma_0$ range

of two decades ($0.004<\gamma_0<1$). The yielding was linked to two dominant microstructural processes. First, the strain amplitude at which intracycle flow is initially observed coincided with internal rupture and compression of dense fractal domains. Second, the strain amplitude signifying the completion of yielding (where the intracycle yielding and flow processes saturate) results from breakage and suspension of dense clusters of interconnected droplets.

Three regions of yielding were determined based on nonlinear wave form parameters from an analysis of Lissajous figures as sequence of physical processes. In region I, the bicontinuous gel structure is only weakly perturbed, and the nonlinear waveform can be described by an elastoplastic intracycle strain softening of the residual gel network. In region II, the dense phase undergoes significant compression-mediated viscoplastic rupture of fractal domains, resulting eventually in a sequence of intracycle yielding and flow. In this region, significant frequency dependence is also observed, which is hypothesized to be caused by poroelastic flow of fluid from the dense domains into newly formed fluid voids at large length scales of tens of microns. Ultimately, the rupture of fractal domains at sufficiently high strain amplitudes results in degradation of the network, eventually causing suspension of fractal clusters in region III. This results in a relatively "simple" intracycle yielding response in the flowing state, where the residual nonlinear elastic modulus, yield stress, and recoverable strain all become independent of $\gamma_0$. The wave form analysis revealed that interpretations of LAOS data based solely on the linearized moduli $G'$ and $G'$ are insufficient to describe yielding. Nonlinear rheological measures that have been used to quantify the yielding of the gel included an intracycle yield strain and stress, a residual modulus as well as a local viscosity during the flowing portion of the oscillation cycle. Lastly, a "phase map" for intracycle yielding, which shows a sequence of elastic, elastoplastic softening, viscoplastic, yielding and flow behavior, has been constructed from the instantaneous moduli $R'$ and $R''$.

In summary the results in this thesis show the diversity of the LAOS experiment applied to dispersed systems and complex heterogeneous fluids in general. Nonlinear phenomena like yielding and intracycle stiffening or thinning behavior can be characterized in frequency dependent investigations. This leads to a more detailed description of the materials' mechanical behavior.

# Outlook

The results of this thesis point towards several directions for future research. The assessment of the reproducibility of LAOS measurements will probably lead to the definition of standardized testing procedures on certified standard materials. This will facilitate LAOS experiments for new users and comparisons across different laboratories.
The modeling approach using a simple modification of the most widely known model for viscoelasticity, the Maxwell model, will draw interest of rheologists who are not proficient with tensor calculus. It can serve as a basis for better understanding the more intricate 3D constitutive models. Comparing intrinsic nonlinear signatures such as $Q_0$ or intrinsic Chebishev coefficients from libraries of various constitutive models to experimental data will lead to enhanced characterization possibilities.
The results obtained in the nanoemulsion gel investigation are a first step into combined rheo-scattering investigations of colloidal gels and need to be extended to other systems (depletion-attraction gels and gels of crosslinking polymers) to check the generality of the found signatures. Furthermore, the intracycle yielding behavior needs to be investigated by recently developed, time resolved measurements of the structure by binning techniques in neutron scattering (Kim, Eberle, et al. 2014) or fast x-ray scattering (Lettinga et al. 2012; Meins et al. 2012). Expanded studies should examine the rate dependence of the applied deformation and combine them with modeling of the compression process of the dense phase by poroelastic models with viscoelastic matrices.
New measurements of the nonlinearity of colloidal glasses similar to the experiments presented here for fluid systems will be required to validate mode coupling theory predictions as soon as they are computable for systems beyond the glass transition. Moreover, the initial quadratic scaling of $Q_0$ might be investigated by using model suspensions in a dispersant of higher viscosity than water to overcome sensitivity challenges at very low angular frequencies. Additionally, a comparison of LAOS behavior across different glassy and jammed soft matter systems (gels, emulsions, suspensions and foams) is desirable, similar to a comparison recently made for steady shear measurements (Ikeda et al. 2013).
The samples investigated in this thesis were model systems for fundamental investigations. Eventually, future applications of LAOS flow will also focus more on complex real life systems such as foods, examples might be chocolate, dough, sauces, dressings and various foams and gels. Other dispersed systems which lend themselves to LAOS characterization can be found in biomaterials, where first investigations have been made: blood (Kempen

et al. 2015), human skin (Lamers et al. 2013) and other tissues or fluids that are under repetitive large deformation display fascinating nonlinear mechanical behavior which can be measured using the LAOS experiment.

# Bibliography


Abbasi, M., Ebrahimi, N. G., and Wilhelm, M. (2013). "Investigation of the rheological behavior of industrial tubular and autoclave LDPEs under SAOS, LAOS, transient shear, and elongational flows compared with predictions from the MSF theory". *J. Rheol.* 57, pp. 1693–1714.

Ackerson, B. J. (1990). "Shear induced order and shear processing of model hard sphere suspensions". *J. Rheol.* 34, pp. 553–590.

Allegra, G., Raos, G., and Vacatello, M. (2008). "Theories and simulations of polymer-based nanocomposites: From chain statistics to reinforcement". *Prog. Polym. Sci.* 33, pp. 683–731.

Amman, C. and Fuchs, M. (2014). "Transient stress evolution in repulsion and attraction dominated glasses". *J. Rheol.* 58, pp. 1191–1217.

Atalik, K. and Keunings, R. (2004). "On the occurrence of even harmonics in the shear stress response of viscoelastic fluids in large amplitude oscillatory shear". *J. Non-Newton. Fluid.* 122, pp. 107–116.

Bae, J.-E., Lee, M., Cho, K. S., Seo, K. H., and Kang, D.-G. (2013). "Comparison of stress-controlled and strain-controlled rheometers for large amplitude oscillatory shear". *Rheol. Acta* 52, pp. 841–857.

Ballauff, M., Brader, J. M., Egelhaaf, S. U., Fuchs, M., Horbach, J., Koumakis, N., Krüger, S., Laurati, M., Mutch, K. J., Petekidis, G., Siebenbürger, M., Voigtmann, T., and Zausch, J. (2013). "Residual Stresses in Glasses". *Phys. Rev. Lett.* 110, p. 215701.

Barker, J. G., Glinka, C. J., Moyer, J. J., Kim, M. H., Drews, A. R., and Agamalian, M. (2005). "Design and performance of a thermal-neutron double-crystal diffractometer for USANS at NIST". *J. Appl. Crystallogr.* 38, pp. 1004–1011.

Bauer Th. Lunkenheimer, P. and Loidl, A. (2015). "Nonlinear dielectric response of Debye, $\alpha$, and $\beta$ relaxation in 1-propanol". *J. Non-Cryst. Solids* 407, pp. 66–71.

Bauer, T., Lunkenheimer, P., and Loidl, A. (2013). "Cooperativity and the Freezing of Molecular Motion at the Glass Transition". *Phys. Rev. Lett.* 111, p. 225702.

Beaucage, G. (1996). "Small-Angle Scattering from Polymeric Mass Fractals of Arbitrary Mass-Fractal Dimension". *J. Appl. Cryst.* 29, pp. 134–146.

Bharadwaj, N. A. and Ewoldt, R. H. (2015). "Constitutive model fingerprints in medium-amplitude oscillatory shear". *J. Rheol.* DOI: 10.1122/1.4903346.

Bharadwaj, N. A. and Ewoldt, R. H. (2014). "The general low-frequency prediction for asymptotically nonlinear material functions in oscillatory shear". *J. Rheol.* 58, pp. 891–910.

Bhatia, S. R. (2005). "Ultra-small-angle scattering studies of complex fluids". *Curr. Opin. Colloid Interface Sci.* 9, pp. 404–411.

Bingham, E. (1916). "An Investigation of the Laws of Plastic Flow". *Bur. Stand. (U.S.), Bull.* 13, pp. 309–353.

Biot, M. A. (1942). "General Theory of Three-Dimensional Consolidation". *J. Appl. Phys.* 12, pp. 155–164.

Bird, R. B., Armstrong, R. C., and Hassager, O. (1987). *Dynamics of Polymeric Liquids*. John Wiley & Sons.

Bird, R. B. and Giacomin, A. J. (2012). "Who conceived the 'complex viscosity'?" *Rheol. Acta* 51, pp. 481–486.

Blackwell, B. C. and Ewoldt, R. H. (2014). "A simple thixotropic-viscoelastic constitutive model produces unique signatures in large-amplitude oscillatory shear (LAOS)". *J. Non-Newton. Fluid.* 27, pp. 208–209.

Boisly, M., Kästner, M., Brummund, J., and Ulbricht, V. (2014). "Large Amplitude Oscillatory Shear of the Prandtl Element Analysed by Fourier Transform Rheology". *Appl. Rheol.* 24, p. 35478.

Boukany, P. E., Wang, S.-Q., and Wang, X. (2009). "Step Shear of Entangled Linear Polymer Melts: New Experimental Evidence for Elastic Yielding". *Macromolecules* 42, pp. 6261–6269.

Boyd, R. W. (2008). *Nonlinear Optics*. Ed. by R. W. Boyd. Elsevier, Academic Press.

Brader, J. M., Cates, M. E., and Fuchs, M. (2012). "First-principles constitutive equation for suspension rheology". *Phys. Rev. E* 86, p. 021403.

Brader, J. M., Siebenbürger, M., Ballauff, M., Reinheimer, K., Wilhelm, M., Frey, S. J., Weysser, F., and Fuchs, M. (2010). "Nonlinear response of dense colloidal suspensions under oscillatory shear: Mode-coupling theory and Fourier transform rheology experiments". *Phys. Rev. E* 82, p. 061401.

Bragg, W. H. and Bragg, W. L. (1913). "The Reflection of X-rays by Crystals". *Proc. Roy. Soc. A* 88, pp. 428–438.

Bushel, G. C., Yan, Y. D., Woodfield, D., Raper, J., and Amal, R. (2002). "On techniques for the measurement of the mass fractal dimension of aggregates". *Adv. Colloid Interface Sci.* 95, pp. 1–50.

Cappelaere, E., Cressely, R., and Decruppe, J. (1995). "Linear and non-linear rheological behaviour of salt-free aqueous CTAB solutions". *Colloids Surf., A* 104, pp. 353–374.

Carotenuto, C. and Minale, M. (2013). "On the use of rough geometries in rheometry". *J. Non-Newton. Fluid.* 198, pp. 39–47.

Chambon, F. and Winter, H. H. (1987). "Linear viscoelasticity at the gel point of a cross linking PDMS with imbalanced stoichiometry". *J. Rheol.* 8, pp. 683–697.

Chan, H. K. and Mohraz, A. (2012). "Two-step yielding and directional strain-induced strengthening in dilute colloidal gels". *Phys. Rev. E* 85, p. 041403.

Chase, B., Chmilowski, W., and Dang, Y. (1997). "Clear fracturing fluids for increased well productivity". *Oilfield Review* 9, pp. 20–33.

*Chempro*. `http://www.chempro.in/palmoilproperties.htm`. Accessed: 2015-07-31.

Chen, Y.-L. and Schweizer, K. S. (2004). "Microscopic theory of gelation and elasticity in polymer-particle suspensions". *J. Chem. Phys.* 120, pp. 7212–7222.

Cho, K. S., Hyun, K., Ahn, K. H., and Lee, S. J. (2005). "A geometrical interpretation of large amplitude oscillatory shear response". *J. Rheol.* 49, pp. 747–758.

Clasen, C. and Kulicke, W.-M. (2001). "Determination of viscoelastic and rheo-optical material functions of water-soluble cellulose derivatives". *Prog. Polym. Sci.* 26, pp. 1839–1919.

Courtens, E. and Vacher, R. (1987). "Structure and Dynamics of Fractal Aerogels". *Z. Phys. B - Condensed Matter* 68, pp. 355–361.

Cox, W. P. and Merz, E. H. (1958). "Correlation of dynamic and steady flow viscosities". *J. Polym. Sci.* 28, pp. 619–622.

Crandall, S. H., Dahl, N. C., Lardner, T. J., and Sivakumar, M. S. (2012). *An Introduction to Mechanics of Solids*. Tata McGraw-Hill.

Crassous, J. J., Régisser, R., Ballauff, M., and Willenbacher, N. (2005). "Characterization of the viscoelastic behavior of complex fluids using the piezoelastic axial vibrator". *J. Rheol.* 49, pp. 851–863.

Crassous, J. J., Siebenbürger, M., Ballauff, M., Drechsler, M., Hajnal, D., Henrich, O., and Fuchs, M. (2008). "Shear stresses of colloidal dispersions at the glass transition in equilibrium and in flow". *J. Chem. Phys.* 128, p. 204902.

Crassous, J. J., Wittemann, A., Siebenbürger, M., Schrinner, M., Drechsler, M., and Ballauff, M. (2008). "Direct imaging of temperature-sensitive core-shell latexes by cryogenic transmission electron microscopy". *Colloid. Polym. Sci.* 286, pp. 805–812.

Cross, M. M. (1968). *Polymer Systems: Deformation and Flow*. Ed. by Wetton and Whorlow. Macmillan.

Cziep, M. A., Abbasi, M., Heck, M., and Wilhelm, M. (2015). "Effect of molecular weight, monomer and polydispersity of linear homopolymer melts on the intrinsic mechanical nonlinearity in MAOS". *submitted to Macromolecules*.

Dealy, J. M. and Larson, R. G. (2006). *Structure and Rheology of Molten Polymers*. Hanser.

Dealy, J. M. (2010). "Weissenberg and Deborah Numbers - Their Definition and Use". *Rheol. Bull.* 79, pp. 14–18.

Debbaut, B. and Burhin, H. (2002). "Large amplitude oscillatory shear and Fourier-transform rheology for a high-density polyethylene: Experiments and numerical simulation". *J. Rheol.* 46, pp. 1155–1176.

Debye, P. and Bueche, A. M. (1949). "Scattering by an Inhomogeneous Solid". *J. Appl. Phys.* 20, pp. 518–525.

Dimitriou, C. J., Ewoldt, R. H., and McKinley, G. H. (2013). "Describing and prescribing the constitutive response of yield stress fluids using large amplitude oscillatory shear stress (LAOStress)". *J. Rheol.* 57, pp. 27–70.

Dingenouts, N., Norhausen, C., and Ballauff, M. (1998). "Observation of the Volume Transition in Thermosensitive Core-Shell Latex Particles by Small-Angle X-ray Scattering". *Macromolecules* 31, pp. 8912–8917.

Dodge, J. S. and Krieger, I. M. (1971). "Oscillatory Shear of Nonlinear Fluids I. Preliminary Investigation". *Trans. Soc. Rheol.* 15, pp. 589–601.

Doi, M. and Edwards, S. F. (1986). *The theory of polymer dynamics*. Oxford University Press.

Doraiswamy, D., Mujumdar, A. N., Tsao, I., Beris, A. N., Danforth, S. C., and Metzner, A. B. (1991). "The Cox-Merz rule extended: A rheological model for concentrated suspensions and other materials with a yield stress". *J. Rheol.* 35, pp. 647–685.

Dörfler, H. (2002). *Grenzflächen und kolloid-disperse Systeme*. Springer.

Dusschoten, D. van and Wilhelm, M. (2001). "Increased torque transducer sensitivity via oversampling". *Rheol. Acta* 40, pp. 295–299.

Einstein, A. (1905). "Über die von der molekularkinetischen Theorie der Wärme geforderte Bewegung von in ruhenden Flüssigkeiten suspendierten Teilchen". *Ann.Phys.* 17, pp. 549–560.

Einstein, A. (1906). "Eine neue Bestimmung der Moleküldimensionen". *AdP* 19, pp. 289–306.

Einstein, A. (1911). "Berichtigung zu meiner Arbeit: Eine neue Bestimmung der Moleküldimensionen". *AdP* 34, pp. 591–592.

Ewoldt, R. H. (2009). "Nonlinear viscoelastic materials: bioinspired applications and new characterization measures". PhD thesis. Massachusetts Institute of Technology.

Ewoldt, R. H., Winter, P., Maxey, J., and McKinley, G. H. (2010). "Large amplitude oscillatory shear of pseudoplastic and elastoviscoplastic materials". *Rheol. Acta* 49, pp. 191–212.

Ewoldt, R. H., Winter, P., and McKinley, G. H. (2007). "MITlaos version 2.1 Beta for MATLAB". *self-published*.

Ewoldt, R. H. (2013). "Defining nonlinear rheological material functions for oscillatory shear". *J. Rheol.* 57, pp. 177–195.

Ewoldt, R. H. and Bharadwaj, N. A. (2013). "Low-dimensional intrinsic material functions for nonlinear viscoelasticity". *Rheol. Acta* 52, pp. 201–219.

Ewoldt, R. H., Hosoi, A. E., and McKinley, G. H. (2008). "New measures for characterizing nonlinear viscoelasticity in large amplitude oscillatory shear". *J. Rheol.* 52, pp. 1427–1458.

Fahimi, Z., Broedersz, C. P., Kempen, T. H. S. van, Florea, D., Peters, G. W. M., and Wyss, H. M. (2014). "A new approach for calculating the true stress response from large amplitude oscillatory shear (LAOS) measurements using parallel plates". *Rheol. Acta* 53, pp. 75–83.

Ferry, J. D. (1980). *Viscoelastic Properties of Polymers*. John Wiley & Sons.

Franck, A. (2003). "Measuring structure of low viscosity fluids in oscillation using rheometers with and without a separate torque transducer". *Ann. T. Nord. Rheol. Soc.* 11, RH090.

Frenet, F. (1852). "Sur les courbes à double courbure". *J. Math. Pures Appl.* 17, pp. 437–447.

Fritschi, S., Fuchs, M., and Voigtmann, T. (2014). "Mode-coupling analysis of residual stresses in colloidal glasses". *Soft Matter* 10, pp. 4822–4832.

Fuchs, M. (1995). "MCT results for a simple liquid at the glass transition". *Transport Theory Statist. Phys.* 24, pp. 855–880.

Fuchs, M. (2003). "Schematic models for dynamic yielding of sheared colloidal glasses". *Faraday Discuss.* 123, pp. 267–286.

Fuchs, M. and Cates, M. E. (2003). "Schematic models for dynamic yielding of sheared colloidal glasses". *Faraday Discuss.* 123, pp. 267–286.

Fuchs, M. and Cates, M. E. (2012). "A mode coupling theory for Brownian particles in homogeneous steady shear flow". *J. Rheol.* 53, pp. 957–1000.

Gaulin, B. D. and Spooner, S. (1987). "Kinetics of Phase Separation in $Mn_{0.67}CuO_{0.33}$". *Phys. Rev. Lett.* 59, pp. 668–671.

Gemant, A. (1935). "The conception of the complex viscosity and its application to dielectrics". *Trans. Faraday Soc.* 31, pp. 1582–1590.

Giacomin, A. J., Bird, R. B., Johnson, L. M., and Mix, A. W. (2011). "Large-amplitude oscillatory shear flow from the corotational Maxwell model". *J. Non-Newton. Fluid. Mech.* 166, pp. 1081–1099.

Giacomin, A. J. and Dealy, J. M. (1998). "Rheological Measurement". Ed. by A. A. Collyer and D. Clegg. Chapman & Hall. Chap. Using large-amplitude oscillatory shear, pp. 327–353.

Giacomin, A. J. and Jeyaseelan, R. S. (1995). "A Constitutive Theory for Polyolefins in Large Amplitude Oscillatory Shear". *Polym. Eng. Sci.* 35, pp. 768–777.

Giacomin, A. J., Jeyaseelan, R. S., and Stanfill, K. O. (1994). "Relating Blow Moldability to Large Amplitude Oscillatory Shear Behavior". *Polym. Eng. Sci.* 34, pp. 888–893.

Giacomin, A. J., Samurkas, T., and Dealy, J. M. (1989). "A Novel Sliding Plate Rheometer for Molten Plastics". *Polym. Eng. Sci.* 29, pp. 499–504.

Giacomin, A. J., Gilbert, P. H., Merger, D., and Wilhelm, M. (2015). "Large-amplitude oscillatory shear: comparing parallel-disk with cone-plate flow". *Rheol. Acta* 54, pp. 263–285.

Gibaud, T., Frelat, D., and Manneville, S. (2010). "Heterogeneous yielding dynamics in a colloidal gel". *Soft Matter* 6, pp. 3482–3488.

Gompper, G., Dhont, J. K. G., and Richter, D. (2003). "Komplexe Materialien auf mesoskopischer Skala". *Phys. Unserer Zeit* 34, pp. 12–18.

Gordon, R. J. and Balakrishnan, C. (1972). "Vortex inhibition: A new viscoelastic effect with importance in drag reduction and polymer characterization". *J. Appl. Polym. Sci.* 16, pp. 1629–1639.

Graessley, W. W. (2008). *Polymeric Liquids and Networks: Dynamics and Rheology*. Ed. by R. L. Rogers. Garland Science.

Guinier, A. and Fournet, G. (1955). *Small-Angle Scattering of X-rays*. Wiley.

Gurnon, K. A. and Wagner, N. J. (2012). "Large amplitude oscillatory shear (LAOS) measurements to obtain constitutive equation model parameters: Giesekus model of banding and nonbanding wormlike micelles". *J. Rheol.* 56, pp. 333–351.

Al-Hadithi, T. S. R., Barnes, H. A., and Walters, K. (1992). "The relationship between the linear (oscillatory) and nonlinear (steady-state) flow properties of a series of polymer and colloidal systems". *Colloid Polym. Sci.* 270, pp. 40–46.

Hayduk, W., Laudie, H., and Smith, O. H. (1973). "Viscosity, Freezing Point, Vapor-Liquid Equilibria, and Other Properties of Aqueous-Tetrahydrofuran Solutions". *J. Chem. Eng. Data* 18, pp. 373–376.

Helden, A. V., Jansen, J., and Vrij, A. (1981). "Preparation and characterization of spherical monodisperse silica dispersions in nonaqueous solvents". *J. Colloid Interface Sci.* 81, pp. 354–368.

Helgeson, M. E. a. (2010). "Formation and Rheology of Viscoelastic "Double Networks" in Wormlike Micelle-Nanoparticle Mixtures". *Langmuir* 26, pp. 8049–8060.

Helgeson, M. E., Gao, Y., Moran, S. E., Lee, J., Godfrin, M., Tripathi, A., Bose, A., and Doyle, P. S. (2014). "Homogeneous percolation versus arrested phase separation in attractively-driven nanoemulsion colloidal gels". *Soft Matter* 10, pp. 3122–3133.

Helgeson, M. E., Moran, S. E., An, H. Z., and Doyle, P. S. (2012). "Mesoporous organohydrogels from thermogelling photocrosslinkable nanoemulsions". *Nat. Mater.* 11, pp. 344–352.

Helgeson, M. E., Reichert, M. D., Hu, Y. T., and Wagner, N. J. (2009). "Relating shear banding, structure, and phase behavior in wormlike micellar solutions". *Soft Matter* 5, pp. 3858–3869.

Helgeson, M. E., Vasquez, P. A., and Wagner, N. J. (2009). "Rheology and spatially resolved structure of cetyltrimethylammonium bromide wormlike micelles through the shear banding transition". *J. Rheol.* 53, pp. 727–756.

Hellweg, T., Dewhurst, C. D., Brückner, E., Kratz, K., and Eimer, W. (2000). "Colloidal crystals made of poly(N-isopropylacrylamide) microgel particles". *Colloid Polym. Sci.* 278, pp. 972–978.

Henrich, O., Weysser, F., Cates, M. E., and Fuchs, M. (2009). "Hard discs under steady shear: comparison of Brownian dynamics simulations and mode coupling theory". *Phil. Trans. R. Soc. A* 367, pp. 5033–5050.

Herschel, W. H. and Bulkley, R. (1926). "Konsistenzmessungen von Gummi-Benzollösungen". *Kolloid-Z.* 39, pp. 291–300.

Heymans, N. (2000). "A Novel Look at Models for Polymer Entanglement". *Macromolecules* 33, pp. 4226–4234.

Hong, J. H., Mun, M. S., and Lim, T.-H. (2001). "Strain Rate Dependent Poroelastic Behavior of Bovine Vertebral Trabecular Bone". *KSME Int. J.* 15, pp. 1032–1040.

Hoyle, D. M., Auhl, D., Harlen, O. G., Barroso, V. C., Wilhelm, M., and McLeish, T. C. B. (2014). "Large amplitude oscillatory shear and Fourier transform rheology analysis of branched polymer melts". *J. Rheol.* 58, pp. 969–997.

Hsiao, L. C., Newman, R. S., Glotzer, S. C., and Solomon, M. J. (2012). "Role of isostaticity and load-bearing microstructure in the elasticity of yielded colloidal gels". *Proc. Natl. Acad. Sci. USA* 109, pp. 16029–16034.

Hunt, A., Ewing, R., and Ghanbarian, B. (2014). *Percolation Theory for Flow in Porous Media*. Springer.

Hyun, K., Kim, W., Park, S. J., and Wilhelm, M. (2013). "Numerical simulation results of the nonlinear coefficient Q from FT-Rheology using a single mode pom-pom model". *J. Rheol.* 57, pp. 1–25.

Hyun, K. and Wilhelm, M. (2009). "Establishing a New Mechanical Nonlinear Coefficient Q from FT-Rheology: First Investigation of Entangled Linear and Comb Polymer Model Systems". *Macromolecules* 42, pp. 411–422.

Hyun, K., Wilhelm, M., Klein, C. O., Cho, K. S., Nam, J. G., Ahn, K. H., Lee, S. J., Ewoldt, R. H., and McKinley, G. H. (2011). "A review of nonlinear oscillatory shear tests: Analysis and application of large amplitude oscillatory shear (LAOS)". *Prog. Polym. Sci.* 36, pp. 1697–1753.

Ikeda, A., Berthier, L., and Sollich, P. (2013). "Disentangling glass and jamming physics in the rheology of soft materials". *Soft Matter* 9, pp. 7669–7683.

Isrealachvili, J. N. (1997). *Intermolecular and Surface Forces*. Academic Press.

Jeyaseelan, R. S. and Giacomin, A. J. (1993). "Best fit for differential constitutive model parameters to non-linear oscillation data". *J. Non-Newton. Fluid. Mech.* 47, pp. 267–280.

Kadoma, I. A., Ylitalo, C., and Egmond, J. W. van (1997). "Structural transitions in wormlike micelles". *Rheol. Acta* 36, pp. 1–12.

Kallus, S., Willenbacher, N., Kirsch, S., Distler, D., Neidhöfer, T., Wilhelm, M., and Spiess, H. W. (2001). "Characterisation of polymer dispersions by Fourier transform rheology". *Rheol. Acta* 40, pp. 552–559.

Kaufmann, L. J. and Weitz, D. A. (2006). "Direct imaging of repulsive and attractive colloidal glasses". *J. Phys. Chem.* 125, p. 074716.

Kempen, T. H. S. van, Donders, W. P., Vosse, F. N. van de, and Peters, G. W. M. (2015). "A constitutive model for developing blood clots with various compositions and their nonlinear viscoelastic behavior". *Biomech. Model. Mechanobiol.* DOI 10.1007/s10237-015-0686-9.

Kempf, M., Ahirwal, D., Cziep, M. A., and Wilhelm, M. (2013). "Synthesis and Linear and Nonlinear Melt Rheology of Well-Defined Comb Architectures of PS and PpMS with a Low and Controlled Degree of Long-Chain Branching". *Macromolecules* 46, pp. 4978–4994.

Khatory, A., Lequeux, F., Kern, F., and Candau, S. J. (1993). "Linear and Nonlinear Viscoelasticity of Semidilute Solutions of Wormlike Micelles at High Salt Content". *Langmuir* 9, pp. 1456–1464.

Kim, J. M., Eberle, A. P. R., Gurnon, K. A., Porcar, L., and Wagner, N. J. (2014). "The microstructure and rheology of a model, thixotropic nanoparticle gel under steady shear and large amplitude oscillatory shear (LAOS)". *J. Rheol.* 58, pp. 1301–1328.

Kim, J., Gao, Y., Hebebrand, C., Peirtsegaele, E., and Helgeson, M. E. (2013). "Polymer-surfactant complexation as a generic route to responsive viscoelastic nanoemulsions". *Soft Matter* 9, pp. 6897–6910.

Kim, J., Merger, D., Wilhelm, M., and Helgeson, M. E. (2014). "Microstructure and nonlinear signatures of yielding in a heterogeneous colloidal gel under large amplitude oscillatory shear". *J. Rheol.* 58, pp. 1359–1390.

Klein, C., Spiess, H. W., Calin, A., Balan, C., and Wilhelm, M. (2007). "Separation of the Nonlinear Oscillatory Response into a Superposition of Linear, Strain Hardening, Strain Softening, and Wall Slip Response". *Macromolecules* 40, pp. 4250–4259.

Kob, W. (2002). "Supercooled liquids, the glass transition, and computer simulations". *Les Houches 2002 Summer School - Session LXXVII.*

Koumakis, N., Moghimi, E., Besseling, R., Poon, W. C. K., Brady, J. F., and Petekidis, G. (2015). "Tuning colloidal gels by shear". *Soft Matter* 11, pp. 4640–4648.

Koumakis, N. and Petekidis, G. (2011). "Two step yielding in attractive colloids: transition from gels to attractive glasses". *Soft Matter* 7, pp. 2456–2470.

Koumakis, N., Schofield, A. B., and Petekidis, G. (2008). "Effects of shear induced crystallization on the rheology and ageing of hard sphere glasses". *Soft Matter* 4, pp. 2008–2018.

Krieger, I. M. and Dougherty, T. J. (1959). "A Mechanism for Non-Newtonian Flow in Suspensions of Rigid Spheres". *Trans. Soc. Rheol.* 3, pp. 137–152.

Krieger, I. M. and Niu, T.-F. (1973). "A rheometer for oscillatory studies of nonlinear fluids". *Rheol. Acta* 12, pp. 567–571.

Kulicke, W.-M. and Porter, R. S. (1980). "Relation between steady shear flow and dynamic rheology". *Rheol. Acta* 19, pp. 601–605.

Kyu, H., Kim, S. H., Ahn, K. H., and Lee, S. J. (2002). "Large amplitude oscillatory shear as a way to classify the complex fluids". *J. Non-Newton. Fluid.* 107, pp. 51–65.

Lamers, E., Kempen, T. H. S. van, Baaijens, F. P. T., Peters, G. W. M., and Oomens, C. W. J. (2013). "Large amplitude oscillatory shear properties of human skin". *J. Mech. Behav. Biomed. Mater.* 28, pp. 462–470.

Langela, M., Wiesner, U., Spiess, H. W., and Wilhelm, M. (2002). "Microphase Reorientation in Block Copolymer Melts As Detected via FT Rheology and 2D SAXS". *Macromolecules* 35(8), pp. 3198–3204.

Larson, R. G. (1999). *The Structure and Rheology of Complex Fluids.* Oxford University Press.

Läuger, J. and Stettin, H. (2010). "Differences between stress and strain control in the non-linear behavior of complex fluids". *Rheol. Acta* 49, pp. 909–930.

Läuger, J., Wollny, K., and Huck, S. (2002). "Direct Strain Oscillation: a new oscillatory method enabling measurements at very small shear stresses and strains". *Rheol. Acta* 41, pp. 356–361.

Laurati, M., Egelhaaf, S. U., and Petekidis, G. (2011). "Nonlinear rheology of colloidal gels with intermediate volume fraction". *J. Rheol.* 55, pp. 673–706.

Laurati, M., Egelhaaf, S. U., and Petekidis, G. (2014). "Plastic rearrangements in colloidal gels investigated by LAOS and LS-Echo". *J. Rheol.* 58, pp. 1395–1417.

Lettinga, M. P., Holmqvist, P., Ballesta, P., Rogers, S., Kleshchanok, D., and Struth, B. (2012). "Nonlinear Behavior of Nematic Platelet Dispersions in Shear Flow". *Phys. Rev. Lett.* 109 (24), p. 246001.

Li, J.-C. and Ross, D. K. (1994). "Dynamical scaling for spinodal decomposition-a small-angle neutron scattering study of porous Vycor glass with fractal properties". *J. Phys.: Condens. Matter* 6, pp. 351–362.

Lionberger, R. A. and Russel, W. B. (1994). "High frequency modulus of hard sphere colloids". *J. Rheol.* 38, pp. 1885–1908.

Macosko, C. W. (1994). *Rheology Principles, Measurements, and Applications*. Weinheim: Wiley-VCH.

MacSporran, W. C. and Spiers, R. P. (1984). "The dynamic performance of the Weissenberg rheogoniometer III. Large amplitude oscillatory shearing - harmonic analysis". *Rheol. Acta* 23, pp. 90–97.

Malkin, A. (2013). "Non-Newtonian viscosity in steady-state shear flows". *J. Non-Newton. Fluid.* 192, pp. 48–65.

Mark, J. E. (2007). *Physical Properties of Polymers Handbook*. Springer.

Mason, T., Graves, S., Wilking, J., and Lin, M. (2006). "Extreme emulsification: formation and structure of nanoemulsions". *Condensed Matter Physics* 9, pp. 193–199.

McKinley, G. H. (2015). "A Hitchhikers Guide to Complex Fluids". *Rheol. Bull.* 84, pp. 14–17.

McMullan, J. M. and Wagner, N. J. (2009). "Directed self-assembly of suspensions by large amplitude oscillatory shear flow". *J. Rheol.* 53, pp. 575–588.

Medronho, B., Fujii, S., Richtering, W., Miguel, M. G., and Olson, U. (2005). "Reversible size of shear-induced multi-lamellar vesicles". *Colloid Polym. Sci.* 284, pp. 317–321.

Megen, W. van and Pusey, P. N. (1991). "Dynamic light-scattering study of the glass transition in a colloidal suspension". *Phys. Rev. A* 43, pp. 5429–5441.

Meins, T., Hyun, K., Dingenouts, N., Fotouhi Ardakani, M., Struth, B., and Wilhelm, M. (2012). "New Insight to the Mechanism of the Shear-Induced Macroscopic Alignment of Diblock Copolymer Melts by a Unique and Newly Developed Rheo-SAXS Combination". *Macromolecules* 45, pp. 455–472.

Merger, D., Abbasi, M., Merger, J., Giacomin, A. J., and Wilhelm, M. (2015). "Simple scalar Maxwell-inspired model for Large Amplitude Oscillatory Shear". *to be submitted to Rheol. Acta.*

Merger, D. and Wilhelm, M. (2014). "Intrinsic Nonlinearity from LAOStrain-Experiments on various strain and stress-controlled rheometers: A quantitative comparison". *Rheol. Acta* 53, pp. 621–634.

Mewis, J. and Wagner, N. J. (2009). "Thixotropy". *Adv. Colloid Interface Sci.* 147, pp. 214–227.

Mewis, J. and Wagner, N. (2012). *Colloidal Suspension Rheology.* Cambridge University Press.

Mezger, T. G. (2006). *The Rheology Handbook.* Vincentz Network.

Monsia, M. D. (2011). "A Simplified Nonlinear Generalized Maxwell Model for Predicting the Time Dependent Behavior of Viscoelastic Materials". *WJM* 1, pp. 158–167.

Morrison, F. A. (2001). *Unterstanding Rheology.* Oxford University Press.

Nam, J. G., Ahn, K. H., Lee, S. J., and Hyun, K. (2010). "First normal stress difference of entangled polymer solutions in large amplitude oscillatory shear flow". *J. Rheol.* 54, pp. 1243–1266.

Oelschlaeger, C., Gutmann, J. S., Wolkenhauer, M., Spiess, H.-W., Knoll, K., and Wilhelm, M. (2007). "Kinetics of Shear Microphase Orientation and Reorientation in Lamellar Diblock and Triblock Copolymer Melts as Detected via FT-Rheology and 2D-SAXS". *Macromol. Chem. Phys.* 208, pp. 1719–1729.

Ostwald, W. (1925). "Ueber die Geschwindigkeitsfunktion der Viskosität disperser Systeme. II". *Kolloid- Z.* 36, pp. 157–167.

Panine, P., Narayanan, T., Vermant, J., and Mewis, J. (2002). "Structure and rheology during shear-induced crystallization of a latex suspension". *Phys. Rev. E* 66, p. 022401.

Payne, A. R. (1962). "The Dynamic Properties of Carbon Black-Loaded Natural Rubber Vulcanizates". *J. Appl. Polym. Sci.* VI, pp. 57–63.

Pearson, D. S. and Rochefort, W. E. (1982). "Behavior of concentrated polystyrene solutions in large-amplitude oscillating shear fields". *J. Polym. Sci., Part B: Polym. Phys.* 20, pp. 83–98.

Phan, S. E., Russel, W. B., Zhu, J. X., and Chaikin, P. M. (1998). "Effects of polydispersity on hard sphere crystals". *J. Chem. Phys.* 108, pp. 9789–9795.

Pignon, F., Magnin, A., Piau, J.-M., Cabane, B., Lindner, P., and Diat, O. (1997). "Yield stress thixotropic clay suspension: Investigations of structure by light, neutron, and x-ray scattering". *Phys. Rev. E* 56, pp. 3281–3289.

Pipkin, A. C. (1972). *Lectures in Viscoelastic Theory.* Springer.

Porcar, L., Pozzo, D., Langenbucher, G., G., M., and Butler, P. D. (2011). "Rheo-small-angle neutron scattering at the National Institute of Standards and Technology Center for Neutron Research". *Rev. Sci. Instrum.* 82, p. 083902.

Poulos, A. S., Renou, F., Jacob, A. R., Koumakis, N., and Petekidis, G. (2015). "Large amplitude oscillatory shear (LAOS) in model colloidal suspensions and glasses: frequency dependence". *Rheol. Acta* DOI: 10.1007/s00397-015-0865-8.

Poulos, A. S., Stellbrink, J., and Petekidis, G. (2013). "Flow of concentrated solutions of starlike micelles under large-amplitude oscillatory shear". *Rheol. Acta* 52, pp. 785–800.

Rajaram, B. and Mohraz, A. (2011). "Dynamics of shear-induced yielding and flow in dilute colloidal gels". *Phys. Rev. E* 84, p. 011405.

Rehage, H. and Hoffmann, H. (1991). "Viscoelastic surfactant solutions: model systems for rheological research". *Mol. Phys.* 74, pp. 933–973.

Reinheimer, K., Grosso, M., Hetzel, F., Kübel, J., and Wilhelm, M. (2012). "Fourier Transform Rheology as an innovative morphological characterization technique for the emulsion volume average radius and its distribution". *J. Colloid Interface Sci.* 380, pp. 201–212.

Reinheimer, K., Grosso, M., and Wilhelm, M. (2011). "Fourier Transform Rheology as a universal non-linear mechanical characterization of droplet size and interfacial tension of dilute monodisperse emulsions". *J. Colloid Interface Sci.* 360, pp. 818–825.

Renou, F., Stellbrink, J., and Petekidis, G. (2010). "Yielding processes in a colloidal glass of soft star-like micelles under large amplitude oscillatory shear (LAOS)". *J. Rheol.* 54, pp. 1219–1242.

Rodrigues, R. K., Silva, M. A. da, and Sabadini, E. (2008). "Worm-like Micelles of CTAB and Sodium Salicylate under Turbulent Flow". *Langmuir* 24, pp. 13875–13879.

Rogers, S., Calabrese, M. A., and Wagner, N. J. (2014). "Rheology of branched wormlike micelles". *J. Colloid Interface Sci.* 19, pp. 530–535.

Rogers, S., Erwin, B. M., Vlassopoulos, D., and Cloitre, M. (2011a). "Oscillatory yielding of a colloidal star glass". *J. Rheol.* 55, pp. 733–752.

Rogers, S. A. (2012). "A sequence of physical processes determined and quantified in LAOS: An instantaneous local 2D/3D approach". *J. Rheol.* 56, pp. 1129–1151.

Rogers, S. A., Erwin, B. M., Vlassopoulos, D., and Cloitre, M. (2011b). "A sequence of physical processes determined and quantified in LAOS: Application to a yield stress fluid". *J. Rheol.* 55, pp. 435–458.

Rogers, S. A. and Lettinga, M. P. (2012). "A sequence of physical processes determined and quantified in large amplitude oscillatory shear (LAOS): Application to theoretical nonlinear models". *J. Rheol.* 56, pp. 1–25.

Rouyer, F., Cohen-Addad, S., Höhler, R., Sollich, P., and Fielding, S. M. (2008). "The large amplitude oscillatory strain response of aqueous foam: Strain localization and full stress Fourier spectrum". *Eur. Phys. J. E* 27, pp. 309–321.

Rutgers, R. (1962). "Relative viscosity and concentration". *Rheol. Acta* 2, pp. 305–348.

Saeed2011, F., Ansarifar, A., Ellis, R. J., Haile-Meskel, Y., and Irfan, M. S. (2011). "Two Advanced Styrene-Butadiene/Polybutadiene Rubber Blends Filled with a Silanized Silica Nanofiller for Potential Use in Passenger Car Tire Tread Compound". *J. Appl. Polym. Sci.* 123, pp. 1518–1529.

Saengow, C., Giacomin, A. J., and C., K. (2015). "Exact Analytical Solution for Large-Amplitude Oscillatory Shear Flow". *Macromol. Theory Simul.* 24, pp. 352–392.

Sagis, L., M., R., and Linden, E. van der (2001). "Constitutive equations for an elastic material with anisotropic rigid particles". *Phys. Rev. E* 63, p. 051504.

Schiener, B., Böhmer, R., Loidl, A., and Chamberlin, R. V. (1996). "Nonresonant Spectral Hole Burning in the Slow Dielectric Response of Supercooled Liquids". *Science* 274, pp. 752–754.

Schweizer, T. (2003). "Comparing cone-partitioned plate and cone-standard plate shear rheometry of a polystyrene melt". *J. Rheol.* 47, pp. 1071–1085.

Serret, J.-A. (1851). "Sur quelques formules relatives à la théorie des courbes à double courbure". *J. Math. Pures Appl.* 16, pp. 193–207.

Seyboldt, R. (2013). "Higher harmonics in colloid rheology". MA thesis. Universität Konstanz.

Shao, Z., Negi, A. S., and Osuji, C. O. (2013). "Role of interparticle attraction in the yielding response of microgel suspensions". *Soft Matter* 9, pp. 5492–5500.

Shaw, M. T. (2012). *Introduction to Polymer Rheology*. Wiley.

Showalter, R. and Momken, D. (2002). "Single-phase flow in composite poroelastic media". *Math. Methods Appl. Sci.* 25, pp. 115–139.

Siebenbürger, M. (2006). "Viskoelastizität von konzentrierten kolloidalen Suspensionen und der Glasübergang". MA thesis. Universität Bayreuth.

Siebenbürger, M., Fuchs, M., Winter, H., and Ballauff, M. (2009). "Viscoelasticity and shear flow of concentrated, noncrystallizing colloidal suspensions: Comparison with mode-coupling theory". *J. Rheol.* 53, pp. 707–726.

Sirota, E. B., Ou-Yang, H. D., Sinha, S. K., and Chaikin, P. M. (1989). "Complete Phase Diagram of a Charged Colloidal System: A Synchrotron X-Ray Scattering Study". *Phys. Rev. Lett.* 13, pp. 1524–1527.

Snijkers, F. and Vlassopoulos, D. (2014). "Appraisal of the Cox-Merz rule for well-characterized entangled linear and branched polymers". *Rheol. Acta* 53, pp. 935–946.

Song, C. H. and Huang, L. H. (2000). "Laminar poroelastic media flow". *J. Eng. Mech.* 126, pp. 358–366.

Souza Mendes, P. R. de, Thompson, R. L., Alicke, A. A., and Leite, R. T. (2014). "The quasilinear large-amplitude viscoelastic regime and its significance in the rheological characterization of soft matter". *J. Rheol.* 58, pp. 537–561.

Spalla, O., Lyonnard, S., and Testard, F. (2003). "Analysis of the small-angle intensity scattered by a porous and granular medium". *J. Appl. Crystallogr.* 36, pp. 338–347.

Struth, B., Hyun, K., Kats, E., Meins, T., Walther, M., Wilhelm, M., and Grübel, G. (2011). "Observation of New States of Liquid Crystal 8CB under Nonlinear Shear Conditions as Observed via a Novel and Unique Rheology/ Small-Angle X-ray Scattering Combination". *Langmuir* 27, pp. 2880–2887.

Tarzia, M., Biroli, G., Lefèvre, A., and Bouchaud, J.-F. (2010). "Anomalous nonlinear response of glassy liquids: General arguments and a mode-coupling approach". *J. Chem. Phys.* 132, p. 054501.

Teixeira, J. (1988). "Small-Angle Scattering by Fractal Systems". *J. Appl. Cryst.* 21, pp. 781–785.

Thompson, R. L., A, A., Alicke, and Souza Mendes, P. R. de (2015). "Model-based material functions for SAOS and LAOS analyses". *J. Non-Newton. Fluid.* 215, pp. 19–30.

Ting, R. Y. and Hunston, D. L. (1977). "Polymeric Additives as Flow Regulators". *Ind. Eng. Chem. Prod. Res. Dev.* 16, pp. 129–136.

Vaart, K. van der, Rahmani, Y., Zargar, R., Hu, Z., Bonn, D., and Schall, P. (2013). "Rheology of concentrated soft and hard-sphere suspensions". *J. Rheol.* 57, pp. 1195–1209.

Wagner, M., Rolón-Garrido, V. H., Hyun, K., and Wilhelm, M. (2011). "Analysis of medium amplitude oscillatory shear data of entangled linear and model comb polymers". *J. Rheol.* 55, pp. 495–516.

Wang, S.-Q. (2015). "Nonlinear rheology of entangled polymers at turning point". *Soft Matter* 11, pp. 1454–1458.

Weast, R. C., ed. (1976). *Handbook of Chemistry and Physics*. CRC Press.

Whitaker, S. (1986). "Flow in Porous Media I: A Theoretical Derivation of Darcy's Law". *Transport Porous Med.* 1, pp. 3–25.

White, J. L. and Metzner, A. B. (1963). "Development of constitutive equations for polymeric melts and solutions". *J. Appl. Polym. Sci.* 7, pp. 1867–1889.

Wilhelm, M., Maring, D., and Spiess, H.-W. (1998). "Fourier-transform rheology". *Rheol. Acta* 37, pp. 399–405.

Wilhelm, M., Reinheimer, P., and Ortseifer, M. (1999). "High sensitivity Fourier-transform rheology". *Rheol. Acta* 38, pp. 349–356.

Wilhelm, M. (2002). "Fourier-Transform Rheology". *Macromol. Mater. Eng.* 287, pp. 83–105.

Wilhelm, M., Reinheimer, K., and Kübel, J. (2012). "Optimizing the Sensitivity of FT-Rheology to Quantify and Differentiate for the First Time the Nonlinear Mechanical Response of Dispersed Beer Foams of Light and Dark Beer". *Z. Phys. Chem.* 226, pp. 547–567.

Wilhelm, M., Reinheimer, P., Ortseiferer, M., Neidhöfer, T., and Spiess, H. W. (2000). "The crossover between linear and non-linear mechanical behavior in polymer solutions as detected by Fourier-transform rheology". *Rheol. Acta* 39, pp. 241–246.

Willenbacher, N., Vesaratchanon, J. S., Thorwarth, O., and Bartsch, E. (2011). "An alternative route to highly concentrated, freely flowing colloidal dispersions". *Soft Matter* 7, pp. 5777–5788.

Winter, H. H. (1987). "Can the gel point of a crosslinking polymer be detected by the G'-G" crossover?" *Polym. Eng. Sci.* 27, pp. 1698–1701.

Wong, P. and Cao, Q. (1992). "Correlation function and structure factor for a mass fractal bounded by a surface fractal". *Phys. Rev. B* 45, pp. 7627–7633.

Wyss, H. M., Tervoort, E. V., Meier, L. P., Müller, M., and Glauckler, L. J. (2004). "Relation between microstructure and mechanical behavior of concentrated silica gels". *J. Colloid Interface Sci.* 273, pp. 455–462.

Yan, Y., Dhont, J. K. G., Smits, C., and Lekkerkerker, H. N. W. (1994). "Oscillatory-shear-induced order in nonaqueous dispersions of charged colloidal spheres". *Physica A* 202, pp. 68–80.

Yang, J. (2002). "Viscoelastic wormlike micelles and their applications". *Curr. Opin. Colloid Interface Sci.* 7, pp. 276–281.

Yasuda, K., Armstrong, R., and Cohen, R. (1981). "Shear flow properties of concentrated solutions of linear and star branched polystyrenes". *Rheol. Acta* 20, pp. 163–178.

Yosick, J. A., Giacomin, A. J., and Moldenaers, P. (1997). "A kinetic network model for nonlinear flow behavior of molten plastics in both shear and extension". *J. Non-Newton. Fluid. Mech.* 70, p. 103.

Young, R. J. and Lovell, P. A. (2011). *Introduction to Polymers*. CRC Press.

Zacharatos, A. and Kontou, E. (2015). "Nonlinear viscoelastic modeling of soft polymers". *J. Appl. Polym. Sci.* DOI: 10.1002/APP.42141.

Zhang, Z. and Christopher, G. F. (2015). "The nonlinear viscoelasticity of hyaluronic acid and its role in joint lubrication". *Soft Matter* 11, pp. 2596–2603.

Zou, W., Tang, X., Weaver, M., Koenig, P., and Larson, R. G. (2015). "Determination of characteristic lengths and times for wormlike micelle solutions from rheology using a mesoscopic simulation method". *J. Rheol.* 59, pp. 903–934.

# Appendix

## Coefficients for the solution of the corotational Maxwell model

The following table lists the Deborah number ($De = \lambda\omega$) dependent coefficients for Eqs. 4.5 through 4.8 in Section 4.3, page 61, rewritten from the work of Giacomin et al. (2015).

| $m$ | $n$ | $A_{mn}$ | $B_{mn}$ |
|---|---|---|---|
| 3 | 1 | $\frac{1}{2(1+4De^2)}$ | $\frac{De}{(1+4De^2)}$ |
| 5 | 1 | $-\frac{5}{16(1+4De^2)(1+9De^2)}$ | $-\frac{15De}{16(1+4De^2)(1+9De^2)}$ |
| 3 | 3 | $\frac{\left(1-11De^2\right)}{6(1+4De^2)(1+9De^2)}$ | $\frac{\left(1-De^2\right)De}{(1+4De^2)(1+9De^2)}$ |
| 5 | 3 | $-\frac{\left(5-130De^2\right)}{32(1+4De^2)(1+9De^2)(1+16De^2)}$ | $-\frac{\left(45-120De^2\right)De}{32(1+4De^2)(1+9De^2)(1+16De^2)}$ |
| 5 | 5 | $-\frac{1-85De^2+274De^4}{32(1+4De^2)(1+9De^2)(1+16De^2)(1+25De^2)}$ | $-\frac{(15-225De^2+120De^4)De}{32(1+4De^2)(1+9De^2)(1+16De^2)(1+25De^2)}$ |
| $m$ | $n$ | $C_{mn}$ | $D_{mn}$ |
| 3 | 1 | $\frac{3}{4(1+4De^2)}$ | $\frac{3De}{(1+4De^2)}$ |
| 5 | 1 | $-\frac{5}{8(1+4De^2)(1+9De^2)}$ | $-\frac{15De}{8(1+4De^2)(1+9De^2)}$ |
| 3 | 3 | $\frac{\left(1-11De^2\right)}{4(1+4De^2)(1+9De^2)}$ | $\frac{3\left(1-De^2\right)De}{2(1+4De^2)(1+9De^2)}$ |
| 5 | 3 | $-\frac{\left(5-130De^2\right)}{8(1+4De^2)(1+9De^2)(1+16De^2)}$ | $-\frac{\left(45-120De^2\right)De}{16(1+4De^2)(1+9De^2)(1+16De^2)}$ |
| 5 | 5 | $-\frac{1-85De^2+274De^4}{16(1+4De^2)(1+9De^2)(1+16De^2)(1+25De^2)}$ | $-\frac{(15-225De^2+120De^4)De}{16(1+4De^2)(1+9De^2)(1+16De^2)(1+25De^2)}$ |

**Table 8.3:** Coefficients for the solution of the corotational Maxwell model in Eqs. 4.5 through 4.8 from Section 4.3, page 61.

## Coefficients for the solution of the modified Maxwell model with Cox-Merz rule

The following table lists the Deborah number ($De = \lambda\omega$) dependent coefficients for the $I_{3/1}$ expression in the modified Maxwell model (Eq. 5.13) from Section 5.2, page 85. The solution has been derived by Mahdi Abbasi.

| $m$ | $n$ | $G'_{mn}$ | $G''_{mn}$ |
|---|---|---|---|
| 1 | 1 | $G\frac{De^2}{1+De^2}$ | $G\frac{De}{1+De^2}$ |
| 3 | 1 | $-\frac{1}{2}G\frac{De^4}{(1+De^2)^2}$ | $\frac{1}{8}G\frac{De^3(De^2-3)}{(1+De^2)^2}$ |
| 3 | 3 | $-\frac{1}{2}G\frac{De^4}{(1+De^2)(1+9De^2)}$ | $\frac{1}{8}G\frac{De^3(3De^2-1)}{(1+De^2)(1+9De^2)}$ |

**Table 8.4:** Coefficients for the $I_{3/1}$ expression in the modified Maxwell model (Eq. 5.13) from Section 5.2, page 85.

# MATLAB code for numerical calculations and Fourier transform analysis

Numerical calculations in Chapter 5 were performed using the following MATLAB scripts and functions.
The main script that handles parameter input ($G$, $\lambda$, sampling rate, number of cycles to be calculated, $\gamma_0$ and $\omega$ range), performs data analysis and plots figures is *ModelingScript.m*.

### *ModelingScript.m*

```
%% Script for numerical solutions of differential constitutive ...
    equations
%  Dimitri Merger 21.08.2015

close all
clear all

set(0,'defaulttextinterpreter','tex')

% Switches and ...
    parameters_____________________________________________
%_____________________________________________________________________________
fileName = 'results';               %specify name of the results file


liss = 1;   % [0 or 1] switch for lissajous figure display,
            %setting to 1 shows lissajous figures for every ...
                calculates pair
            %of angular frequency and strain amplitude

% Excitation and sampling parameters ...
    ---------------------------------------

w_range = [1];          %specify angular frequency w (or range)
g0_range = [1] ;    % specfify strain amplitude g0 (or range)

s_rate = 512;       % sampling rate, time points calculated per cycle
nocy = 35;          % number of cycles per w and g0
Ncycles = [];       % initialize additinal variable for number of ...
    cycles
Amp = [];           % initialize additinal variable for g0


% Model parameters ...
```

```
    ------------------------------------------------------
30
31 lambda = 1;       % [s] relaxation time in the model
32 lambda2 = 100;    % [s] additional relaxation time in the two ...
    relaxation...
33                   % time model, will be ignored in other models
34 G = 10;           % [Pa] Elastic modulus
35 eta = G*lambda;   % [Pas] Zero shear viscosity
36 eta_inf = eta/100;      % [Pas] high frequency limiting viscosity
37                         % (will be only used if the correct model is ...
                               chosen)
38
39 c = 0.6;           % []alpha = c-1 !!!set to 0 for newton,
40                   % to -1 for max shear thinning
41                   % (will be only used if the correct model is chosen)
42 alpha = c-1;       % c = alpha + 1, if c = 1 ->Newton
43
44 scrsz = get(0,'ScreenSize');
45
46 %% _____________________ Calculation loops ...
    ----------------------------
47 for w_index = 1:length(w_range)          % loop through all w
48
49  w = w_range(w_index); % [rad/s]
50  f = w/2/pi;           % [Hz]   frequency
51  T = 1/f;              % Duration of a cycle [s]
52  De = w.*lambda;       % Deborah number
53
54 for index = 1:length(g0_range) % loop through all amplitudes
55
56 Amp{index} = g0_range(index);   % pick strain amplitude from range
57
58 %_____________________ call solver passing all relevant parameters
59 [t, strain, rate, sig2] = solver(Amp{index},G, lambda, lambda2, ...
    eta, eta_inf, alpha, f, nocy, s_rate);
60
61 %____________________________ cut off start-up ...
    _________________________%
62 Ncycles{index} = 5;     % specify # of last cycles will be analyzed
63                          % if 5 then the 5 final cycles go to FT, all
64                          % preceding cycles will be discarded for the
65                          % analysis
66 start = (nocy-Ncycles{index})*s_rate+1;
67 t_c = t(start:end-1);
68 strain_c = strain(start:end-1);        % trimmed  strain signal
69 rate_c = rate(start:end-1);            % trimmed  rate signal
```

```
70 sig_c = sig2(start:end-1);              % trimmed  stress signal
71
72 %_____________________________ Call FT function  ...
       _________________________%
73 [stressA0{index}, stressAn{index}, stressBn{index}] = ...
       Fourier_Transform(sig_c);
74
75
76 %_____________________________ Calculate intensities   ...
       _________________________%
77 InS{index} = sqrt(stressAn{index}.^2 + stressBn{index}.^2); % ...
       Magnitude spectrum
78
79 I1{index} = InS{index}(1*Ncycles{index});   % I1
80 delta1{index} = atan( stressAn{index}(Ncycles{index}) / ...
       stressBn{index}(Ncycles{index}));     % 1st phase
81
82 Gp{index} = I1{index}/Amp{index}*cos(delta1{index});    % G'
83 Gpp{index}= I1{index}/Amp{index}*sin(delta1{index});    % G''
84
85 I21{index} = ...
       InS{index}(2*Ncycles{index})/InS{index}(Ncycles{index});   % ...
       relative 2nd harmonic
86 delta2{index} = atan( stressAn{index}(2*Ncycles{index}) / ...
       stressBn{index}(2*Ncycles{index}));     % 2nd phase
87
88 I31{index} = ...
       InS{index}(3*Ncycles{index})/InS{index}(Ncycles{index});   % ...
       relative 3rd harmonic
89 delta3{index} = atan( stressAn{index}(3*Ncycles{index}) / ...
       stressBn{index}(3*Ncycles{index}));     % 3rd phase
90
91 I51{index} = ...
       InS{index}(5*Ncycles{index})/InS{index}(Ncycles{index});   % ...
       relative 5th harmonic
92 delta5{index} = atan( stressAn{index}(5*Ncycles{index}) / ...
       stressBn{index}(5*Ncycles{index}));     % 5th phase
93
94 I71{index} = ...
       InS{index}(7*Ncycles{index})/InS{index}(Ncycles{index});   % ...
       relative 7th harmonic
95 delta7{index} = atan( stressAn{index}(7*Ncycles{index}) / ...
       stressBn{index}(7*Ncycles{index}));     % 7th phase
96
97 InSnorm{index} = InS{index}./I1{index};  % normalized spectrum
98
```

```
99 Q{index} = I31{index}/(Amp{index}^2);   % Q coefficient, ! not Q0 !
100
101 %_________________________ Plotting Section ...
      ------------------------------
    %%%%%%%%%%%%%%%%%%%%%% X-Axis for FT spectra %%%%%%%%%%%%%%%%%%%%%%
103
104 SpecRes{index} = 1/Ncycles{index};
105 SpecResAxis{index} = (SpecRes{index}: SpecRes{index}: ...
      (length(InS{index})/Ncycles{index}));
106
107
108  %%%%%%%%%%%%%Print .txt files for Frequency spectrum of each ...
       measurement
109 newfilename = strrep(fileName, '.txt', '');
110
111 savefile = ['FT' char('_') 'Spectrum' char('_') 'g=' ...
      num2str(Amp{index}) 'w=' num2str(w) '.txt' ];
112 FFTTable = [SpecResAxis{index} ;InSnorm{index} ];
113
114 %___________ Lissajous plots and spectra _________________________
115 if liss == 1;
116     Title = ['G = ' num2str(G) ' Pa; ' '\lambda = ' num2str(lambda) ...
          ' s; '];
117     Title = [Title 'De = ' num2str(De) ' ; ' '\gamma_0 = ' ...
          num2str(Amp{index},'%6.2e')];
118     figure('Position', [scrsz(3)/10 scrsz(4)/10 scrsz(3)/1.4 ...
          scrsz(4)/1.4])
119
120
121     subplot(2,2,1)
122     plot(rate, sig2);set(gca,'fontsize', 15,'FontWeight','bold')
123     xlabel('shear rate[1/s]'); ylabel('\sigma [Pa]');
124     title(Title);
125
126     subplot(2,2,2)
127     plot(strain, sig2);set(gca,'fontsize', 15,'FontWeight','bold')
128     xlabel('strain'); ylabel('\sigma [Pa]');
129
130     subplot(2,2,3)
131     plot(t/T, rate/max(rate), t/T, strain/max(strain), ...
          t/T,sig2/max(sig2));set(gca,'fontsize', 15,'FontWeight','bold')
132     xlabel('t/t_0'); ylabel('\sigma [Pa]');
133     legend('norm. shear rate','norm. strain','norm. stress');
134
135     subplot(2,2,4)
136     semilogy(FFTTable(1,:),FFTTable(2,:));set(gca,'fontsize', ...
```

```
        15,'FontWeight','bold')
137     xlabel('\omega/\omega_0'); ylabel('I_{n/1}');
138
139 end
140 % _________________ Save Spectra and Time tables
141
142     myfile{index} = fopen(savefile,'wt');
143     fprintf(myfile{index}, 'Frequency  \t InSnorm \n');     ...
        %SpecResAxis{index} ;InSnorm{index}
144     fprintf(myfile{index}, ' %g \t %g   \n',FFTTable);
145     fclose(myfile{index});
146
147     timedatatable = [rate' strain' sig2];
148
149     savefile2{index} = ['Timedata' char('_') 'g=' ...
        num2str(Amp{index}) 'w=' num2str(w) '.txt' ];
150     myfile{index} = fopen(savefile2{index},'wt');
151     fprintf(myfile{index}, 'rate  \t strain \t stress \n');     ...
        %SpecResAxis{index} ;InSnorm{index}
152     fprintf(myfile{index}, ' %g \t %g \t %g  \n',timedatatable');
153     fclose(myfile{index});
154
155 end                     % end of strain amplitude loop
156
157 FigureName = ['omega = ' num2str(w) ' rad_s-1'];
158
159 savefile = [fileName  char('_') 'w=' num2str(w) '.txt' ];
160 %___________ collect and save results from individual strain ...
    amplitudes
161 matrixI31{w_index} = cell2mat([Amp; I1; Gp; Gpp; delta1; I31; I21; ...
    delta3; I51; delta5; Q;]);
162 %___________ note the 'append' call, data will not be overwritten
163 dlmwrite(savefile,matrixI31{w_index}','-append', 'delimiter','\t')
164
165 %_______    final plots for ...
    overview_____________________________________
166 figure('Name', FigureName,'Position', [scrsz(3)/10 scrsz(4)/10 ...
    scrsz(3)/1.4 scrsz(4)/1.4]);
167 subplot(2,1,1)
168
169 loglog(matrixI31{w_index}(1,:),matrixI31{w_index}(3,:)...
170     ,matrixI31{w_index}(1,:),matrixI31{w_index}(4,:));
171 set(gca,'fontsize', 15,'FontWeight','bold')
172 legend('G''','G''''');
173 xlabel('\gamma_0'); ylabel(['G''' ', ' 'G'''' [Pa]']);
174
```

```
175 subplot(2,1,2)
176 loglog(matrixI31{w_index}(1,:),matrixI31{w_index}(6,:),...
177     matrixI31{w_index}(1,:),matrixI31{w_index}(9,:), ...
178     matrixI31{w_index}(1,:),matrixI31{w_index}(7,:))
179 set(gca,'fontsize', 15,'FontWeight','bold')
180 legend('I_{3/1}','I_{5/1}','I_{2/1}');
181 xlabel('\gamma_0'); ylabel('I_{n/1}');
182
183
184 end    % end of w loop
185
186 disp('done :)')
```

The function *solver.m* is used in *ModelingScript.m* to calculate $\sigma(t)$ for LAOS excitation according to $\gamma(t) = \gamma_0 \sin(\omega t)$, specified by $\omega$ and $\gamma_0$. It contains the main model of Chapter 5 (Maxwell model with the Cox-Merz rule, Eq. 5.12) and the modifications with the power law viscosity (Eq. 5.16) and high frequency limiting viscosity (Eq.5.20) as well as the two relaxation time modification (Eq. 5.22). Which of the model is used can be set by a switch in *solver.m*.

***solver.m***

```
1  function [t, strain_o, rate_o, sig2]= solver(g0, G, lambda, ...
       lambda2, eta, eta_inf, alpha, f, nocy, s_rate)
2
3  %close all
4  % initial value, input signal, material parameters
5  sig_0 = 0;
6
7  w = f*2*pi;       % [rad/s]
8
9  rate =@(t) g0*w*cos(w*t);         % quick definition of rate function
10 strain = @(t) g0*sin(w*t);        % quick definition of strain function
11
12 tmax = nocy/f;                   %
13 Q = nocy*s_rate+1;
14 dt = tmax/(Q-1);
15 t = linspace(0,tmax,Q);
16 sig = zeros(Q,1);
17 sig(1) = sig_0;
18
19 % LIST of models
20 % 1   -  Maxwell type viscosity function using cox-merz = Main model
21 % 2   -  Maxwell model for code validation
22 % 3   -  nonlinear dashpot only carreau type, explicit calculation
```

```
% 4   -  Maxwell type viscosity function using cox-merz and high ...
    shear rate viscosity
% 5   -  spring + powerlaw dashpot
% 6   -  two relaxation times model
model = 1;  % choose model here
switch(model)

    case 1 % Maxwell type viscosity function using cox-merz = Main ...
        model
    h = @(t) eta.*sqrt(1./(1+lambda^2.*rate(t).^2)); % shear rate ...
        dependent viscosity
    f =@(t,y) (rate(t) - y./h(t))*G;   % differential equation
    options = odeset('AbsTol',1e-15, 'RelTol',1e-6);
    [T,sig2] = ode45(f, t ,sig_0,options);

    case 2 % Maxwell model for code validation
    f =@(t,y) (rate(t) - y/eta)*G;
    options = odeset('AbsTol',1e-15, 'RelTol',1e-6);
    [T,sig2] = ode45(f, t ,sig_0,options);

    case 3 % nonlinear dashpot only carreau type, explicit calculation
     sig2 = eta.*rate(t)./(1+(lambda.*abs(rate(t))).^alpha);
     sig2 = sig2';

    case 4
    % maxwell type viscosity function using cox-merz and high shear ...
        rate viscosity
    h = @(t) eta_inf + ...
        (eta-eta_inf).*sqrt(1./(1+lambda^2.*rate(t).^2));
    f =@(t,y) (rate(t) - y./h(t))*G;   % DiffEq.
    options = odeset('AbsTol',1e-15, 'RelTol',1e-6);
    [T,sig2] = ode45(f, t ,sig_0,options);

    case 5  % spring + powerlaw dashpot
    h = @(t) eta.*abs(rate(t)).^(alpha);
    f =@(t,y) G*(rate(t) - y./h(t)); % standard DiffEq. with shear ...
        rate dependend eta
    options = odeset('AbsTol',1e-15, 'RelTol',1e-6);
    [T,sig2] = ode45(f, t ,sig_0,options);

    case 6  % two relaxation times model
    eta = G*lambda2;    % uses lambda2 to set zero shear viscosity eta
    h = @(t) eta.*sqrt(1./(1+lambda^2.*rate(t).^2)); % shear rate ...
        dependent viscosity
    f =@(t,y) (rate(t) - y./h(t))*G;   % differential equation
    options = odeset('AbsTol',1e-15, 'RelTol',1e-6);
```

```
62      [T,sig2] = ode45(f, t ,sig_0,options);
63  end
64
65  rate_o = rate(t);
66  strain_o = strain(t);
67
68
69  end
```

The Fourier transform in *ModelingScript.m* is done by the function *Fourier_Transform.m*. For a signal $\sigma(t)$ this functions calculates the real and imaginary spectrum, $\Re(\omega)$ and $\Im(\omega)$. *Fourier_Transform.m* has been originally written by Randy H. Ewoldt (University of Illinois, Urbana-Champaign). It is published under the name *FTtrig_MITlaos.m* for the MITlaos software, version 2.1 (Ewoldt et al. 2007; Ewoldt 2009).

### *Fourier_Transform.m*

```
1  function[A0, An, Bn] = Fourier_Transform(f)
2
3
4  %------------
5  %   A0 = offset
6  %   An = real spectrum
7  %   Bn = imaginary spectrum
8  if int32(length(f)/2) == length(f)/2
9      %do nothing
10 else
11     %trim last data point to force even number of data points
12     %f MUST HAVE EVEN NUMBER OF DATA POINTS!
13     d=f; % d is placeholder
14     clear f
15     f = d(1:length(d)-1);
16     clear d
17 end
18
19 n=length(f);
20 N=n/2;        %N will be the number of harmonics to consider
21
22 Fn(n)=zeros; %initialize complex transform vector
23             % this will make it a ROW vector
24             % which is necessary for combination later
25
26 sizef = size(f);
27 if sizef(1) == 1 %if ROW vector
28     Fn = fft(f); %let Fn be ROW vector
```

```
else
    frow = f';
    Fn = fft(frow); %compute FT Fn=[ low > high | high < low ]
                    %force input to fft to be ROW vector
end
Fn_new = [conj(Fn(N+1))  Fn(N+2:end)  Fn(1:N+1)];
%rearrange values such that: Fn_new = [ high < low | low > high ]

Fn_new(:) = Fn_new(:)/n;  %scale results

A0 = Fn_new(N+1);
An = 2*real(Fn_new(N+2:end));    %cosine terms
Bn = -2*imag(Fn_new(N+2:end));   %sine terms
end
```

Additionally, if *ModelingScript.m* is to be used for the analysis of experimental data, the line which calls *solver.m* in *ModelingScript.m* can be commented out, instead experimental data can be read. This data has to be trimmed such that the stress signal comprises an integer number of oscillation cycles and the respective strain signal has a phase of zero, meaning that it starts at $\gamma(t = 0) = 0$. For this purpose *LAOS_Stress_Trimming.m* is used, which has also been written by Randy H. Ewoldt (*cycletrim_MITlaos.m* in the MITlaos package, Ewoldt et al. 2007; Ewoldt 2009). *LAOS_Stress_Trimming.m* trims $N$ cycles at the points where the strain changes the sign, resulting in $N - 1$ cycles, the respective stress signal is trimmed at the same data points. The trimmed data set has still a finite, albeit small, phase difference $\Delta\delta$ due to discretization during acquisition (Ewoldt 2013), which can be determined by an additional FT of $\gamma(t)$. Consequently, the corresponding experimental spectra of the stress signal $\Re_{exp}(\omega)$ and $\Im_{exp}(\omega)$ have to be corrected for this small phase difference according to Eqs. 8.1 and 8.2. This leads to the phase corrected spectra $\Re(\omega)$ and $\Im(\omega)$, which are referenced to perfect sinusoidal strain input. Note that for the numerically calculated signals this phase correction step was not necessary because the strain input is set to be a pure sine with zero phase in the calculations.

$$\Re(\omega) = \Re_{exp}(\omega)\cos(\Delta\delta) - \Im_{exp}(\omega)\sin(\Delta\delta) \tag{8.1}$$

$$\Im(\omega) = \Im_{exp}(\omega)\cos(\Delta\delta) + \Re_{exp}(\omega)\sin(\Delta\delta) \tag{8.2}$$

***LAOS_Stress_Trimming.m***

```
%%%%%%%%%%%%%%%%%%%%%%%%%%%%%%%%%%%%%%%%%%%%%%%%%%%%%%%%%%%%%%%%%%%%%%%%
%   Function to cut strain and stress signals to an interger number of
%   cycles such that strain starts at 0,
%   by detection of sign changes in the strain
```

```
5 %
6 %
7 %%%%%%%%%%%%%%%%%%%%%%%%%%%%%%%%%%%%%%%%%%%%%%%%%%%%%%%%%%%%%%%%%%%%%%%%
8 function [istrain, istress, instress, Ncycles, istart, istop] = ...
      LAOS_Stress_Trimming(strain,stress,nstress)
9
10 d_zero=[];  %location of sign changes
11
12 k=0;        %k is a counter for the number of times gamma changes sign
13
14 sign_gam = sign(strain);
15
16 for i = 1 : length(strain)-1
17     if sign_gam(i) ~= sign_gam(i+1)
18         k=k+1;
19         d_zero(k)=i+1;  %index location after sign change
20     end
21 end
22
23 lgth = length(d_zero);  % number of sign changes
24
25 if lgth/2 ~= round(lgth/2)   % Check if lgth is odd
26         istart = d_zero(1);     %set start of window
27         istop  = d_zero(end) - 1;   %set end of window
28         Ncycles = (lgth - 1)/2;      % calculate number of full cycles
29 else                            % lgh is even
30         istart = d_zero(1);     % set start of window
31         istop  = d_zero(end-1) - 1;     %set end of window
32         Ncycles = (lgth - 2)/2;      %calculate number of full cycles
33 end
34
35
36 %trim arrays of strain, stress and nstress according to the window
37 istrain = strain(istart:istop);
38 istress = stress(istart:istop);
39 instress = nstress(istart:istop);
40 end
```

# Danksagung/Acknowledgments

An dieser Stelle möchte ich allen danken, die mich bei dieser Arbeit unterstützt haben. Besonders erwähnen möchte ich:

- Prof. Manfred Wilhelm

  Vielen Dank für die Möglichkeit bei Ihnen zu promovieren und dafür, dass Sie seit der Vorlesung im Hauptstudium in mir die Begeisterung für die Polymerchemie und -physik geweckt haben. Ihre Ideen und die Freiheiten, die Sie mir während der Doktorarbeit gelassen haben, weiss ich sehr zu schätzen, denn so konnte ich mich mit vielfältingen Themen von der Kolloidchemie bis zur mathematischen Modellierung von rheologischen Experimenten beschäftigen. Neben der fachlichen Ausbildung haben Sie auch viel für mich persönlich getan: ein großartiger Auslandsaufenthalt, Kontakte zur Industrie, eigenständiges Schreiben und Reisen zu Konferenzen waren wichtige Eckpunkte meiner Zeit bei Ihnen, wofür ich sehr dankbar bin.

- Prof. Matthew E. Helgeson und Juntae Kim

  Dear Matt, dear Juntae, thank you very much for the terrific time in Santa Barbara and the opportunity to work with your nanoemulsions. During this time, I learned a lot about how things are going in the USA. Scientifically, our work combining colloidal science, rheology and scattering was challenging and fascinating.

- Prof. A. J. Giacomin

  Dear Jeff, we had a fun time this summer in 2014, when you were visiting, lots of barbecues and alcohol free Weißbier. You taught me about the corotational Maxwell model, which pulled me into the theoretical and modeling side of rheology, which I never anticipated. Thank you for that.

- Prof. Matthias Ballauff, Prof. Matthias Fuchs, Rabea Seyboldt und Miriam Siebenbürger

  Danke für die Bereitstellung der Dispersionen und die tolle Zusammenarbeit am MCT/LAOS Projekt. Die Kern-Schale Partikel waren ein fasznierendes System für rheologische Experimente und die Modenkopplungstheorie war ein spannender Einblick in die statistische Mechanik.

- Jennifer Kübel

  Thanks for great discussions during coffee breaks and on all other occasions, dinners and field trips. You're a vital part of the group's work and social life and I am grateful that you are with us. Also, thank you for proofreading my texts, the English language is not as easy it might seem.

- Kathrin Reinheimer

  Danke für die Betreuung während der Diplomarbeit und das Einarbeiten in die Welt der nichtlinearen Rheologie. Du hast mit deinem DFG Antrag für meine finanzielle Sicherheit während der Doktorarbeit gesorgt, vielen Dank auch dafür.

- Mahdi Abbasi

  Thank you for helping me with the numerical calculations and providing the analytical solution, an important part of the work on the modified Maxwell model.

- Nico Dingenouts

  Danke für die Unterstützung in allen Fragen zur Streuung.

- Alle Mitglieder der Arbeitsgruppe Wilhelm

  Vielen Dank für großartige Aktivitäten mit euch: die zahlreichen Filme, die wir geschaut und gedreht haben, die gebauten Doktorwagen und Grillabende, sowie die Konferenzbesuche. Auch eure technische Unterstützung im Bereich der Rheometer, der Software oder allen weiteren Analytikmethoden, war wichtig für das Gelingen meiner Arbeit.

- Prof. Norbert Willenbacher and seine Arbeitsgruppe

  Vielen Dank für die Möglichkeit bei Ihnen rheologische Experimente an den MCR Rheometern und am PAV durchführen zu können.

- Für die finanzielle Unterstützung durch die *Deutsche Forschungsgemeinschaft* und das *Karlsruhe House of Young Scientists* bin ich sehr dankbar.

Zuletzt möchte ich herzlich meinen Eltern, meinem Bruder und Dagmar dafür danken, daß sie mich in diesen Jahren fortwährend unterstützt haben.

# Publications and conference contributions

### Publications

Merger, D. and Wilhelm, M. (2014). “Intrinsic Nonlinearity from LAOStrain-Experiments on various strain and stress-controlled rheometers: A quantitative comparison”. *Rheol. Acta* 53, pp. 621–634.

Kim, J., Merger, D., Wilhelm, M., and Helgeson, M. E. (2014). “Microstructure and nonlinear signatures of yielding in a heterogeneous colloidal gel under large amplitude oscillatory shear”. *J. Rheol.* 58, pp. 1359–1390.

Giacomin, A. J., Gilbert, P. H., Merger, D., and Wilhelm, M. (2015). “Large-amplitude oscillatory shear: comparing parallel-disk with cone-plate flow”. *Rheol. Acta* 54, pp. 263–285.

Merger, D., Reinheimer, K., Grosso, M., Brader, J. M., Ballauff, M., Kim, J., Helgeson, M. E., and Wilhelm, M. (2015). “Colloid Process Engineering”. Ed. by M. Kind., W. Peukert, H. Rehage, and H. P. Schuchmann. Springer. Chap. Large Amplitude Oscillatory Shear Applications for the Characterization of Dispersed Systems, pp. 113–142.

Merger, D., Abbasi, M., Merger, J., Giacomin, A. J., and Wilhelm, M. (2015). “Simple scalar Maxwell-inspired model for Large Amplitude Oscillatory Shear”. *to be submitted to Rheol. Acta.*

**Conference contributions**

Merger, D., Reinheimer, K., Grosso, M., and Wilhelm, M. (2013). "Characterisation of emulsions and foams by FT-Rheology (oral presentation)". *84th Annual Meeting of The Society of Rheology.*

Merger, D., Kim, J., Wilhelm, M., and Helgeson, M. E. (2014a). "Microstructure and nonlinear signatures of yielding in a heterogeneous colloidal gel under large amplitude oscillatory shear (oral presentation)". *Annual European Rheology Conference.*

Merger, D., Kübel, J., Reinheimer, K., and Wilhelm, M. (2014). "Application of FT-Rheology to the Characterization of Foams (poster)". *SEPAWA Congress and European Detergents Conference.*

Merger, D., Reinheimer, K., Grosso, M., and Wilhelm, M. (2014b). "FT-Rheology, a nonlinear mechanical characterisation method for polydisperse emulsions (poster)". *SEPAWA Congress and European Detergents Conference.*

Merger, D., Kim, J., Wilhelm, M., and Helgeson, M. E. (2015a). "Microstructure and nonlinear signatures of yielding in a heterogeneous colloidal gel under large amplitude oscillatory shear (oral presentation)". *Jahrestagung der Deutschen Physikalischen Gesellschaft.*

Merger, D., Kim, J., Wilhelm, M., and Helgeson, M. E. (2015b). "Rheo-SANS investigation of a polymer mediated nanoemulsion gel (poster)". *Frontiers in Polymer Science.*